SCUOLA DI DOTTORATO
UNIVERSITÀ DEGLI STUDI DI MILANO-BICOCCA

Dipartimento di
Fisica

Dottorato di Ricerca in Fisica e Astronomia Ciclo 30

Curriculum in Fisica Subnucleare e Tecnologie Fisiche

TOSCA NEUTRON GUIDE AND SPECTROMETER UPGRADE

Cognome: Pinna Nome: Roberto Simone

Matricola: 708837

Tutore: Prof. Dr. Francesco Terranova

Cotutore: Prof. Dr. Giuseppe Gorini

Supervisor: Dr. Svemir Rudic

Coordinatore: Prof. Dr. Marta Calvi

ANNO ACCADEMICO 2017 - 2018

UNIVERSITÀ DEGLI STUDI DI MILANO-BICOCCA

Department of Physics

Ph.D. Program in Physics and Astronomy - XXX cycle

Applied Physics

TOSCA NEUTRON GUIDE AND SPECTROMETER UPGRADE

Ph.D. Thesis of

Roberto Simone Pinna

Tutor: Prof. Dr. Francesco Terranova

Co-tutor: Prof. Dr. Giuseppe Gorini

Supervisor: Dr. Svemir Rudic

Coordinator: Prof. Dr. Marta Calvi

Academic Year 2017 - 2018

Contents

Acknowledgments

The author gratefully acknowledge the UK Science & Technology Facilities Council for financial support, access to beam time at ISIS, and use of the e-Science SCARF cluster at the Rutherford Appleton Laboratory. This work has been partially supported within the framework of past and present CNR-STFC agreements for collaborative research between Italy and ISIS. I also thank all the members of the Molecular Spectroscopy group for the scientific support and the ISIS Engineering group that offered technical information and consultancy. This work would not have been possible without the financial support given by the University of Milano-Bicocca and the scientific guidance provided by the local Plasma Physics group.

Abstract

TOSCA is an indirect-geometry inelastic neutron spectrometer optimised for high resolution vibrational spectroscopy in the region between 0 and 4000 cm^{-1} [1, 2]. In its current form the instrument has been operational for almost two decades and during that time has set the standard for broadband chemical spectroscopy with neutrons [3]. In autumn 2013 as part of the international beamline review it was concluded that for TOSCA to be able to participate in strategic research areas, an increase in the incident neutron flux via the provision of a neutron guide was essential. Such a development would allow detailed studies of the industrially relevant systems containing weak neutron scatterers as well as faster parametric studies, particularly for hydrogen containing molecules such as hydrocarbons. Additionally, studies of smaller samples which cannot be produced, or are too expensive to produce, in larger quantities would be possible [2]. Since then, this major upgrade has been implemented and has involved the complete redesign of the TOSCA primary spectrometer to house a state-of-the-art, high-m neutron guide and associated chopper system to boost the incident flux. The instrument was closed between the end of May 2016 until mid-February 2017 when the installation of the final (so called C2) configuration was completed. After the two weeks of commissioning measurements the instrument was returned to the user programme. By the end of November 2016, all sections of the guide were in place, apart from the new TOSCA shutter that contains the initial section of the guide, in this phase the latter remained the same as before the upgrade. Since the overwhelming majority of the guide was installed we have tested the setup for enhanced neutron flux, as well as in order to have a better idea about the influence of the guide inside the shutter (installed subsequently) on the neutron flux, beam profile, spectral resolution and background. We will refer to this interim configuration as the C1 configuration, while the configuration before the upgrade will be denoted as C0. The entrance of the new 1.937 m long shutter is positioned at a distance of 1.626 m from the moderator centre, and the shutter contains a $m = 5$ straight square guide with an aperture of 100 mm x 100 mm. The remaining nine sections of the guide are tapered, starting from the 100 mm x 100 mm entrance of section 2 all the way to the end of section 10 with 40 mm x 40 mm aperture (positioned at a distance of 16.262 m from the moderator center, i.e. 0.748 m from the sample position). The angle of 0.136494^{o} [4] has been kept equal in each section, while the m-factor was increased in steps from $m = 5$ for sections 2 to 6, $m = 6$ for sections 7 to 9, and $m = 7$ for section 10. The data show good beam homogeneity at the TOSCA sample position, thanks to our efforts on the theoretical guide design to ensure that the chain of reflections causes minimal beam profile

inhomogeneity. As a result of the guide being installed on TOSCA the neutron flux at the sample position has been significantly increased. The experimental gain in neutron flux is 6 times for neutrons with wavelength of 0.5 Å, 46 times for neutrons with wavelength of 2.5 Å, and 82 times for neutrons with wavelength of 4.6 Å, i.e. the most significant gain is for the low energy neutrons used to study low energy molecular vibrations and collective motion within the lattice (phonons).

A further upgrade requires the redesign of the TOSCA secondary spectrometer, and their combined effect will be to improve the utilization efficiency of the neutron source. The consequence of each step in the upgrade process can be evaluated by means of calculations and measurements, i.e. benchmark experiments. The flat analyzer currently used on TOSCA can be approximated with a square shape with an area 144 cm^2, and the centre of the analyzer surface is placed at a 45° grazing angle and at an average distance of 320 mm with respect to the sample. The analyzer is made of highly oriented pyrolythic graphite (HOPG) and the chosen reflection plane is the (0, 0, 2) that has a lattice spacing of 3.354 Å. The analyzer crystal has a rocking angle full width at half maximum (mosaic spread) of 2.5°. This material is particularly suitable for the specific reflection of cold and thermal neutrons thanks to its high reflectivity and sharp diffraction peaks. The reflectivity for a 1 mm thick HOPG crystal can exceed 74% and HOPG finds a number of important applications for 4.5 Å, that coincides with the fixed wavelength of the TOSCA secondary spectrometer. The current INS banks are also equipped with a beryllium filter and cadmium foils to cut the higher wavelength harmonics diffracted by the analyzer. Furthermore, each beryllium filter is cooled to 30 K to improve the beryllium transmission. In the current configuration, the analyzer and the filter are very close together, which partially explains the original choice for a small analyzer, but this feature strongly limits the neutron collection efficiency of the assembly. In this Ph.D. project, the TOSCA spectrometer upgrade focused on the design of a double bent analyzer and a new beryllium filter by means of the McStas software. In order to proceed with the simulation of the new analyzer we had to create a custom component which can meet the TOSCA needs. We used several HOPG tiles arranged on a parametric surface that can follow two different curvatures, namely spherical and parabolic. Several simulations were performed by means of this component, in order to study the performance of the future TOSCA setup; HOPG analyzer with different areas and radii of curvature were considered and each parameter has been optimized independently via numerical analysis. We found that, with the appropriate focusing and mosaicity, it is possible to increase the current analyzer area and to achieve a large gain in the detected flux. From the calculations, it seems that for larger analyzers the parabolic geometry outperforms the spherical geometry thanks to its better focusing properties. This performance can be further increased by tuning the HOPG mosaicity to expand the analyzer bandwidth and simulations show that an order-of-magnitude overall gain is within reach. Furthermore, the gain from a curved analyzer can be considerably improved when an optimal HOPG mosaicity is chosen, to enable a more efficient use of the scattered beam. This im-

portant upgrade can be achieved with limited effects on resolution, thanks to the extensive optimization we performed on the curved geometry, namely the multi-parametric optimization in this study has been computationally implemented using the MATLAB package in conjunction with the McStas software. That proved necessary since the future wide curved analyzer needs extensive calculations to assess its time and energy focusing capability with respect to the parallel plane geometry that TOSCA currently implements. In relation to the current setup, the shape of the future curved analyzer could expand radially to accomplish the shape of the 60° INS module. Our calculations focused initially on three different configurations of double-bent analyzer having different surface extensions up to an area of 1450 cm^2; for each case a parabolic and a spherical curvature were considered and thus a total of 6 different configurations were studied so far. This route for the TOSCA upgrade appears feasible and a similarly large HOPG monochromator (1428 cm^2) with horizontal and vertical spherical curvature has been successfully implemented at NIST, which represents a significant advance in double focusing technology and a great improvement in the efficiency of the MACS [5] instrument.

The author can be contacted at pinna.robertosimone@gmail.com.

List of attached papers

- Pinna RS, Rudic S, Parker SF, Gorini G, Fernandez-Alonso F. Monte Carlo simulations of the TOSCA spectrometer: Assessment of current performance and future upgrades. EPJ Web of Conferences, 2015.
- Druzbicki K, Pinna RS, Rudic S, Jura M, Gorini G, Fernandez-Alonso F. Unexpected Cation Dynamics in the Low-Temperature Phase of Methylammonium Lead Iodide: The Need for Improved Models. The Journal of Physical Chemistry letters, 2016.
- Pinna RS, Rudic S, Capstick MJ, McPhail DJ, Pooley DE, Howells GD, Gorini G, Fernandez-Alonso F. Detailed characterisation of the incident neutron beam on the TOSCA spectrometer. Nuclear Instruments and Methods in Physics Research Section A: Accelerators, Spectrometers, Detectors and Associated Equipment, 2017.
- Pinna RS, Rudic S, Parker SF, Armstrong J, Zanetti M, Skoro G, Waller SP, Zacek D, Smith CA, Capstick MJ, McPhail DJ, Pooley DE, Howells GD, Gorini G, Fernandez-Alonso F. The neutron guide upgrade of the TOSCA spectrometer. Submitted to Nuclear Instruments and Methods in Physics Research Section A: Accelerators, Spectrometers, Detectors and Associated Equipment, 2017.
- Pinna RS, Rudic S, Zanetti M, Zacek D, Parker SF, Gorini G, Fernandez-Alonso F. Monte Carlo Simulations for the TOSCA Secondary Spectrometer Upgrade. RAL Technical Report, RAL-TR-2017-013, 2017.

- Pinna RS, Zanetti M, Rudic S, Parker SF, Armstrong J, Waller S, Zacek D, Smith C, Harrison S, Gorini G, Fernandez-Alonso F. The TOSCA Spectrometer at ISIS: The Guide Upgrade and Beyond. Journal of Physics: Conference Series, 2017.

1. Introduction

This chapter is meant to give the reader a general introduction to the neutron properties, basic theory of neutron scattering, with particular consideration on thermal neutrons. We also discuss the techniques employed for neutron production, detection and shielding.

1.1. Neutron Physics

1.1.1. Neutron properties

The neutron is a subatomic hadron particle and the interaction of neutrons with matter depends on their energy (see Tab. 1.1), hence a convenient classification method is based on the kinetic energy. In particular, thermal neutron properties open the possibility to perform measurements that are complementary to other probes, such as X-rays and optical light [6].

- Thermal neutrons have wavelength comparable to lattice spacing in solids. Therefore, they offer an ideal probe for determining the atomic arrangement in condensed matter and for studying excitations mode, such as phonons and magnons in crystals.
- They have a weak interaction with matter and thus a high penetration capability. This allows the study for the bulk properties of materials.
- The atomic scattering amplitude is not linked to the number of shell electrons. Therefore the magnitude of the interaction changes for different isotopes of an element, and allows for isotopic composition studies.
- The neutron magnetic moment interacts with the magnetic moment of unpaired electrons, allowing the study of magnetic properties in materials.

The wavelength λ of a neutron is related to its velocity v through the de Broglie relation Eq. 1.1 [6].

$$\lambda = \frac{h}{m_n v} \tag{1.1}$$

Classification	Kinetic energy range
High energy neutrons	> 40 MeV
Fast neutrons	100 KeV - 40 MeV
Slow neutrons	1 - 100 keV
Epithermal neutrons	0.2 eV - 1 keV
Thermal neutrons	0.025 eV - 0.2 eV
Cold neutrons	0 - 0.025 eV

Table 1.1. – Classification of neutrons depending on energy [6].

Lifetime τ	886 $\pm$ 1 s
Rest mass m_n	939.57 MeV
Wavelength λ	1.798 Å at 2200 m/s
Energy E	25.3 meV at 2200 m/s
Spin S	1/2
Magnetic moment μ_n	-1.913043 nuclear magnetons

Table 1.2. – Main properties of the neutron [6].

Lifetime

A neutron not bound to other nucleons is an unstable particle and it decays in a β^- process. As a beta-emitter, it decays spontaneously into a proton, an electron and an electron anti-neutrino Eq. 1.2 [6].

$$n \rightarrow p^+ + e^- + \overline{\nu}_e \tag{1.2}$$

The neutron lifetime, see Tab. 1.2, is denoted by parameter τ and corresponds to the time after which $1/e$, or 0.37 of the original population remains.

$$N(t) = N(0)e^{-\frac{t}{\tau}} \tag{1.3}$$

In the scientific exploitation of neutrons, the magnitude of the decay time does not constitute a problem since the time taken by neutrons to traverse the distance from source to detector is typically much less than their half-life.

1.1.2. Neutron scattering

Energy

The kinetic energy of a neutron defines a characteristic wavelength that determines the interaction properties of the neutron. Using the neutron wavelength defined by the De Broglie law, the corresponding kinetic energy E, which is $\frac{1}{2}mv^2$, is given by

$$E = \frac{h^2}{2m_n\lambda^2} \tag{1.4}$$

Assuming that $E = k_bT$, where E is in given in eV and T is given in Kelvin, one can calculate that at room temperature, 300 K, the energy of a thermal neutron is normally distributed around 0.025 eV.
The atoms in a solid material are not perfectly stationary, the thermal motion causes the motion of an atom from its equilibrium position and also collective vibrations can propagate in the lattice of the solid. The energy associated with these waves is distributed in packets of energy called phonons, which are collective excitations of the crystal lattice. In the inelastic scattering of neutrons, an exchange of energy between neutrons and nuclei causes these excitations and a phonon is generated or absorbed in the sample, the neutron thus can lose or gain that fixed amount of energy. In molecular compounds this exchange of energy causes vibrations and rotations of molecules. Thermal neutrons are useful to study these excitations, as the typical exchange of energy is of the same order of magnitude as the initial kinetic energy of the neutrons.

Elastic incoherent scattering

In scattering by a single nucleus, as pictured in Fig. 1.1, a neutron can be represented as a plane wave $\psi(z) = e^{ikz}$ traveling in z direction incident to a nucleus in origin O. The result of the interaction is a spherical wave $\psi'(r) = -\frac{b}{r}e^{ikr}$ centered in the nucleus position, where b is the *scattering length* of the nucleus, r the distance from the nucleus and k the wavenumber. In this case we assume that the nucleus is fixed so that the scattering is elastic.

In the Born approximation, only a fraction of the incidents neutrons interacts because the nuclear potential is short range and depends on the time a neutron spend in the proximity of a nucleus. When a plane wave moves accross a lattice of nuclei, diffracted waves are generated from each nucleus and constructive interference occurs if the path difference between the scattered waves equals the wavelength of the incident plane wave. The same constructive interference appears also if the path difference equals an integer multiple of the wavelength. This leads to the Bragg law, Eq. 1.5 and Fig. 1.1

$$n\lambda = 2dsin\theta \tag{1.5}$$

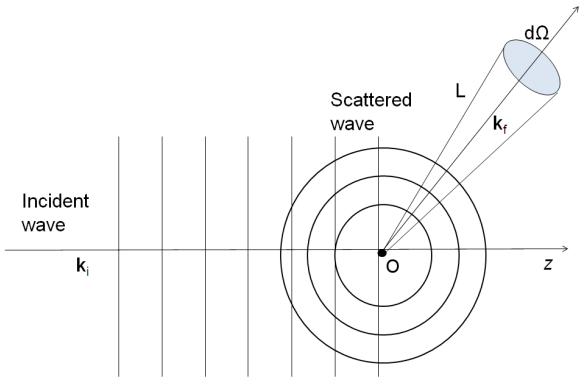

Figure 1.1. – The scattering of a plane wave of neutrons by a single nucleus.

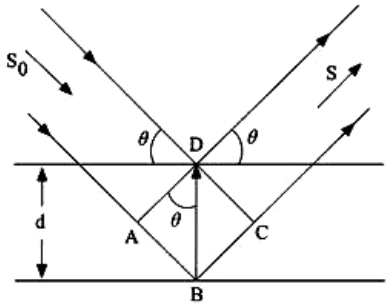

Figure 1.2. – Plane wave incident and reflected by two lattice planes at the angle θ. The constructive interference between the reflected waves occurs only if the Bragg condition is met.

where λ is the neutron wavelength, n is an integer, d is the lattice spacing and θ is the angle of incidence.

We could also account for the thermal motion of the nuclei, which causes a decrease in intensity I of the diffracted beam because the scattered waves may have the phase scrambled by the random motion of nuclei. The Bragg law is indeed affected by lattice thermal vibration, to account for this d is replaced by the average value $< d >$ and the peaks intensity I is reduced, see Eq. 1.6. The Debye-Waller W factor was introduced to take into account this intensity dampening and it increases with the material temperature.

$$I = I_0 e^{-2W} \tag{1.6}$$

Coherent and incoherent scattering

To quantify the interaction probability of a neutron, one should first consider the scattering length b of the target nucleus, which determines its cross section with respect to the scattering of a neutron. The different isotopes of a chemical element have their own characteristic scattering lengths, while the nucleus spin also

influences the scattering length in relation with the spin of the incident neutron. In a typical compound the existence of various isotopes and spin effects gives rise to coherent and incoherent scattering effects. As shown in Fig. 1.3, the coherent part determines interference effects and shows space and time relationships between different atoms, its pattern is composed of peaks (e.g. Bragg peaks). The incoherent part arises from the deviation of the scattering lengths from the mean value of the material, it does not cause interference so its pattern is a flat background and gives information about the properties of individual atoms [6]. The scattering cross section differentiated with respect to the scattering angle can be written as

$$\frac{d\sigma}{d\Omega} = \sum_{j,j'} < b >^2 \, exp\left[i\mathbf{Q} \cdot (\mathbf{r}_j - \mathbf{r}_{j'})\right] + \sum_{j} \left(< b^2 > - < b >^2 \right)_j \tag{1.7}$$

Where $\mathbf{Q} = \mathbf{k}_i - \mathbf{k}_f$ and $\mathbf{r}_j$ is the position of the j-th nucleus.

The first summation in Eq. 1.7 describes the coherent scattering component, in which there is scattering from each nucleus in $\mathbf{r}_j, \mathbf{r}_{j'}$. In this picture each nucleus possess a scattering length equal to the average of the compound <b>. The second summation represents the incoherent scattering component, interference peaks are not possible and its magnitude is determined by the mean-square deviation of the scattering length from its average value [6].

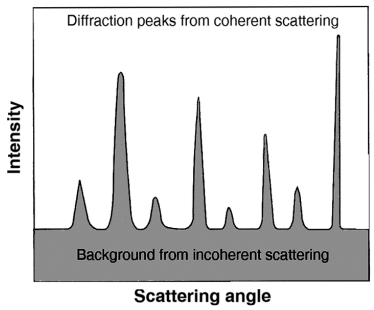

Figure 1.3. – A schematic diffraction pattern for neutron scattering.

Inelastic scattering spectroscopy

In inelastic neutron scattering (INS) the initial and final wavevectors are different ($\mathbf{k}_i \neq \mathbf{k}_f$), so the momentum transferred is

$$\hbar\mathbf{Q} = \hbar\left(\mathbf{k}_i - \mathbf{k}_f\right) \tag{1.8}$$

while the transmitted energy is

$$\hbar\omega = E_i - E_f = \frac{\hbar^2}{2m}\left(\mathbf{k}_i^2 - \mathbf{k}_f^2\right) \tag{1.9}$$

Thus a scattering event is characterized by $(\mathbf{Q}, \omega)$ and because of the energy conservation law there is only one accessible region of the $(\mathbf{Q}, \omega)$ space. Thus the scattering law results

$$\mathbf{Q}^2 = k_i^2 + k_f^2 - 2k_i k_f cos\theta \tag{1.10}$$

which reduces to the Bragg law for elastic scattering ($k_i = k_f$).

Optical techniques like infrared and Raman spectroscopy are widely used for studying molecular vibrations and are completed by INS because the latter technique has a number of advantages in comparison to them [7].

- INS measurements are suitable to study hydrogen atom vibrations. In fact, optical techniques are mainly used to investigate heavy atoms, because of their high Z value, while they fail when the sample is made of light elements. On the other hand, the neutron scattering cross section on hydrogen is higher than any other atom.
- INS does not follow the rules of optical selection, all vibrations are theoretically measurable. Neutrons exchange momentum with the atom during the scattering process thus INS measurements are not confined to the Brillouin zone centre, like the optical techniques. The measured INS intensities are also sensitive to the relative concentration of components in the material.
- Neutrons have no charge and do not interact with shell electrons, while photons are easily scattered or absorbed. This give neutrons a good penetration capability and allows the study of bulk properties in samples.
- INS spectrometers can investigate the molecular vibrational range from 16 - 4000 cm^{-1}, see Fig. 1.4. In particular the energy range below 50 cm^{-1}, where infrared and Raman spectroscopies fail, is also accessible.
- INS experiments measure the scattering intensity as a function of momentum and energy transfer. The INS spectrum is generally presented in neutron energy loss and energy is exchanged from the incident neutrons to the atoms in the material.
- If long range order in a sample is absent or complex, diffraction techniques are not effective and the INS spectroscopy can fulfill this task.

The drawbacks of such spectroscopic technique is the demand of time and effort, since the neutron facilities across the globe are rare.

1.1.3. Neutron guides

Given the absence of charge in a neutron, its trajectory is difficult to influence with interactions other than the nuclear forces, thus generally the neutron path to the sample is mostly rectilinear and the neutron flux undergoes a geometrical decrease.

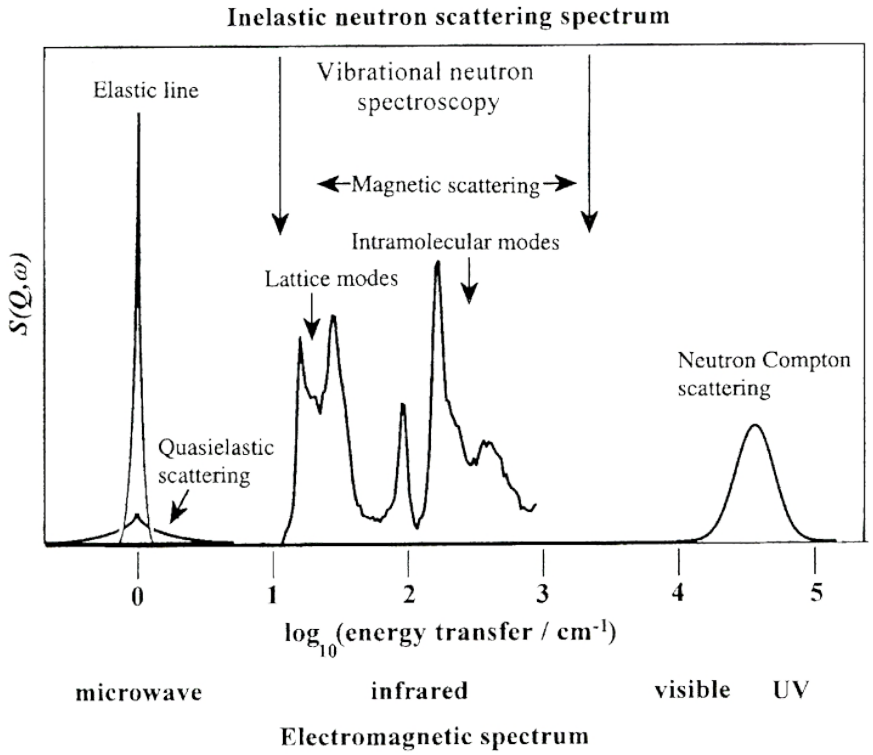

Figure 1.4. – INS spectrum in relation to optical spectroscopies. The vertical axis is the neutron scattering intensity expressed as the scattering function. Courtesy of Mitchell et al. [7].

With a collimation beam-line having a length d_i from moderator to sample, the neutron flux varies as $\frac{1}{d_i^2}$. The evident need to keep d_i short can be obviated, at least for instruments requiring cold and thermal neutrons, by the use of neutron guides. These devices are tubes made of optically flat glass that has been appropriately coated. The principle behind this devices relies on the total external reflection of neutrons from the metal surface. Neutrons with scattering angles lower than the critical angle of reflection γ_c relative to the guide surface are retained within the guide walls, see Eq. 1.11

$$sin\gamma_c \approx \gamma_c = \lambda \cdot \sqrt{\frac{< \rho_N >< b_{coh} >}{\pi}} \tag{1.11}$$

where λ is the neutron wavelength in Å, $< \rho_N >$ is the mean numerical density of scattering atoms and $< b_{coh} >$ is their mean coherent scattering length.

Neutron guides are useful to

- Optimize the utilization of the source.
- Optimize the use of spaces.
- Curve the neutron beam (if curved guides are in use).

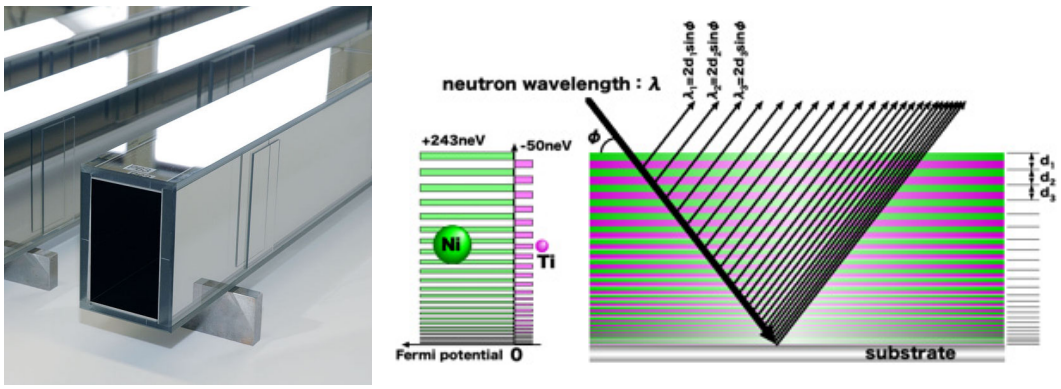

Figure 1.5. – Appearance of a supermirror neutron guide of rectangular cross section (left) and multilayer coating of a supermirror which leads to multiple constructive interference enhancing the reflection capability of the surface. Courtesy of Swiss Neutronics.

The law of total reflection is well known for electromagnetic waves and the total reflection is also possible for neutrons, although with much smaller reflection angles. The coating material originally used for the guides is ^{58}Ni since this has a large value of $< b_{coh} >$ and hence $\frac{\gamma_c}{\lambda} \approx 0.1\,\text{Å}^{-1}$. Moreover, given the wavelength dependence in Eq. 1.11, a degree of energy selection is inevitably introduced and this makes the nickel guide ineffective for the energies needed in vibrational spectroscopy. Nevertheless this problem can be reduced thanks to the supermirror technology, which employs alternating layers of materials with different scattering length and density; usually ^{58}Ni and ^{48}Ti are the materials of choice to manufacture the layers, see Fig. 1.5. This process increases the critical angle by a multiplication factor m, which is the ratio of the critical angle of the supermirror with respect to the nickel. The value m has steadily improved over the years and the state-of-the-art supermirrors presently have $m = 8$. Such devices constitute a considerable opportunity to increase the efficiency of neutron instruments, see Fig. 1.6. For supermirrors, the critical angle of reflection for neutron is predicted roughly by Eq. 1.12

$$\gamma_c = m \cdot \lambda \cdot \sqrt{b \cdot \rho} \tag{1.12}$$

where b is the average scattering length of the nuclei in the coating, ρ is the density of the guide material and m is the ratio mentioned above. γ_c is the angle between the guide surface and the direction of the incident neutron, every neutron which collides against the surface with an angle lower than γ_c will be likely reflected.

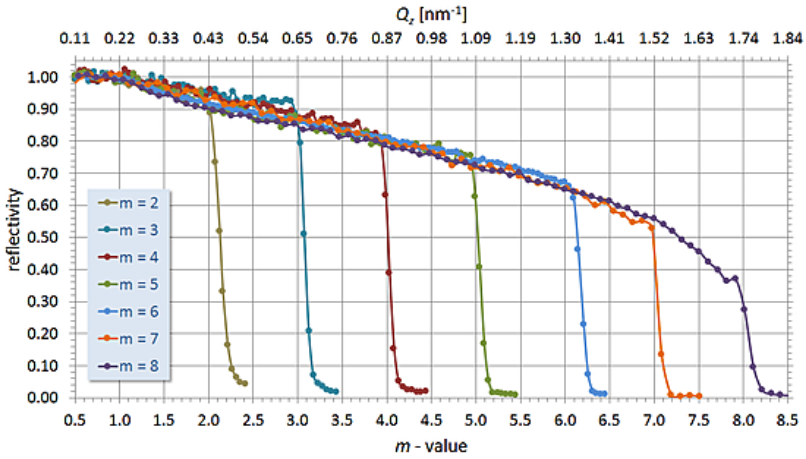

Figure 1.6. – Guide reflectivity curve for different m values. Courtesy of Swiss Neutronics.

1.2. Instrument systems

Neutrons are unique particles because they are neutral and penetrate deeply into matter. The consequent disadvantage is that neutrons are difficult to stop, either to detect and eliminate. On TOSCA, high efficiency ^{3}He detectors are in use, these unique detectors allow TOSCA to improve its use of the neutron beam because they ensure that most of the neutrons scattered in their direction will be effectively detected.

1.2.1. Neutron detection

An important requirement of a particles detector is that it should detect only the particles of interest and an ideal detector would discriminate between particles of different energy. This is not possible in most neutron detectors because they use nuclear reactions triggered by neutrons and the energy of the particle is generally a tiny fraction of the energy generated by the nuclear reaction. All methods rely on neutron induced reactions to produce the charged particles that ionize the surrounding medium. The most used reactions are:

$$n +^3 He \rightarrow {}^3H + {}^1H + 0.77\, Mev \quad \sigma_{th} = 5330\, barns$$

$$n +^6 Li \rightarrow {}^4He + {}^3H + 4.79\, Mev \quad \sigma_{th} = 940\, barns$$

$$n +^{10} B \rightarrow {}^4He + {}^7Li + \gamma(0.48\, Mev) + 2.3\, Mev \quad \sigma_{th} = 3840\, barns,\ P = 93\%$$

These reaction cross sections are strongly dependent on the incident neutron energy E and have roughly a $1/\sqrt{E}$ dependence [8]. Two main kinds of neutron detectors exist, gas chambers and scintillation detectors. ^{3}He and ^{10}B (in the form of BF_3) are used in gas chambers and ^{6}Li is used in scintillators. For research purposes the BF_3 is not widely used because of its low detection efficiency and safety concerns, while for vibrational spectroscopy ^{3}He gas chambers are commonly used. To reduce errors due to false detection, the electrical pulses from the detector are sorted by the electronics. The common method is to discriminate against signals that are too weak or too strong, so the fast analogue electronics set a lower and a higher level of discrimination to accept and transmit the signals in-between. Every signal transmitted is stored as a count.

Scintillator detectors

On instruments a lithium glass scintillator is often used as a beam monitor. All neutron instruments require beam monitors to measure the incident flux. There may also be a transmission monitor after the sample. Since the incident flux should remain as high as possible, monitors are nearly transparent to neutrons. Monitors can be either a low pressure ^{3}He tube or a low efficiency scintillator. For cases where the limitations of helium tubes pose a problem, scintillator detectors are used instead. These are solid state detectors where the ^{6}Li is doped into a scintillating glass, usually ZnS, which emits photons when the ions generated by the nuclear reaction pass through it. The photons are thus detected and converted into electrical signals by a photomultiplier tube (PMT). The PMT can be attached directly to the scintillator or can be remotely coupled to it by a light pipe, lens or fiber optic system. The scintillator material is denser than a gas so it can be much thinner (1 mm is typical), hence their spatial resolution is more accurate. Unfortunately scintillators are sensitive to light and gamma rays and their PMT also requires shielding against magnetic fields.

Helium detectors

Fig. 1.7a shows an example of ^{3}He neutron detector. The assembly consist of a grounded steel chamber filled with pressurized ^{3}He gas and an anode wire along the axis of the tube, the gas pressure is usually around 10 bar. Between the wire and the chamber walls, a high voltage (1800 V) is applied. Once a neutron crosses the chamber, if it is involved in a nuclear reaction, a proton and a triton are produced with high kinetic energy. These energetic ions cause further ionization inside the chamber and the resultant free electrons are promptly accelerated by the electric field towards the anode, they in turn generate other charges along their path (avalanche effect). This charge multiplication guarantees a signal gain up to 10^5 and allows the detection of a single neutron [8].

Fig. 1.7b shows an idealized output from a helium tube. In the keV range there are a large number of events from gamma ray ionization. One can see steps at 0.19 MeV

and 0.58 MeV, and a large peak with a sharp cut-off at 0.77 MeV. Conservation of momentum requires that the proton and triton are emitted in opposite directions and the total energy released, 0.77 MeV, is partitioned as 0.58 MeV to the proton and 0.19 MeV to the triton. Because of the detector walls two steps can be seen in the spectrum, they correspond to the event where the triton or the proton is trapped by the detector wall before traveling a significant distance in the gas. The intense peak at 0.77 MeV is where both particles contribute to the ionization and maximize the electric pulse collected at the anode. ^{3}He chambers can also be arranged in an array to obtain a position sensitive detector. When discriminating which tube detects the neutron, it is possible to have information about the position in a single direction. To measure the position along a single tube a resistive wire is used as central anode. The charge collected by a single neutron event travels along the wire towards both ends. The spatial resolution in such an assembly is typically 10 - 20 mm, this resolution is generally worse than other kind of detectors [6]. ^{3}He tubes present some advantages in neutron spectroscopy, namely they are insensitive to gamma rays and magnetic fields and they have a low background ($\sim$ 4 counts/hour for the class installed on TOSCA). Some disadvantages of this kind of detectors can be the spatial resolution mentioned above and the presence of a blind zone at both ends of the tube because of the electrical connections. It is worth to observe that these detectors are not suitable for high count-rate applications, because of the slow positive ion drift speed. However, for vibrational spectroscopy this is not a problem because count-rates are generally tolerable for these devices.

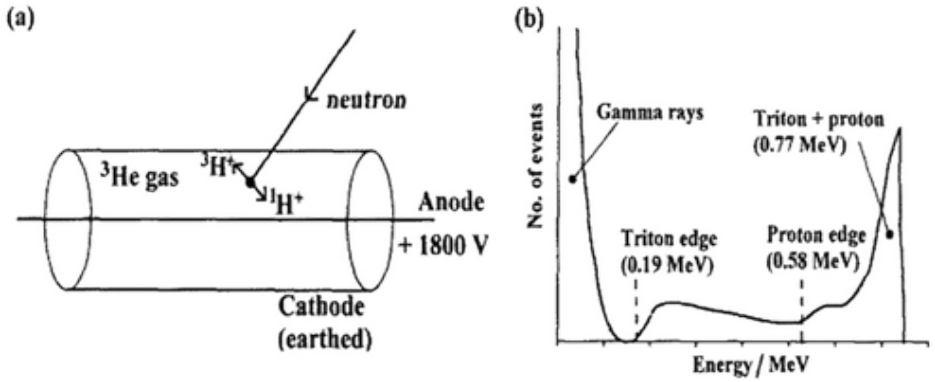

Figure 1.7. – a) Schematic of ^3He gas tube and b) its idealized pulse height spectrum.

1.2.2. Neutron background suppression

Ideally, detectors would only be exposed to neutrons that carry information about the sample; all the other neutrons simply contribute to the instrument background and they must be reduced to a minimum. This goal is achieved by using appropriate shielding. The neutron shielding exploits the moderation process followed by absorption. In general, slower neutrons are more easily absorbed, in fact most materials

have a $(velocity)^{-1}$ dependence to their absorption cross section. As explained in [7], boron, cadmium and gadolinium are the most common materials used to shield instrument components from neutrons. The three elements have different absorption behavior. Fig. 1.8 shows their absorption cross sections as a function of energy; metal shielding materials are often chosen upon their neutron-capture resonances, most metals have several resonances, usually at MeV energies. Cadmium presents a low energy resonance and this metal is effective in absorbing low energy neutrons. Its main disadvantage is the emission of gamma rays that requires further shielding. Boron is a typical $1/v$ absorber, thus it is effective for thermal neutrons and is used in mixture with a moderating compound. For bulk shielding, borated wax tanks are used; when this material solidifies it has sufficient mechanical strength to be used as a structural element in the beamline, while having excellent shielding properties. Boron is also used as B_4C particles in resin; the resin content varies depending on the application. Low resin content (4-10 wt %) is used when it is important to absorb rather than scatter neutrons. Nevertheless, to shield small items, borated polyethylene can be used. Furthermore, gadolinium has a considerable absorption cross section at low energies and has nuclear resonances at high energies. However, it is expensive and is often found as gadolinium paint to provide an additional layer of shielding.

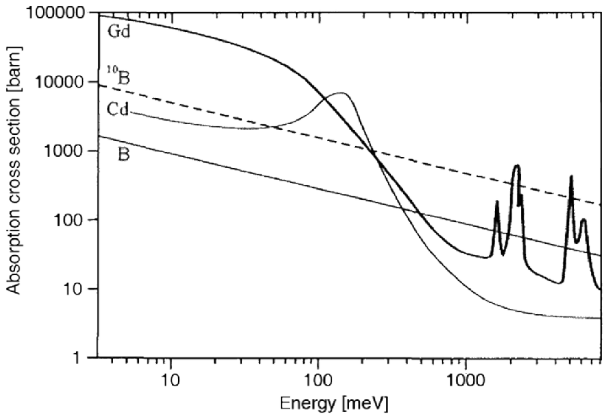

Figure 1.8. – Absorption cross section of boron, cadmium and gadolinium as a function of energy.

1.3. ISIS neutron source

The ISIS pulsed neutron and muon source at the Rutherford Appleton Laboratory in Oxfordshire is owned and operated by the Science and Technology Facilities Council (STFC). Across the globe, the spallation neutron sources are less common than reactor sources because spallation facilities have a high complexity and are difficult to run and maintain. In many cases, the two types of source are complementary because of the different spectrum and brilliance they produce. The main feature of

spallation sources is the pulsed nature of the beam; this allows use of broadband time-of-flight spectrometers which can achieve high neutron energy resolution in a wide range of energies.

1.3.1. Spallation process

In Fig. 1.9 one can see a schematic representation of the spallation process, in which a high-energy proton pulse from an accelerator bombards a heavy material target. Protons hit the nuclei in the target and leave them in a highly excited state, causing the emission of nucleons and gamma radiation as de-excitation products. Typically a single incident proton results in about 1000 collisions in the target and its surrounding components [9]. Moreover, the incident protons can trigger an intranuclear cascade, where pions and nucleons are emitted. Some neutrons, emitted by these nuclear reactions will leave the target, whilst other neutrons will instead lead to further reactions within the target. The high-energy proton range in the target is in the order of 10^1 cm, thus the neutron yield is high. In fact, each proton that crosses the target causes the emission of about 20 - 30 neutrons [10]. This process results in a very intense neutron pulse and only a limited heat generation compared to reactor source. At ISIS spallation neutron source, the time averaged heat production within the target is about 160 kW, but during the pulse, the neutron flux exceeds that of the most advanced steady state sources. The power of a reactor with an equivalent steady flux would be 16 GW [7]. Neutrons produced at ISIS emerge from the target with an average energy of ~ 2 MeV and theoretically they can reach energies up to the proton beam energy (800 MeV).

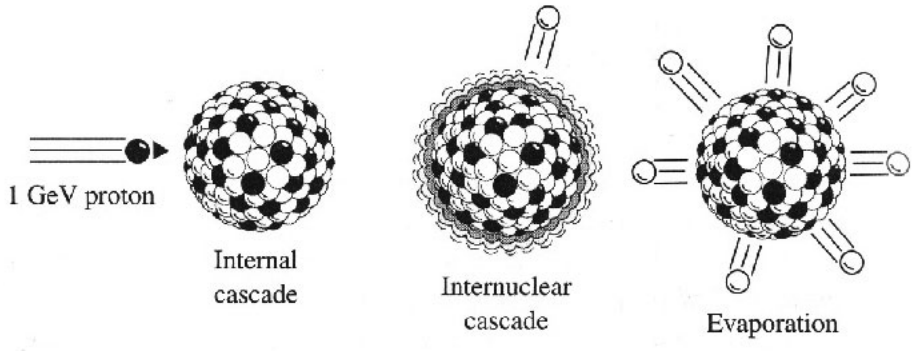

Figure 1.9. – Diagram which shows the process of proton spallation on heavy nuclei.

The Fig. 1.10 shows the ISIS facility, constituted from four main sections: the linac, the synchrotron, the Target Station 1 (TS-1) and Target Station 2 (TS-2). The first two sections perform the main processes that lead to the production of the 800 MeV proton beam.

The generation of the proton beam starts in the ion source, where H^- ions are produced from a plasma discharge that causes dissociation of H_2 gas and subsequent

electron transfer from a caesium-coated cathode that sits on a high voltage platform at -35 kV. The ion source uses a gaseous mixture of hydrogen and caesium. The role of the caesium is to reduce the workload of the cathode, enhancing its capability to donate electrons to the positively charged hydrogen ions, and thus improving H^- production. The beam passes through a 90 degrees magnet that removes any free electrons from the beam. The system delivers $\sim$ 50 mA H^- current pulses that are $\sim$ 200 – 250 μs long at the repetition rate of 50 Hz. The particles energy at the end of this section is 35 keV [11].

The 35 keV H^- ions are extracted by an electric field towards a quadrupole radio-frequency (RFQ) accelerator which operates at 202.5 MHz and accelerates the beam to an energy of 665 keV. The discrete bunches of H^- ions are then injected into the linear accelerator (linac). Similar to the RFQ, the ions acceleration in the linac is provided by high intensity radio-frequency fields. The linac accelerates the beam up to 70 MeV (37% of the speed of light), generating pulses of H^- with duration of 200 - 250 μs [12]. During the extraction from the linac, the beam passes through an aluminium oxide foil, in order to strip all the electrons from the H^- ions and thus to obtain a proton beam. At this point the proton beam is injected in the synchrotron.

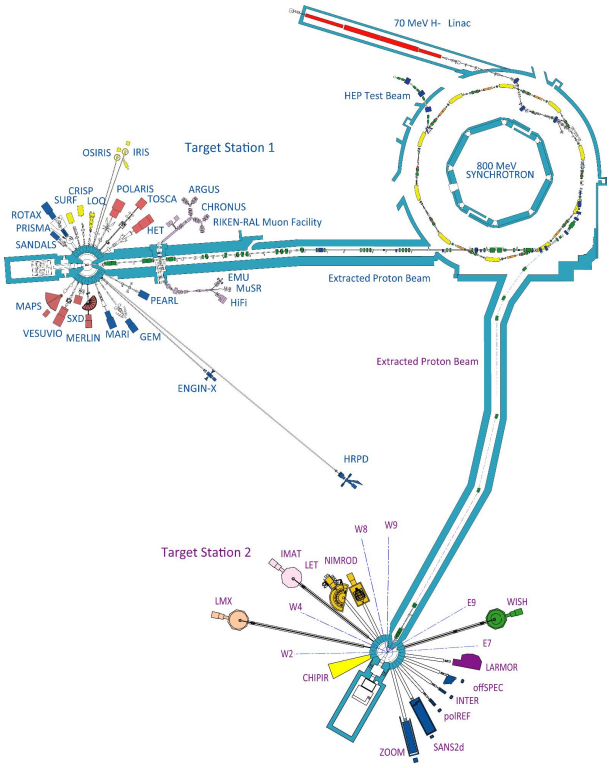

Figure 1.10. – Schematic drawing of the ISIS facility, the Linac, the Synchrotron, TS-1 and TS-2. In each target station are operational instruments for elastic and inelastic neutron scattering, absorption, diffraction, transmission and reflectometry studies. Courtesy of ISIS Neutron and Muon Source.

ISIS synchrotron is a 52 m diameter ring that for a single pulse receives the beam from the linac during 130 cycles to allow the accumulation of $4.2 \cdot 10^{13}$ protons with limited spatial charge effects [7]. Once the accumulation is completed, protons are confined in two bunches and accelerated up to 800 MeV (84% of the speed of light). This acceleration is performed in 10 ms by 10 radio-frequency resonant cavities that provide an electrical potential of 140 kV, in order to accelerate the protons at each revolution inside the accelerator ring. Simultaneously, ten dipole bending magnets force the beam to travel on a circular orbit, and quadrupole magnets keep the beam tightly focused. The proton beam makes around 10000 revolutions prior to being extracted from the synchrotron by the kicker magnets. In these magnets the current is raised from 0 to 5 kA within 100 ns. In this transient, an intense magnetic field is generated in order to send the proton beam towards the target stations. Just before the extraction from the synchrotron, the two bunches are separated by 230 ns and they have a duration of 100 ns, these constitute a single beam pulse with a total time-width of 430 ns. One beam pulse is sent toward a target station every 20 ms (a frame). As shown in Fig. 1.11, all the protons from the synchrotron are then transported along a 155 m long extracted proton beamline (EPB-1) to TS-1, or along a second extracted proton beamline (EPB-2) 143 m long, into which one pair out of every five pairs of proton pulses is deflected by a *septum magnet* from EPB-1 and transported to TS-2 [11]. In the EPB-1 the proton beam is lifted from the synchrotron and it is shaped to produce a 70 mm spot on the target in TS-1 [9]. ISIS neutron source can reach an average proton current of 200 μA distributed in 50 pulses per second, a time averaged neutron flux of $2 \cdot 10^{13} \frac{n}{s\,cm^2}$ and a peak flux of $8 \cdot 10^{15} \frac{n}{s\,cm^2}$ [7], see Fig. 1.12.

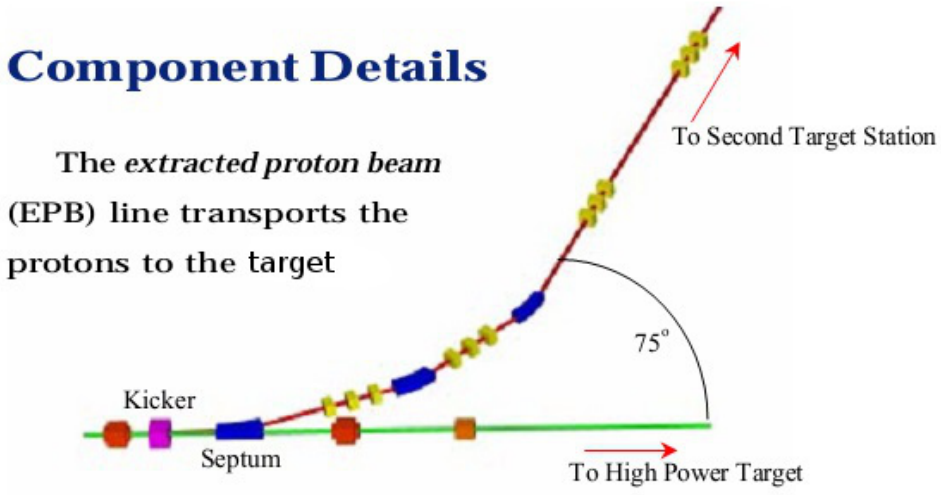

Figure 1.11. – Section of ISIS beam-line which allows the diversion of the proton beam; please note that one pulse out of five is redirected towards TS-2.

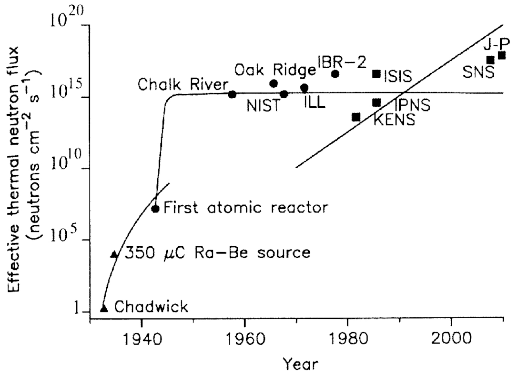

Figure 1.12. – Effective thermal neutron flux in different facilities. Courtesy of Mitchell *et al.* [7].

Target

ISIS was originally built with a depleted uranium neutron-producing target, but in the early 1990s the target material was changed to tantalum, and more recently in 2001 to tantalum-coated tungsten. ISIS targets are at the end of the extracted proton beam, each target consists of several thin plates that are surrounded by a D_2O which acts as a coolant. The coolant is necessary because the average heat load sustained by the target is 160 kW and its temperature can reach 600 K at the centre line [10]. The target lies within the beryllium reflector, with small moderators below and above it. Neutrons produced in the target pass through the moderators and lose their energy in each collision with the nuclei. The neutrons exiting from the moderator towards an open neutron port can reach the instrument and so these can be used for the experiments. Otherwise, neutrons have a chance to be reflected back into the moderator by the beryllium reflector or can possibly escape the target assembly. The target assembly is heavily confined and shielded. The biological shielding required in spallation neutron sources is larger than the one in fission reactor sources, because most of the neutrons emitted from the target remain unmoderated and thus highly energetic and very penetrating [8]. The average energy of the neutrons emerging from the target is about 2 MeV and the duration of each fast neutron pulse is $\sim$ 100 ns. The exact spectrum is unimportant for determining the moderated neutron spectrum, but it is fundamental to the design of the biological shielding. In TS-1, around the target there are 4 moderators and 18 beam channels, 9 per side, which feed the neutron scattering instruments.

As mentioned before, depleted uranium targets with a suitable cladding have also been used. Compared to tungsten, the use of uranium is more advantageous since it gives a larger (up to double) neutron yield per proton. That is a consequence of fission reactions that occur in uranium even after the proton pulse. As a result, the uranium target produces an almost continuous neutron beam that can be useful for some instruments, as well as detrimental for instruments which need low background.

Additionally, there is an intermediate target along the EPB-1, which is 1 cm thick

graphite sheet and is employed to produce muons. It is oriented at 45° in the beam and is placed ∼ 20 m before the neutron-producing target. Upon collision the proton beam produces pions in the graphite and subsequently pions decay to muons [11].

1.3.2. Moderators

The choice of the moderator determines the spectrum provided by the beamline. The moderators are placed above and below the target. As shown by Fig. 1.13, they have small dimensions with a volume of about 0.5 liters and are surrounded by a cooled beryllium reflector which scatters neutrons back into the moderators and increase the actual flux of neutrons. The moderators contain a low molecular weight material, in order to make the neutrons lose energy as quickly as possible. Thus a material with high slowing down power and/or high moderation ratio is required. The moderators in use at ISIS are made of liquid H_2O, liquid CH_4, solid CH_4 or liquid H_2. In TS-1 there are four moderators in total:

- Two moderators above the target, 300 K liquid H_2O.
- Two moderators below the target, 110 K liquid CH_4 and 20 K liquid H_2.

In TS-2 there are two moderators with dimensions of 150 x 150 x 30 mm^3 combined with two ambient water pre-moderators:

- One above the target at 40 K, containing solid CH_4.
- One below the target at 17 K, containing liquid H_2.

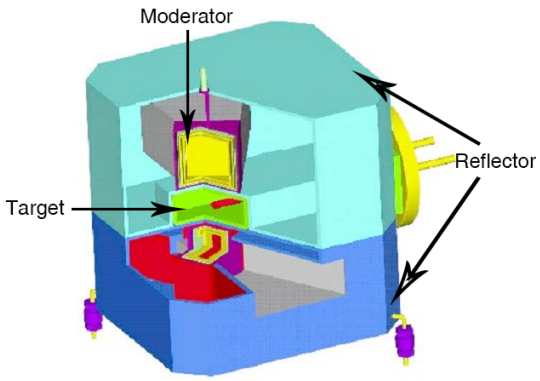

Figure 1.13. – TS-1 Neutron source assembly. Target (green), beryllium reflectors (blue and aquamarine), moderators (violet). Courtesy of ISIS Neutron and Muon Source.

Each moderator provides neutrons with an energy distribution that resembles the Maxwell-Boltzmann distribution at the temperature of the moderator. Ideally, the neutrons coming from the target pass through the moderator and they reach the thermal equilibrium with the material by collisions with the nuclei. Clearly, the high

energies involved and the limited dimensions of the moderators leave a significant part of the neutrons under-moderated, so a high-energy tail (epithermal neutrons) is observed in every spectrum collected at spallation neutron sources. As with reactor sources, the neutrons initially produced in the target are very energetic (average energy $\sim$ 2 MeV) and must be moderated to useful energies. A major difference between spallation and reactor sources is that the pulsed source moderators are very small and thermal equilibrium is not fully achieved, as explained above. The small size of the moderators also means that all neutrons are created within a very short period of time, this period determines the pulse width. Short pulse widths, $\sim$ 10 μs, are essential for good energy resolution. Moderators run at different temperatures to produce peak neutron flux at different energies. Water moderators at$\sim$ 300 K produce peak fluxes at 200 cm^{-1} (25 meV, 1.81 Å), liquid methane ($\sim$ 100 K) at 70 cm^{-1}(9 meV, 2.56 Å) and dihydrogen ($\sim$ 20 K) at 20 cm^{-1} (2.5 meV, 5.72 Å) [6]. The flux distribution, $J(E_i)$, of the ISIS moderators is shown in Fig. 1.14. In the Maxwellian region, the distribution is described by

$$J(E_i) = X_n \left(\frac{E_i}{(k_b T_{eff})^2} \right) exp \left(-\frac{E_i}{k_b T_{eff}} \right) \tag{1.13}$$

where X_n is the integrated Maxwellian intensity, T_{eff} is the effective moderator temperature and k_b is the Boltzmann constant. The values of T_{eff} for the different moderators are: H_2O, 390 K; CH_4, 128 K; H_2, 32 K. These are slightly higher than the measured moderator temperature showing that the neutrons are not fully moderated.

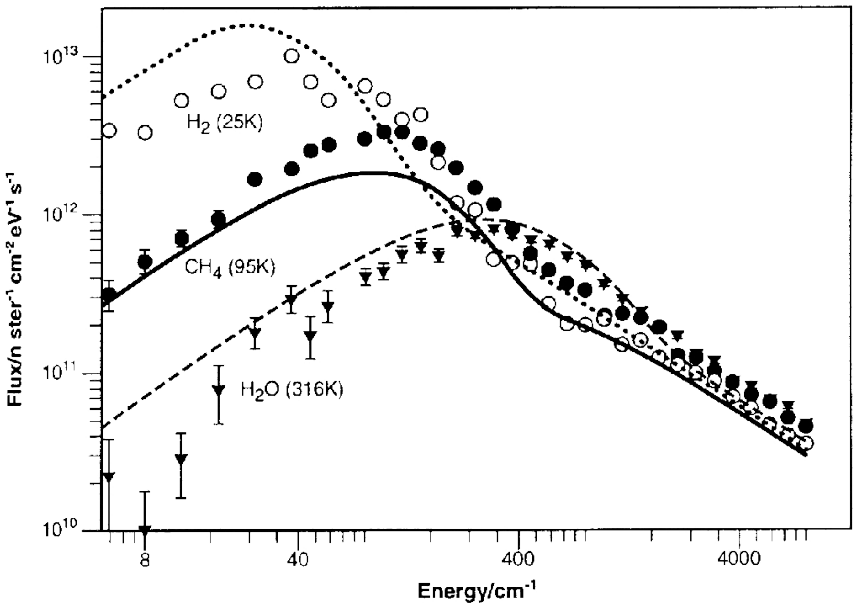

Figure 1.14. – Flux spectrum from the TS-1 moderators in the Maxwellian region. The points are measured data, the lines are from Eq. 1.13. Courtesy of Mitchell et al.[7].

1.3.3. Spallation and reactor source

Research nuclear reactors use thermal neutrons to induce fission in a critical mass of a fissile material, for instance ^{235}U, to produce high-energy (fast) neutrons.

$$n + ^{235}U \rightarrow 2.5\, n_{fast} + fission\, products + 200\, MeV$$

Of the average 2.5 neutrons produced per fission event, one is required to maintain the nuclear reaction, 0.5 neutrons are lost to absorption and one is available to leave the core and be used experimentally. One of the most powerful research reactors is at the Istitut Laue Langevin (ILL, Grenoble, France), which has a power of 57 MW. However, 20 MW research reactors are more common. The fast neutrons from fission have an average energy of 2 MeV and are brought to lower energies (i.e. moderated) by multiple inelastic collisions in the D_2O coolant contained within the relatively large swimming pool. Neutrons achieve approximate thermal equilibrium with the moderator temperature (300 K) with a mean energy of 25 meV [10]. However, the distribution of thermal neutrons is not optimal for many experiments for which higher or lower energies are desirable. In fact, small and specialized moderators can be present within the ambient moderator pool. These moderators operate at temperatures different from the pool and produce their peak neutron fluxes at different neutron energies.

Reactor sources are much more common than spallation sources, and there are around 20 reactors that produce core fluxes larger than $10^{14}\, \frac{n}{s\, cm^2}$. Compared to a reactor, a spallation source has the advantage to produce a lower time averaged heat-load per spallation neutron. The neutron energy spectra produced by the two types of source is distinctly different as shown in Fig. 1.15. This difference allows these source to be complementary: in fact reactors produce mostly cold and thermal neutrons, while spallation targets produce high-energy neutrons. Nevertheless, vibrational measurements over the whole energy range require epithermal neutrons and spallation sources are the most suitable choice, but when the experiments are operated in a limited energy range, reactors can be an effective source. There are also political and environmental reasons, for instance fissile material is not required in spallation sources and less active waste is produced.

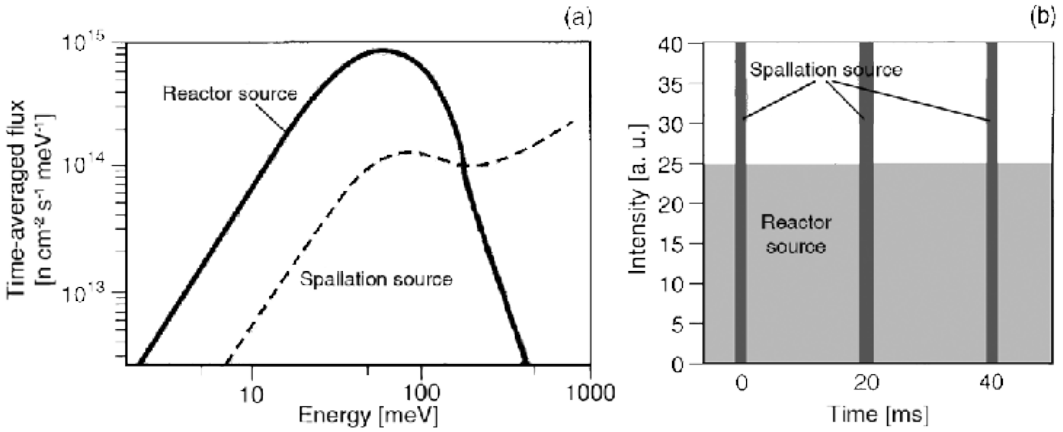

Figure 1.15. – a) Energy spectrum of reactor and spallation neutron sources. b) Time distribution of the neutrons from the two sources.

1.4. McStas

1.4.1. Monte Carlo method

Neutron scattering is a low signal technique due to its relatively low flux levels. Hence it is very important to optimize the neutron instrumentation through neutron ray-trace simulations such as McStas. Analytical methods are often used to simulate instruments with a small number of optical elements by the use of phase-space theory. This approach reaches its limit with a high number of optical elements, due to increased coupling between neutron parameters becoming ever stronger as discussed by P. Willendrup [13]. Monte Carlo methods have been recognized as a powerful tool in performing calculations that are normally too complex for an analytical approach and require great amount of effort to compute. The Monte Carlo technique is used in the determination of numerical solutions to problems that cannot be solved classically, and it is often required in the design and optimization of neutron instruments. McStas works by the principle of probability sampling (Monte Carlo method) where, for instance, neutron scattering events are densely probed over all neutron trajectories resulting in estimates of measurable quantities. An example of the Monte Carlo method for the determination of an integral is shown below. The integral function is solved at n random points (avoiding bias) and then the resulting values are summed. It gives a numerical approximation to the integral in Eq. 1.14

$$\lim_{n\to\infty} \frac{1}{n} \sum_{i=1, a\leq u_i\leq b}^{n} f(u_i) = \int_a^b f(u)du \tag{1.14}$$

where u_i is a randomly chosen value according to Monte Carlo sampling in which $f(u)$ is a finite continuous integral function with limits between a and b.

Since 1950s and the appearance of powerful computers, Monte Carlo methods gained an ever increasing amount of attention as they allowed more precise predictions of physical experiments [13]. Presently, neutron scattering instrumentation consists of a series of materials that propagate neutrons from a source to a detector. This is where statistical sampling becomes important, and Monte Carlo methods are the set of statistical tools used for computational modeling of such cases. It is based on a simple idea of probability sampling of the incoming neutron trajectories. Integrating over all neutron trajectories of a given system results in measurable quantities. The basic principle of Monte Carlo integration is to statistically integrate a given function over some domain D. Monte Carlo integration picks random points over a simple domain D', which contains D. Suppose D is a circle and we desire to evaluate its integral numerically with Monte Carlo. Now suppose D' is a rectangle of dimensions to perfectly fit the circle. Evaluating the integral of the rectangle is simple compared to the circle, it is simply equal to L^2. Now suppose we have a source of neutrons located some distance away from our square. Monte Carlo propagates neutrons by the use of random number generators. In our particular case we are interested in propagating neutrons randomly towards the square. Thus the total number of neutrons incident on the circle inside our square divided by the number of neutron incident on both the circle and the square gives us the ratio of the two integrals [14]. In the ideal case this ratio is equal to the area $\pi \left(\frac{L}{2}\right)^2$ of the circle divided by the area L^2 of the square. The more neutrons our source propagates, the more accurate the statistics of Monte Carlo integration. For complex neutron instruments it is usually necessary to simulate many millions or billions of neutrons to achieve good statistics at the final detectors.

1.4.2. McStas neutron ray-trace package

McStas is a software package designed to perform Monte Carlo simulations of neutron scattering instruments of high complexity. McStas is available for Windows, Macintosh, and UNIX/Linux systems. MatLab was used in conjunction with McStas to visualize the instrument geometry in a 3D view. McStas is a versatile neutron ray-tracing simulation software that offers the ability to determine accurate estimates of flux, resolution, optimization of parameters and designs where analytical calculations cannot be used. The software package was originally developed in 1997 at Riso, Denmark, and was later adopted by other institutions such as ILL in France and ISIS in the UK. Based on a meta-language specifically designed for neutron scattering, it is translated efficiently into ANSI-C which is then compiled into an executable, that performs the simulation. The meta-language allows the building of an instrument from individual components, where a library of standard components, maintained by its user community, is included as part of McStas. Each component

is programmed in C and serves the purpose of emulating a corresponding physical component, all of which compose a neutron scattering instrument [13]. Well-known examples of this include components such as moderators, guides, choppers, samples, analyzer crystals and detectors. Such components can also be designed by the user with their own specifications and then used in their instrument. An obvious advantage of neutron ray-tracing simulations is the ability to place monitors at any desired location to monitor the neutrons path, without influencing the beam.

The neutron weight and statistical uncertainty

McStas uses the idea of neutron weighting in order to perform fast simulations of complex instruments with large statistics. Neutron rays are assigned with a weight, and these weightings are adjusted according to their path. This means for example, a number of rays entering a component of a certain reflectivity, results in all rays reflecting in the component only that their weighting is adjusted according to this reflectivity. By this method, all rays are kept and lower statistics may be used in Monte Carlo simulations. In a real experiment of such an instrument, only those neutrons that are reflect would then be used, meaning that most neutrons up until that point are wasted. The Monte Carlo approach to simulation is that the neutron weight is adjusted to resemble the behavior of real physical properties. The weight representation can be made as follows

$$p_n = p_0 \cdot \prod_{j=1}^{n} \pi_j \tag{1.15}$$

where p_0 denotes the initial weight of a single neutron, p_n is its final weight after passing through the instrument and π the multiplication factor of the j-th component of the instrument. The resulting p_n is an estimate of the mean number of neutrons hitting the detector per second in a real experiment [13].

This mean number of neutrons hitting the detector is the intensity I

$$I = \sum_i p_i = N \cdot \overline{p} \tag{1.16}$$

Where p_i is the weight of the i-th neutron path, N the number of neutron rays per second and $\overline{p}$ the averaged neutron weight. This leads to an approximate statistical uncertainty of

$$\sigma(I)^2 \approx \sum_i p_i^2 \tag{1.17}$$

In McStas, the main detector parameters are:

- Spectrum: 2D or 3D plot of variables chosen by the user.
- Intensity: average number of neutron rays detected by a monitor per channel.

- I: total integrated neutron intensity.
- Err: error of the integral.
- N: total number of neutrons detected by a monitor.
- X_0: X-value at maximum intensity (peak value).

1.4.3. McStas components used for TOSCA

Moderator

For TOSCA the neutron beam emerges from a 300 K water moderator. The spectrum was simulated using a moderator component file created in 2013 by S. Ansell and G. Skoro (Neutronics Group, ISIS). The file was generated using MCNP-X and it provides a detailed model of the neutron beam emerging from the moderator of the beamline N8. The model resembles the flux intensity, the wavelength spectrum and the time structure of the real beam. The dimensions of the moderator aperture towards the beamline was set to 0.12 x 0.115 m^2. For this reason, for the neutron guide simulations the moderator was set to focus the neutrons on a 0.12 x 0.115 m^2 rectangle at 1.625 m from the moderator centre. In the diffraction and INS simulations the moderator focus was set directly onto the sample area to strongly improve the computational efficiency.

Neutron guide

During the TOSCA beamline upgrade, a neutron guide replaced the original collimator on the N8 beamline which serves this instrument [15, 4]. In order to simulate it, the component *guide* was used [16]. It models a rectangular guide centered on the Z-axis (direction of the beam) while the entrance lies on the X-Y plane. A neutron guide is characterized by two main aspects: its geometry and the internal coating. While the coating determines the reflectivity as a function of the momentum transfer, the geometry of the guide influences the angle at which a neutron impacts on the guide, and thus the final reflectivity. The guide component can be tapered and this geometry is rather suitable for the N8 beamline, which has a moderator face bigger than the typical sample dimensions of the instruments downstream, namely TOSCA and INES. This component allows to specify the desired m factor for the internal coating, where $m = 0$ means completely absorbing wall, $m = 1$ simulates a standard nickel guide and $m > 1$ means supermirror coating [17]. The simulated neutron guide has been divided in different sections, and it includes some gaps between them according to the engineering group upgrade design. This component is not inteded to also simulate the gravitational effect on the neutron beam, this choice is justified by the relatively short length of the guide which makes such effect negligible.

Geometries of the neutron guide other than linear and tapered are available; in our case the preliminary feasibility analysis excluded the use of elliptical or more

complex geometries, in order to focus our resources on an advanced supermirror coating of the guide. In fact, while the elliptic shape may lead to a relevant increase in the intensity transmitted to the target, it is more expensive to manufacture and it considerably increases the particles divergence at the target, as Liouville theorem dictates. Instead, a high-m guide coating still improves intensity by decreasing the absorption rate in the guide and with no added complexity.

Monochromators

Analyzer crystals, known in McStas as monochromators, provide an effective and simple way of selecting a monochromatic beam from a white beam. They work on the principle of the Bragg scattering, neutrons in this physical frame are treated like waves. If a neutron is incident on a crystal surface at an angle θ, depending on its λ it undergoes destructive or constructive interference. Thus only specific wavelengths are diffracted from the crystal at the same angle θ. This technique is commonly used on neutron-based instruments to produce monochromatic beams. Different scattering angles and different plane spacing of the crystal select different neutron wavelengths.

The McStas component used for TOSCA is the *monochromator curved* [16], it simulates an infinitely thin mosaic crystal which can be bent by specifying a radius of curvature. TOSCA has flat monochromators, consequently the radius of curvature is infinite. Nevertheless, *monochromator curved* was often used because it allows a higher grade of customization and gives results as accurate as *monochromator flat* component [18]. The component uses a small-mosaicity approximation and if specified it could take into account also higher order harmonics of the Bragg scettering The mosaic of the lattice, defined as angular deviation of crystal lattice planes from a perfectly ordered crystal structure, is anisotropic Gaussian, with different FWHMs in the Y and Z directions. Furthermore, *monochromator curved* allows the use of reflectivity and transmission tables of different materials. In the TOSCA model the HOPG reflectivity was used. In fact, the component works in reflection, but also transmits the non-diffracted beam.

In this project we also built custom curved monochromator component that lies on a parametric surface. It was used to simulate and design the upgrade of the TOSCA secondary spectrometer, the details of this work are presented in the scientific paper attached to this thesis [19].

Beryllium filter

The beryllium filter is installed on TOSCA to filter the higher harmonics coming from the HOPG analyzer. The filter is cooled to enhance the sharpness of the cut-off and to reduce the Debye-Waller factor which dampens the neutron scattering. In TOSCA McStas model, this filter could be simulated by placing in front of each detector a *PowderN* component of appropriate dimensions and set to the beryllium

scattering table, the Debye-Waller factor was also adjusted to resemble the measured temperature of the real filter.

Monitors

- Position Sensitive Detector (PSD Monitor): it is a position-sensitive monitor that detects incident neutron rays in an x-y plane split up into pixel columns (n_y) and rows (n_x). This monitor is not time dependent. It also indicates the total integrated intensity across the surface of the PSD together with the error associated with it.
- Divergence monitors: there are two different divergence monitors used, one monitor is the 1D divergence sensitive monitor which gives beam intensity as a function of horizontal divergence (deg). This allows the detailed analysis of homogeneity at its placement position to be investigated. By rotating such a monitor the vertical divergence can be measured. The second type is a 2D divergence sensitive monitor in which intensity is measured as a function of both horizontal and vertical divergence in degrees.
- Time-of-flight (TOF) monitor: it is a rectangular monitor that measures intensity as a function of TOF.
- TOF λ monitor: it is a 2D detector of intensity as a function of TOF and wavelength of neutron rays. Thus the wavelength-time distribution is readily extracted at the desired location.
- Wavelength and energy monitor: they are rectangular monitors that measure the wavelength and energy of incoming neutrons respectively.

2. TOSCA spectrometer

In this chapter we present the main features of TOSCA instrument, a neutron indirect geometry spectrometer located in TS-1 at ISIS Neutron and Muon source, Chilton, UK. This instrument has features that make it one of the most relevant spectrometer of its kind in the world. Such an apparatus consists of several modules that will be described below. In addition to the technical description of the apparatus we also present the calibration and efficiency checks that were performed as part of the Ph.D. project.

2.1. Introduction to TOSCA

TOSCA is an indirect geometry spectrometer for INS experiments which is used for vibrational spectroscopy and optimized to measure in the region between 0 meV and 500 meV. It has been part of the ISIS facility since the beginning of the research on the site, started in 1985 [20]. The first generation of the instrument was called TFXA and measured inelastic back-scattering with both time and energy focusing to achieve high resolution in the energy spectrum of interest [7]. During the period from April 1985 to February 1998, TFXA underwent several small upgrades that reduced the background and improved the resolution slightly. In 1998, it revealed necessary to implement a new instrument with greater sensitivity and improved resolution and these goals were subsequently achieved with the design of TOSCA [21]. This project was jointly funded by CNR (Italy) and HFCE (UK). The spectrometer was installed in two distinct phases, the first phase was TOSCA-I which showed a slightly improved resolution compared to TFXA and a greater surface area of detection, which resulted in a greater count-rate and better quality spectra [22]. The second phase was TOSCA-II, installed in 2000 and it is the current TOSCA secondary branch. This latest upgrade produced improvements in the resolution, due to the extension of the primary flight path from 12 m to 17 m which reduced the timing error in the time-of-flight (TOF). The sensitivity has been also increased thanks to the installation of 5 additional detector banks in the forward-scattering [7, 23].

TOSCA is located along the N8 beamline in the TS-1 at ISIS and its sample position is 17.01 m away from a room temperature water moderator which emits a pulsed beam mainly composed of thermal and epithermal neutrons. The neutrons scattered from the sample cover a wide range of wavelengths and they need to be energy

selected by a filtering system located around the sample. After the sample, the first device on the neutron path is a pyrolytic graphite crystal operated in reflection mode, which acts as a low-pass filter for the wavelengths, thanks to the Bragg diffraction principle. The instrument exploits the first harmonic of the Bragg diffraction; thus higher order neutrons are removed by a beryllium filter, equipped with cadmium foils to eliminate the cross-talk and kept at cryogenic temperature. This filter in turn acts as a high-pass filter for the wavelengths, and such configuration is intended to narrowly select the final energy at $\backsim$ 4 meV. This represents the working principle of an indirect geometry spectrometer, since it guarantees a direct relationship between energy transfer (E_T, cm^{-1}) and momentum transfer (Q, $Å^{-1}$) that occurs between the neutrons and the sample material, namely TOSCA has $E_T \sim 16Q^2$ [7]. The INS assembly on TOSCA is composed of ten banks, while each bank has 13 ^{3}He detector tubes. Five banks are placed in the forward-scattering position (i.e. at an average scattering angle of $\backsim$ 47.5°) and five in back-scattering (i.e. $\backsim$ 132.5°) [23] with respect to the neutron beam. At 9.455 m from the moderator, a double disk chopper is placed along the N8 beamline to block the slow neutrons tail of the first three pulses (out of four), in order to avoid the frame overlap between subsequent pulses. The fourth pulse is not chopped because it is followed by a 40 ms interval without new pulse, due to the last pulse of the frame being redirected towards TS-2. Hence the chopper does not cut the last TOSCA pulse, allowing the exploitation of the slow neutrons tail for the study of the elastic line ($E_N \sim 4$ meV, $E_T = 0$). The whole design of TOSCA was intended to achieve an unprecedented INS resolution ($\sim$ 1.25 % of E_T), see Fig. 2.1. This result was successfully achieved thanks to the combination of the factors listed below:

- Small time-width of the neutron pulse emerging from the target ($\sim$ 400 ns).
- Good moderation performance of the water moderator in terms of time required to emit neutrons of a certain wavelength ($\sim$ 12 µs/Å).
- Longer primary flight path which allowed reduction of the statistical errors in the TOF.
- Small bandwidth of the filter assembly.
- Detector geometry optimized to operate in time and energy focusing [23].

2.1.1. Moderator

TOSCA neutron beam is composed of a broad range of wavelengths (mainly below 6 Å), which are emitted by a water moderator kept at 300 K and poisoned by a thin gadolinium foil at a depth of 20 mm [23]. The water is contained in an aluminium vessel, placed above the tungsten target and encased in a beryllium reflector. The moderator outlet is 120 mm wide and 115 mm high [24]. The water moderator emits thermal and epithermal neutrons to the sample position with a moderation performance of $\sim$ 12 µs/Å [25]. As anticipated earlier, the main chromatic range of

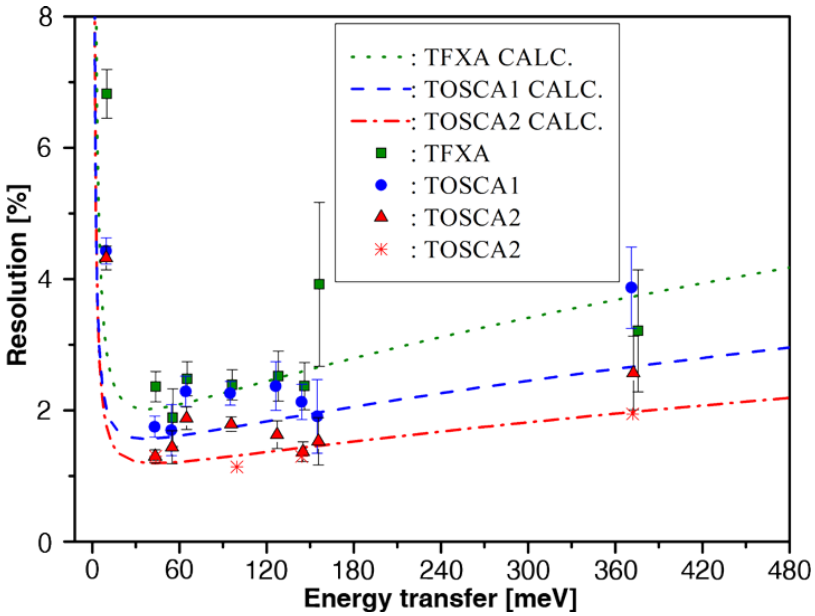

Figure 2.1. – Resolution spectra of TFXA, TOSCA-I and TOSCA-II in their operative range. The lines represent the analytical calculations.

the incident beam is broad, from 0.3 Å to 6 Å (from 2.5 meV to 1000 meV), that allows the study of a wide range of vibrational transitions in materials. Nevertheless, the major part of the incident neutrons and consequently the TOSCA main operative range is located between 0.4 Å and 5 Å (energies between 3 and 500 meV). Thus, the installation of a neutron guide was beneficial along the N8 beamline in order to increase the utilization efficiency of the beam and to extend the experimental capabilities of TOSCA.

2.1.2. Beam monitor

Along the TOSCA beamline a pair of beam monitors is placed, upstream from the sample and located before and after the beam chopper. These monitors analyze the TOF spectra of the neutron flux to perform the normalization of the experimental data, according to the moderator fingerprint. The detectors are composed of lithium dots embedded in scintillating glass. The neutron detection is performed by means of nuclear fragments emitted after the neutron absorption into lithium nuclei, as a result the positive charged fragments emitted by the reactions cause the photon emission (scintillation) of the glass matrix. The bunch of photons is measured by a photo multiplier tube (PMT) optically coupled to the glass, and the PMT generates an analog signal which in turn triggers a TOF counter. The main purpose of this detectors is to measure the neutron spectrum with minimal detriment on the neutron flux at the sample. Thus lithium is organized into small dots of Li_2O uniformly dispersed within the glass to reduce flux inhomogeneity of the transmitted beam. Furthermore the detector is specifically designed with a low detection efficiency.

In general, the typical specifications of the beam monitors in use are:

- Ratio of scintillating material to total area: R $\sim 10^{-5}$.
- Wavelength dependent attenuation coefficient: A $\sim$ 1 mm^{-1} $Å^{-1}$.
- Thickness: L $\sim 10^{-1}$ mm.

These parameters allow to calculate the calibration curve as a function of wavelength, which extrapolates from the detector data the actual wavelength spectrum incident on the sample. The number of neutrons detected N^{λ}_{det} at a certain wavelength is given by

$$N^{\lambda}_{det} = N^{\lambda}_{tot} E(\lambda) \tag{2.1}$$

Where N^{λ}_{tot} is the actual number of neutrons at wavelength λ that crossed the detector and $E(\lambda)$ is the detector efficiency function, Eq. 2.2, shown in Fig. 2.2.

$$E(\lambda) = R\left(1 - e^{-AL\lambda}\right) \tag{2.2}$$

Where R, A, L are the detector parameters mentioned earlier. Consequently, the actual number of neutrons with wavelength λ that reach the sample is given by

$$N^{\lambda}_{tot} = \frac{N^{\lambda}_{det}}{E(\lambda)} \tag{2.3}$$

On TOSCA these detectors measure the incident flux as a function of the elapsed time (TOF) with respect to the proton pulse t_0 mark, and the wavelengths of the detected neutrons are linearly obtained considering the measured TOF and detector distance from the moderator.

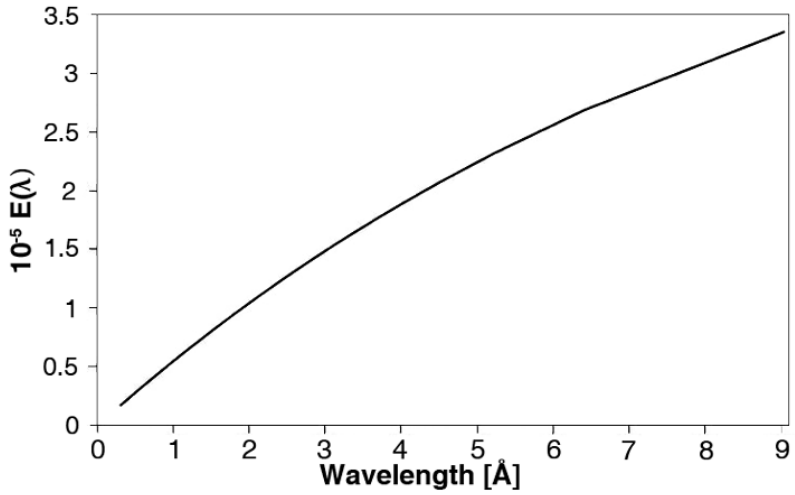

Figure 2.2. – Efficiency curve $E(\lambda)$ of the TOSCA beam monitor as a function of wavelength.

2.1.3. Beamline structure

In the original TOSCA beamline, the neutrons emitted from the moderator were sent to the sample along simple beam tubes. The first beam tube was placed as close to the moderator as possible, to maximize the intercepted flux and arranged in order to avoid a direct view of the target, in order to reduce gamma rays and fast neutrons background. Beam tubes do not influence the neutron trajectories and thus the flux is proportional to the solid angle subtended by the sample. Therefore, if the moderator to sample distance is d_i, the flux varies as $\frac{1}{d_i^2}$ and the incident flight-path must be kept as short as possible [7]. The collimation of a neutron beam is achieved by a series of rings made by neutron absorbing material, and these diaphragms define the beam size. B_4C rings were in use along the TOSCA beamline, and TOSCA original beamline was only partially evacuated to avoid the beam attenuation by air scattering. We estimate that the overall attenuation coefficient due to air was 0.53 (i.e. only 53% of the usable beam reached the sample).

Section	Distance (mm)	Length (mm)	Inlet opening (mm)	Outlet opening (mm)	Coating (m)
G1	1 626	1 937	100	100	5
G2	3 669	2 370	100	88.7	5
G3	6 050	1 530	88.7	81.4	5
G4	7 581	1 447	81.4	74.5	5
G5	9 131	317	74.0	72.5	5
G6	9 514	506	72.2	69.7	5
G7	10 031	2 069	69.7	59.8	6
G8	12 101	1 960	59.8	50.5	6
G9	14 062	1 750	50.5	42.1	6
G10	15 930	332	41.6	40.0	7

Table 2.1. – Technical specifications of the TOSCA guide geometry. Distances are measured from the moderator center to the guide inlet, and cross sections are all squared.

The TOSCA beamline has been upgraded with a supermirror neutron guide divided in 10 sections, see Tab. 2.1. The different sections are kept in vacuum and each vacuum vessel is sealed by thin aluminium windows. The guide geometry, see Fig. 2.3, and the coating of its internal surface, which determines the guide reflectivity, were designed on the basis of extensive Monte Carlo calculations [2]. The guide cross section is squared and also it is tapered from the monolith to the sample. It starts with a section of 100 x 100 mm^2 facing the moderator and ends with a section of 40 x 40 mm^2. The expected air attenuation coefficient is 0.94 and it has been improved thanks to the evacuation of all the guide sections. The entire flight path is surrounded by a biological shielding made of concrete and steel to stop the escaping radiation.

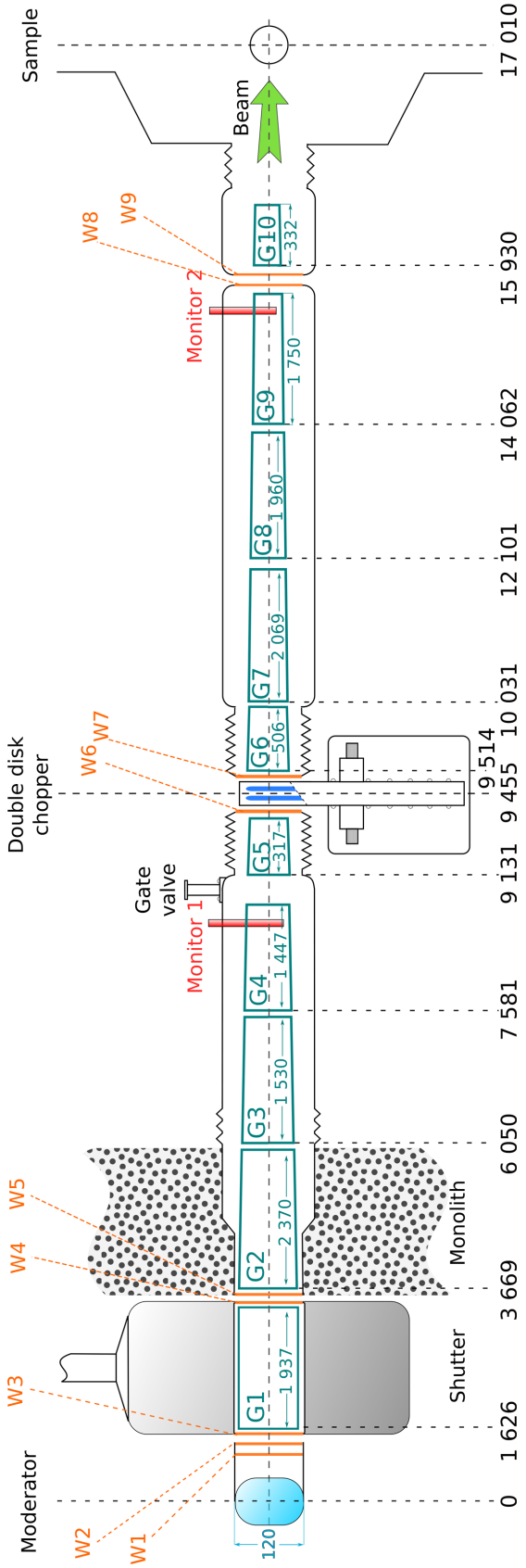

Figure 2.3. – Schematic view of TOSCA current beamline, the guide G1 is placed inside the shutter and it is straight, the following guides are tapered. All sections are enclosed into vacuum vessels that are separated by aluminium windows (depicted in orange). All units are in millimeters.

2.1.4. Chopper

The sample location at 17.01 m from the moderator allows a high spectral resolution but it restricts the energy transfer range to values above 3 meV (25 cm^{-1}). This occurs because the elastic line has a TOF of $\sim$ 23000 µs and since ISIS operates at 50 Hz, a neutron pulse occurs every 20000 µs (a frame), thus fast neutrons would overlap with slow neutrons from the preceding pulse. This is problematic for TOF analysis since the travel time dependency would be scrambled, making the measure unreliable. Nevertheless as TS-2 takes one pulse out of five from the accelerator, the resulting TS-1 input is composed of three 20000 µs frames followed by a 40000 µs frame. Thus such operation mode give TOSCA the capability to measure energy transfers below 3 meV during the last pulse. Hence a double disk chopper was designed to stop the slow neutron tail in the first four pulses and to allow them to pass during the fourth pulse. As a result of this design, the TOSCA dynamic range extends down to -3 meV, thus it includes the elastic line. This broader spectral range allows, for instance, TOSCA to be used for elastic and quasi-elastic neutron scattering studies [1]. Furthermore, the double disk chopper provides a faster transition time when chopping compared to single disk choppers, and this is beneficial for the overall resolution at low energy transfers.

Defining τ_{min} and τ_{max} the minimum and maximum flight time from moderator to detector selected by the chopper, the necessary condition to avoid overlap between subsequent pulses is $\tau_{max} - \tau_{min} \leq \tau$. Thus, the widest wavelength range accepted is given by Eq. 2.4

$$\Delta\lambda \leq \tau \left(\frac{h}{m_n L} \right) \tag{2.4}$$

where τ is the duration of a frame, h is the Planck constant, m_n is the neutron mass and L is the distance between the moderator and the sample.

The chopper median line is located at 9455 mm from the moderator centre and consists of two counter-rotating disk, each contains 4 blades that absorb neutrons. Each blade is composed of an aluminum casing that encloses a sheet of cadmium. This material has a high absorption cross section for neutrons with energy below 500 meV ($\sigma_{abs} \approx 10^4$ barns), and it is very effective in absorbing slow neutrons of the pulse tail. The chopper phase can be fine tuned depending on the experimental requirements, i.e. one can select the energy range of the chopped pulses. The McStas moderator model has been implemented to simulate a single pulse from the source, and for this reason the use of a chopper component in the simulated TOSCA instrument is of no practical purpose in the current configuration.

2.1.5. Diffractometers

Since its installation TOSCA has modest high-resolution diffraction capabilities, composed of four squashed ^{3}He detector tubes where each tube is $\sim$ 10 mm wide. Those are positioned in back-scattering geometry over the angular range $\pm$ 177-179° relative to the incoming beam, at the same height as the sample. The secondary flight-path related to these detectors is 1.210 m. It is worth noting that this diffraction assembly on TOSCA is capable of providing a coverage of the d-space from 0.2 Å to 20 Å [21].

Currently this capability is not used extensively because the detection area is small and this results in a very low count rate. Furthermore coherent scattering is typically swamped by incoherent backgrounds in hydrogenous systems. However, the interest in non-hydrogenous materials is currently increasing and the higher incident flux due to the neutron guide would extend the use of diffraction measurements on TOSCA.

2.1.6. INS spectrometer assembly

TOSCA is an indirect geometry spectrometer used mainly for studies of the vibrational modes in materials *via* inelastic neutron scattering. The sample size is 40 x 40 cm^2 and the neutrons scattered by the sample are Bragg reflected by a pyrolytic graphite analyzer towards a beryllium filter which transmits certain wavelengths to the ^{3}He tubes bank. The whole instrument is shielded by B_4C wax, steel and cadmium plates [23]. A closed cycle refrigerator is embedded in the spectrometer to regulate the temperature inside the cryostat, this allows measurements in the range between 10 K and room temperature [26]. The sample position marks the end of the primary flight-path, 17.01 m away from the moderator, and the beginning of the secondary flight-path, $\sim$ 0.65 m long, toward the detectors.

Thanks to the analyser and the filter, it is possible to select a narrow final wavelength range and to keep the instrument resolution relatively constant at different energy transfers in the sample. Moreover, by means of the time-of-flight technique and the fixed final wavelength, TOSCA can exploit the whole incident neutron spectrum on the sample. Neutrons can lose energy and momentum through incoherent inelastic scattering on the sample molecules, generating phonons into the material and being scattered isotropically around the sample. Since the final wavelength, and thus speed, of the each neutron is known and its travel time from the source to the detector is measured, it is possible to calculate the initial speed of the neutron and to retrieve how much energy has been transferred from a neutron to the sample in a single scattering. This measurement originates a scattering spectrum of the sample, which shows elastic and inelastic peaks at defined energy transfers. Therefore TOSCA can probe the vibrational transitions of the sample molecules and investigate their chemical properties.

2.1.7. Analysers

Crystal monochromators (analyzers), see Fig. 2.5, provide a convenient way of selecting monochromatic neutrons from a white beam. Considering the Bragg law, when a polychromatic neutron beam is incident onto the planes of a single crystal at a glancing angle, depending on the plane spacing, a set of wavelength will be diffracted from the crystal at the same angle. This assembly acts as a low pass filter for the wavelengths, the Bragg scattered neutrons have wavelength λ and its subsequent harmonics ($\lambda/2$, $\lambda/3$, ...). This energy selection technique is commonly used in optical and neutron instruments. TOSCA analysers are kept at room temperature and placed in forward-scattering (glancing angle $\sim 47.50°$) and back-scattering position (glancing angle $\sim 132.30°$) from the sample center. There are 5 monochromators in the back-scattering position and other 5 in the forward-scattering position. They are placed in the vertical plane at 60°, 120°, 180°, 240° and 300° around the beam axis, see Fig. 2.4. The analyzers in use are slabs of highly oriented pyrolytic Graphite (HOPG) 2 mm thick which reflect on the 002 crystallographic plane. This plane corresponds to a d-spacing of 3.354 Å with a mosaic spread of 2.5° (150 arcmin) [23]. Typical values for the d-spacing spread of the highest grade HOPG lies between 0.03 % and 0.07 % [27]. In the simulations the d-spacing spread of the analyzers was assumed to be ± 0.03 %, and the mosaic spread of the crystal was equally taken into account. The dimensions of the analysers are approximately 120 x 100 mm^2, see Fig. 2.5. The neutrons reflected at the aforementioned glancing angles are selected in energy, the first harmonic ranges between 3.5 and 4.1 meV (~ 4.5 Å) and this interval defines the elastic line [23]. The higher harmonics (ca. 16, 36, ... meV) reflected by the analyzer represent spurious signal and are suppressed by the filter illustrated in the next section.

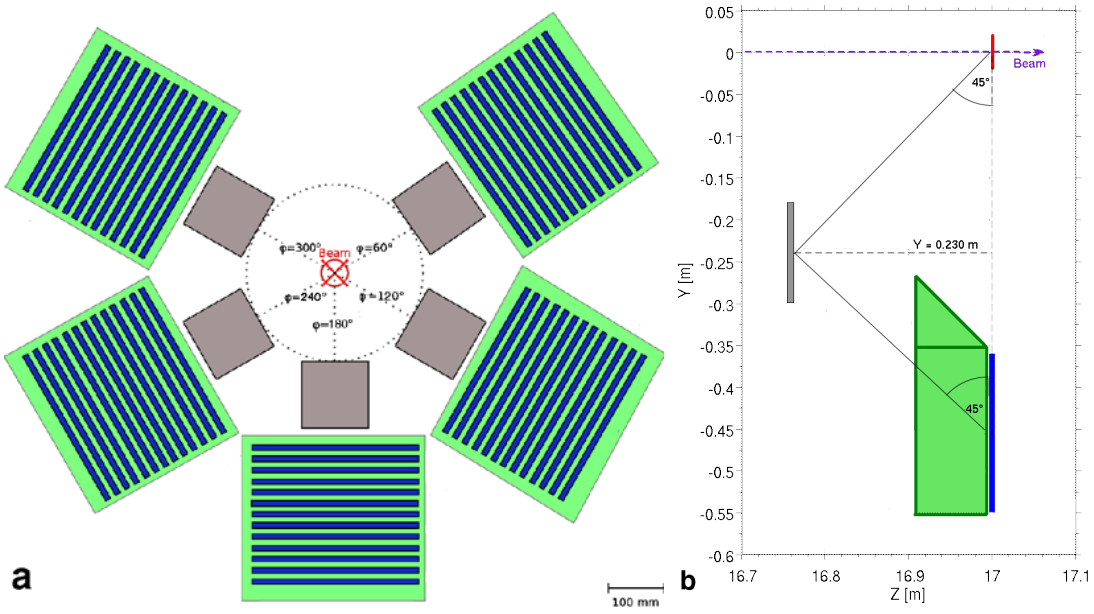

Figure 2.4. – a) Scheme of TOSCA spectrometer back-scattering banks, upstream view. b) Single back-scattering bank, side view. Sample is depicted in red while analysers are shown in gray, Be filters in green and detectors in blue.

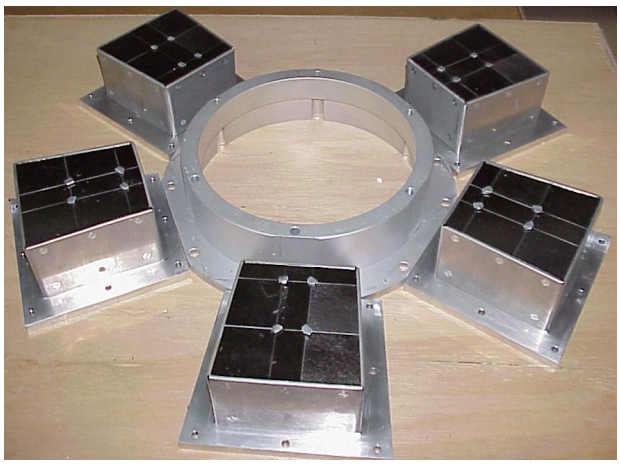

Figure 2.5. – Photo of the TOSCA HOPG crystal monochromators. Courtesy of ISIS Engineering Group.

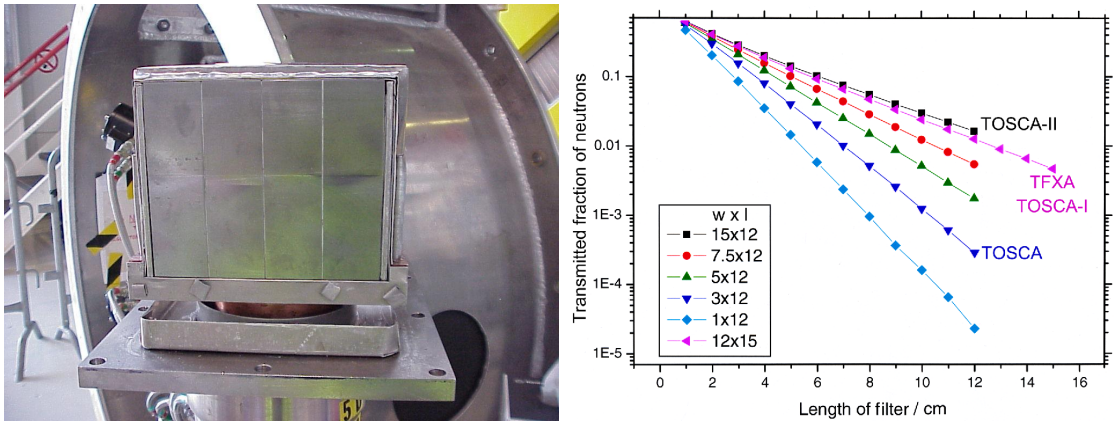

Figure 2.6. – (Left) TOSCA beryllium filter dismantled. Courtesy of ISIS engineering group. (Right) Transmission of higher-order neutrons through the beryllium filter as a function of the width (w) and length (l) of the filter, in centimeters. The filter sizes used for TFXA, TOSCA-I and the initial (TOSCA-II) and final implementation (TOSCA) are indicated. Courtesy of Mitchell *et al.* [7].

2.1.8. Beryllium-cadmium filters

The Cd-separated beryllium filter is a high-pass filter for the neutron wavelengths. Together with the HOPG analyzer, it creates a band-pass filter which fixes the final neutron energy between 3.5 meV and 4.1 meV by transmitting only the first harmonic from the analyzer to the detectors. The Be filter is 120 mm thick, cooled to temperatures below 35 K by helium refrigerators to enhance the effectiveness of the beryllium scattering cut-off [26]. Beryllium has high transmission for neutrons that have energy below 5 meV while it is a strong neutron scatterer for higher

energies. The beryllium cut-off is very sharp, especially if cooled below 100 K. In fact at 100 K, a 15 cm thick filter has a transmission factor of 0.75 for energies below the cut-off and 10^{-4} above the cut-off [7]. Each beryllium filter is sectioned into 4 blocks along the direction of flight, and each block is 3 cm wide and separated by 1 mm thick sheets of cadmium, see Fig. 2.6. The beryllium scatters and thus removes the undesired neutrons from the flight path, while cadmium is an excellent neutron absorber up to epithermal energies and acts as an absorbing medium for the scattered neutrons. The presence of cadmium sheets helps to further reduce the instrumental background by a factor of 10 [1]. In Fig. 2.6 the performance of this filter is presented and compared to the previous solutions adopted for the instrument.

2.1.9. Detector banks

As explained by Colognesi *et al.* [23], the TOSCA inelastic spectrometer is composed of ten detector banks lying on the sample plane: five for back-scattered neutrons and five for forward-scattered neutrons, see Fig. 2.4. Each bank contains 13 squashed tubes with dimensions of 10 x 250 x 2.5 mm^3, the same as in TOSCA-I, but thinner compared to TFXA. High ^{3}He pressure is used to compensate further the small thickness of the squashed tubes. Namely the tubes are pressurized at 20 bar and kept at room temperature. These tubes are intended to detect neutrons in a relatively low and limited energy range, from 3.5 to 4.1 meV as explained earlier, thus the detection efficiency is kept high and constant. The detector array is the last step of the secondary flight path, which has a total length that ranges between 550 and 770 mm, depending on the neutron flight path. The measurement of the incident neutron energy is made by evaluating the total TOF t through the kinematic relation $t = \frac{L_0}{v_0} + \frac{L_1}{v_1}$. Where L_0 and L_1 are respectively the primary and the secondary flight path, while v_0 and v_1 are respectively the incident and the scattered neutron velocity, where v_1 is fixed by the analyzer-filter assembly. As aforementioned, in TOSCA the typical values of the neutron flight paths are $L_0 = 17.01$ m and $L_1 = 0.55$ - 0.77 m. The uncertainty of L_1 dominates the instrument energy resolution when operated at low energy transfers, thus to compensate the error on L_1 a two-dimensional focusing of t was arranged for the detectors, such that the appropriate magnitude of v_1 would reduce the time differences [10]. This feature has been implemented at TOSCA by placing the detector banks on a circular geometry around the beam axis and aligning the sample and each detector tube on parallel planes, these planes are again parallel to the plane of the analyzer, see Fig. 2.4. In addition, to further improve the energy resolution, the Marx principle [28] was applied by positioning the ^{3}He tubes tangentially to the sample, see Fig. 2.7.

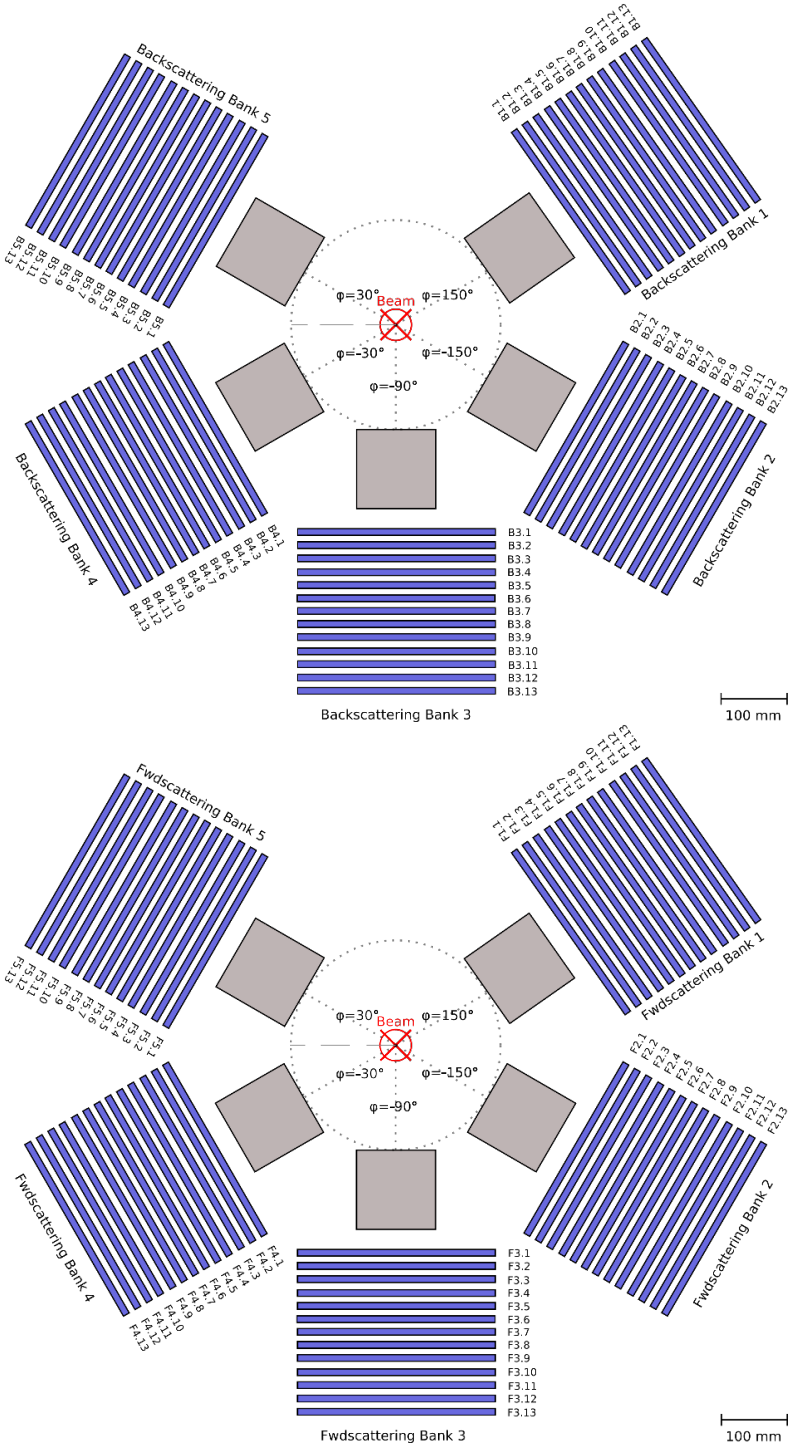

Figure 2.7. – Scheme of the TOSCA ^{3}He detectors and analyzer assembly. Upstream view of the back-scattering (up) and forward-scattering (down) banks. Analysers (grey) and detectors (blue) are shown. The cryostat which contains the sample is located at the center of the structure.

2.2. Spectrometer optimization

2.2.1. Detection system check

We performed a 757.1 µAh calibration run on TOSCA, using a 60 x 60 x 1 mm^3 vanadium plate kept at 20 Kelvin to assess the performance of each of the 130 ^{3}He tubes, which constitute the detection system of the INS assembly on TOSCA. In the present section all the detector spectra which showed possible anomalous signals are presented. However, in the current configuration the detectors which present spurious signal are not going to affect the quality of the measurement, since these data streams are promptly rejected by the Mantid [29] control routines. Rather this would affect only the speed of the measurement, because the detector assembly would not operate at its maximum capability. On the basis of the experimental results observed in this campaign, it is recommendable to check the status of each single detector prior to start a measurement cycle.

Back-scattering banks

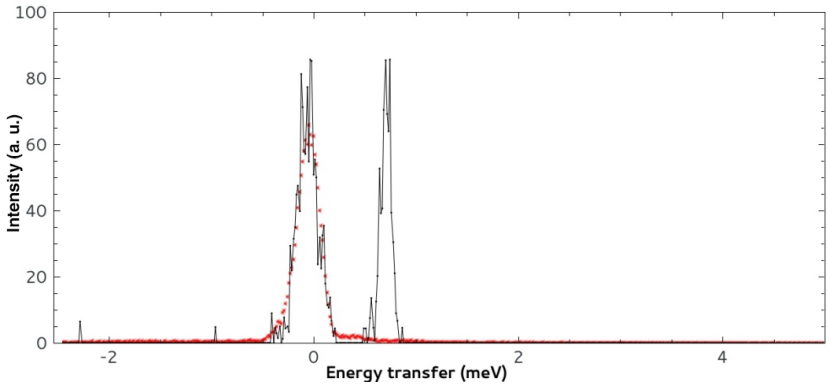

Figure 2.8. – Back-scattering bank 1, the detector 13 (black line) shows an anomalous peak at about 0.7 meV energy transfer. The average spectrum of the back-scattering apparatus is also shown as red dots for comparison.

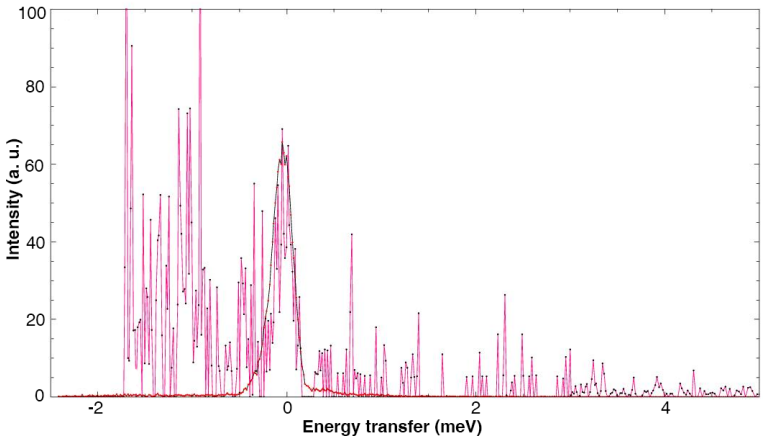

Figure 2.9. – Back-scattering bank 2, the detector 17 (pink line) shows a strong signal at negative energy transfers and possible noise at positive energy transfer. The average spectrum of the back-scattering apparatus is also shown as red dots for comparison.

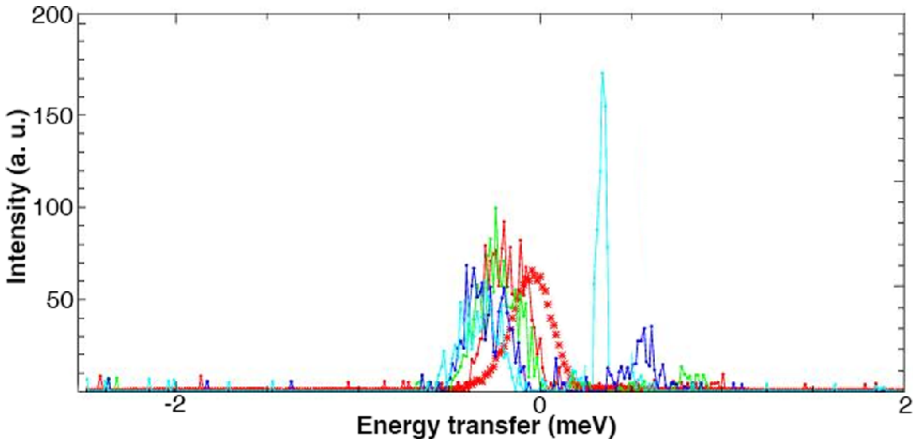

Figure 2.10. – Back-scattering bank 3, the detectors 42 (green line), 43 (blue line) and 44 (red line) have the elastic peak shifted towards negative energy transfers. This is a hint of a biased TOF calibration of these detectors with respect to the real TOF of the incident neutrons. The detector 45 (cyan line) shows a very strong peak at about 0.5 meV energy transfers. The average spectrum of the back-scattering bank is also shown as red dots for comparison.

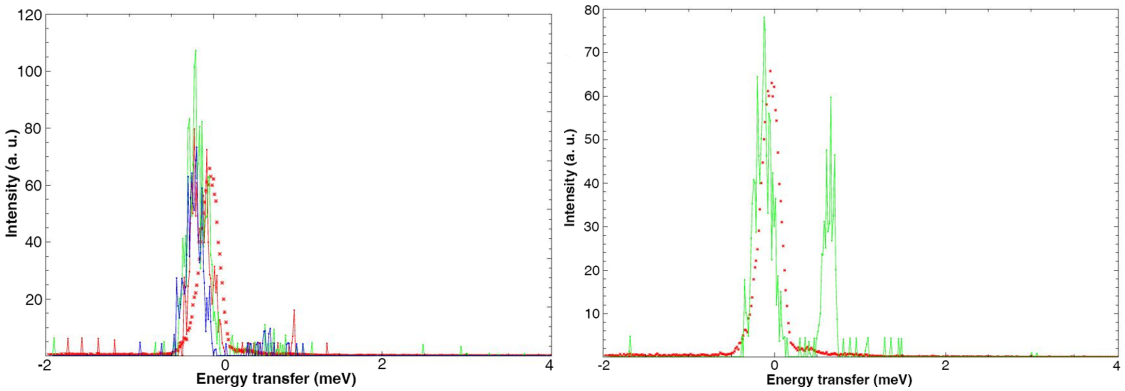

Figure 2.11. – (left) Back-scattering bank 4, the detectors 59 (green line), 60 (blue line), 61 (red line) have the elastic peak shifted towards negative energy transfers. The average spectrum of the back-scattering bank is also shown as red dots.
(right) Back-scattering bank 5, the detector 77 (green line) has an anomalous strong peak at about 0.5 meV. The average spectrum of the back-scattering bank is also shown as red dots for comparison.

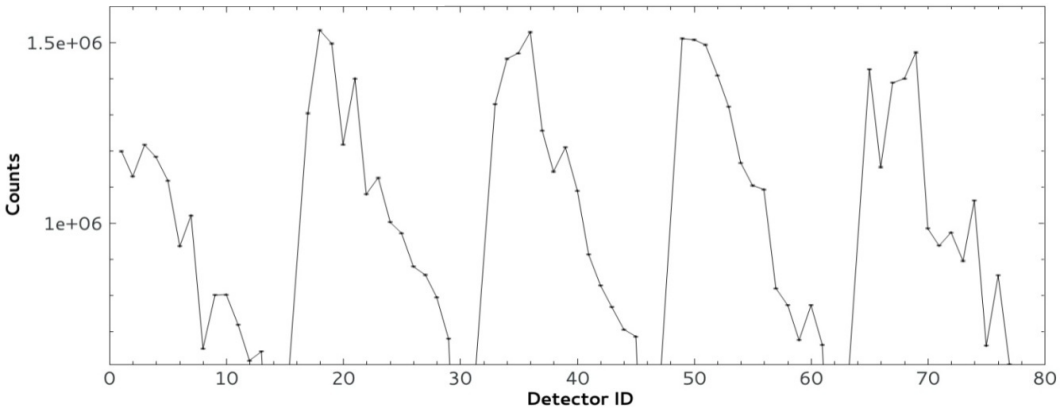

Figure 2.12. – Integral counts of each back-scattering detector. The detectors are arranged into five groups, within each group the count rate decrease almost linearly with the Detector ID. This is due to the geometrical arrangement of the detector banks, where the detectors with lower IDs lie closer to the analyzer. The detector ID is a label assigned by the Mantid software to identify uniquely the detectors, between each bank 3 IDs are usually kept empty. One could observe that the performance of the Bank 1 is below the average. In fact at the time of the measurement the undercooled beryllium filter (T $\sim$ 80 K) was serving this bank and it transmitted fewer neutrons to the detectors.

Forward-scattering banks

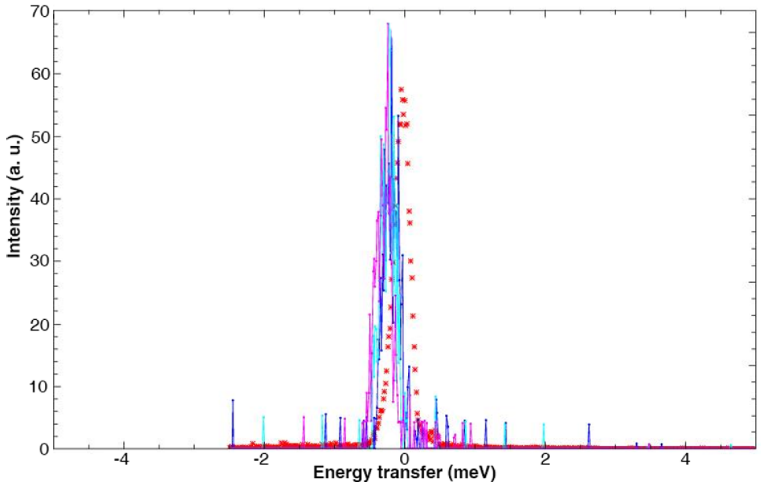

Figure 2.13. – Forward-scattering bank 2, the detectors 107 (purple line), 108 (blue line), 109 (cyan line) have the elastic peak slightly shifted towards negative energy transfers. The average spectrum of the forward-scattering apparatus is also shown as red dots for comparison.

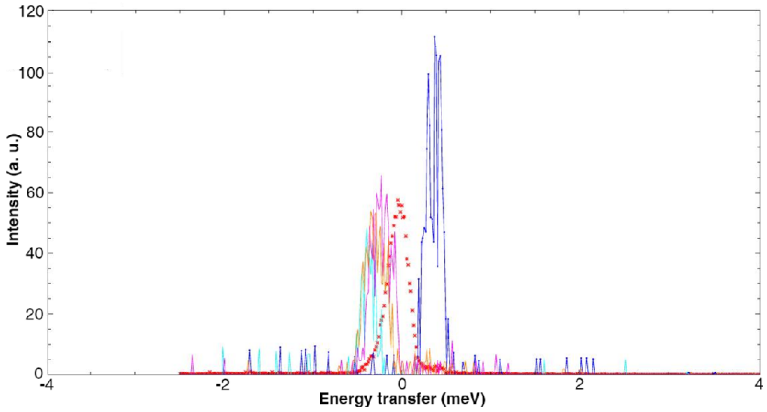

Figure 2.14. – Forward-scattering bank 3, the detector 113 (blue line) has the elastic peak misplaced at around 0.5 meV. The detectors 117 (yellow line), 124 (cyan line), 125 (purple line) have the elastic peak shifted towards negative energy transfers. The average spectrum of the forward-scattering apparatus is also shown as red dots for comparison.

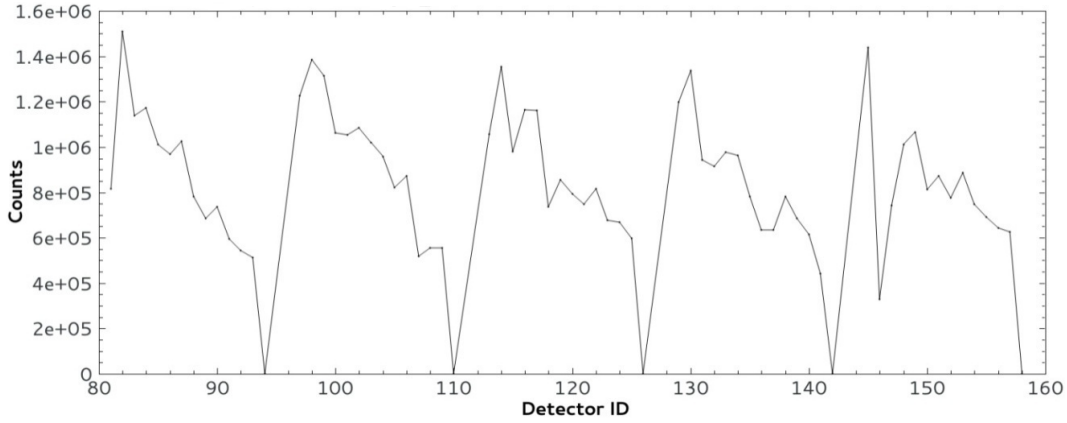

Figure 2.15. – Integral counts of each forward-scattering detector. As the back-scattering side, the detectors are arranged into five groups and within each group the count rate decrease almost linearly with the Detector ID. The detector ID is a label assigned by the Mantid software to identify uniquely the detectors, between each bank 3 IDs are usually kept empty. In this case there is no systematic under-performance among the detector banks.

Background

We also performed experiments to assess the level of background on the TOSCA instrument. The first run was a measurement for which we accumulated counts with the shutter closed, thus the signal should not be related with neutrons coming from the beamline. On average we detected 0.02 counts/µAh/detector in the E > 1000 meV range and 0.01 counts/µAh/detector in the E < 1000 meV range. Thus the detectors are remarkably quiet when the neutron beam is absent.

The second run was an empty cryostat measurement in which we accumulated counts with the shutter open and without sample in the cryostat, the detected flux was on average 281 counts/µAh/detector in the E > 1000 meV range and 0.30 counts/µAh/detector in the E < 1000 meV range. During a calibration experiment this background would constitute 50 % of the signal for E > 1000 meV and 29 % for E < 1000 meV. However, it is worth to mention that neutrons above 1000 meV does not interfere with the TOSCA typical measurements. Furthermore all these experiments were performed before the TOSCA beamline upgrade, thus the background should have improved further thanks to the better focusing and shielding of the new beamline.

2.2.2. Beryllium filter performance

A TOSCA Xpress measurement has been exploited to perform the calibration of the instrument using the 2,5 diiodotiophene standard sample cooled below 15 K. The aim of this experiment was to study the response of the inelastic spectrometer at different temperature of the beryllium filters, with particular attention to the efficiency of the filtering system and the detection capability of the instrument. In fact, these parameters can affect the overall sensitivity of TOSCA. Furthermore, when the performance is not a priority, one can consider the possibility to increase the beryllium filter temperature from the current 33 K while operating. In doing so one would reduce the operational cost of the instrument.

In each measurement we selected a different temperature range of the beryllium filters and we performed the analysis of the integrated flux in a single bank with appropriate discrimination in incident energy E_i. In the detected TOF spectra, two distinct energy ranges have been selected:

- E_i < 1000 meV to observe only the neutrons related with elastic/inelastic scattering within the sample
- E_i > 1000 meV to observe neutrons related with the prompt pulse.

The latter energy range constitutes most of the signal. If it were not rejected during the analysis, the resulting instrument sensitivity would not be accurate since TOSCA measurements do not exploit neutron scattering above 1000 meV. This experiment was performed during two different neutron cycles and some baseline shifts have occurred over time, these different experimental conditions were taken into account in the data analysis and are addressed below. Namely, we measured an overall flux $\sim$ 15 % lower than the corresponding measurements in the previous campaign, this is mostly explained with the fact that the forward bank 4 was offline for technical reasons during the latest cycle. To compensate such difference in the detected flux we introduced an appropriate correction factor while calculating the average neutron flux over the 10 banks and while calculating the average over the forward-scattering banks. Nevertheless, the results obtained in the previous campaign have slightly different intensities (of the order of 5 %) probably due to a different alignment of

the sample and different proton beam features. Moreover, in the latest measurement the temperature of the sample was 3.5 K rather than 14 K which was the temperature of the previous measurement. This happened thanks to the repair of the vacuum sealing inside the TOSCA cryostat. However, this change did not affect significantly our measurements because such decrease in the sample temperature has the effect to slightly improve the resolution keeping the flux constant.

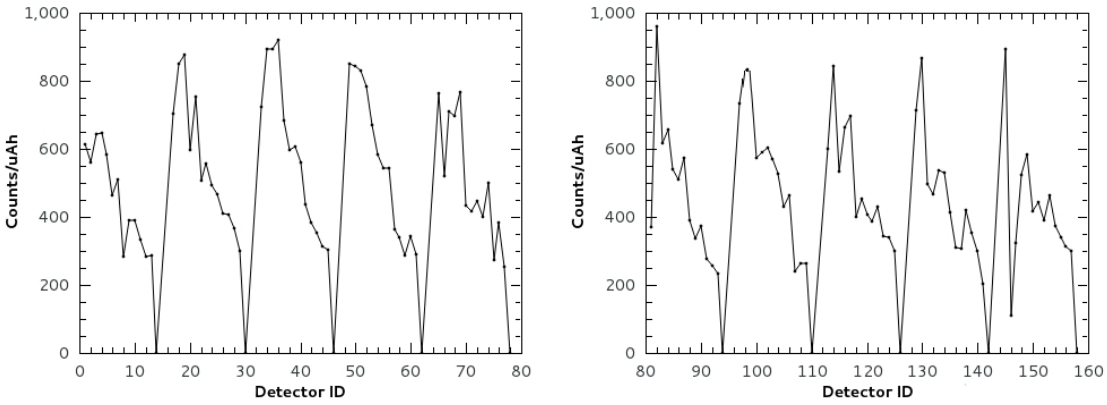

Figure 2.16. – Integrated counts of each detector in the back-scattering (left) and forward-scattering (right) banks for energy above 1000 meV, normalized by the proton current.

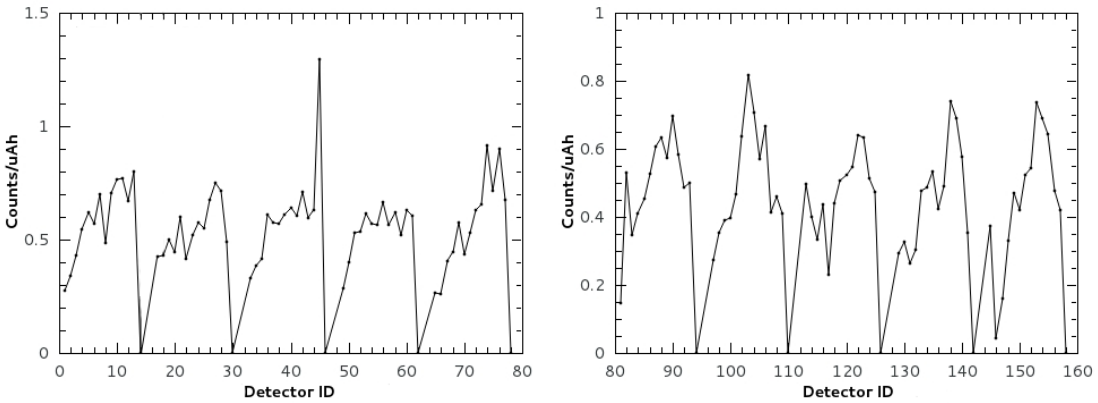

Figure 2.17. – Integrated counts of each detector in the back-scattering (left) and forward-scattering (right) banks for energy below 1000 meV, normalized by the proton current.

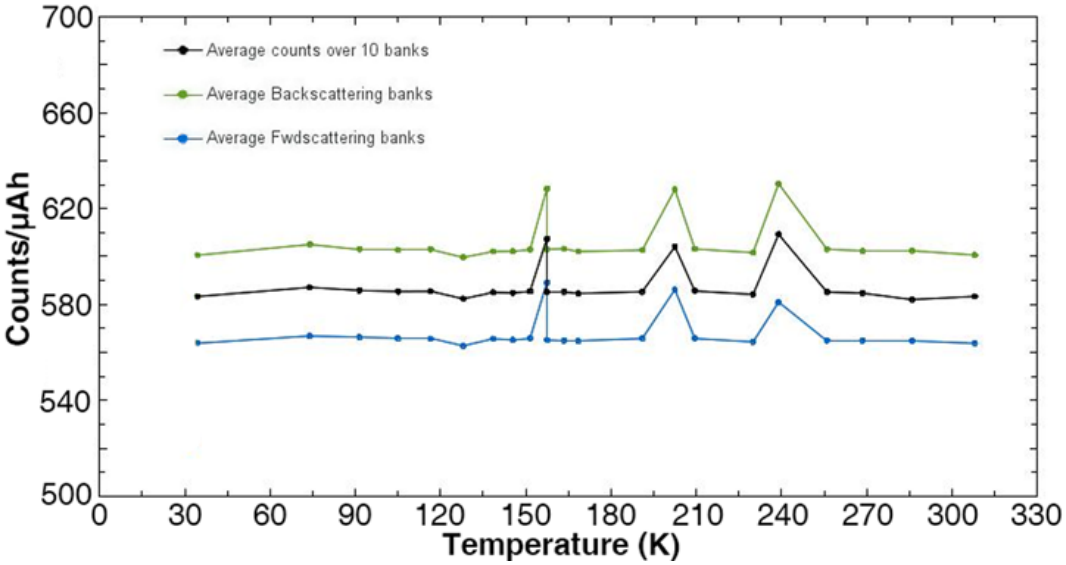

Figure 2.18. – Average integrated counts per μAh normalized per single detector, as a function of the beryllium filter temperature and considered for neutrons with energy above 1000 meV.

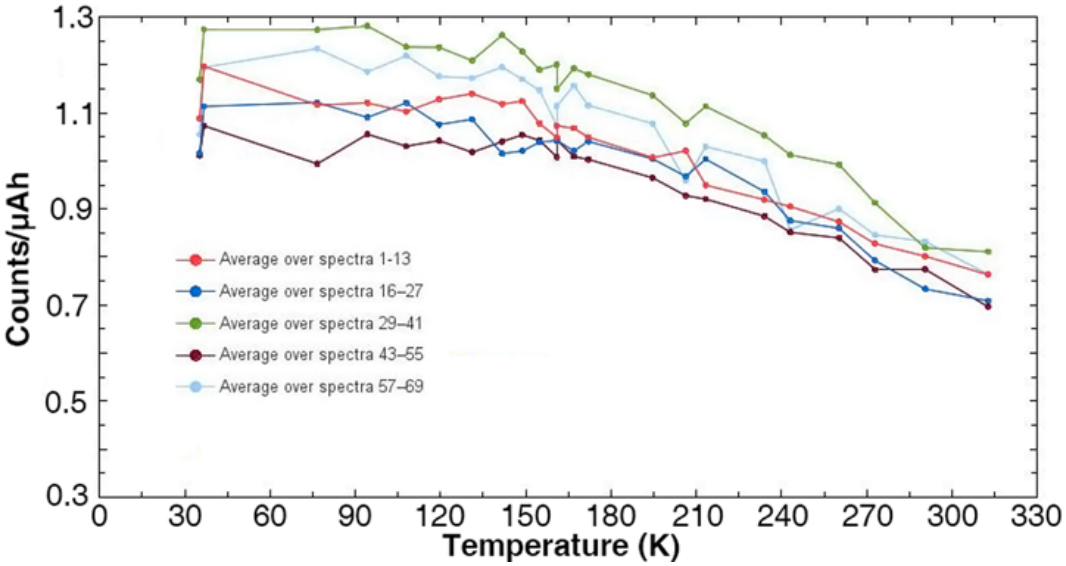

Figure 2.19. – Average integrated counts per μAh normalized per single detector for each of the five five back-scattering banks. As a function of the beryllium filter temperature and considered for neutrons with energy below 1000 meV.

In Fig. 2.16 one can see the integrated counts of detectors for $E_i > 1000$ meV. In each bank the number of counts decreases as the detector ID increases in the 13 elements array (i.e. the 13th detector is positioned farther from the beam centre). This result is in agreement with the data from the vanadium calibration experiment

reported in the previous section. Nevertheless, if we look only into the $E_i < 1000$ meV range, see Fig. 2.17, this trend is less evident. This evidence is expected and suggests that detectors placed farther from the beam centre may have a higher signal to background ratio, since they are by 30 - 40 % less sensitive to the prompt neutrons. Thus these detectors are more sensitive to the inelastic scattered neutrons compared to the detectors closer to the beam centre. The TOF technique allows to separate the neutron background from the neutrons scattered in the sample, so this discrepancy is promptly corrected during the data reduction.

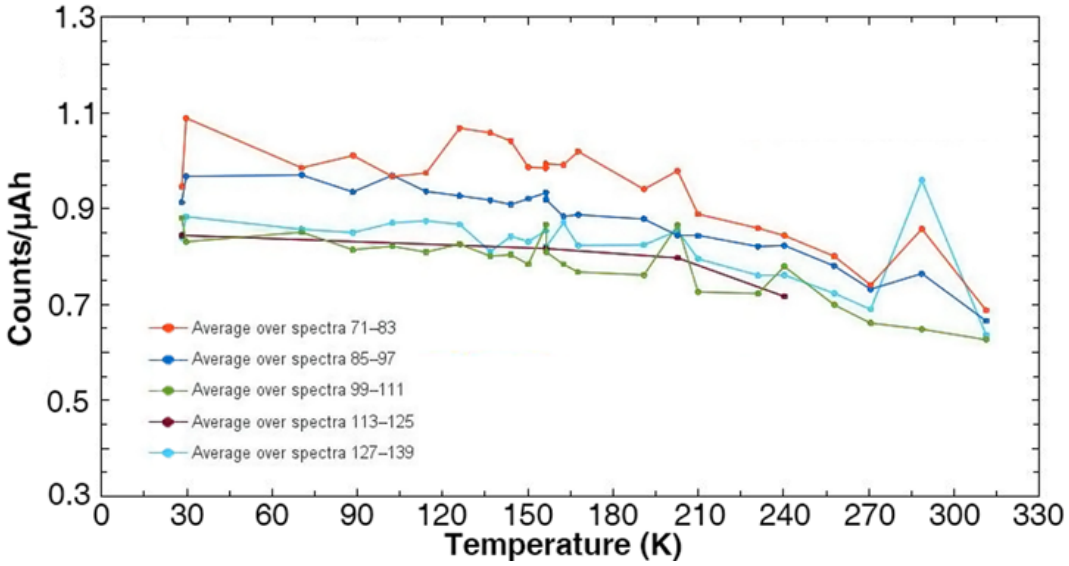

Figure 2.20. – Average integrated counts per µAh normalized per single detector for each of the five forward-scattering banks. As a function of the beryllium filter temperature and considered for neutrons with energy below 1000 meV.

With regards to the detection efficiency as a function of the filter temperature, in Fig. 2.18 one can see that in the $E_i > 1000$ meV region, the neutron flux is mostly independent from the Be filter temperature, this suggests that the neutrons detected in this region may not be influenced by the filtering system (HOPG analyzer and Be-Cd filter) or they are rather reaching the detectors by different paths. On the other hand, in the $E_i < 1000$ meV range, the observed trend is a linear increase in the detector counts as the beryllium filters temperature decreases, see Fig. 2.19. Sign of saturation appears between 150 K and 33 K. In fact when cooling the Be filter temperature from 310 K to 150 K, the detected flux increased by 67 % for the back-scattering banks and 60 % for the forward-scattering banks; while in the range from 150 K to 35 K the flux increased just by 7.3 % for the back-scattering banks and 8.7 % for the forward-scattering banks. In the lower energy range (below 1000 meV) the back-scattering banks on average performed better, with 25 % more flux than the forward-scattering banks. In the range above 1000 meV this out-performance of the back-scattering bank narrowed to 3 %.

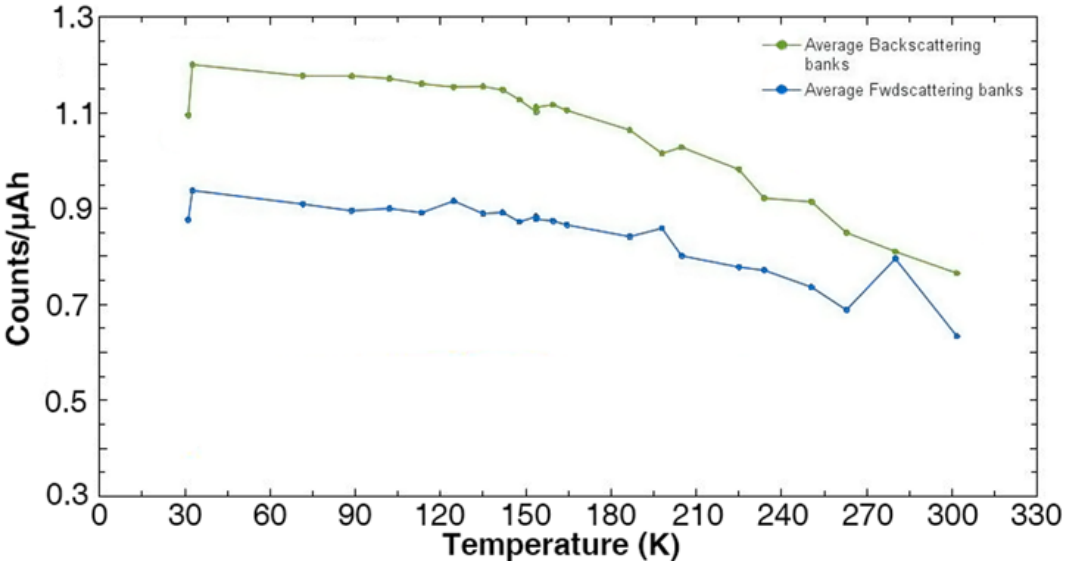

Figure 2.21. – Average integrated counts per µAh normalized per single detector for the two detection assemblies, as a function of the beryllium filter temperature and considered for neutrons with energy below 1000 meV.

An unwanted correlation between detectors noise and cryo-system status has been also observed, due to mechanical vibrations of the system. When the cooling system was running, noise and spurious signals were measured by a number of detectors, often affecting the capability of the single detector. The noise disappeared from almost all the detectors when the cryo-system was off or idle. The affected detectors were 3, 4, 17, 55, 56, 77, 81, 82, 83, 84, 85, 87, 106 (detector IDs). Detector 45 instead showed a strong and sharp spurious peak before the elastic line, this peak should not be related with the sample, since it appeared also in the calibration measurements, when no sample was in the cryostat. Detector 17 was completely saturated by noise even when the cryosystem was at idle, this may be explained considering that one faulty cooling head could not cool the filter below 80 K and thus it was always active. That cooling head is close to the detector 17 and this malfunction leads to a perpetual cooling cycle and a consequent unceasing spurious signal in the mentioned detector. In 2017, after these problems were addressed, the cooling heads were entirely refurbished. Moreover, all the detectors which show a noise level above a fixed threshold are automatically excluded by Mantid and they do not affect the final data quality.

2.3. TOSCA data reduction

The geometrical specifications of the TOSCA spectrometer are included in the Mantid software [29] and were obtained from an accurate inspection of the instrument. We summarize hereafter the procedure of data reduction which is applied to the raw

data files. This section address the features of the raw TOF data, namely a peak in a single measurement has a different TOF position depending on which of the 13 detectors in a single array is considered. This is due to the different glancing angle a single detector views from the HOPG monochromator, which in turn defines a different energy of the selected neutron. This peak shift is constant for each detector and is corrected during the data processing, otherwise it would negatively affect the instrument resolution [7, 15]. Moreover TOSCA secondary spectrometer has a specific geometric arrangement which implements the principle of time and energy focusing that will be explained below, this feature reduces the magnitude of the TOF shifts from one detector to another.

2.3.1. Time focusing

Generally crystal analyzer spectrometers similar to TOSCA implement a geometry aimed to improve the resolution, namely exploiting the time and energy focusing. The incorporation of these geometrical features improves the resolution at both high and low energy transfer region. The key requirement of time focusing is that the planes of the sample, analyzer and detectors must be parallel, as shown in Fig. 2.22. On TOSCA, the length of the secondary flight path from the sample to detector, d_f, is given by:

$$d_f = \frac{2d_a}{sin\theta} \tag{2.5}$$

where d_a is the horizontal distance from the sample to analyzer, which on TOSCA is held equal to the horizontal distance from the analyzer to the detector array, as depicted in Fig. 2.22. θ is the Bragg reflection angle on the analyzer, that for TOSCA is $\theta = 45°$ nominally.

The wavelength λ_f of any scattered neutron is then given by

$$\lambda_f = \frac{h}{m_n}\left(\frac{t_f}{d_f}\right) \tag{2.6}$$

where t_f is the flight time along d_f.

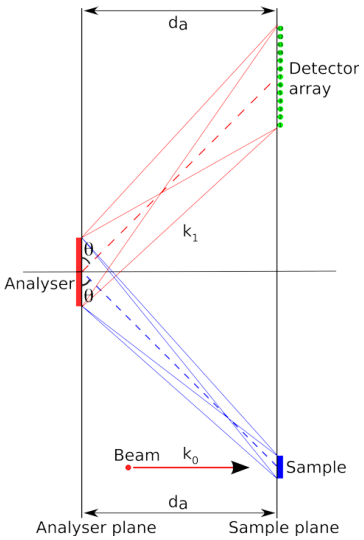

Figure 2.22. – Schematic of the TOSCA secondary spectrometer.

We can implement these equations in the Bragg law, where the HOPG crystal planes are separated by $d_{PG} = 3.354$ Å

$$\lambda_f = 2d_{PG}sin\theta \tag{2.7}$$

thus we get

$$\frac{h}{m_n}\frac{t_f}{d_f} = 2d_{PG}\frac{2d_a}{d_f} \tag{2.8}$$

and finally

$$t_f = 4d_{PG}d_a\left(\frac{m_n}{h}\right) = constant \tag{2.9}$$

Therefore the travel time of a neutron from the sample to the detector is independent from the neutron energy. This property does not apply to the total TOF but just to the travel time along the secondary spectrometer (i.e. t_f). Time focusing theory demonstrates that eventually, and under certain conditions, the time uncertainty on the final flight-path is the same for all neutrons irrespective of their initial energy. At high energy transfer, where neutrons travel the primary spectrometer quickly (i.e. small t_i), t_f is a significant contribution to the total flight time. Then keeping constant the uncertainty on t_f, its relative contribution to the total uncertainty is easier to account and the resolution is improved. This property is a direct consequence of the Bragg law which regulates the neutron reflection from the HOPG to the detectors. On the real instrument, we have that sample, analyzer and the detector array are not point-like, then the angle of reflection is included in a range

of angles around the nominal value of $\theta = 45°$. Considering neutrons which are reflected with angles $\theta_A > \theta$, the total flight path of these neutrons is clearly shorter than those scattering at θ, see Fig. 2.22. Following the Bragg law, the wavelength of the neutrons scattering at θ_A must be longer, hence the energy and the speed are lower than those neutrons scattering at θ. The greater speed of the neutrons scattering at θ compensates for the longer path length and the travel time along d_f is the same in both cases.

2.3.2. Principle of energy focusing (Marx principle)

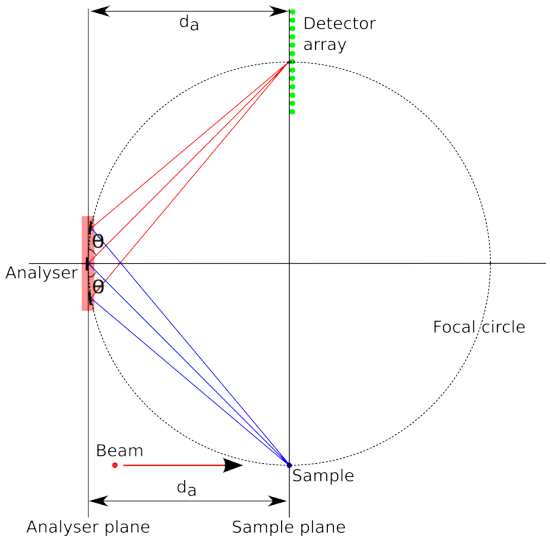

Figure 2.23. – Illustration of the Marx principle. Scattered neutrons of the same energy are reflected by differently oriented crystallites in the analyzer and focused on to the same detector. The focal circle for the 7th detector is shown, a different focal circle exists for each detector. A point-like sample is shown for clarity purpose.

The Marx principle is applied when the spectrometer requires that neutrons of a given wavelength have to reach a certain focal point, as illustrated in Fig. 2.23. For a point-like sample, reflection in the analyzer produces a series of focal points in a certain energy interval and these points fall on a plane parallel to the analyzer [23]. For a given neutron wavelength, the flight path from the analyzer to the focal plane has the same length as the path from the sample to the analyzer. As shown in Fig. 2.23, divergent rays of the same wavelength traveling from the sample will be reflected towards the focal point only by crystallites in the analyzer with appropriate orientations [7]. In this case the mosaicity of the analyzer is being exploited as a mean of focusing the scattered neutrons. This emphasizes the need for a specific mosaicity in the analyzer, this can be achieved by using different grades of HOPG and it is one of the reasons for the use of this material. The Marx principle improves the resolution mainly at low energy transfers. In fact this technique provides that

the scattered neutrons of the same energy travel with similar t_f towards a specific point in space, and this reduces the uncertainty in the final energy, which is a large contribution to the resolution at low energy transfer. The energy focusing is more restrictive than time focusing, because it is not only necessary to have sample, analyzer and detector planes parallel, but it is also required that sample and detector planes are co-planar.

2.3.3. TOF peak shift

In principle, thanks to the design of the TOSCA secondary spectrometer [15], at low or zero energy transfers we should not see any differences in the TOF position of equivalent peaks in different detectors. This is not evident in the raw experimental data when one looks at the elastic peak in each single detector of an array. In fact, the elastic peak has a different TOF position from a detector to another and on TOSCA it distributes across a time interval of 4 ms. Such result was further confirmed by McStas simulations. This shift is justified by the fact that the time and energy principle act only on the secondary spectrometer branch to cancel out TOF differences between neutrons with different energies [28]. This does not apply to the primary spectrometer branch, thus even a slight difference in incident energy on the sample results in a different travel time along the beamline. This is the main reason for the observed and calculated time shift of the elastic peak. This shift is predictable and it is corrected by the Mantid data reduction algorithms, since it can be calculated once the geometrical parameters of the instruments are well established. At high energy transfers the correction of the shift becomes less fundamental because the speed of the neutrons along the primary spectrometer is higher and the travel time is reduced accordingly. Thus the relative error on the energy selection decreases and the magnitude of the peak shift from a detector to another narrows down considerably, see Tab. 2.2.

ΔE (meV)	Mean peak position (ms)	Time interval (ms)	Relative error (%)
0	21.133	4.007	19.0
10	11.262	0.559	5.0
20	8.735	0.246	2.8
50	6.050	0.072	1.2
100	4.561	0.027	0.6
200	3.467	0.010	0.3
500	2.474	0.003	0.1

Table 2.2. – Calculated peak position for different energy transfers across the 13 detectors in a single array. The peak position is averaged over all the detectors in the single array and the peaks are distributed in the indicated time interval around the average. The peaks for a single energy transfer fall in a time interval which is broader at low energy transfers (ΔE).

3. Conclusions and outlook

The beam profile measurements on TOSCA in the wavelength range of interest to TOSCA (from 0.28 Å to 4.65 Å) showed evidence that the incident beam prior to the upgrade had a strongly collimated square shape, with a steep fall in intensity outside the main region [30]. The penumbra of the beam was a 0.5 cm crown around the main beam spot at its broadest size at the bottom. The beam appeared reasonably homogeneous across the 3.0 (H) $\times$ 3.5 (W) cm^2 surface, although some intensity variation could be observed. The total illuminated area was approximately 3.8 (H) $\times$ 4.0 (W) cm^2. The time averaged wavelength integrated flux at the TOSCA sample centre, was around $1.3{\cdot}10^6$ neutrons cm^{-2} s^{-1} and we measured a flux of $7.3{\cdot}10^5$ neutrons cm^{-2} s^{-1} Å^{-1} at the moderator peak ($\sim$ 1 Å) which represents the Maxwellian component of the incident spectrum. In comparison with Monte Carlo calculations of the TOSCA baseline, the measurements revealed that the neutron beam profile had $\sim$ 35 % smaller area, and the neutron flux in the beam centre, spatially averaged across the area that is 3.0 $\times$ 3.0 cm^2, was 1.77 smaller than calculations. We also corrected the calculated values of the flux to account for the air attenuation, that occurred in the real collimation tubes that were not evacuated.

After the beamline upgrade, we performed the beam profile measurement using a coherent methodology with respect to the previous experiments, and also the results of the Monte Carlo calculations were benchmarked with the experimental data. The TOSCA primary spectrometer upgrade consisted of removing the simple collimator tube between the moderator and the instrument, in order to install a supermirror guide that was designed by means of extensive McStas calculations during this project [2]. This upgrade has increased considerably the neutron flux at the sample position and our measurement provided a baseline for the new TOSCA beam. The results evidenced that the incident beam on TOSCA has kept a square shape, focused on the sample area. The main beam size reduced slightly to a 2.5 (H) x 2.5 (W) cm^2 surface where it showed a homogeneous distribution, and the total illuminated area was approximately 4.5 (H) x 4.5 (W) cm^2 when considering the lower intensity region. The time averaged wavelength-integrated flux at the TOSCA sample centre, increased to $2.54 \cdot 10^7$ neutrons cm^{-2} s^{-1}. We measured a flux of $1.38 \cdot 10^7$ neutron cm^{-2} s^{-1} Å^{-1} at the moderator peak ($\sim$ 1.1 Å), which is the Maxwellian fingerprint of the TOSCA spectrum [4]. With respect to the calculations, the measured beam profile was $\sim$ 27 % larger by area, and the neutron flux, spatially averaged across the sample area, was 2.22 times smaller than predicted by the Monte Carlo calculations. We observe that the simulations provided a good insight of the guide effect on the beam, while systematically underestimating the average flux magnitude at the sample. This bias could be ascribed to the moderator

model which fed the beamline, and it could be offset with the appropriate calibration factor based on the real data. On average we measured an order-of-magnitude gain in the neutron flux thanks to the neutron guide with very limited effects on resolution, the results averaged on a 3.0 x 3.0 cm^2 illuminated area are summarized in Tab. 3.1. The improved flux now allows faster measurements with better signal to noise ratio and will allow experiments with samples of smaller mass or made of weakly scattering elements.

Beamline	Average flux (n cm^{-2} s^{-1})	Elastic line FWHM (meV)
C0	$1.20 \cdot 10^6$	0.237
C2	$2.11 \cdot 10^7$	0.241

Table 3.1. – Experimental values of the neutron flux spatially averaged across 3.0 x 3.0 cm^2 surface around the beam centre and within the wavelength range of interest to TOSCA (from 0.28 Å to 4.65 Å), the related spectral resolution of the 2,5-diiodothiophene is presented as well. The comparison is made between the pre-upgrade TOSCA beamline (C0) and the fully upgraded beamline (C2). Note that the spectral resolution is essentially unchanged at the elastic line.

This project focused also on the upgrade possibilities of the TOSCA secondary spectrometer. At present, each analyzer bank on TOSCA consists of a square 144 cm^2 area, sitting at an average distance of 320 mm from the sample position. The analyzer banks are placed at a glazing angle of 45° relative to the scattered beam, in order to diffract the first harmonic at $\sim$ 3.5 meV. A beryllium-cadmium filter is placed between HOPG analyzer and detectors to suppress higher-order harmonics, and is cooled to 30 K to increase its efficiency. In the current instrument, the analyzer and the Be-Cd filter are very close to each other. While being a compact and practical solution requiring a relatively small analyzer area, this feature also limits the overall neutron-collection efficiency of the secondary spectrometer. To circumvent these limitations, we assessed other potential geometries that also build upon recent experience with similar instruments worldwide. Using the McStas package, we have created a custom component, see Appendix C, where HOPG tiles are arranged on either a spherical or parabolic surface of variable area. Preliminary Monte Carlo simulations and associated geometric optimizations have been performed as a function of analyzer area and radius of curvature. These calculations show that an upgrade of the secondary can bring an additional order-of-magnitude increase in detected flux, particularly via the use of a parabolic (as opposed to spherical) analyzer geometry [19]. We have also found that the detected flux can be increased by optimizing parameters such as the mosaicity of the HOPG array. In ideal circumstances, the shape of the curved HOPG analyzer could be increased up to an angular width of 60°. We performed calculations for three different sizes of doubly bent HOPG analyzers of either spherical or parabolic shape. Our largest-area analyzer amount to $\sim$ 1500 cm^2, a similar size to the one used earlier on the MACS instrument at NIST to improve the performance of cold-neutron spectrometers [5]. In a wider context,

we note that the original conceptual design and subsequent scientific specification of TOSCA decades ago were solely performed on the basis of analytical calculations, a task that necessarily relied on a number of mathematical approximations at the time. This situation is particularly true for the trade-off between flux and spectral resolution, as well as for the conditions required to attain an optimal match of the many different contributions to the neutronic response that are associated with both primary and secondary spectrometers. The present work used modern neutron-transport codes and algorithms specifically built for TOSCA, therefore it offers the exciting prospects of assessing with quantitative calculations the relative importance of these parameters, including analyzer shape and size, as well as time and energy focusing conditions. We, therefore, anticipate that the results presented in this work will also have important implications to the optimal neutronic design of similar instrumentation in the foreseeable future.

4. Synopsis of attached papers

The abstracts of the papers attached to this thesis have been collected in this section.

1. **Monte carlo simulations of the TOSCA spectrometer: Assessment of current performance and future upgrades**
   We describe and assess the performance of a detailed computational description of the high-resolution TOSCA spectrometer at ISIS using neutron-transport Monte Carlo simulations. Extensive calculations using the McStas software package have been performed using the present instrument geometry and compared with available experimental data. The agreement between expected and measured performance is satisfactory in terms of the incident flux spectrum, associated time structure, and spectroscopic resolution. Encouraged by these results, we also consider the upgrade of the primary spectrometer with a tapered high-m guide. This instrument development offers the exciting prospects of providing order-of-magnitude gains in detected neutron flux over the energy-transfer range of the instrument whilst preserving its outstanding spectroscopic capabilities.

2. **Unexpected Cation Dynamics in the Low-Temperature Phase of Methylammonium Lead Iodide: The Need for Improved Models**
   High-resolution inelastic neutron scattering and extensive first-principles calculations have been used to explore the low-temperature phase of the hybrid solar-cell material methylammonium lead iodide up to the well-known phase transition to the tetragonal phase at ca. 160 K. Contrary to original expectation, we find that the Pnma structure for this phase can only provide a qualitative description of the geometry and underlying motions of the organic cation. A substantial lowering of the local symmetry inside the perovskite cage leads to an improved atomistic model that can account for all available spectroscopic and thermodynamic data, both at low temperatures and in the vicinity of the aforementioned phase transition. Further and detailed analysis of the first principles calculations reveals that large-amplitude distortions of the inorganic framework are driven by both zero-point-energy fluctuations and thermally activated cation motions. These effects are significant down to liquid-helium temperatures. For this important class of technological materials, this work brings to the fore the pressing need to bridge the gap between the long-range order seen by crystallographic methods and the local environ-

ment around the organic cation probed by neutron spectroscopy.

3. **Detailed characterisation of the incident neutron beam on the TOSCA spectrometer**
   We report a detailed characterization of the incident neutron beam on the TOSCA spectrometer. A bespoke time-of-flight neutron monitor has been designed, constructed and used to perform extensive spatially resolved measurements of the absolute neutron flux and its underlying time structure at the instrument sample position. The obtained data give a quantitative understanding of the current instrument beyond neutronic simulations and provide a baseline in order to assess the performance of the upgraded instrument. At an average proton current on- target of 153 μA (ISIS Target Station 1; at the time of measurements) we have found that the wavelength-integrated neutron flux (from 0.28 Å to 4.65 Å) at the position of the TOSCA instrument sample (spatially averaged across the 3 × 3 cm^2 surface centered around (0,0) position) is approximately $1.2 \cdot 10^6$ neutrons $cm^{-2}s^{-1}$, while the whole beam has a homogeneous distribution across the 3.0 × 3.5 cm^2 sample surface. The spectra reproduced the well-known shape of the neutrons moderated by the room temperature water moderator and exhibit a neutron flux of $7.3 \cdot 10^5$ neutrons cm^{-2} s^{-1} $Å^{-1}$ at 1 Å.

4. **The neutron guide upgrade of the TOSCA spectrometer**
   The primary flightpath of the TOSCA indirect geometry neutron spectrometer has been fitted with the high-m 14.636 meters (including 0.418 m of air gaps) long neutron guide composed of ten sections in order to boost the neutron flux at the sample position. The upgraded incident neutron beam has been characterised with the help of the time-of-flight neutron monitor, and the beam profile and the gain in the neutron flux data are presented. At an average proton current-on-target of 160 μA (ISIS Target Station 1; at the time of the measurements) we have found that the wavelength-integrated neutron flux (from 0.28 Å to 4.65 Å) at the position of the TOSCA instrument sample (spatially averaged across a 3.0 x 3.0 cm^2 surface centered around (0, 0) position) is approximately $2.11 \cdot 10^7$ neutrons $cm^{-2}s^{-1}$. The instrument excellent spectral resolution and low spectral background have been preserved upon the upgrade. The much improved count rate allows faster measurements as well as experiments involving smaller samples that were not possible in the past.

5. **TOSCA Secondary Spectrometer Upgrade, RAL Technical Report**
   For TOSCA to move forward beyond the current state-of-the-art in key scientific areas such as gas and charge storage, the most urgent need is for greater sensitivity via the secondary spectrometer upgrade that would make TOSCA competitive with other similar instruments, such as VISION at the SNS, in terms of total count rate. The here proposed upgrades can improve the col-

lection efficiency of the neutrons scattered from the sample and the effects in terms of resolution have to be evaluated alongside. This document is focused on the design of a TOSCA double bent analyzer by means of McStas suite, which currently does not implement a component that can simulate a curved monochromator along multiple axis. Therefore, to proceed with the simulation of the secondary spectrometer, we had to create a custom component which can meet the TOSCA needs. We used several Highly Oriented Pyrolytic Graphite tiles arranged on a parametric surface up to an area of 1450 cm^2 that can have two different curvatures, spherical and parabolic. Several simulations have been performed with this component to study the performance of the current and future TOSCA setup at the elastic line. Graphite analyzers with different areas and radii of curvature have been considered and each parameter has been optimized *via* computational analysis. From the simulations, we found that with the appropriate focusing, it is possible to increase the current analyzer area by tenfold reaching a flux gain of ~ 7. It is also evident that for larger analyzers the parabolic geometry outperforms the spherical one thanks to its better focusing properties. The calculations also show that this gain result is achieved without detrimental effects on resolution, provided that an extensive optimization is performed on the parameters of curved geometry. The geometric optimization in this study has been computationally implemented using MATLAB routines in conjunction with McStas.

6. **The TOSCA Spectrometer at ISIS: the Guide Upgrade and Beyond**
We describe progress to date with the most significant upgrade of the TOSCA spectrometer since it first became operational over fifteen years ago. This major project to boost the incident flux on the instrument by over an order of magnitude has been implemented over the past couple of years and has involved the complete redesign of the primary spectrometer to house a state-of-the-art, high-m neutron guide and associated chopper system. Engineering design and subsequent installation and commissioning efforts have been supported by extensive neutron-transport simulations and baseline studies of neutronic response in the context of the ISIS TS1 Project. Looking further ahead, we also outline ongoing feasibility studies to upgrade the secondary spectrometer, with a view to additional order-of-magnitude gains in neutronic and scientific performance.

Paper I

EPJ Web of Conferences **83**, 03013 (2015)
DOI: 10.1051/epjconf/20158303013

Monte carlo simulations of the TOSCA spectrometer: Assessment of current performance and future upgrades

Roberto S. Pinna[1,2], Svemir Rudić[1], Stewart F. Parker[1], Giuseppe Gorini[2] and Felix Fernandez-Alonso[1,3,a]

[1]ISIS Facility, Rutherford Appleton Laboratory, Chilton, Didcot OX11 0QX, UK
[2]CNISM, Università degli Studi di Milano-Bicocca, Piazza della Scienza 3, 20126 Milano, Italy
[3]Department of Physics and Astronomy, University College London, Gower Street, London WC1E 6BT, UK

Abstract. We describe and assess the performance of a detailed computational description of the high-resolution TOSCA spectrometer at ISIS using neutron-transport Monte Carlo simulations. Extensive calculations using the McStas software package have been performed using the present instrument geometry and compared with available experimental data. The agreement between expected and measured performance is satisfactory in terms of the incident flux spectrum, associated time structure, and spectroscopic resolution. Encouraged by these results, we also consider the upgrade of the primary spectrometer with a tapered high-*m* guide. This instrument development offers the exciting prospects of providing order-of-magnitude gains in detected neutron flux over the energy-transfer range of the instrument whilst preserving its outstanding spectroscopic capabilities.

1. Introduction

TOSCA [1] is a broadband, indirect-geometry inelastic neutron spectrometer optimised for high-resolution chemical spectroscopy up to energy transfers of ca. 500(4000) meV(cm^{-1}) in neutron-energy loss (1 meV = 8.065 cm^{-1}). The secondary spectrometer sits at 17 m from a room-temperature water moderator on ISIS Target Station I and has been operational for over a decade, superseding its predecessor TFXA [2].

As shown schematically in Fig. 1, energy analysis is performed after the interaction of the incident neutron beam with the sample under investigation. Scattered neutrons are Bragg-reflected from a pyrolytic graphite (PG) analyser and higher-order reflections beyond (002) are suppressed by a cooled Be filter (T < 50 K) so as to define a unique final energy of ∼4(32) meV (cm^{-1}). The instrument is comprised of a total of ten inelastic banks each having thirteen squashed ^{3}He tubes with an effective length(thickness) of 25(0.25) cm. Five banks are located in forward scattering (scattering angle ∼45°) and five in backscattering (∼135°). The use of a low (fixed) final energy translates into a direct relationship between energy transfer (E_T, meV) and momentum transfer (Q, Å^{-1}) such that $E_T \approx 2Q^2$. A disc chopper to prevent frame overlap is positioned at 8 m from the moderator. A recent chopper upgrade uses the 40-ms time frame during the operation of both target stations at ISIS to extend the incident-wavelength bandwidth of the instrument down to −3(24) meV(cm^{-1}). At ISIS, this wide energy-transfer range provides overlap with both low (IRIS [3], LET [4], and OSIRIS [5]) and high energy-transfer spectrometers (MAPS [6] and VESUVIO [7]). TOSCA has been optimised to deliver an outstanding ('chemical') resolution across its spectral range as a consequence of several factors, including: a relatively narrow energy bandpass of the PG002/Be analyser system; tight moderator pulse widths; a long incident flight path; and a time- and energy-focused detector geometry. Instrument backgrounds are negligible, thus low-cross-section measurements beyond hydrogen-containing materials are not only feasible but also a growing area of research on the instrument. Quantitatively, the above design choices translate into an absolute spectral resolution of ∼0.3 meV for elastic events (E_T = 0 meV) and ∼12 meV at E_T = 500 meV. The latter energy transfer lies in the vicinity of the H-H stretch mode in molecular hydrogen and, therefore, represents an absolute upper bound for vibrational dynamics in condensed matter. TOSCA has also had modest high-resolution diffraction capabilities from its inception, with two pairs of ^{3}He tubes located in backscattering geometry over the angular range ±177–179°.

In terms of its science programme, TOSCA has set the standard for broadband chemical spectroscopy with neutrons over the past decade or so, as evidenced by a ratio of publication to accepted proposal of ca. 0.8 in the past five years – this figure increases to 0.9 if its vibrant Xpress access system is also taken into account [8]. It has also been the inspiration for next-generation chemical spectrometers such as VISION at the SNS, Oak Ridge, USA [9–11]. Owing to the higher source intensity of the SNS and the use of state-of-the-art neutron technology [11], VISION can provide significantly higher detected fluxes than TOSCA. The similarity of design also means that VISION should also enjoy negligible backgrounds. In addition, the new instrument IN1-Lagrange at ILL [12] delivers a much higher average flux than TOSCA (and possibly even more than VISION), as inferred from recent studies on this instrument by some of the authors [13,14]. However, the resolution of IN1-Lagrange

[a] Corresponding author: felix.fernandez-alonso@stfc.ac.uk

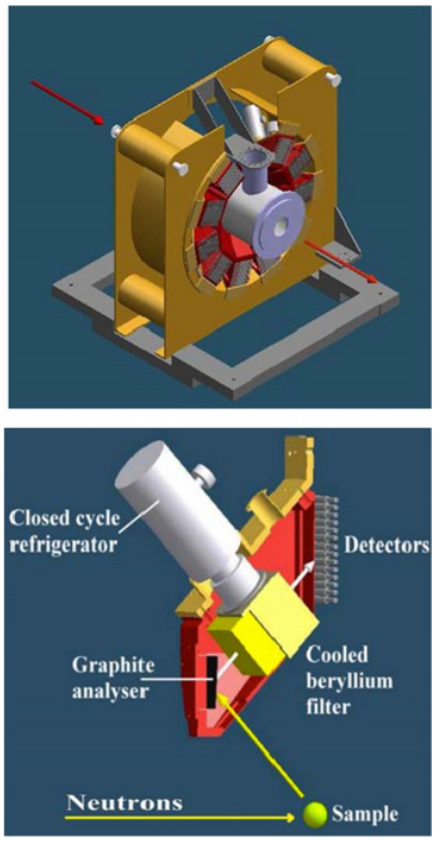

Figure 1. Top: schematic drawing of the TOSCA secondary spectrometer. The red arrows indicate the direction of incident (top left) and transmitted (bottom right) neutron beams. Bottom: detailed view of an inelastic bank. For further details, see the text. (Credit: Consiglio Nazionale delle Ricerche, Italy.)

remains comparable to TFXA (i.e., similar to that of most currently operating instruments). As a neutron spectrometer at a steady reactor source, background runs will always be important, necessarily restricting signal-to-background ratios to moderate values. It is also a scanning spectrometer and spectral contamination by higher orders from the incident monochromator may be problematic to discern subtle spectral features, particularly at low energy transfers. Nonetheless, IN1-Lagrange is probably the spectrometer of choice for very small samples (few mg or less) and extensive parametric studies, particularly over narrow energy-transfer ranges.

As a world-leading neutron spectrometer, TOSCA has been constantly evolving, with significant improvements to its performance over the past few years as a result of a number of small and medium upgrades [15]. In this work, we describe parallel efforts to provide (for the first time) an accurate computational description of the instrument using neutron-transport Monte Carlo simulations, with a view on a detailed assessment of potential upgrade routes in the short, medium, and long terms.

2. Current performance

All Monte Carlo simulations have been performed using the parallelised version of the McStas software package [16]. Computations were performed on the SCARF-RAL

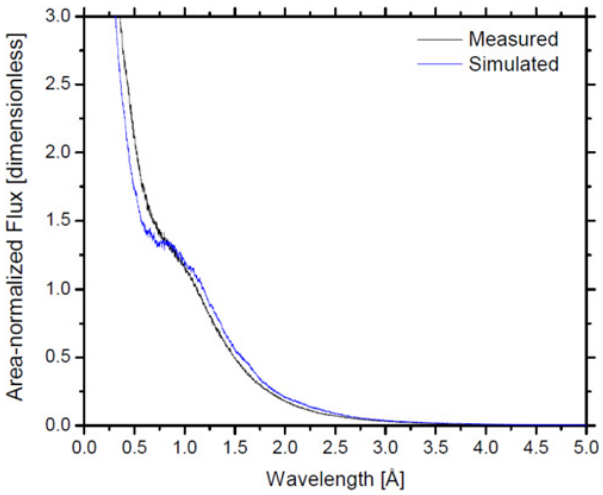

Figure 2. Measured and simulated incident neutron spectra on TOSCA. To facilitate comparison, both histograms have been normalised over the neutron-wavelength range 0.3–5.0 Å. For further details, see the text.

cluster [17] using up to 128 nodes. The geometry of both primary and secondary spectrometers has been taken from current engineering drawings of the instrument.

Figure 2 shows a comparison between experimental and simulated incident neutron spectra at the position of the primary monitor. This monitor is located upstream from the sample position at 15.795 m from the room-temperature water moderator. Experimental raw data have been corrected by the (measured) wavelength-dependent efficiency of this lithium-glass scintillator detector over the incident-wavelength range of the instrument (0.3–5.0 Å). Simulated spectra were calculated using the ISIS Target Station I water-moderator module released in 2008 and available on the McStas package.

Overall, the Monte Carlo calculations provide a satisfactory description of the experimental incident spectrum, although some differences are to be noted in terms of the extent of the "moderated hump," which appears to be more pronounced in the simulated dataset. These differences are of the order of 20–25% around the fingerprint region of vibrational spectra (10–125 meV or 100–1000 cm^{-1}). Notwithstanding the above differences, both experimental and simulated data evince a predominantly epithermal-looking incident spectrum. We also note that these discrepancies have a minor effect on reduced inelastic neutron spectra, as these are always normalised to the incident neutron-flux distribution prior to subsequent analysis or comparison with the predictions of computational models.

In addition to incident neutron spectra, the performance of an inverted-geometry instrument like TOSCA critically depends on the time structure of neutron pulses reaching the sample position. On TOSCA, experimental access to this information is facilitated by the availability of a high-resolution diffraction bank in backscattering geometry. In this configuration, the observed time widths of well-defined Bragg reflections become most sensitive to the temporal spread of neutron pulses arriving at the sample position, as detailed in recent Monte Carlo

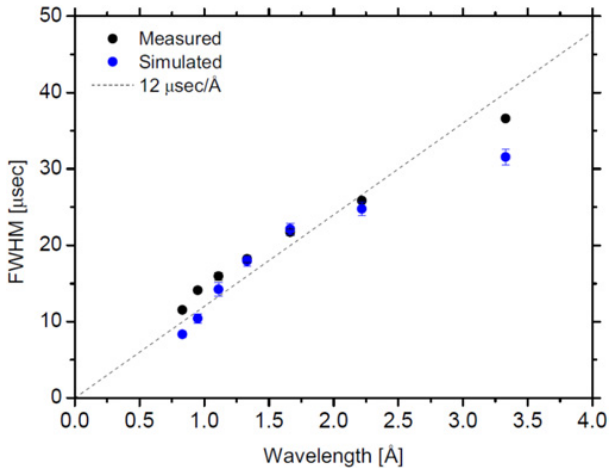

Figure 3. Measured and simulated time widths as a function of incident neutron wavelength. For further details, see the text.

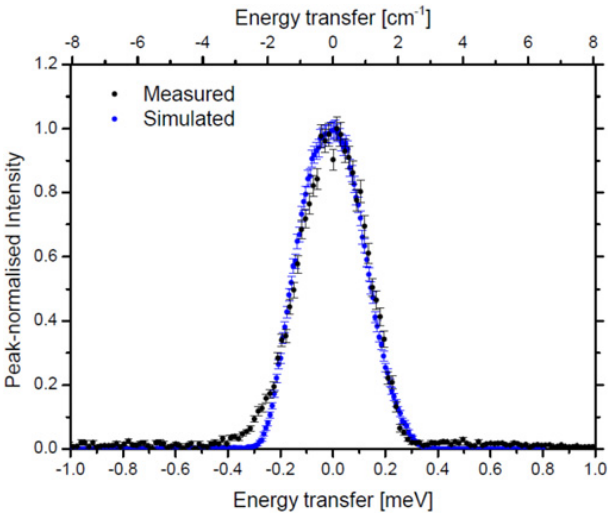

Figure 4. Experimental and simulated spectra of ice at a temperature of 10 K using the inelastic backscattering bank at a (nominal) scattering angle of 135°.

simulations of the OSIRIS spectrometer [18]. In the particular case of TOSCA, measurements at a temperature of 10 K were performed on a $40 \times 20 \times 2\,\mathrm{mm}^3$ highly oriented pyrolytic graphite (HOPG) standard with a mosaicity of $0.8 \pm 0.2°$ along the c-axis. This standard was aligned with the a–b plane perpendicular to the incident beam and its c-axis rotated so as to maximise (00l) Bragg intensities on detector 147, located at a distance of 1.21 m upstream from the sample position at a scattering angle of 178.28°. For comparison, an identical experimental setup was implemented on McStas.

Figure 3 shows a comparison of the wavelength dependence of time widths associated with (00l) HOPG Bragg reflections, as obtained from least-squares fits of both experimental and simulated data using a type-I extreme-value line shape. All widths reported in this work correspond to full-width-at-half-maxima (FWHM) and the associated error bars denote uncertainties in the data fits. In both cases, the widths are dominated by the temporal response of the primary spectrometer and, in particular, the time structure emerging from the moderator face. Other contributions associated with time uncertainties between moderator and sample are relatively minor in comparison. Overall, the agreement between experiment and simulation is quite satisfactory, particularly in terms of an overall increase in FWHM with neutron wavelength in the thermal and cold regimes. At the longest wavelength investigated (3.33 Å), simulations are within 10–15% of experimental values, and consistently provide a safe lower bound to observation. These results are also in agreement with a moderator term of $\sim$12 μs/Å inferred from previous calibrations of the instrument [2, 19]. On the basis of the present comparison, this moderator term provides a good description of time structure below ca. 3.0 Å. At the higher wavelength investigated, the time width shows signs of saturation, as one would expect for the moderation of cold neutrons at a short-pulse spallation source [20]. These results also highlight the superb diffraction capabilities of the instrument, characterised by a d-spacing resolution of $\Delta d/d \sim 5 \times 10^{-3}$ over its operating wavelength range. This unique feature of inverted-geometry instrumentation at a short-pulse spallation neutron source could be further exploited via a significant increase in detector area relative to current (and quite modest) capabilities on TOSCA, as already demonstrated on the low-energy spectrometer OSIRIS [5].

The above comparisons between experimental and simulated performance were primarily concerned with a characterisation of the primary spectrometer. To assess the validity of our current description of the entire instrument, we have also compared experimental and simulated spectra around the elastic line for ice at a temperature of 10 K, as shown in Fig. 4. For the purposes of benchmarking the McStas simulations, this case represents a convenient scenario characterised by high scattering levels (potentially leading to an increase in instrumental backgrounds), as well as comparable contributions to the resolution function from both primary (moderator) and secondary spectrometers (inelastic banks). As shown in Fig. 4, the agreement between experiment (FWHM = 0.3 meV) and simulation (0.29 meV) is excellent aside from a slight excess in scattered intensity for neutron-energy gain processes. Elucidating the precise origin of this second-order feature in the observed spectrum is beyond the scope of the present work, as it would require a detailed and systematic line shape analysis similar to that conducted recently for the OSIRIS spectrometer [18]. Overall, these results further confirm the adequacy of our computational model for a quantitative description of the spectroscopic response of the instrument in its present incarnation.

3. More neutrons for chemistry

In view of current developments in chemical spectroscopy with neutrons around the globe, the current sensitivity of TOSCA could be greatly enhanced via the provision of a neutron guide in the primary spectrometer. To assess possible gain factors relative to current capabilities, extensive McStas simulations have been performed for a

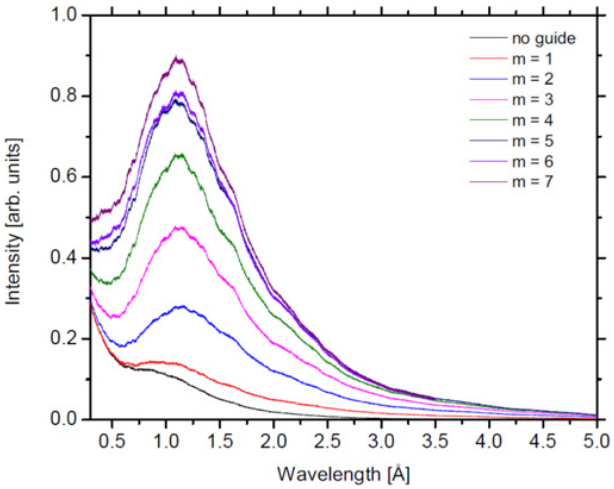

Figure 5. Incident-wavelength spectra at the sample position as a function of guide m-number. The black trace corresponds to the current spectrometer (no guide).

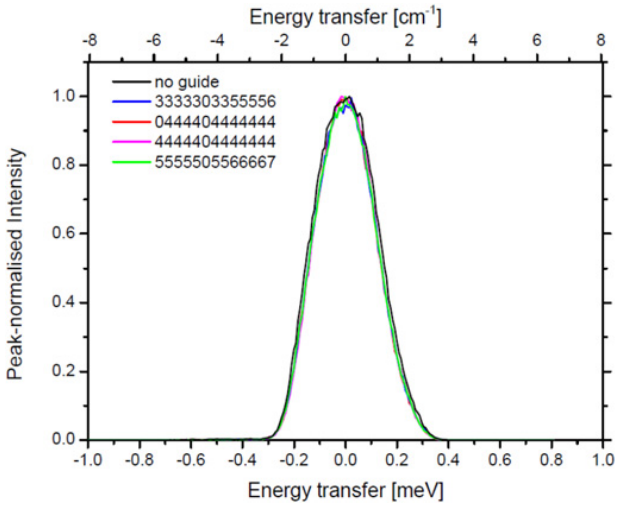

Figure 6. Simulated spectra of ice at a temperature of 10 K using the inelastic backscattering bank at 135°. The legend indicates different guide configurations as described in the text.

range of guide configurations using realistic reflectivity profiles as described in Chapter 5 of the McStas user manual [16]. This exercise must necessarily take into account the cost effectiveness of any proposed guide geometry, as well as other spatial and operational constraints on a busy instrument like TOSCA.

A tapered guide represents the most sensible geometry to transmit neutrons over a wide wavelength range. Such a guide can be placed at a minimum distance from the moderator of 1.625 m with a cross sectional area of $10 \times 10\,\mathrm{cm}^2$, followed by thirteen independent sections ending at a distance of 0.75 m from the sample position ($4 \times 4\,\mathrm{cm}^2$). Figure 5 shows how the flux at the sample position would evolve as a function of guide m-number.

The highest absolute gains are observed around 1 Å, approaching an order-of-magnitude enhancement in flux for the highest m-numbers investigated. We also note a monotonic (and quite significant) increase in flux up to $m \sim 5-6$, values which are well within reach owing to advances in neutron-guide technology over the past decade. In relative terms, the largest gains are observed at the longest wavelengths, with factors exceeding 50 around the elastic line of the instrument at ca. 5 Å. The energy transfers accessible in this neutron-wavelength range correspond to the hard-to-access THz range in optical spectroscopy ($1\,\mathrm{THz} = 4.13\,\mathrm{meV} = 33.3\,\mathrm{cm}^{-1}$), as well as provide much-needed overlap with the higher-resolution instruments IRIS and OSIRIS at ISIS. These two instruments have already demonstrated a phenomenal energy resolution for inelastic studies up to energy transfers of ca. $20(160)\,\mathrm{meV}(\mathrm{cm}^{-1})$ [21–23], and could very well complement the broadband capabilities afforded by TOSCA at shorter wavelengths. The above flux gains in the THz window drop relatively quickly with decreasing wavelength to values of 2–3 below 1 Å. We also find that a progressive increase in m-number across the primary spectrometer tends to provide a more balanced gain across the spectral range of the instrument. Likewise, the net transport of high incident wavelengths (4–5 Å) can be maximised by having a guide insert inside the shutter assembly, as close to the moderator face as present space constraints on ISIS Target Station I may allow. A high m-number closer to the sample can also increase the flux at the sample by factors of 2–3 for the shorter wavelengths ca. 1 Å.

From extensive simulations to assess the relative performance of a total of forty different guide geometries, the configuration of choice corresponds to [5555505566667], where each single digit within square brackets denotes the m-value for each independent section along the primary spectrometer, starting closest to the moderator face. Predicted gains for this configuration are 52 and 3 for the highest and lowest incident wavelengths available on the instrument, respectively. Use of a high-m guide ($m > 4$) close to the source ensures reasonable gain factors above $20(160)\,\mathrm{meV}(\mathrm{cm}^{-1})$.

As an additional test, Fig. 6 shows that the spectral resolution of the instrument around the elastic line is largely insensitive to a rather substantial increase in the m-number of the guide in the primary spectrometer. These results are to be taken as a worst-case scenario, given the linear dependence of beam divergence on both incident wavelength and m-number. We therefore conclude that the predicted gains reported in Fig. 5 are not accompanied by a concomitant degradation of the spectroscopic capabilities presently afforded by TOSCA.

4. Outlook

Monte-Carlo simulations of the TOSCA spectrometer using the McStas software package provide a satisfactory description of the current performance of the instrument in terms of incident-flux spectra, associated time structure, and spectroscopic response. Encouraged by these results, we have also assessed potential flux gains associated with the installation of a neutron guide in the primary spectrometer. Unlike a decade ago when the instrument became operational, judicious use of state-of-the-art guide technology to upgrade the primary spectrometer offers

the exciting prospects of providing order-of-magnitude gains in sensitivity whilst preserving the outstanding spectroscopic capabilities of the instrument.

On the scientific front, this much-needed upgrade implies a concomitant reduction in counting times, a transformational development as it would enable detailed studies of industrially relevant systems exhibiting low scattering cross sections. To name a few, these include studies of molecular adsorbates such as CO, NO, or SO_2 on catalysts, where inelastic neutron scattering can uniquely provide information on the low-energy modes underpinning adsorbate-surface interactions; or of proton-conducting pathways in charge-storage materials containing minute amounts of hydrogen. Detailed parametric studies would become routine as well, particularly for hydrogen-containing systems such as polymers and nanostructured materials. Moreover, the (very popular) TOSCA Xpress service could also be expanded and automated beyond its current remit to provide an efficient outreach tool.

In conjunction with ongoing efforts at ISIS to improve neutronic performance, the upgrade possibilities described herein will certainly keep TOSCA at the forefront of chemical spectroscopy with neutrons in the foreseeable future.

The authors gratefully acknowledge the UK Science & Technology Facilities Council for financial support, access to beam time at ISIS, and use of the e-Science SCARF cluster at the Rutherford Appleton Laboratory. We also thank Peter Philips and Colin French from the ISIS Experimental Operations Division for the precise machining of the HOPG standards. This work has been partially supported within the framework of past and present CNR-STFC agreements for collaborative research between Italy and ISIS.

References

[1] www.isis.stfc.ac.uk/instruments/tosca/ (last accessed 22 September 2014)
[2] D. Colognesi, M. Celli, F. Cilloco, R. J. Newport, S.F. Parker, V. Rossi-Albertini, F. Sacchetti, J. Tomkinson, and M. Zoppi, Appl. Phys. A **74**, S64–S66 (2002)
[3] www.isis.stfc.ac.uk/instruments/iris/ (last accessed 22 September 2014)
[4] www.isis.stfc.ac.uk/instruments/let/ (last accessed 22 September 2014)
[5] www.isis.stfc.ac.uk/instruments/osiris/ (last accessed 22 September 2014)
[6] www.isis.stfc.ac.uk/instruments/maps/ (last accessed 22 September 2014)
[7] www.isis.stfc.ac.uk/instruments/vesuvio/ (last accessed 22 September 2014)
[8] www.isis.stfc.ac.uk/apply-for-beamtime/ (last accessed 22 September 2014)
[9] P.A. Seeger, L.L. Daemen, and J.Z. Larese, Nucl. Instr. Meth. Phys. Res. A **604**, 709 (2009)
[10] neutrons.ornl.gov/vision/ (last accessed 22 September 2014)
[11] C. Wildgruber, personal communication
[12] www.ill.eu/instruments-support/instruments-groups/instruments/in1-taslagrange/ (last accessed 22 September 2014)
[13] F. Fernandez-Alonso, M.J. Gutmann, S. Mukhopadhyay, D.B. Jochym, K. Refson, M. Jura, M. Krzystyniak, M. Jimenez-Ruiz, and A. Wagner, J. Phys. Soc. Jpn. **82**, SA001 (2013)
[14] S. Mukhopadhyay, M.J. Gutmann, M. Jura, D.B. Jochym, M. Jimenez-Ruiz, S. Sturniolo, K. Refson, and F. Fernandez-Alonso, Chem. Phys. **427**, 95 (2013)
[15] S.F. Parker *et al.*, J. Phys.: Conf. Series (in the press, 2014)
[16] www.mcstas.org/ (last accessed 22 September 2014)
[17] www.scarf.rl.ac.uk/ (last accessed 22 September 2014)
[18] K. Pokhilchuk, Rutherford Appleton Laboratory Technical Report RAL-TR-2013-008 (Chilton, 2013, ISSN 1358-6254). Report available at: epubs.stfc.ac.uk/work/65985 (last accessed 22 September 2014)
[19] V. Rossi Albertini, D. Colognesi, and J. Tomkinson, J. Neutron Research **8**, 245 (2000)
[20] M. Arai, in *Neutron Scattering – Fundamentals*, F. Fernandez-Alonso and D.L. Price eds. (Academic Press, New York, 2013), Chapter 3
[21] F. Fernandez-Alonso et al., Phys. Rev. Lett. **98**, 215503 (2007)
[22] A. Lovell et al., Phys. Rev. Lett. **101**, 126101 (2008)
[23] F. Demmel et al., Eur. Phys. J. (accepted, 2014)

Paper II

THE JOURNAL OF PHYSICAL CHEMISTRY Letters

Letter

pubs.acs.org/JPCL

Unexpected Cation Dynamics in the Low-Temperature Phase of Methylammonium Lead Iodide: The Need for Improved Models

Kacper Drużbicki,[†,‡] Roberto Simone Pinna,[§,∥] Svemir Rudić,[§] Marek Jura,[§] Giuseppe Gorini,[∥] and Felix Fernandez-Alonso*[,§,⊥]

[†]Faculty of Physics, Adam Mickiewicz University, Umultowska 85, 61-614 Poznan, Poland

[‡]Frank Laboratory of Neutron Physics, Joint Institute for Nuclear Research, 141980, Dubna, Russia

[§]ISIS Facility, Rutherford Appleton Laboratory, Chilton, Didcot, Oxfordshire OX11 0QX, United Kingdom

[∥]CNISM, Università degli Studi di Milano-Bicocca, Piazza della Scienza 3, 20126 Milano, Italy

[⊥]Department of Physics and Astronomy, University College London, Gower Street, London, WC1E 6BT, United Kingdom

Supporting Information

ABSTRACT: High-resolution inelastic neutron scattering and extensive first-principles calculations have been used to explore the low-temperature phase of the hybrid solar-cell material methylammonium lead iodide up to the well-known phase transition to the tetragonal phase at ca. 160 K. Contrary to original expectation, we find that the *Pnma* structure for this phase can only provide a qualitative description of the geometry and underlying motions of the organic cation. A substantial lowering of the local symmetry inside the perovskite cage leads to an improved atomistic model that can account for all available spectroscopic and thermodynamic data, both at low temperatures and in the vicinity of the aforementioned phase transition. Further and detailed analysis of the first-principles calculations reveals that large-amplitude distortions of the inorganic framework are driven by both zero-point-energy fluctuations and thermally activated cation motions. These effects are significant down to liquid-helium temperatures. For this important class of technological materials, this work brings to the fore the pressing need to bridge the gap between the long-range order seen by crystallographic methods and the local environment around the organic cation probed by neutron spectroscopy.

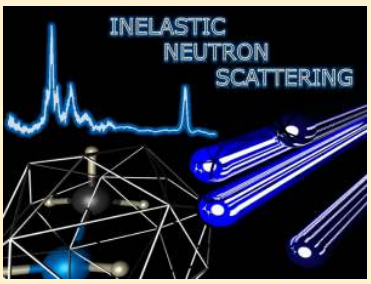

Since its first use as a sensitizer in 2009,[1] methylammonium lead iodide ($CH_3NH_3PbI_3$, hereafter abbreviated MAPI) has emerged as one of the most promising light-absorbing materials for solar-energy applications. When deposited on TiO_2 scaffolds, its light-conversion efficiency exceeds 20%, an unprecedented performance for alternative photovoltaic technologies.[2] Recent advances in MAPI-based solar-cell devices have triggered intense research efforts to establish the fundamental properties of this material. At ambient pressure, three crystallographic phases have been identified as shown in Figure 1, namely: a high-temperature cubic phase ($Pm\bar{3}m$; $T >$ 327 K); a room-temperature tetragonal phase ($I4/mcm$; $T >$ 160 K); and a low-temperature phase ($Pnma$, $T <$ 160 K).[3,4] In the cubic structure, the methylammonium cation (hereafter MA^+) becomes highly disordered along all unit-cell directions, i.e., MAPI becomes a fully fledged plastic crystal.[4] Recent studies have also indicated that the phase transformation to the tetragonal phase results in the tilting of PbI_6 octahedra about the crystallographic *c*-axis, whereby MA^+ adopts four possible orientations characterized by a substantial degree of dynamical disorder.[5]

Early work solved the low-temperature structure using the $Pna2_1$ space group,[6] yet more recent and comprehensive single-crystal X-ray diffraction (XRD) experiments at 100 K by Baikie et al.[3] have revisited this assignment and favor the use of *Pnma* symmetry. Using this space group, centrosymmetric constraints dictate that MA^+ may adopt a single anticlinic orientation relative to the inorganic framework. Baikie et al.[3] have also reported unusual features in the Fourier maps, and these have been interpreted qualitatively as abnormal anharmonic displacements of the iodine atoms. Alternatively, it has been surmised that angular distortions of the octahedral may also play a role.[3,7] The interplay between hydrogen-bond (HB) strength and octahedral distortion has been explored further by Lee et al.[8] using density-functional-theory (DFT) calculations. It was found that octahedral tilting is stabilized by NH···I interactions with a binding strength proportional to such a distortion. Extension to the tetragonal phase indicates the presence of two distinct types of HB interactions.[9] These findings are also in line with recent molecular dynamics (MD) simulations, which suggest that spontaneous bidirectional ordering of MA^+ underpins the emergence of the tetragonal phase.[10] The potential disturbance of the lead-iodide perovskite lattice by MA^+ motions cannot be ruled out either, and this possibility is consistent with the observation of the aforementioned anomalous diffuse scattering by Baikie et al.[3]

Received: August 12, 2016
Accepted: November 2, 2016
Published: November 2, 2016

DOI: 10.1021/acs.jpclett.6b01822
J. Phys. Chem. Lett. 2016, 7, 4701−4709

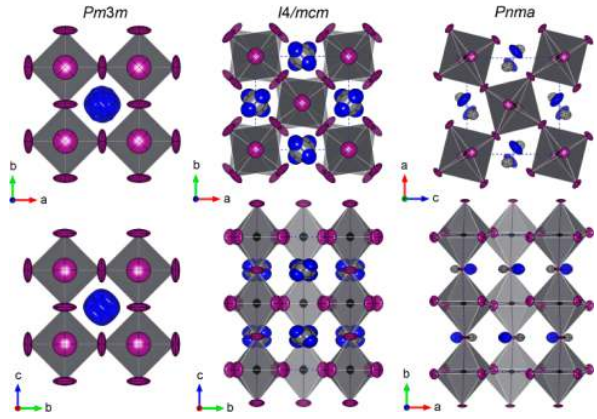

Figure 1. Structures of the three known phases of MAPI at ambient pressure obtained from diffraction studies (lead: black; iodine: purple; nitrogen: blue; carbon: dark gray). For simplicity, hydrogens have been omitted from these images. Left and center: cubic ($Pm\bar{3}m$, T = 350 K) and tetragonal ($I4/mcm$, T = 295 K) phases from single-crystal neutron diffraction.[4] Right: *Pnma* structure from single-crystal XRD at T = 100 K.[3] Anisotropic-displacement ellipsoids are given with 90% probability, as obtained from the refinement of crystallographic data (99% for *Pnma*).

From the discussion presented above, one would expect that both the tetragonal and low-temperature phases are related to each other via a continuous distortion of the inorganic perovskite framework. As rightly pointed out by Baikie et al. in their seminal XRD work,[3] this view is at odds with the absence of a direct group−subgroup relationship between *I4/mcm* and *Pnma* symmetries, i.e., it is not possible to effect a continuous structural change to transform one phase into the other. It is, therefore, expected that a (possibly transient) intermediate phase may exist, but experimental confirmation of its presence has proven elusive. Instead, it has been recently confirmed that both phases can coexist below the phase transition into the higher-temperature tetragonal structure at ca. 160 K.[11] Also, phase coexistence all the way down to 10 K has been observed in thin-film specimens,[12] and recent real-space studies using scanning-tunnelling microscopy at 77 and 10 K reveal significant deviations from bulk behavior associated with nontrivial surface-reconstruction and reorientational effects.[13,14] Although it is generally accepted that the *Pnma* phase is devoid of static or dynamical disorder, Fabini et al.[15] have recently shown that MAPI can exhibit glassy dynamics at low temperatures, and that these are potentially coupled to local distortions of the PbI_6 sublattice.

Taken altogether, these observations pose a number of open questions related to the arrangement and underlying motions of MA^+, as well as on our ability to provide a quantitative description of the low-temperature phase of MAPI consistent with all available experimental data. Spectroscopic techniques sensitive to the local environment can offer additional insights into these, and both tetragonal and low-temperature phases have been the subject of a growing number of such studies, with an emphasis on the use of photon-based spectroscopies.[16−23] These reports have explored quite extensively the far- and mid-infrared (IR) range, spanning optically accessible motions of both MA^+ and its underlying inorganic framework. The interpretation of these spectroscopic data has relied heavily on the use of harmonic lattice-dynamics (HLD) calculations within the framework of solid-state DFT. The upper spectral range above ca. 1000 cm^{-1} is dominated by MA^+ modes, and their assignment has been reported in earlier works.[16,17,19] The interpretation of spectral features at lower energies remains relatively unexplored. Another complication arises from the lack of separation of MA^+ vs framework modes in the overall optical response, leading to both spectral congestion and a fair degree of ambiguity in the interpretation of these data.

In this work, we use high-resolution inelastic neutron scattering (INS) to probe MA^+ motions and the surrounding environment. Owing to the large incoherent cross section of hydrogen, INS is superbly sensitive to hydrogen motions, as discussed in more detail in Section 1 of the Supporting Information (SI). Moreover, INS intensities are not subjected to selection rules and, as such, are directly related to the underlying vibrational density of states (VDOS) of the entire (bulk) material, thereby facilitating comparison with theoretical predictions.[24] These features make INS a suitable probe of the local environment and motions of MA^+ in MAPI, enabling a quantitative appraisal of our current understanding of the physicochemical behavior of this important material.

As described in more detail in the Experimental Section, INS experiments were carried out on the high-resolution TOSCA spectrometer at the ISIS Pulsed Neutron & Muon Source, Rutherford Appleton Laboratory, U.K.[25−27] Figure 2 summarizes our INS results, obtained in the vicinity of the phase transition at T = 162.2 K[6] and at lower temperatures. Qualitatively, the low-temperature data exhibit a number of sharply defined features in the range 10−400 cm^{-1}. Above this range, spectral intensities fall off very rapidly with increasing energy transfer. This behavior is indicative of strong contributions from so-called phonon wings, i.e., combination bands associated with the simultaneous excitation of internal MA^+ vibrations and lower-energy intermolecular modes.

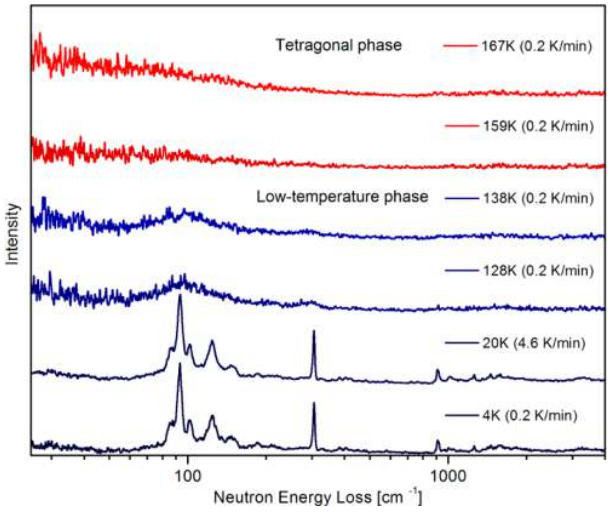

Figure 2. Temperature evolution of the INS spectrum of MAPI obtained at a cooling rate of 0.2 K/min across the phase transition from the tetragonal phase. The legend indicates the average temperature during the cooling runs. The data set labeled 159 K was collected over the range 165 → 154 K as the sample crossed the phase transition over a period of ca. 1.5 h, and thus it contains contributions from both phases. The low-temperature data shown at the bottom of the figure includes the INS spectrum measured at a much-faster cooling rate of 4.6 K/min. For further details, see the main text.

DOI: 10.1021/acs.jpclett.6b01822
J. Phys. Chem. Lett. 2016, 7, 4701−4709

From inspection of the INS data, it is evident that the spectral response is different above and below 160 K. These changes are also seen as an increase of elastically scattered neutrons as one enters the low-temperature phase. We note that the high-temperature INS data in either phase are quite featureless, and that the low-temperature phase is characterized by the presence of two distinct bands below 400 cm^{-1}. The overall envelope of these features is retained all the way down to 4 K. These results suggest that MA^+ has not been fully frozen and that it remains quite floppy inside the halide cage even after undergoing this phase transition upon cooling. A similar spectral broadening has been reported in recent temperature-dependent Raman studies of MAPI.[28] Figure 2 also shows that the resulting low-temperature INS spectrum is insensitive to the use of slow (0.2 K/min) or fast (4.6 K/min) cooling rates across the phase transition. This is an important result, as it indicates that phase metastability upon entering the low-temperature phase is either very unlikely or very hard to avoid in the first place. Our experimental findings can also be placed in the context of recent quasielastic neutron scattering studies.[29,30] In particular, Chen et al.,[26] have interpreted their experimental results in the tetragonal phase in terms of MA^+ motions along 4- (C_4) and 3-fold (C_3) symmetry axes normal to the C−N bond. According to this work, only C_3 rotations remain active in the low-temperature phase. The persistence of motions at low temperatures is also in line with a relatively small change in hydrogen mean-square displacements reported by Leguy et al.[30] when crossing the phase transition at ca. 160 K. In a similar vein, Bakulin et al.,[31] have used pump−probe ultrafast 2D vibrational spectroscopy to follow the dynamics of MA^+ in the tetragonal phase. This study has revealed two characteristic time constants of motion, identified as fast "wobbling-in-a-cone" (~300 fs) and slower "jump-like" reorientations of the molecular dipole with respect to the inorganic lattice (~3 ps). The presence of faster, wobbling-in-a-cone motions is consistent with our INS results as well as the work of Mattoni et al.[32] Notwithstanding the insights provided so far by these experimental data, the emergence of an ordered structure via a first-order phase change accompanied by an order−disorder-type transition of the MA^+ ensemble remains a puzzling phenomenon, and recent work has suggested a close interplay between the strength of HBs and octahedral tilting of the inorganic cage, the latter being regarded as a suitable order parameter.[9]

For a quantitative interpretation of the INS data presented above, we have resorted to the use of periodic DFT calculations, and to HLD and Born−Oppenheimer MD (BOMD) methodologies to simulate INS spectra for direct comparison with experiment; for further details, see the Computational Section. Figure 3 shows the most relevant models explored in this work; for more details, see the SI. We have made INS predictions using both fully as well as partially optimized models. Full-cell relaxation of the *Pnma* structure was performed with the dispersion-corrected PBE-TS functional. These calculations yielded cell constants a = 9.023 Å, b = 12.691 Å, and c = 8.480 Å, in very good agreement with available experimental data (a = 8.816 Å, b = 12.598 Å, and c = 8.564 Å).[29]

Figure 4 shows a comparison of the computational predictions against the experimental INS data. Above 1000 cm^{-1}, the spectral response is dominated by internal MA^+ modes. These have been analyzed in detail in previous works[16,17,19,28,32] and, as shown in Figure 4, can be described satisfactorily using the *Pnma* structure. These internal molecular modes are relatively insensitive to the local environment of the MA^+ cation. In addition to fundamental (0⇒1) band heads in this region, we also observe the presence of multiple higher-order transitions arising from overtones and phonon wings. It is also important to note that *Pnma* provides a fair description of fundamental modes in this range, yet it cannot reproduce at a quantitative level higher-order transitions arising from the coupling to low-energy external modes.

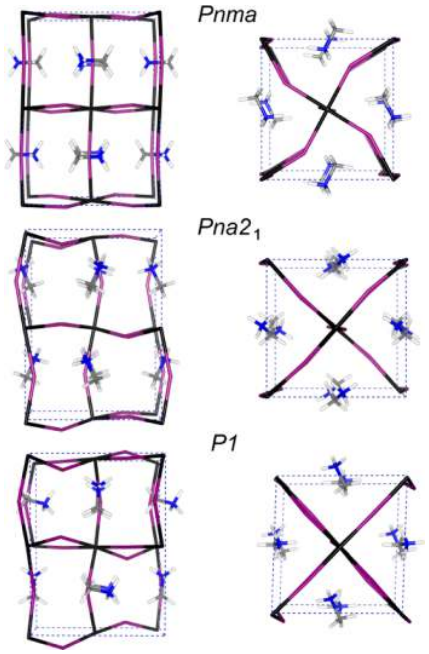

Figure 3. Fully optimized DFT structures for the most relevant low-temperature models explored in this work (*Pnma*, *Pna*2_1 and *P*1). Please note the different MA^+ orientations relative to the inorganic cage in each case. For further details, see the main text and the SI.

In addition to *Pnma*, the other two models shown in Figure 3 reflect other possible symmetries of the unit cell and these were explored in detail during a systematic search involving several dozens of possible alternatives with and without explicit symmetry constrains; for further details on the search procedure and associated criteria for model selection, see Sections 2 and 3 of the SI. Overall, our search revealed a very flat potential energy surface around MA^+, making the calculations increasingly challenging upon a reduction of the number of symmetry operations. One important and quite general finding relates to the coupling of MA^+ to inorganic-cage coordinates. The lead-iodide framework was found to be extremely flexible, its geometry being largely dictated by the specific orientation of MA^+ and the underlying (and dominant) HB interactions with the inorganic cage.

At lower energy transfers, we note the presence of a manifold of closely spaced transitions below 200 cm^{-1}, followed by a single and sharp feature above 300 cm^{-1}. As shown in more detail in Table 1 below and the SI, this feature can be assigned in all models to a disrotatory mode, and it is particularly sensitive to the local MA^+ environment. The results shown in the left panels of Figure 4 also serve to demonstrate that the specific orientation of MA^+ has a marked impact on the resulting INS response below 400 cm^{-1}. For *Pnma*, MA^+ is preferentially oriented along the perpendicular to the long axis

DOI: 10.1021/acs.jpclett.6b01822
J. Phys. Chem. Lett. 2016, 7, 4701−4709

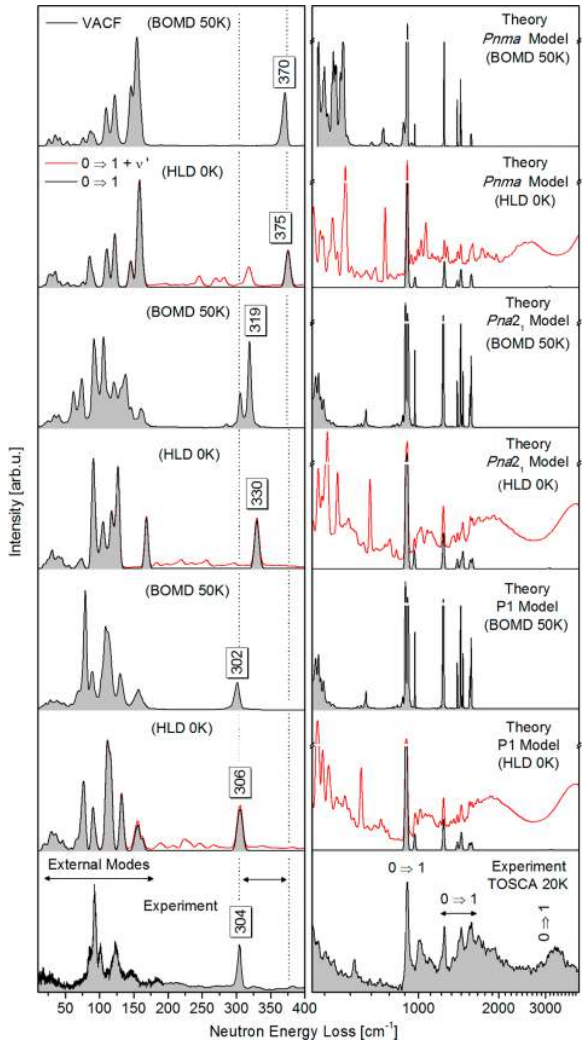

Figure 4. Comparison of experimental and theoretical INS spectra over the range 10−400 cm^{-1} (left) and 400−4000 cm^{-1} (right, note the log-scale for the abscissa). Theoretical spectra have been obtained using both HLD and BOMD calculations. In the latter case, VACF refers to the velocity autocorrelation function, as explained in more detail in the Computational Section. These predictions correspond to the models presented in Figure 3, calculated via full-cell optimization. For HLD predictions, fundamental transitions ($0 \Rightarrow 1$) are compared to those including overtones and combination bands ($0 \Rightarrow 1 + \nu'$), the latter represented by red lines. We note that the suppression of spectral intensities caused by the Debye−Waller factor is only accounted for by HLD.

of the unit-cell on the *ac* plane, as shown in Figure 3. For this model, we find that HLD calculations greatly overestimate the frequency of the feature observed experimentally at 304 cm^{-1}. BOMD results can help us capture nonharmonic corrections to this transition energy and show a very slight shift of this mode, from 375 down to 370 cm^{-1}. Also, we note that all solid-state calculations for the low-temperature phase reported in the literature predict the appearance of this feature at 350−400 cm^{-1}, as recently presented in refs 17 and 32. Moreover, both HLD and BOMD calculations using *Pnma* predict a prominent and inverted band head peaking at ca. 150 cm^{1}, in contrast with the reverse trend seen in the experimental INS data. Similar considerations apply to $Pna2_1$, where the C−N axis is preferentially oriented parallel to the long axis of the unit cell. In this case the isolated mode above 300 cm^{-1} is still overestimated and the relative intensities and positions of lower-lying modes below 200 cm^{-1} do not match those seen in the INS data, even if experimental cell volumes are used in the calculation. Similarly, other high-symmetry alternatives including $P2_1$, $P2_1/c$, Pc, and $P2_12_12_1$ do not describe the experimental INS data in a quantitative fashion.

From the analysis presented above, we can conclude that *Pnma* and $Pna2_1$ can only provide a qualitative description of the INS data. At a more quantitative level, the lower-symmetry *P*1 model provides the best quantitative match to the experimental INS data, as shown by the corresponding BOMD spectrum. In particular, this model can account for the additional (and weak) features observed in the range 300−400 cm^{-1} by including overtone and combination bands arising from the stronger features at lower energy transfers. From these INS data, we find no evidence to indicate the presence of other dominant geometries at low temperatures. The performance of a wide range of DFT exchange-correlation functionals to describe the INS data is reported in Section 2 of the SI. As figures of merit, this analysis has considered the overall agreement between experiment and calculation, as well as the location of the aforementioned spectral feature at 300 cm^{-1}. From this exercise, we conclude that our level of confidence that the *P*1 model constitutes an improved description of the INS results using state-of-the-art DFT is >95%. In terms of local structure, the organic cation in this model is oriented in both vertical and horizontal directions with equal probability. As such, this model is reminiscent of the higher-temperature tetragonal phase. A more detailed description is given in Section 3 of the SI, where it is also shown that the INS data is insensitive to the periodicity of the *P1* unit cell used in the PW-DFT calculations. To facilitate comparison with *Pnma* and $Pna2_1$, the *P*1 model is based on a $Z = 4$ symmetry-unconstrained superstructure, although it can be further simplified to a $Z = 2$ primitive cell corresponding to *Cc* symmetry. This primitive cell is shown in Figure 5, in order to

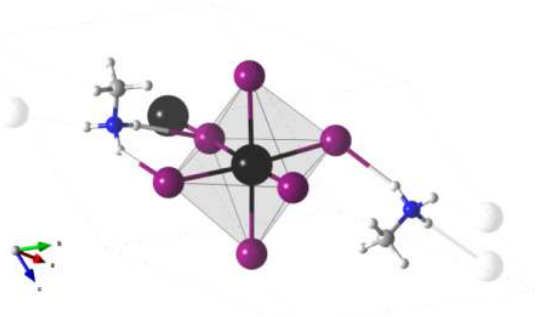

Figure 5. Primitive cell with $Z = 2$ and *P*1 symmetry. Iodine atoms outside the cell boundaries are represented as translucent balls.

illustrate its main structural motifs in the immediate vicinity of MA^+. These alternative views of the *P*1 model result in indistinguishable INS spectra and, therefore, are equivalent representations of the same local structure around MA^+ in MAPI. As such, our *P*1 model constitutes a suitable starting point for more detailed structure-search studies using experimental probes that are sensitive to both intermediate- and long-range order.[33,34] Sections 1 and 3 of the SI provide a

DOI: 10.1021/acs.jpclett.6b01822
J. Phys. Chem. Lett. 2016, 7, 4701−4709

more detailed discussion of the additional assumptions required to bridge the long-range order seen by XRD and the local environment around MA^+ as probed in this work via INS. One should further note that a *Cc* space group is acentric and, therefore, our model is consistent with previous findings by Filippetti et al.[35] in which the low-temperature phase of MAPI may be viewed as a disordered superparaelectric exhibiting spontaneous polarization at the nanoscale and polar compensation at the macroscale.

The top panel in Figure 6 shows the experimental INS spectrum below 400 cm^{-1} along with optical-spectroscopic data

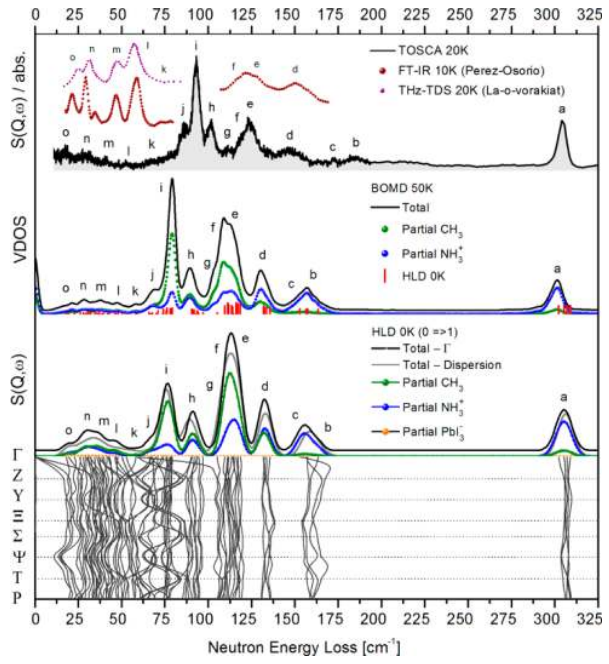

Figure 6. Spectroscopic data (top abcissa) and detailed analysis using the *P*1 model (bottom abscissa). Top: available experimental data at low energies including the INS spectrum (this work), as well as FT-IR and THz-TDS data from refs 22 and 23, respectively. For clarity, different optical data sets have been offset along the ordinate axis by arbitrary constants. Middle: partial and total VDOSs from BOMD calculations. Bottom: partial and total VDOSs using HLD with and without dispersion. To facilitate comparison with experimental data, all VDOSs have been weighted by their corresponding neutron cross sections. A more detailed comparison over the entire spectral range as well as normal-mode animations are given in the SI.

reported in the literature.[22,23] To facilitate comparison, spectral features in the INS data are labeled *a* thru *o*, starting from the highest-energy feature at 304 cm^{-1}. The first thing to note is that both INS and optical data share a number of common features below 200 cm^{-1}, although the intense triplet around 90 cm^{-1} is only present in the INS data. Figure 6 also presents BOMD and HLD predictions of the INS data using the *P*1 model. In particular, the BOMD INS spectrum provides a superb description of the INS data. We can further decompose the BOMD VDOS in terms of CH_3 and NH_3^+ contributions where, as expected on purely qualitative grounds, the INS response is dominated by hydrogen motions. This analysis also shows that the isolated spectral feature at 304 cm^{-1} is primarily associated with NH_3^+ motions, whereas at lower energies both CH_3 and NH_3^+ groups contribute in a similar way to the observed spectral intensities. These BOMD calculations can reproduce at a quantitative level all observed spectroscopic transitions.

The HLD predictions shown in Figure 6 have been further dissected into CH_3, NH_3^+, and PbI_3^- contributions, further confirming the BOMD results presented above. We also compare calculations at the Γ-point to those including full mode dispersion, and observe very similar results in both cases for those bands associated with MA^+ vibrations. These similarities imply that MA^+ motions are primarily local in nature, with little long-range coupling across cages. PbI_3^- modes contribute up to around 120 cm^{-1} and these modes exhibit a more pronounced dispersive character. Further, comparison of HLD with BOMD results also shows that anharmonicity has a more marked effect on relative intensities than on band positions, particularly for MA^+ modes labeled e−j in the figure. Within the HLD framework, we can further decompose the INS response in terms of normal modes and a detailed assignment of these is shown in Table 1 and the SI. The most intense feature at 93 cm^{-1} (labeled *i*) corresponds to $\circlearrowleft(N{-}CH_3)$ librations. This mode can only be observed via INS, as the Raman activity of this band is related to $\nu(Pb{-}I)$ contributions rather than to MA^+ motions. The most significant deviations in our predictions correspond to bands *b* and *c*, observed at 182 and 173 cm^{-1} and underestimated by the calculations by 15−20 cm^{-1} (see also Figure 6). These bands arise from NH_3^+ librations and hydrogen-bridge $\nu(N{-}H{\cdots}I)$ stretches. The corresponding average NH···I distances obtained from 50 ps BOMD trajectories at 50 K are 2.589, 2.594, and 2.633 Å for *Pnma*, $Pna2_1$, and *P*1 models, respectively. Although these distances compare well with an experimental value of 2.613 Å,[5] the INS results suggest that the PBE-TS exchange-correlation functional tends to underestimate the strength of these interactions.

Our predictions also allow for a robust assignment of previous FT-IR,[22] Raman,[16] and MD[32] results reported in the literature. Specifically, the distinct and isolated feature observed at 304 cm^{-1} and associated with disrotatory $\tau(NH_3^+)$-$\tau(CH_3)$ motions retains its character across all models investigated in this work, as it corresponds to a normal mode of vibration that is largely decoupled from framework vibrations and is not mixed with other internal modes. As such, its degenerate character in the INS data imposes strong constraints on the adequacy of the underlying structural model to describe the INS data. Furthermore, this feature is not Raman-active and, therefore, cannot be assigned to the broad Raman feature observed by Quarti et al.[16] at ca. 250 cm^{-1}. This feature has also been reported in MD simulations of a tightly bound cation using *Pnma*.[32] The recent assignment of this elusive transition by Ledinský et al.[20] as a resonantly enhanced second-order Raman signal thus appears to be more a more reasonable assignment, given the absence of fundamentals in the range 190−300 cm^{-1}. Features *a*,*d*, and *f* in Figure 6 have been previously reported by Pérez-Osorio et al.[23] using FT-IR and are assigned in Table 1. Using the HLD calculations, we can also make specific predictions of thermodynamic properties as a function of temperature. These results are shown in Section 4 of the SI. In particular, Figure S11 of the SI shows the temperature dependence of the molar heat capacity compared with the recent experimental results of Fabini et al.[15] Below 100 K, the agreement between experiment and our computational predictions for $Pna2_1$ and the *P*1 is excellent, whereas *Pnma* tends to underestimate this observable in a systematic fashion.

DOI: 10.1021/acs.jpclett.6b01822
J. Phys. Chem. Lett. 2016, 7, 4701−4709

Table 1. Comparison to Experiment and Spectroscopic Assignments Using the *P*1 Model[a]

ν [cm^{-1}]			Assignment
INS	HLD	BOMD	
3141	3093	3108	ν(CH) + ν(NH)
1584	1588	1585	δ(NH_3^+)
1557	1558	1560	
1448	1456	1454	
1413	1402	1402	$\delta_{sym}(CH_3)$
1253	1249	1240	ρ(NH_3^+) + ρ(CH_3)
911	898	896	
304[(a)]	306	302	*disrotatory* τ(NH_3^+)-τ(CH_3)
182[(b)]	157	157	*lib.* ↺ (C-NH_3^+) / ν(NH···I)
173[(c)]	153	153	
146[(d)]	132	130	*lib.* ↺ (C-NH_3^+) / ν(NH···I) + τ(CH_3)
124[(e)]	116	115	*lib.* ↺ ($CH_3NH_3^+$)
118[(f)]	111	109	*lib.* ↺ (N-CH_3) / τ(CH_3) + ν(PbI$_6$) $E_g(O_h)$
110[(g)]	105	106	*lib.* ↺ (N-CH_3) + ν(Pb-I)
102[(h)]	91	90	
93[(i)]	79	79	
87[(j)]	71	68	
66[(k)]	58	58	δ(I-Pb-I) $T_{1u}(O_h)$
53[(l)]	47	47	rocking / twisting PbI_6 deformation
40[(m)]	37	38	
30[(n)]	31	28	
18[(o)]	23	21	↺ (PbI_6) / *transl.* ⇒ Pb

[a]Superscripts a–o correspond to those shown in Figure 6. Hyperlinks to computer animations of all normal modes can be found in Table S3 of the SI.

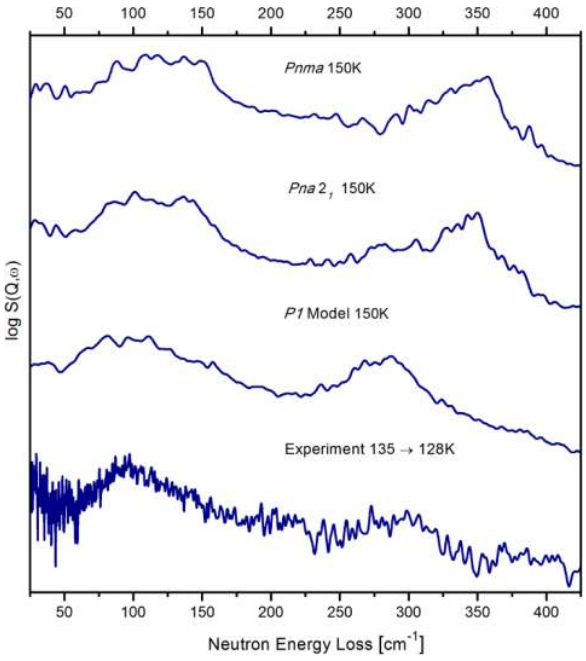

Figure 7. Low-energy INS spectra of the low-temperature phase of MAPI in the vicinity of the phase transition to the tetragonal phase. Bottom: experimental data. Other traces correspond to BOMD predictions using the PBE-TS functional. For further details, see the main text and the SI.

Along with the higher total free energy relative to $Pna2_1$ and *P*1 shown in Figure S10 of the SI, this result confirms the inadequacy of the *Pnma* model to describe MAPI at a quantitative level. Also, these heat-capacity data shows that a phonon-based description of atomic motions starts breaking down at ca. 100 K, a result that is entirely in line with the experimental INS data presented in Figure 2, as well as with an increasing contribution of stochastic motions associated with MA^+ reorientations within the perovskite cage.

As an additional and independent check of our predictions, we have performed BOMD calculations in the vicinity of the phase transition to the tetragonal phase. A comparison of these calculations with experiment is shown in Figure 7. Once more, we note that the *P*1 model provides a quantitative description of the experimental data relative to the qualitative agreement of either *Pnma* or $Pna2_1$. In particular, the broad band originating from orientationally averaged disrotatory $\tau(NH_3^+)$-$\tau(CH_3)$ motions moves below 300 cm^{-1} at these temperatures and is reproduced quantitatively by the *P*1 model, whereas *Pnma* or $Pna2_1$ predict the position of this feature ca. 100 cm^{-1} above. This finding indicates that the potential-energy landscape around MA^+ is considerably softer than previously anticipated and also explains why our experimental INS data differ from the MA^+-projected VDOSs recently reported by Mattoni et al.[32] using *Pnma*. More recent BOMD results by Lahnsteiner et al.[36] also highlight qualitative and nontrivial differences between the reorientational dynamics of the low-, intermediate-, and high-temperature phases of MAPI, whereby dynamical correlations between neighboring MA^+ cations show a maximum at room temperature, whereas in the lower- and higher-temperature phases these motions are less correlated. Figure S13 of the SI shows a more detailed evolution of BOMD spectra as a function of temperature, where the onset of significant spectral broadenings starts at ca. 60 K, in agreement with the slowing-down in relaxation dynamics upon cooling observed by Fabini et al.[15] This onset also sheds light on recent findings on the thermal conductance of MAPI films in the low-temperature phase,[37] where a Debye–Gallaway model becomes invalid just above 60 K and the temperature-dependence of the thermal conductivity can only be described with a glass-like model. We also note that Filippetti et al.[35] have reported that clear ferroelectric behavior can only be observed below 40–50 K when considering planar disorder of *Pm* symmetry. At higher temperatures, the polarization is expected to be progressively suppressed, as ferroelectric ordering is hindered by a large configurational entropy, findings that are consistent with our experimental and computational results.

We also recall that the *Pnma* crystallographic structure of MAPI has been obtained from single-crystal XRD at 100 K.[3] At this temperature, our BOMD results show that the reorientational dynamics of MA^+ is very pronounced, and that these motions are strongly coupled to the surrounding cage. This behavior is quite evident in the temperature dependence of BOMD spectra shown in Figure S13 of the SI, where the intensity of the two bands at 95 and 125 cm^{-1} (features *i* and *e* in Table 1) grow quite considerably. These two bands originate from HB-hindered MA^+ librations and their overall amplitude reflects distortions of the halide cage. These findings provide a starting point to account for the unusual behavior seen by Baikie et al.[3] in their Fourier maps and interpreted as anharmonic displacements of the iodine atoms. Figures S14–S17 in the SI confirm this picture. These images show cumulative BOMD coordinates at 100 and 150 K for the three models presented in detail in this work, as well as how these compare with the average atomic positions obtained from the aforementioned XRD studies. The first thing to note is the

DOI: 10.1021/acs.jpclett.6b01822
J. Phys. Chem. Lett. 2016, 7, 4701–4709

massive spatial delocalization of MA^+ at these temperatures, a situation where average atomic positions certainly cannot be taken as robust structural descriptors. Moreover, the PbI_3^- cage is far from being a static spectator of MA^+ motions. This is particularly the case for the iodine atoms, which respond quite sensitively to the proximity and relative orientation of MA^+ via H···I bonding. These motions have characteristic energies around 90 cm^{-1} (see features h–j in Table 1). This situation persists down to temperatures below 20 K, where the spatial delocalization of hydrogen is still considerable due to zero-point-energy fluctuations involving a large number of normal modes with mixed MA^+-PbI_3^- character (cf. Table 1 above and Table S3 in the SI). In particular, the most significant angular distortions of PbI_6 octahedra occur at energies below 50 cm^{-1}, and the lowest-lying optical transitions predicted at ca. 20 cm^{-1} still involve considerable MA^+ motions with mixed rotational–translational character.

In view of the growing interest in understanding phase coexistence and metastability and their relation to the photophysical properties of MAPI,[11,12,38] Table S2 in the SI provides a summary of calculated properties of *Pnma*, $Pna2_1$, and *P1*, bearing in mind that these predictions assume perfect long-range periodicity based on these unit-cell structures and, therefore, exclude yet-to-be-explored possibilities such as cell doubling, or the presence of domains or grain boundaries in the real material (cf. Sections 1 and 3 in the SI). These properties include cell parameters, total electronic energies, and associated band gaps. Although the shapes of both unit cells are very similar, the *P1* model is characterized by a slightly larger unit-cell volume, a higher electronic energy, and a lower electronic band gap. As explained in more detail in Section 3 in the SI, the reported unit-cell structure associated with the *P1* model is best viewed as a building block of intermediate and long-range order in the real material. We also emphasize that bridging the local environment around MA^+ (as probed by INS in this work) and the long-range order of the perovskite cage seen by crystallographic techniques remains an open challenge to the field.

In conclusion, the combined use of high-resolution INS experiments and state-of-the-art first-principles calculations has provided, for the first time, a detailed and quantitative view of the local environment and dynamics of MA^+ and its surrounding inorganic framework in the low-temperature phase of MAPI. We find that this phase is characterized by a highly disordered and mobile MA^+ both at low temperatures and in the vicinity of the transition to the tetragonal phase at 160 K. A substantial lowering of the local symmetry relative to *Pnma* is needed to attain quantitative agreement with available spectroscopic (INS and optical) as well as thermodynamic data. The present work, therefore, provides further impetus to understand at a fundamental level the structural and dynamical behavior of the low-temperature phase of MAPI, as well as suggests that the metastable character of this phase cannot be ruled out at present, rendering this material far more interesting than previously anticipated. As such, the improved model introduced in this work constitutes a suitable starting point for more detailed structure-search studies to describe intermediate- and long-range order in MAPI. At this point in time, we anticipate that this goal could be achieved via a detailed analysis of both Bragg features and underlying diffuse scattering of neutron and X-ray diffraction data as a function of temperature using pair-distribution-function analysis in conjunction with additional spectroscopic input and computational modeling. From a physicochemical viewpoint, our analysis also reveals that motions associated with MA^+ and the inorganic framework are inextricably coupled to each other all the way down to liquid-helium temperatures. We also emphasize that the HLD calculations performed in this work include (to first-order) zero-point-energy effects associated with the quantum nature of atomic motions. These appear to affect quite significantly both the structure and dynamics of the MA^+ moiety in MAPI, and also call for the full inclusion of nuclear motions in the description of its optical response and photovoltaic performance by taking advantage of recent and exciting methodological developments.[39]

EXPERIMENTAL SECTION

Sample Preparation. A 5-g powder sample of MAPI (CAS No 69507-98-8, purity >99%) was purchased from Xi'an Polymer Light Technologies and used as received. Prior to the INS experiments, the integrity and crystallinity of the specimen was checked at room temperature using a Rigaku MiniFlex 600 X-ray diffractometer.[40]

Inelastic Neutron Scattering. High-resolution INS measurements using a total sample mass of 4.3 g contained in a vacuum-tight flat aluminum cell of cross-sectional area 4 × 4 cm^2 were performed on the TOSCA spectrometer at the ISIS Pulsed Neutron & Muon Source, Rutherford Appleton Laboratory, United Kingdom.[25−27] TOSCA is a so-called inverted-geometry neutron spectrometer spanning energy-transfers up to 4000 cm^{-1}. The spectral resolution of TOSCA is comparable to more conventional infrared and Raman techniques, and amounts to ca. 2% across the spectral range of interest to this work. Numerous examples of TOSCA data can be found in ref 41. In this particular study, sample temperatures ranged from 4 to 180 K during data acquisition. Sample cooling was achieved via the use of a dedicated closed-cycle helium refrigerator. Additional heaters and sensors directly attached to the sample enabled fine temperature control over this temperature range.

COMPUTATIONAL SECTION

First-Principles Calculations. The periodic plane-wave (PW) DFT calculations presented in the main text were performed with the CASTEP 16.1 code.[42] The initial unit cell was constructed based on the *Pnma* structure reported in ref 3 using the cell constants measured by Chen et al. at T = 4 K.[29] Alternative models were examined by modifying this reference structure, and a detailed account of this procedure can be found in Section 3 of the SI. The computations were performed using fixed and fully relaxed cell methodologies at atmospheric pressure. Exchange and correlation were defined all throughout with the Perdew–Burke–Ernzerhof (PBE) functional[43] with the addition Tkatchenko-Scheffler (TS) dispersion corrections,[44] hereafter referred to as PBE-TS. Core electrons were represented via the use of norm-conserving pseudopotentials, and electronic wave functions were expanded using a PW basis set with a kinetic-energy cutoff of 900 eV. The *k*-point grid was adjusted to maintain a constant spacing in reciprocal space of 0.05 $Å^{-1}$, and the self-consistent-field energy was converged with a tolerance of 1 × 10^{-12} eV per atom. For geometry optimization, Hellmann–Feynman forces acting on individual ions were minimized down to 10^{-5} eV, and the associated stress components converged to within 10^{-4} GPa. These choices of the level of theory and convergence criteria have been shown to be adequate for a quantitative description of the spectral

DOI: 10.1021/acs.jpclett.6b01822
J. Phys. Chem. Lett. 2016, 7, 4701−4709

response of HB systems at low energy transfers, as recently illustrated in refs 45 and 46. HLD calculations at zero temperature were performed using Density-Functional Perturbation Theory (DFPT) as currently implemented in the CASTEP code.[47] These calculations provide phonon frequencies and associated eigenvectors as input for the simulation of neutron observables. HLD-derived INS spectra were modeled within the incoherent approximation using the aClimax program.[48,49] HLD is a suitable framework to describe the low-temperature INS data and allows for the inclusion of the Debye−Waller factor in these calculations, which reproduce the strong suppression of INS features above 1000 cm^{-1} in MAPI. In order to study anharmonic corrections and thermally induced spectral broadenings at higher temperatures, BOMD simulations were also performed for selected models without symmetry constraints. We recall that these simulations assume that nuclear motions can be treated classically and, therefore, their realm of applicability is restricted to the higher temperatures. Calculated Debye temperatures using HLD and shown in Figure S12 of the SI show that BOMD becomes an adequate approach above 25−30 K. These BOMD simulations were performed using the same numerical settings and the same *k*-point spacing. In this case, self-consistent-field convergence criteria were reduced to 2.5×10^{-8} eV per atom. BOMD calculations were performed up to temperature range 150 K using the canonical (NVT) ensemble with a Nose−Hoover thermostat. Cell volumes were kept fixed to those obtained at zero temperature using PBE-TS. A time step of 0.5 fs was used all throughout. NVT ensemble temperatures were equilibrated for 5 ps, followed by NVE production runs of at least 50 ps. From these production runs, VDOSs were obtained via the Fourier-cosine integral transform of the VACF using the nMoldyn code.[50]

■ ASSOCIATED CONTENT

Supporting Information

The Supporting Information is available free of charge on the ACS Publications website at DOI: 10.1021/acs.jpclett.6b01822.

Comparison of diffraction and INS observables, influence of exchange-correlation DFT functionals on INS spectra, current and alternative models, thermodynamic properties, ab initio molecular dynamics, detailed spectroscopic assignments, and normal-mode animations (PDF)

■ AUTHOR INFORMATION

Corresponding Author

*E-mail: felix.fernandez-alonso@stfc.ac.uk.

Notes

The authors declare no competing financial interest.

■ ACKNOWLEDGMENTS

The authors thank the anonymous referees for a detailed set of insightful comments on the original submission of this work. The UK Science & Technology Facilities Council is acknowledged for financial support, and access to beam time and laboratory equipment at the ISIS Facility. This research was partially supported by the PLGrid Infrastructure, the PROMETHEUS facility (Grant IDs latticedynamics, latticedynamics02), and the 2014-2020 CNR-STFC Agreement for collaborative scientific research at ISIS.

■ REFERENCES

(1) Kojima, A.; Teshima, K.; Shirai, Y.; Miyasaka, T. Organometal Halide Perovskites as Visible-Light Sensitizers for Photovoltaic Cells. *J. Am. Chem. Soc.* **2009**, *131*, 6050−6051.

(2) Adams, A. M.; Marin-Beloqui, J. M.; Stoica, G.; Palomares, E. The Influence of the Mesoporous TiO_2 Scaffold on the Performance of Methyl Ammonium Lead Iodide (MAPI) Perovskite Solar Cells: Charge Injection, Charge Recombination and Solar Cell Efficiency Relationship. *J. Mater. Chem. A* **2015**, *3*, 22154−22161.

(3) Baikie, T.; Fang, Y.; Kadro, J. M.; Schreyer, M.; Wei, F.; Mhaisalkar, S. G.; Graetzel, M.; White, T. J. Synthesis and Crystal Chemistry of the Hybrid Perovskite $(CH_3NH_3)PbI_3$ for Solid-State Sensitised Ssolar Cell Applications. *J. Mater. Chem. A* **2013**, *1*, 5628−5641.

(4) Ren, Y.; Oswald, I. W. H.; Wang, X.; McCandless, G. T.; Chan, J. Y. Orientation of Organic Cations in Hybrid Inorganic−Organic Perovskite $CH_3NH_3PbI_3$ from Subatomic Resolution Single Crystal Neutron Diffraction Structural Studies. *Cryst. Growth Des.* **2016**, *16*, 2945−2951.

(5) Weller, M. T.; Weber, O. J.; Henry, P. F.; Di Pumpo, A. M.; Hansen, T. C. Complete Structure and Cation Orientation in the Perovskite Photovoltaic Methylammonium Lead Iodide Between 100 and 352 K. *Chem. Commun.* **2015**, *51*, 4180−4183.

(6) Poglitsch, A.; Weber, D. Dynamic Disorder in Methylammoniumtrihalogenoplumbates (II) Observed by Millimeter-Wave Spectroscopy. *J. Chem. Phys.* **1987**, *87*, 6373−6378.

(7) Worhatch, R. J.; Kim, H.-J.; Swainson, I. P.; Yonkeu, A. L.; Billinge, S. J. L. Study of Local Structure in Selected Organic−Inorganic Perovskites in the Pmpm Phase. *Chem. Mater.* **2008**, *20*, 1272−1277.

(8) Lee, J.-H.; Bristowe, N. C.; Bristowe, P. D.; Cheetham, A. K. Role of Hydrogen-Bonding and its Interplay With Octahedral Tilting in $CH_3NH_3PbI_3$. *Chem. Commun.* **2015**, *51*, 6434−6437.

(9) Lee, J. H.; Lee, J.-H.; Kong, E.-H.; Jang, H. M. The Nature of Hydrogen-Bonding Interaction in the Prototypic Hybrid Halide Perovskite, Tetragonal $CH_3NH_3PbI_3$. *Sci. Rep.* **2016**, *6*, 21687.

(10) Deretzis, I.; Di Mauro, B. N.; Alberti, A.; Pellegrino, G.; Smecca, E.; La Magna, A. Spontaneous Bidirectional Ordering of $CH_3NH_3^+$ in Lead Iodide Perovskites at Room Temperature: The Origins of the Tetragonal Phase. *Sci. Rep.* **2016**, *6*, 24443.

(11) Kong, W.; Ye, Z.; Qi, Z.; Zhang, B.; Wang, M.; Rahimi-Iman, A.; Wu, H. Characterization of an Abnormal Photoluminescence Behavior upon Crystal-Phase Transition of Perovskite $CH_3NH_3PbI_3$. *Phys. Chem. Chem. Phys.* **2015**, *17*, 16405−16411.

(12) Tahara, H.; Endo, M.; Wakamiya, A.; Kanemitsu, Y. Experimental Evidence of Localized Shallow States in Orthorhombic Phase of $CH_3NH_3PbI_3$ Perovskite Thin Films Revealed by Photocurrent Beat Spectroscopy. *J. Phys. Chem. C* **2016**, *120*, 5347−5352.

(13) Ohmann, R.; Ono, L. K.; Kim, H.-S.; Lin, H.; Lee, M. V.; Li, Y.; Park, N.-G.; Qi, Y. Real-Space Imaging of the Atomic Structure of Organic−Inorganic Perovskite. *J. Am. Chem. Soc.* **2015**, *137*, 16049−16054.

(14) She, L.; Liu, M.; Zhong, D. Atomic Structures of $CH_3NH_3PbI_3$ (001) Surfaces. *ACS Nano* **2016**, *10*, 1126−1131.

(15) Fabini, D. H.; Hogan, T.; Evans, H. A.; Stoumpos, C. C.; Kanatzidis, M. G.; Seshadri, R. Dielectric and Thermodynamic Signatures of Low-Temperature Glassy Dynamics in the Hybrid Perovskites $CH_3NH_3PbI_3$ and $HC(NH_2)_2PbI_3$. *J. Phys. Chem. Lett.* **2016**, *7*, 376−381.

(16) Quarti, C.; Grancini, G.; Mosconi, E. O.; Bruno, P.; Ball, J. M.; Lee, M. M.; Snaith, H. J.; Petrozza, A.; De Angelis, F. The Raman Spectrum of the $CH_3NH_3PbI_3$ Hybrid Perovskite: Interplay of Theory and Experiment. *J. Phys. Chem. Lett.* **2014**, *5*, 279−284.

(17) Brivio, F.; Frost, J. M.; Skelton, J. M.; Jackson, A. J.; Weber, O. J.; Weller, M. T.; Goni, A. R.; Leguy, A. M. A.; Barnes, P. R. F.; Walsh, A. Lattice Dynamics and Vibrational Spectra of the Orthorhombic, Tetragonal, and Cubic Phases of Methylammonium Lead Iodide. *Phys. Rev. B: Condens. Matter Mater. Phys.* **2015**, *92*, 144308.

DOI: 10.1021/acs.jpclett.6b01822
J. Phys. Chem. Lett. 2016, 7, 4701−4709

(18) Mattoni, A.; Filippetti, A.; Saba, M. I.; Delugas, P. Methylammonium Rotational Dynamics in Lead Halide Perovskite by Classical Molecular Dynamics: The Role of Temperature. *J. Phys. Chem. C* **2015**, *119*, 17421.
(19) Niemann, R. G.; Kontos, A. G.; Palles, D.; Kamitsos, E. I.; Kaltzoglou, A.; Brivio, F.; Falaras, P.; Cameron, P. J. Halogen Effects on Ordering and Bonding of $CH_3NH_3^+$ in $CH_3NH_3PbX_3$ (X = Cl, Br, I) Hybrid Perovskites: A Vibrational Spectroscopic Study. *J. Phys. Chem. C* **2016**, *120*, 2509−2519.
(20) Ledinský, M.; Löper, P.; Niesen, B.; Holovský, J.; Moon, S.-J.; Yum, J.-H.; De Wolf, S.; Fejfar, A.; Ballif, C. Raman Spectroscopy of Organic−Inorganic Halide Perovskites. *J. Phys. Chem. Lett.* **2015**, *6*, 401−406.
(21) Glaser, T.; Müller, C.; Sendner, M.; Krekeler, C.; Semonin, O. E.; Hull, T. D.; Yaffe, O.; Owen, J. S.; Kowalsky, W.; Pucci, A.; et al. Infrared Spectroscopic Study of Vibrational Modes in Methylammonium Lead Halide Perovskites. *J. Phys. Chem. Lett.* **2015**, *6*, 2913−2918.
(22) La-o-Vorakiat, C.; Xia, H.; Kadro, J.; Salim, T.; Zhao, D.; Ahmed, T.; Lam, Y. M.; Zhu, J.-X.; Marcus, R. A.; Michel-Beyerle, M.-E.; et al. Phonon Mode Transformation Across the Orthohombic−Tetragonal Phase Transition in a Lead Iodide Perovskite $CH_3NH_3PbI_3$: A Terahertz Time-Domain Spectroscopy Approach. *J. Phys. Chem. Lett.* **2016**, *7*, 1−6.
(23) Pérez-Osorio, M. A.; Milot, R. L.; Filip, M. R.; Patel, J. B.; Herz, L. M.; Johnston, M. B.; Giustino, F. Vibrational Properties of the Organic−Inorganic Halide Perovskite $CH_3NH_3PbI_3$ from Theory and Experiment: Factor Group Analysis, First-Principles Calculations, and Low-Temperature Infrared Spectra. *J. Phys. Chem. C* **2015**, *119*, 25703−25718.
(24) Price, D. L.; Fernandez-Alonso, F. In *Neutron Scattering − Fundamentals*; Fernandez-Alonso, F., Price, D. L., Eds.; Academic Press: San Diego, CA, 2013; pp 1−136.
(25) www.isis.stfc.ac.uk/instruments/tosca (Accessed 26 Oct 2016).
(26) Pinna, R. S.; Rudić, S.; Parker, S. F.; Gorini, G.; Fernandez-Alonso, F. Monte Carlo Simulations of the TOSCA Spectrometer: Assessment of Current Performance and Future Upgrades. *EPJ Web Conf.* **2015**, *83*, 03013−5.
(27) Parker, S. F.; Fernandez-Alonso, F.; Ramirez-Cuesta, A. J.; Tomkinson, J.; Rudić, S.; Pinna, R. S.; Gorini, G.; Fernández Castañón, J. Recent and Future Developments on TOSCA at ISIS. *J. Phys.: Conf. Ser.* **2014**, *554*, 012003−9.
(28) Leguy, A. M. A.; Goñi, A. R.; Frost, J. M.; Skelton, J.; Brivio, F.; Rodríguez-Martínez, X.; Weber, O. J.; Pallipurath, A.; Alonso, M. I.; Campoy-Quiles, M. Dynamic Disorder, Phonon Lifetimes, and the Assignment of Modes to the Vibrational spectra of Methylammonium Lead Halide Perovskites. *Phys. Chem. Chem. Phys.* **2016**, *18*, 27051.
(29) Chen, T.; Foley, B. J.; Ipek, B.; Tyagi, M.; Copley, J. R. D.; Brown, C. M.; Choi, J. J.; Lee, S.-H. Rotational Dynamics of Organic Cations in the $CH_3NH_3PbI_3$ Perovskite. *Phys. Chem. Chem. Phys.* **2015**, *17*, 31278−31286.
(30) Leguy, A. M. A.; Frost, J. M.; McMahon, A. P.; Sakai, V. G.; Kochelmann, W.; Law, C.; Li, X.; Foglia, F.; Walsh, A.; O'Regan.; et al. The Dynamics of Methylammonium Ions in Hybrid Organic−Inorganic Perovskite Solar Cells. *Nat. Commun.* **2015**, *6*, 7124.
(31) Bakulin, A. A.; Selig, O.; Bakker, H. J.; Rezus, Y. L. A.; Müller, C.; Glaser, T. S.; Lovrincic, R.; Sun, Z.; Chen, Z.; Walsh, A.; et al. Real-Time Observation of Organic Cation Reorientation in Methylammonium Lead Iodide Perovskites. *J. Phys. Chem. Lett.* **2015**, *6*, 3663−3669.
(32) Mattoni, A.; Filippetti, A.; Saba, M. I.; Caddeo, C.; Delugas, P. Temperature Evolution of Methylammonium Trihalide Vibrations at the Atomic Scale. *J. Phys. Chem. Lett.* **2016**, *7*, 529−535.
(33) Keen, D. A.; Goodwin, A. L. The crystallography of correlated disorder. *Nature* **2015**, *521*, 303−309.
(34) Egami, T.; Billinge, S. J. L. *Underneath the Bragg Peaks: Structural Analysis of Complex Materials*; Pergamon Press/Elsevier: Oxford, 2003; pp 1−424.
(35) Filippetti, A.; Delugas, P.; Saba, M. I.; Mattoni, A. Entropy-Suppressed Ferroelectricity in Hybrid Lead-Iodide Perovskites. *J. Phys. Chem. Lett.* **2015**, *6*, 4909−4915.
(36) Lahnsteiner, J.; Kresse, G.; Kumar, A.; Sharma, D. D.; Franchini, C.; Bokdam, M. Room Temperature Dynamic Correlation between Methylammonium Molecules in Lead-iodine Based Perovskite: An Ab-initio Molecular Dynamics Perspective. *arXiv.org, e-Print Arch., Condens. Matter* **2016**, No. arxiv.org/abs/1608.04991.
(37) Chen, Q.; Zhang, C.; Zhu, M.; Liu, S.; Siemens, M. E.; Gu, S.; Zhu, J.; Shen, J.; Wu, X.; Liao, C.; et al. Efficient Thermal Conductance in Organometallic Perovskite $CH_3NH_3PbI_3$ Films. *Appl. Phys. Lett.* **2016**, *108*, 081902.
(38) Panzer, F.; Bässler, S.; Hüttner, S.; Köhler, J.; Moos, R.; Thelakkat, M.; Hildner, R.; Köhler, A.; et al. Reversible Laser Induced Amplified Spontaneous Emission from Coexisting Tetragonal and Orthorhombic Phases in Hybrid Lead Halide Perovskites. *Adv. Opt. Mater.* **2016**, *4*, 917−928.
(39) Zacharias, M.; Giustino, M. One-Shot Calculation of Temperature-Dependent Optical Spectra and Phonon-Induced Band-Gap Renormalization. *Phys. Rev. B: Condens. Matter Mater. Phys.* **2016**, *94*, 075125.
(40) www.isis.stfc.ac.uk/support-laboratories/materials-characterisation-lab/rigaku-miniflex-60015292.html (Accessed 26 Oct 2016).
(41) www.isis.stfc.ac.uk/instruments/tosca/ins-database (Accessed 26 Oct 2016).
(42) Clark, S. J.; Segall, M. D.; Pickard, C. J.; Hasnip, P. J.; Probert, M. J.; Refson, K.; Payne, M. C. First Principles Methods Using CASTEP. *Z. Kristallogr. - Cryst. Mater.* **2005**, *220*, 567−570.
(43) Perdew, J. P.; Burke, K.; Ernzerhof, M. Generalized Gradient Approximation Made Simple. *Phys. Rev. Lett.* **1996**, *77*, 3865−3868.
(44) Tkatchenko, A.; Scheffler, M. Accurate Molecular Van Der Waals Interactions from Ground-State Electron Density and Free-Atom Reference Data. *Phys. Rev. Lett.* **2009**, *102*, 073005.
(45) Łuczyńska, K.; Drużbicki, K.; Lyczko, K.; Dobrowolski, J. Cz. Experimental (X-ray, ^{13}C CP/MAS NMR, IR, RS, INS, THz) and Solid-State DFT Study on (1:1) Co-Crystal of Bromanilic Acid and 2,6-Dimethylpyrazine. *J. Phys. Chem. B* **2015**, *119*, 6852−6872.
(46) Krzystyniak, M.; Drużbicki, K.; Fernandez-Alonso, F. Nuclear Dynamics in the Metastable Phase of the Solid Acid Caesium Hydrogen Sulfate. *Phys. Chem. Chem. Phys.* **2015**, *17*, 31287−31296.
(47) Refson, K.; Clark, S. J.; Tulip, P. R. Variational Density-Functional Perturbation Theory for Dielectrics and Lattice Dynamics. *Phys. Rev. B: Condens. Matter Mater. Phys.* **2006**, *73*, 155114.
(48) Ramirez-Cuesta, A. J. *Comput. Phys. Commun.* **2004**, *157*, 226−238.
(49) Champion, D.; Tomkinson, J.; Kearley, G. a-CLIMAX: a New INS Analysis Tool. *Appl. Phys. A: Mater. Sci. Process.* **2002**, *74*, S1302−S1304.
(50) Róg, T.; Murzyn, K.; Hinsen, K.; Kneller, G. R. nMoldyn: A Program Package for a Neutron Scattering Oriented Analysis of Molecular Dynamics Simulations. *J. Comput. Chem.* **2003**, *24*, 657−667.

DOI: 10.1021/acs.jpclett.6b01822
J. Phys. Chem. Lett. 2016, 7, 4701−4709

Supporting Information for Publication

Unexpected Cation Dynamics in the Low-temperature Phase of Methylammonium Lead Iodide – The Need for Improved Models

Kacper Drużbicki,[†,‡] Roberto Simone Pinna,[§,‖] Svemir Rudić,[§] Marek Jura,[§] Giuseppe Gorini[‖] and Felix Fernandez-Alonso*[§,⊥]

[†]Faculty of Physics, Adam Mickiewicz University, Umultowska 85, 61-614 Poznan, Poland
[‡]Frank Laboratory of Neutron Physics, Joint Institute for Nuclear Research, 141980, Dubna, Russia
[§]ISIS Facility, Rutherford Appleton Laboratory, Chilton, Didcot, Oxfordshire OX11 0QX, UK
[‖]CNISM, Università degli Studi di Milano-Bicocca, Piazza della Scienza 3, 20126 Milano, Italy
[⊥]Department of Physics and Astronomy, University College London, Gower Street, London, WC1E 6BT, UK

Corresponding Author
*e-mail: felix.fernandez-alonso@stfc.ac.uk

For an online version of this ESI, including normal-mode animations, click here

Contents:

1. Setting the scene: X-ray diffraction and INS of MAPI at low temperatures

For the benefit of the general reader, this section summarizes the complementarity between X-ray Diffraction (XRD) and Inelastic Neutron Scattering (INS), as the former has been used extensively to study the structure of MAPI, whereas this work has used INS for the first time. XRD is primarily sensitive to the heavier Pb and I atoms and their long-range order, whereas INS probes the local environment (short-range order) of the organic cation. Figure S1 serves to illustrate the above.

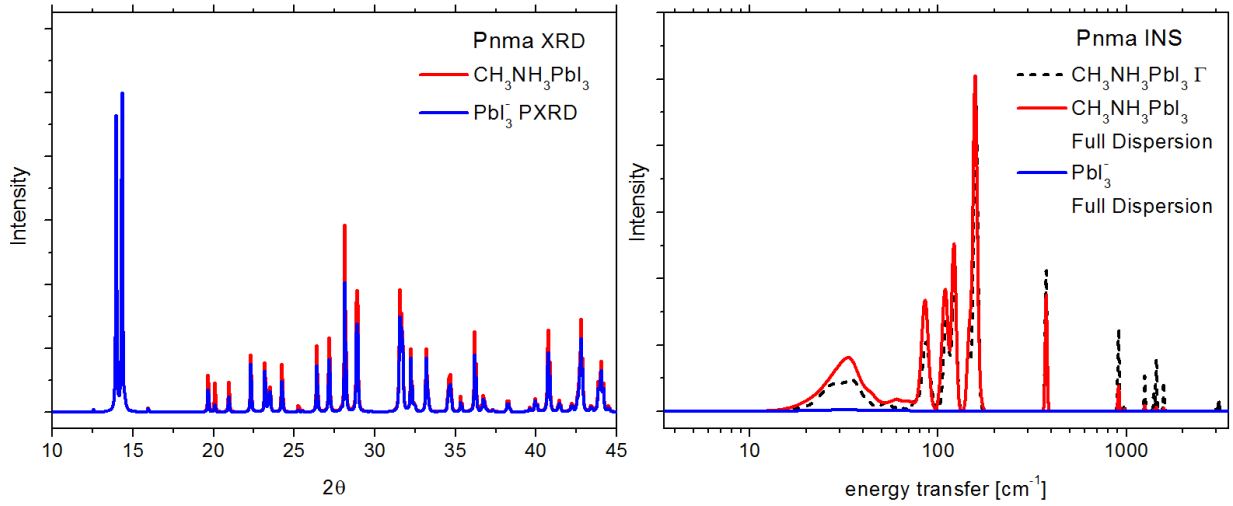

Figure S1. Simulated XRD patterns (left, Cu K-alpha radiation) and INS spectra (right) of the *Pnma* model of MAPI, calculated using PW-DFT (PBE-TS) at T = 0 K. Red(blue) traces in both cases correspond to the presence(absence) of the methylammonium cation in the material. INS spectra have been calculated at the Γ-point (black) and with full dispersion (red and blue) in order to illustrate the local character of the technique, as discussed in the main text.

The left-hand panel of Figure S1 shows simulated powder XRD diffraction patterns data for the *Pnma* model with (red) and without (blue) organic cation inside the cage. The results were obtained for the fully optimized structure using PBE-TS and a temperature of 0 K.[1,2] From this comparison, we note that the total number of Bragg reflections is not affected by the presence of the much-lighter organic cation – thus, its geometry within the unit cell can only be inferred from changes to intensities associated with Bragg reflections of the perovskite framework. In terms of information content, the simulated XRD data is to be regarded as a best-case scenario, as it does not include effects associated with finite temperature (Debye-Waller suppression of Bragg intensities), static or thermal diffuse scattering between the Bragg peaks, or other subtle effects which may be traced back to the partial presence or complete absence of long-range order. New methods developed recently to include diffuse scattering in single-crystal data using lattice dynamics calculations[3] would be useful to analyse diffraction data. The figure on the right shows the corresponding INS data, also calculated with PBE-TS,[1,2] and noting that the situation has been reversed relative to XRD – the INS data primarily probes the organic cation and the potential-energy landscape in its immediate surroundings. Thus, the structural model we propose in this work only accounts for the local environment around the cation and, as such, does not capture far-more subtle effects associated with intermediate- and long-range order (cell-doubling, presence of domains, grain boundaries, etc.). To illustrate further these features, Fig. S1 shows a comparison of INS spectra over the entire Brillouin zone (full dispersion) and at the Γ-point (isolated organic cation). We note that full dispersion tends to give rise to slightly broader spectral features relative to Γ-point calculations, in line with the weak dispersive character of INS features explicitly shown in the bottom panel of Fig. 6 in the main manuscript. These results further reinforce the notion that the coupling of cation motions across neighboring cells is weak and does not affect the INS data. From a chemical viewpoint, Fig. 5 of the main manuscript highlights the main bonding motifs in the immediate surroundings of the cation.

A remaining challenge emphasized throughout this work is to reconcile these two extremes, namely, that of the long-range structure of the inorganic framework (as seen by XRD and currently described by *Pnma*) and the local environment around the cation, as seen by INS and accounted for using a *P1* model over a broad temperature range up to the vicinity of the transition to the tetragonal phase. Such a task is beyond the overall scope of the present work, and calls for further detailed studies, as described in the main manuscript. These include extension of single-crystal crystallographic work to lower temperatures and a detailed analysis of both Bragg features and underlying diffuse scattering. A suitable approach

to achieve this goal would be to perform Pair-Distribution-Function (PDF) analysis of low- temperature crystallographic data. The PDF method analyzes the total scattering where all structure-relevant scattering is used, including Bragg and diffuse scattering over a wide range of reciprocal space. PDF has been recently successfully applied to study structural disorder in the tetragonal phase of MAPI within mesoporous TiO_2,[4] revealing inhomogenities associated with these MAPI nanostructures.

2. Influence of exchange-correlation functional on the calculated INS spectrum

INS spectra of the low-temperature phase of MAPI were calculated using *Pnma* symmetry and shown in Fig. S2. Cell constants were fixed to experimental values at T = 4 K.[5] Spectra were calculated using 'soft' (PBEsol),[6] standard (PBE)[1] and 'hard' (rPBE)[7] formulations of the generalized-gradient approximation (GGA) of the exchange-correlation (XC) functional. Fixed-cell calculations employing the dispersion corrections of Tkatchenko and Scheffler (PBE-TS)[2] are also given for comparison. While these INS spectra differ considerably from each other in the librational range of cation modes below 200 cm^{-1}, none of the aforementioned approaches using *Pnma* provides a quantitative prediction for the transition energy associated with the disrotatory torsional band observed experimentally at *ca.* 300 cm^{-1}.

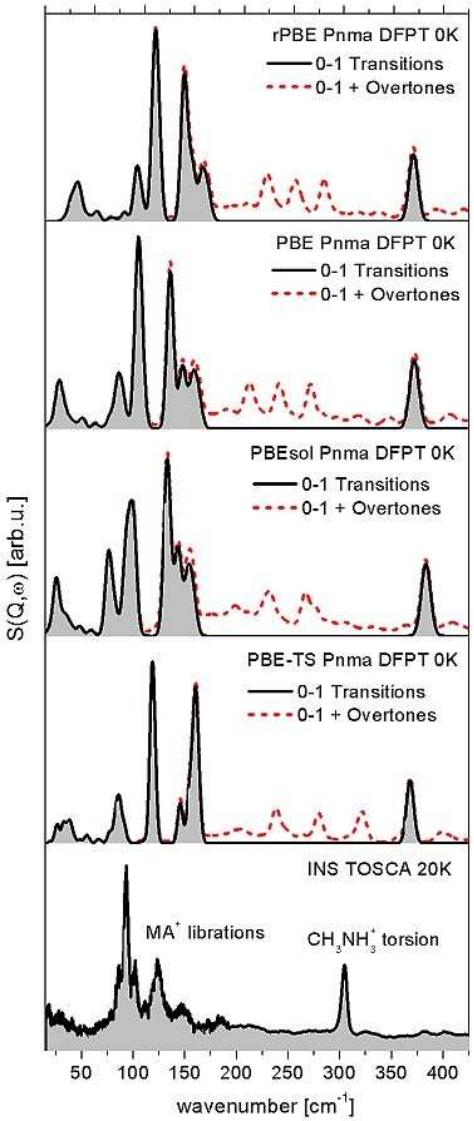

Figure S2. Dependence of INS spectra of the low-temperature phase of MAPI on XC functional. All phonon calculations shown have used DFPT HLD and *Pnma* , as discussed in more detail in the main text. Theoretical spectra have been calculated at the Γ-point and are presented along with the experimental data (bottom panel above).

More advanced approximations to the underlying XC functional were further examined using the linear-combination-of-atomic-orbitals (LCAO) approach in CRYSTAL14.[8] At the moment, this code provides the largest set of XC functionals among all solid-state DFT packages. The organic cation was treated with triple-zeta quality and solid-state-optimized pob-TZVP[9] functions. The large-core pseudopotential basis-sets according to Doll were applied to Pb and I atoms.[10] The computational conditions for the evaluation of the Coulomb and exchange series involved truncation tolerances of 10^{-8}, 10^{-8}, 10^{-8}, 10^{-8}, and 10^{-16} Ha. The integration of the XC contribution to the Fock Matrix was performed with XLGRID. Monkhorst-Pack/Gilat shrinking factors for k-point sampling of reciprocal space were set to 16×16. The convergence criterion on total energies for the SCF cycles was set to 10^{-12} Ha and the total convergence criteria for the geometry optimization process on total energy, atomic displacement, and energy gradient were defined as 10^{-10} Ha, 10^{-5} Å, and 5 x 10^{-5} Ha/Å^{-1}, respectively. In order to avoid spurious internal stresses, harmonic frequencies were calculated with the finite-displacement method for the fully-optimized crystal structures. Various exchange-correlation functionals were adopted, including the Local Density Approximation LDA (SVWN[11,12]), GGA (PBE,[1] PBEsol,[4] BLYP,[13-14] SOGGA[15]), meta-GGA hybrid (Mo6-2X[16]) as well as standard global hybrids (B3LYP,[12,13,14,17] PBE0,[18] PBEsolo,[6,18] PBE0-13,[19] B3PW,[17,20,21,22,23] B97H,[24,25] B1WC[26]), and range-separated functionals (HSE06,[1,18,27] HISS,[28,29] HSEsol,[6,30] LC-WBLYP[31]). Figure S3 shows the performance of these aforementioned functionals to describe the INS data using *Pnma*. PBE-TS calculations performed with CASTEP for all three models considered (*Pnma, Pna21 and P1*) are also given for comparison.

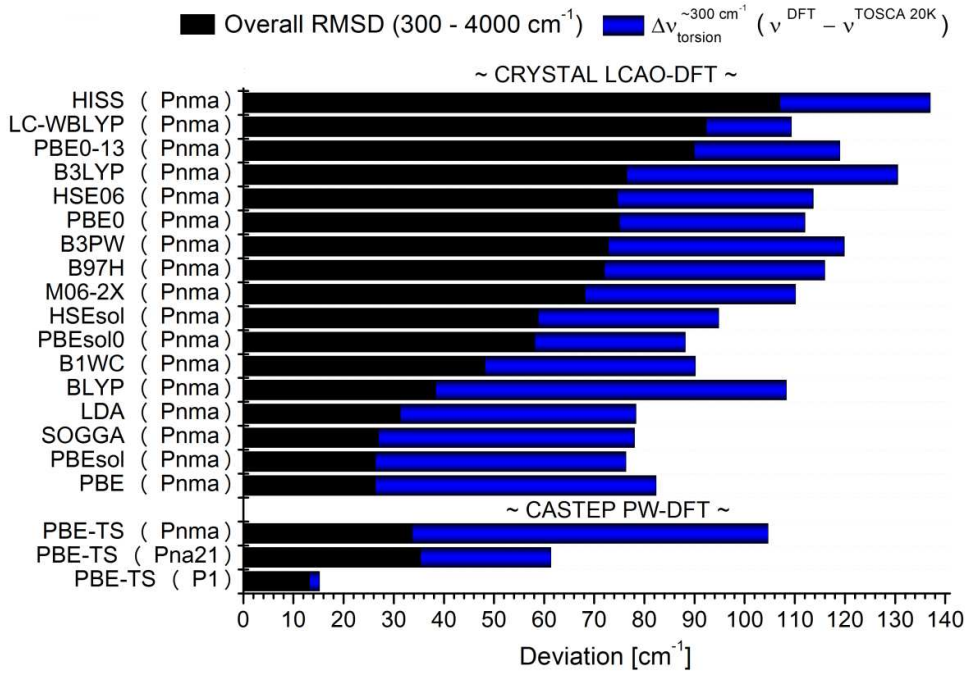

Figure S3. Performance of XC functionals (ordinate axis) in the prediction of observed INS features in the low-temperature phase of MAPI. The results are presented as deviations from experimental INS features measured at T=20K on the TOSCA spectrometer. The overall Room-Mean-Square Deviation (RMSD) for the range of 300 – 4000 cm^{-1} is compared to the deviation from the mode associated with disrotatory torsion at *ca.* 300 cm^{-1} ($\Delta\nu$). All the results obtained with CRYSTAL14 refer to *Pnma*, while CASTEP results consider three different models, as discussed in the main text.

Figure S3 compares both the overall Room-Mean-Square Deviation (RMSD, black) and the deviation of the position of the torsional mode at 300 cm^{-1} ($\Delta\nu$, blue) relative to the INS data. It is interesting to note that these two descriptors appear to be anticorrelated, *i.e.*, a reduction in $\Delta\nu$ for the torsional mode leads to an increase of the overall RMSD. From this figure, it is also clear that all functionals tested with *Pnma* are in distinct disagreement with experiment, and that the P1 model using the PBE-TS functional provides the best match to the experimental data. Given this large set of calculations, we can also provide a statistical level of confidence in favour of the *P1* model. The average and associated standard deviation (66% confidence band) of the RMSD and $\Delta\nu$ for the *Pnma* dataset amount to

61±24 and 42±12 cm^{-1}, respectively, whereas the *P1* model has an RMSD(Δν) of 14(2) cm^{-1}. Using the RMSD(Δν) as a statistical descriptor, these figures translate into an associated probability of 95%(99%) that the experimental INS data is better described by the *P1* model rather than *Pnma*. This analysis reinforces our conclusion that the currently accepted *Pnma* structure cannot be used to describe the experimental INS data in a quantitative manner using state-of-the-art DFT methodologies, and that these differences do not arise from the level of theory we have used.

3. Alternative model of the structure of the low-temperature phase

The starting point to describe the low-temperature phase of MAPI and our INS data using DFT calculations was the *Pnma* model of Baikie *et al.*[32] (see the Pnma *.cif file). As presented in the main manuscript and in Section 2 above, this model could only provide a qualitative description of the experimental INS data at either low (4K) or higher (T>100 K) temperatures within the low-temperature phase – see Figs. 4 and 7 in the main manuscript. These discrepancies prompted us to conduct a more extensive search for alternative models by varying the local geometry of the organic cation. To illustrate our search procedure, Table S1 provides a summary of DFT results using monoclinic *Pm* symmetry. This choice preserves the mirror-plane symmetry associated with planar cation alignment perpendicular to the long unit-cell axis. This mirror-plane symmetry only permits the cations to be reoriented on the *ac* crystallographic plane. To explore this possibility, the cation was reoriented at 0, 90, and 180° and these geometries were fully optimised in terms of both internal coordinates and cell constants. In some cases, this optimization procedure led to the emergence of high-symmetry structures including *Pnma*, *Pmc21*, *Pmn21*, and *P21/m*.

Table S1. Selected properties of the structural models found from a systematic search of configurations with mirror-plane symmetry. The *Pnma* structure corresponds to that reported in the literature. See the text for further details.

Symmetry	Disrotatory mode [cm^{-1}]				Cell Constants				Representative Structure
					a [Å]	*b* [Å]	*c* [Å]	*β* [°]	
Pnma	375	375	377	377	9.02	12.69	8.48	90	Pnma *.cif file
Pm	328	367	373	381	8.58	12.66	8.99	90.5	Pm *.cif file
Pm	323	366	370	372	8.47	12.69	9.03	90.1	Pm *.cif file
Pmc21	354	354	357	357	12.67	8.42	9.07	90	Pmc21 *.cif file
Pm	294	371	374	380	8.56	12.70	8.93	90.2	Pm *.cif file
Pmc21	342	343	345	346	12.68	8.51	8.97	90	Pmc21 *.cif file
Pm	330	341	343	355	8.67	12.80	8.86	90.1	Pm *.cif file
Pm	294	333	347	359	8.65	12.83	8.89	90.0	Pm *.cif file
Pmn21	291	292	335	335	12.79	8.75	8.75	90	Pm *.cif file
Pm	287	328	342	349	8.75	12.89	8.77	90.0	Pm *.cif file
Pm	292	320	325	338	8.77	12.91	8.79	90.1	Pm *.cif file
P21/m	327	328	330	331	8.65	13.01	8.93	90.0	P21/m *.cif file

In addition to the cell constants presented in Table S1, we also report the position of the disrotatory $\tau(NH_3^+)$-$\tau(CH_3)$ mode, as this feature is the one which is most closely related to the interaction of the cation with the perovskite framework via weak H···I hydrogen bonds. The four values shown in the table reflect the presence of a total of four cations per unit cell (Z=4). These data serve to illustrate that agreement with the single spectral feature at *ca.* 300 cm^{-1} observed in the INS experiments may only be attained if these modes are all nearly degenerate. On the basis of these considerations, Table S1 tells us that only two structures with *Pm* symmetry need to be considered further, namely, *Pnma* and *Pmc21* (see the Pmc21 *.cif file). It is interesting to note that *Pmc21* symmetry had been used earlier to describe the low-temperature phase of MAPI, as presented in more detail by Baikie *et al.*[32] Our DFT calculations show that *Pmc21* is 5.68 kJ/mol higher in energy than *Pnma*, yet at the same time the position of the torsional mode at *ca.* 345 cm^{-1} is sensibly closer to experiment than *Pnma* (~375 cm^{-1}). A further decrease in the position of the disrotatory mode is required in order to obtain quantitative agreement with the prominent and isolated INS feature at 300 cm^{-1}. Such a decrease implies breaking mirror-plane *Pm* symmetry, whereby the cation is no longer forced to be horizontally aligned on the *ac* plane. As presented in the main text, an alternative (vertical) alignment of the MA cations provides an improved agreement (*i.e.*, $Pna2_1$ - see the $Pna2_1$ *.cif

file). The best match to the experimental data was achieved using a model with mixed (horizontal and vertical) orientation of the cations in the lattice. We have eventually selected a model of *P*1 symmetry, where the conventional unit cell used in all subsequent simulations consists of four molecular units, Z = 4 (see *P*1 Z=4 *.cif file). This model was used all throughout the main text. To complement Fig. 6 in the main text, Fig. S4 provides an assessment of the performance of the *P1* model to describe both INS and optical-spectroscopic data over the entire spectral range associated with nuclear motions in the low-temperature phase of MAPI. The level of agreement shown is excellent and unprecedented, further illustrating that the *P1* model provides a good description of the local environment around the organic cation.

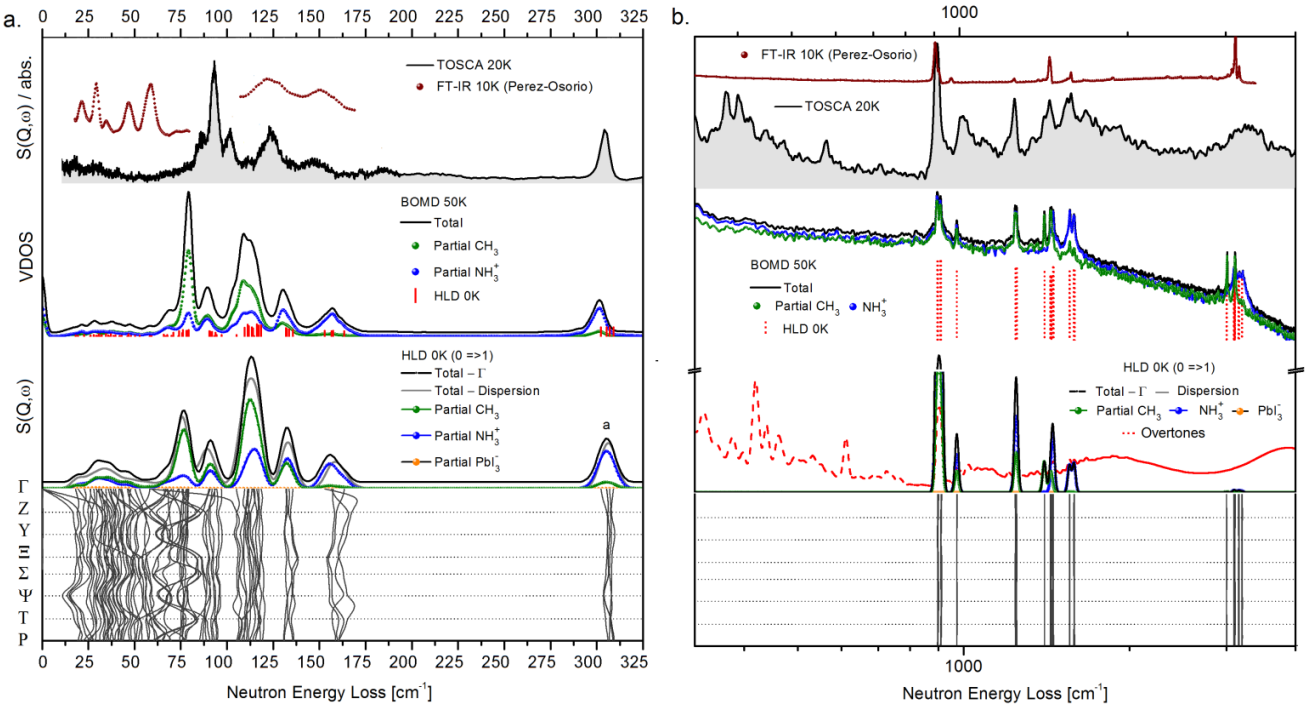

Figure S4. Spectroscopic data and detailed analysis using the *P*1 model. (a) and (b) show low and high energy-transfer regions, respectively. Top: available experimental data at low energies including INS data (this work), as well as FT-IR data from Ref. 33. For clarity, different optical datasets have been offset along the ordinate axis by arbitrary constants. Middle: partial and total VDOSs from BOMD calculations. Bottom: partial and total VDOSs using HLD with and without dispersion. All the partial contributions to the VDOSs have been weighted by their respective neutron cross-sections.

The *P1* model is further compared to *Pnma* in Table S2. Assuming that the *P1* unit cell can be used to describe long-range order, it is found to be higher in energy by 5.81 kJ/mol relative to *Pnma* and, therefore, isoenergetic with the *Pmc21* discussed earlier in the context of our search procedure and lower in energy than *Pna21*. We also note that the cell-optimised *P1* model exhibits slight deviations from a perfect orthorhombic structure. Based on previous studies,[34] we have used Scalar Relativistic (SR) calculations including Spin-Orbit Coupling (SOC) to calculate electronic band gaps. Using SR-SOC and PBE-TS, *P1* is characterized by an electronic band gap ~0.1 eV below *Pnma*. These calculations are in qualitative agreement with the results of Amat *et al.*,[34] where similar differences were found to be the result of a different SOC response and underlying equilibrium volumes. This agreement is further corroborated by an even lower band gap found for *Pna21*. The aforementioned difference is also of the same order as the one presented for formamidinium and methylammonium cations in lead-iodide perovskites.[34]

Table S2. Comparison of *Pnma*, *Pna21*, and *P1* model in terms of cell parameters, total electronic energy difference, and electronic band gap.

Model	*Pnma*	*Pna21*	*P1*
Volume	971.08 Å^3	1000.18 Å^3	990.91 Å^3
a	9.02 Å	8.88 Å	9.17 Å
b	12.69 Å	8.99 Å	12.42 Å
c	8.48 Å	12.53 Å	8.72 Å
α	90.0°	90.0°	86.1°
β	90.0°	90.0°	88.0°
γ	90.0°	90.0°	89.9°
Total Energy	0.00 kJ/mol	7.97 kJ/mol	5.81 kJ/mol
Band Gap (SR-SOC-PBE-TS)	0.96 eV	0.74 eV	0.89 eV

We also note here that this *P*1 model is very close to *Cc* symmetry (see Fig. 5 in the main text and file *Cc* Z=4 *.cif). The conventional unit cells of both *P*1 and *Cc* structures with Z = 4 can be transformed into primitive cells, see *P*1 Z=2 *.cif file and *Cc* Z=2 *.cif file. Projections of both conventional and primitive cells of *P*1 and *Cc* symmetry are shown in Fig. S5. Figure S6 shows the corresponding INS spectra for conventional and primitive models. The calculated INS spectra presented in Fig. S6 are undistinguishable from each other, which further confirms the aforementioned conclusion that the INS response probes the potential-energy landscape in the immediate vicinity of the organic cation.

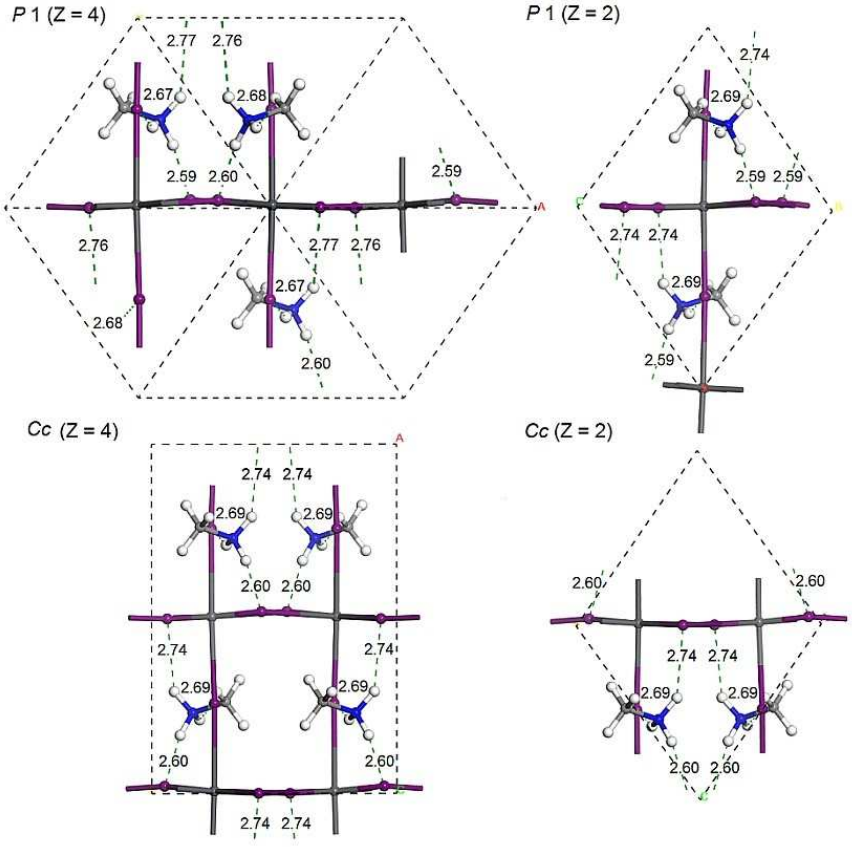

Figure S5. Alternative model of the low-temperature phase of MAPI using conventional (Z = 4) and primitive (Z = 2) cell projections. The *P*1 primitive cell was obtained after a slight symmetrization of the conventional cell (within a tolerance of 0.0015 Å). The *Cc* structure was derived from the original *P*1 cell by symmetrization within a tolerance of 0.045 Å.

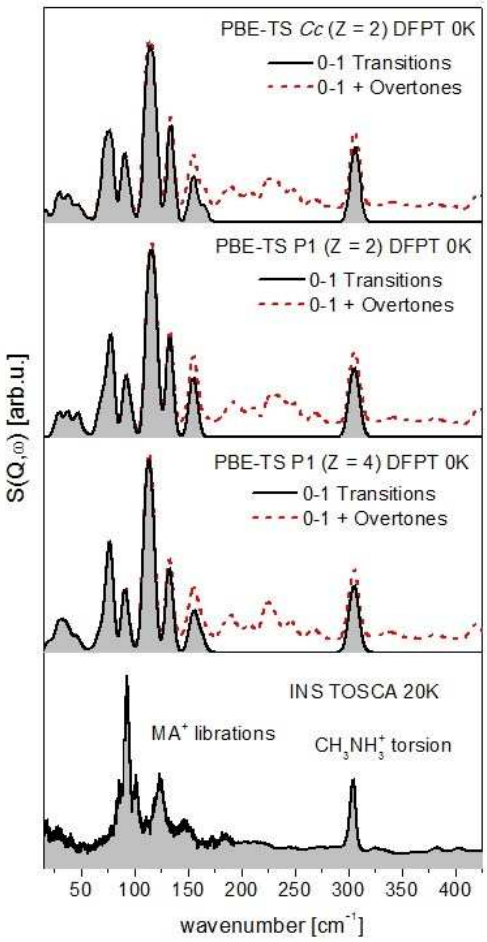

Figure S6. INS spectra of the low-temperature phase of MAPI for the equivalent structural representations presented in Fig. S5 (*P*1 Z = 4; P1 Z = 2; Cc Z = 2). The theoretical results are derived from DFPT HLD (PBE-TS) with a fully a relaxed cell.

With the results obtained so far, the initial comparison between XRD and INS data for *Pnma* presented in Section 1 above can also be extended to explore the information content of these observables for the *Pna21* and *P1* models. These data are presented in Fig. S7, where we note that *Pna21* XRD patterns are very similar to the ones reported for the *I4/mcm* phase (see, *e.g.,* Baikie et al.[32]), while *P1* and *Pnma* (see Fig. S1) are quite similar to each other. At low scattering angles, both *P1* and *Pnma* exhibit a characteristic doublet below 15°, which is not present in *Pna21.* Both *P1* and *Pnma* also show intense Bragg features around 28°. For the weaker Bragg features, there are some differences, particularly the doublet found around 26° in *Pnma*, which is shifted to higher angles at ~30° in *P1*. As deduced from Figs. 1 and 3 in the main manuscript, the resulting *P1* model also differs from both tetragonal and orthorhombic structures. In the tetragonal phase, the octahedra are not tilted in the *ab* plane (*I4/mcm* phase convention - see Fig. 1 in the main text), although it is also to be noted that this is an average picture derived from datasets exhibiting large mean-square displacements of the heavy atoms. These large displacement amplitudes confirm the coupling of cation motions to octahedral orientation. On the contrary, the *Pnma* model assumes a strong octahedral tilt (rotation on the *ac* plane in *Pnma*). In that sense, the *P*1 model resembles the tetragonal structure, where the octahedral tilt is preserved. On the other hand, it also resembles the *Pnma* phase, with a preferable (but slightly different) octahedral tilt with respect to the long unit-cell axis (see Fig. 3 in the main manuscript). Such a conclusion is in support of the possibility of phase metastability or, alternatively, its possible intermediate character between *I4/mcm* and *Pnma,* where the latter assignment, however, cannot be supported using group-theoretical arguments – *i.e.,* in physical terms, the absence of a space-group relation between *I4/mcm* and *Pnma* implies that it is not possible to effect a continuous change of the structure to transform one phase into the other.

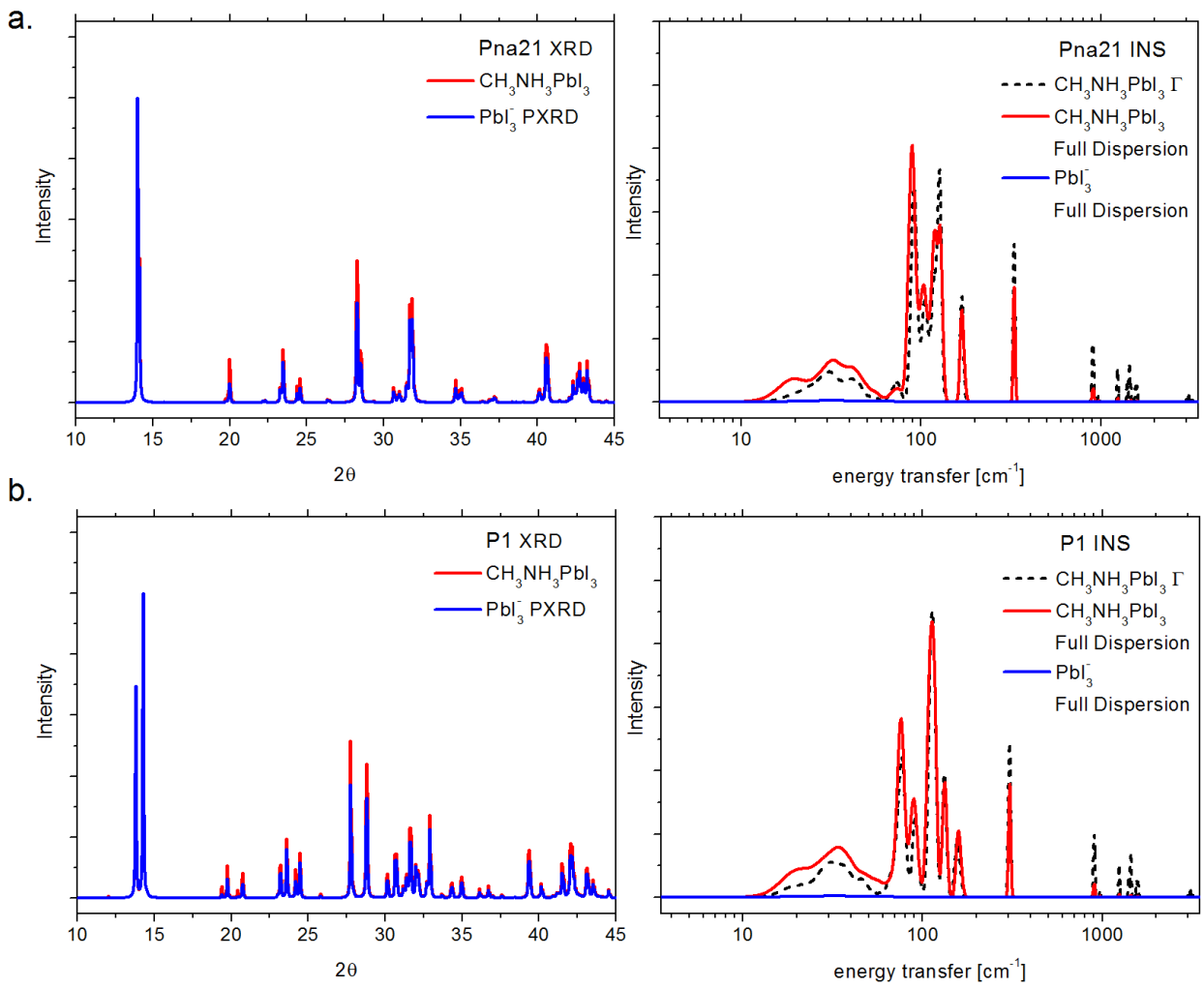

Figure S7. Simulated XRD patterns (left) and INS spectra (right) of *Pna21* (a) and *P1* model (b), calculated using PW-DFT (PBE-TS) at T = 0 K. Red(blue) traces in both cases correspond to the presence(absence) of the organic cation in the material. As in Fig. S1, INS spectra have been calculated at the Γ-point (black) and with full dispersion (red and blue) in order to illustrate the local character of the technique.

The differences observed in the simulated XRD patterns for *Pnma* and the *P1* model need further qualification, as the latter model can only be treated as a first-order approximation to the description of intermediate- and long-range order in MAPI, thus calling for further refinement using other experimental and computational methods sensitive to correlated disorder at the mesoscale.[35] In this context, we recall that the *P1* model and its associated unit cell have been obtained via direct comparison of PW-DFT predictions against INS data, and that the latter is primarily sensitive to the local environment around the organic cation – *cf.* Figs. S1 and S7 above. Taking the smallest unit cell consistent with the *P1* model as our minimal 'building block' for solid MAPI, these may be combined in a multitude of different ways in order to build the material, all of which are still consistent with the INS data. This situation is schematically illustrated in Fig. S8. This figure makes it clear that the number of possibilities increases drastically with supercell size, including the yet-to-be-explored possibility of coexistence of several superstructures.

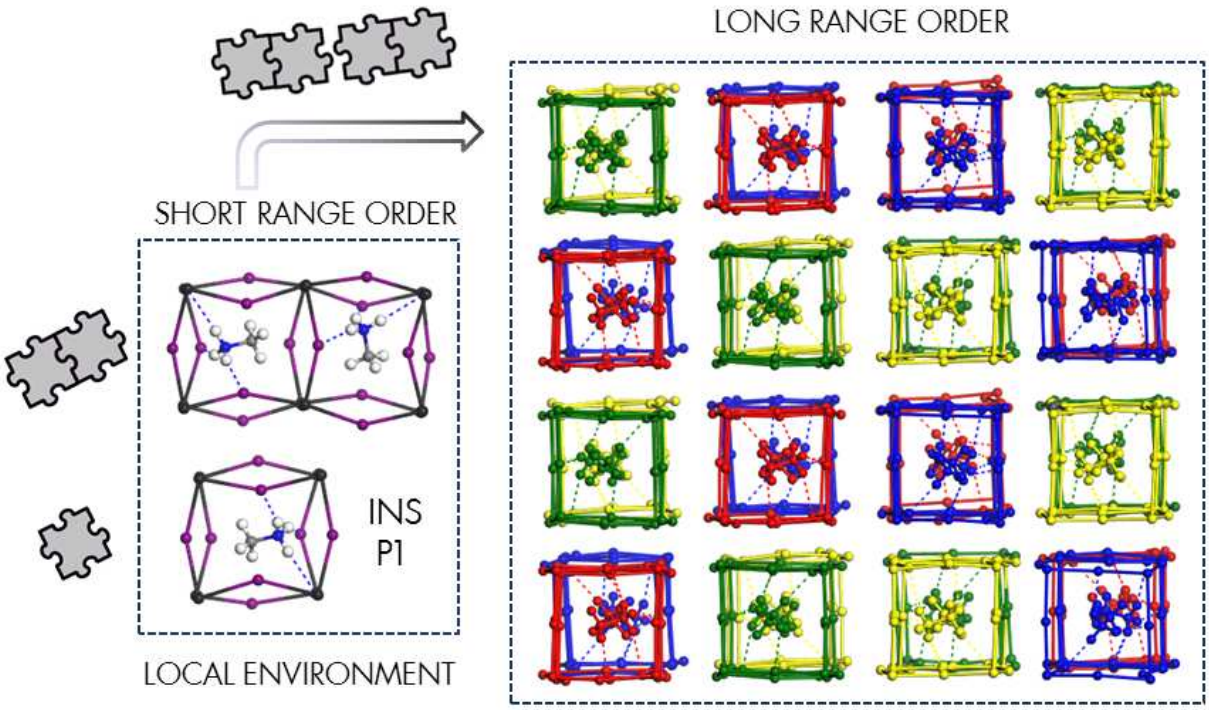

Figure S8. Schematic illustration of long-range order in MAPI taking as starting point the building blocks inferred from INS (see the left panel). These building blocks can be arranged in a number of different possible configurations, all preserving the internal structure of the elementary unit shown on the left-hand side of the figure. A representative arrangement involving Z = 64 is shown in the right panel, where each color represents a different spatial orientation of the two elementary building blocks (Z = 2 in the left-top panel).

The corresponding simulated XRD patterns for Z = 4 and Z = 64 are shown in Fig. S9. Although we note similarities at the lowest scattering angles, these data also show significant qualitative differences between the two *P1* models above 20°, further corroborating the fundamental distinction between XRD and INS observables. From this analysis, we can also conclude that Z = 4 is probably not a sufficiently large unit cell to describe intermediate and long-range order quantitatively. The size of the smallest building block in MAPI, as well as which Bragg features in the XRD data are resilient to static and thermal disorder remain important and pending questions in the field. Other possibilities to account for complex, long-range order include the presence of domains and spatial inhomogeneities, or possible octahedral distorsions promoted by long-range ordering, defects, or grain boundaries. These effects are already known to affect both the structural and photophysical properties of MAPI,[36,37] yet a direct link to bulk properties remains to be established.

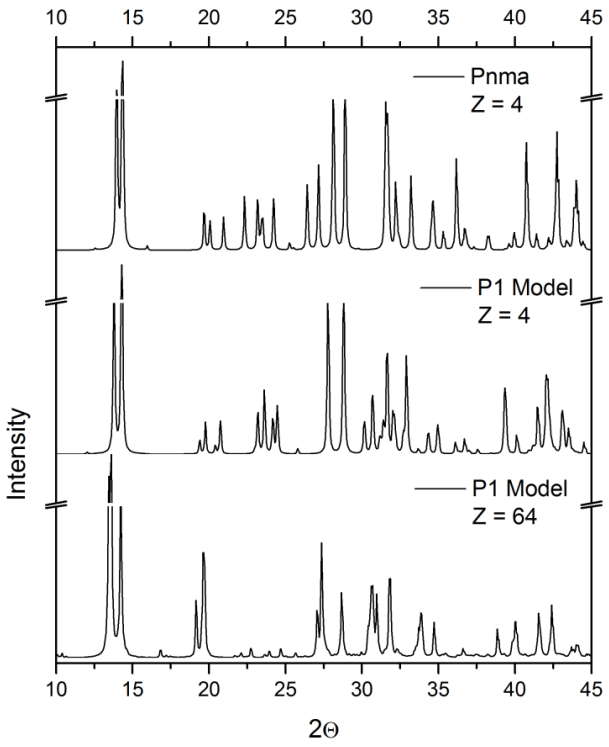

Figure S9. Comparison of simulated XRD patterns of MAPI. From top to bottom: *Pnma* (Z=4); *P1* (Z=4); and *P1* (Z=64). The last model corresponds to the supercell shown on the right-hand side of Fig. S8 (Z=64).

4. Thermodynamics

Thermodynamic properties were obtained from DFPT HLD calculations across the Brillouin zone for each model presented in the main text. All calculations used PBE-TS and fully relaxed unit cells. These results are shown in Figs. S10-S12.

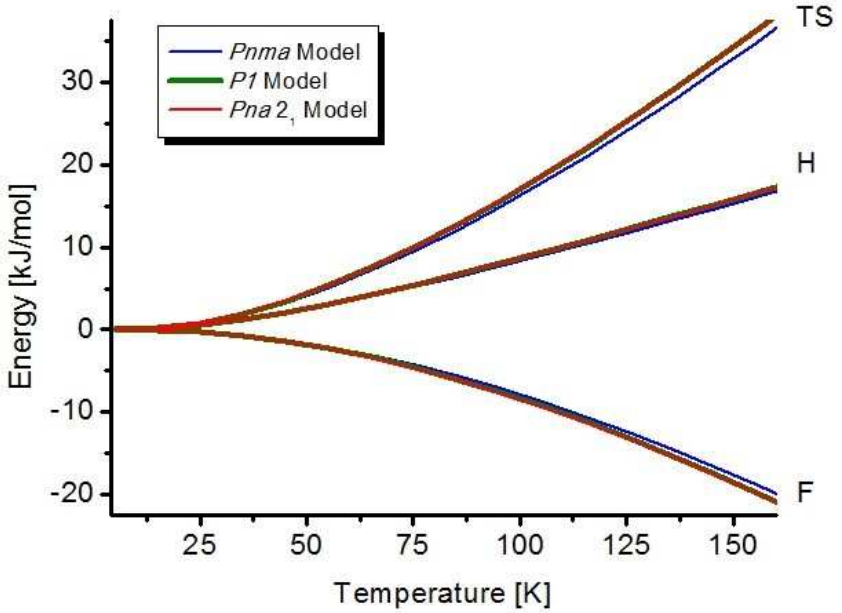

Figure S10. Temperature dependence of the enthalpy (H), entropic term (TS), and free energy (F) for the three models of the low-temperature phase of MAPI discussed in the main text. Full phonon dispersion has been used to obtain these results.

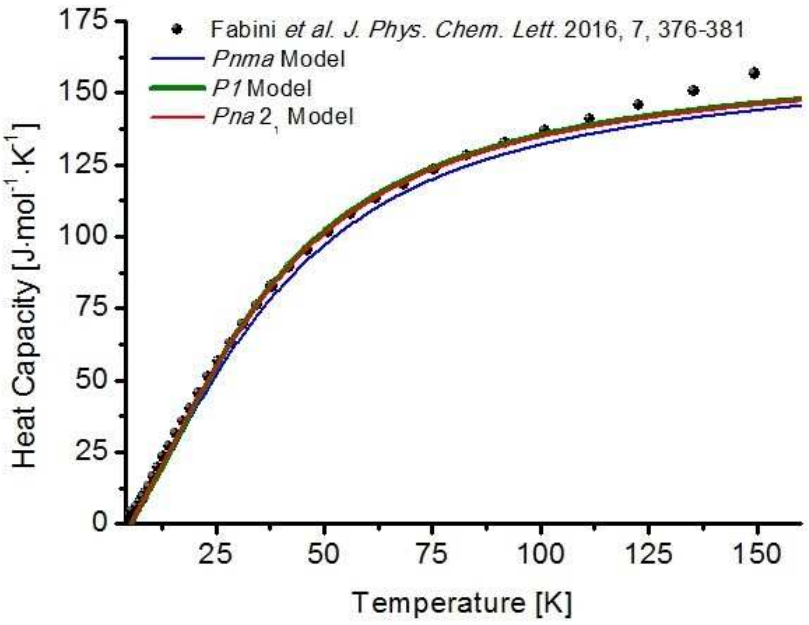

Figure S11. Temperature dependence of the molar heat capacity for the three models of the low-temperature phase of MAPI discussed in the main text. The scatter plot comes from the experimental data of Fabini *et al.*[38] Full phonon dispersion has been used to obtain these results.

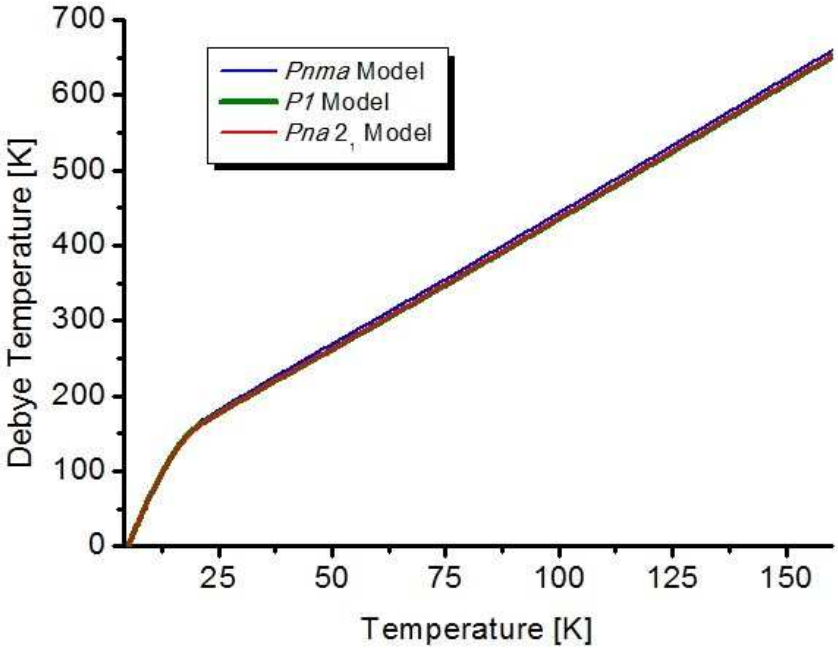

Figure S12. Debye temperature of the low-temperature phase of MAPI for the three models discussed in the main text. Full phonon dispersion has been used to obtain these results.

By inspection of Fig. S12, one can note that the Debye temperature increases monotonically above 25 K. Above this temperature, the BOMD approach has been used to investigate anharmonic effects and thermally induced tumbling motions, as discussed in more detail in the main text.

5. Insights from *ab initio* molecular dynamics

This section provides additional BOMD results using the *P*1 model (Z = 4) and over a wider temperature range than presented in the main text.

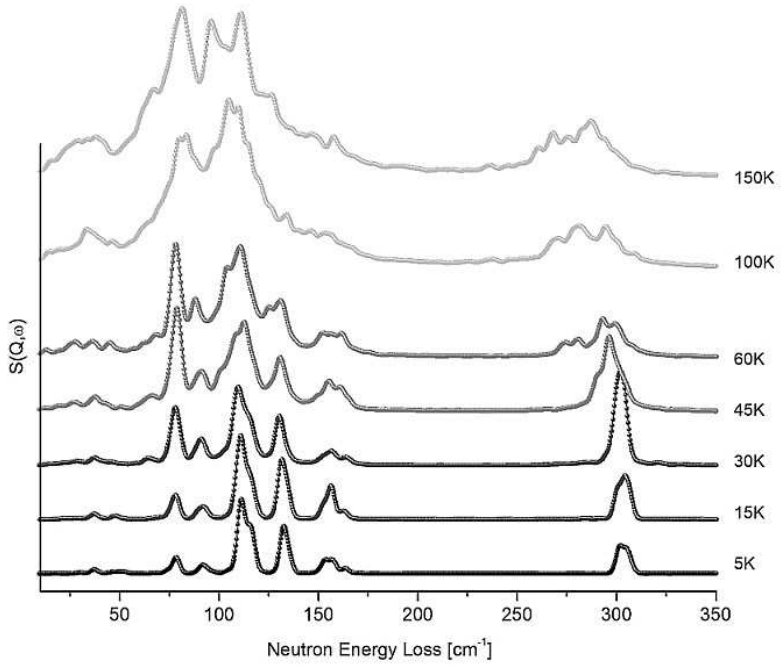

Figure S13. Temperature dependence of the INS spectrum in the low-temperature phase of MAPI using BOMD (PBE-TS) and the *P*1 model. Each spectrum was calculated from 50-ps NVE trajectories after imposing a first-order quantum-harmonic correction.

The BOMD simulations leading to the spectra shown in Fig. S13 show that both the *librational* $\circlearrowleft$(N-CH_3) mode at *ca.* 75 cm^{-1} and the *disrotatory* τ(NH_3^+)-τ(CH_3) mode at ca. 300 cm^{-1} exhibit a distinct temperature dependence. The former mode promotes and accompanies wobbling-in-a-cone motions. By comparison with experiment, the classically thermostated spectrum at 45 K resembles the low-temperature INS data. This result indicates that that zero-point-energy effects for MA^+ can be mimicked at this temperature using a classical description of nuclear motions. It also suggests that the cation remains floppy even down to very low temperatures, since the HLD calculations in Fig. S4 predict a much-lower intensity of the feature at 75 cm^{-1}. There is also a clear onset of molecular reorientations starting at 60 K, and linked to the emergence of a feature at ca. 275 cm^{-1} which evolves into a continuous broad band at higher temperatures, in line with our experimental observations. Figure 7 in the main text shows that only the *P1* model is able to provide a quantitative description of the INS experiments. Given this agreement, it is worthwhile examining the underlying BOMD trajectories in more detail, as well as to compare these with the crystallographic structure obtained at 100 K by Baikie *et al.*[32] To this end, cumulative trajectories are shown in Figs S14 – S17 for 100 and 150K. The crystallographic data provided by Baikie *et al.*[32] are also shown using a yellow CPK model. The first thing to note is the massive spatial delocalization of MA^+ at these temperatures. Due to the aforementioned coupling of MA^+ orientation and the surrounding lead-iodide cage, the heavy atoms are clearly affected by cation motions. These cumulative structures confirm that jump-like reorientations of MA^+ are forbidden, but wobbling motions are highly probable. Moreover, the iodine atoms respond in quite a sensitive manner to the proximity and relative orientation of MA^+. These findings provide an explanation for the unusual behavior seen by Baikie *et al.*[32] in their Fourier maps and interpreted as anharmonic displacements of the iodine atoms. One should also note that the *P1* model is able to capture the almost-isotropic nature of MA^+ motions at these temperatures, as shown in these figures. Likewise, the large displacements of iodine atoms at 100 K clearly resemble those observed in the tetragonal phase.

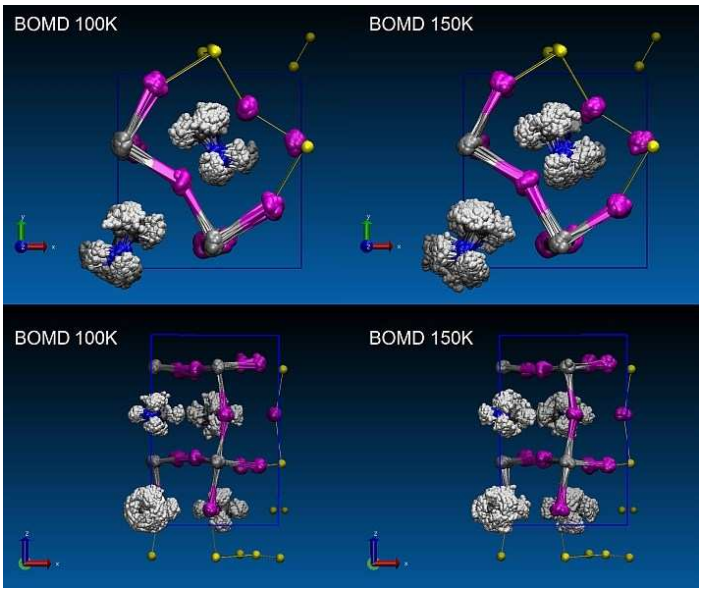

Figure S14. Cumulative coordinates from *ab initio* MD (PBE-TS) simulations using the *Pnma* model at T = 100 and 150K. Both cell constants and the yellow CPK model were taken from single-crystal X-ray diffraction data at T = 100 K (*Pnma* structure after Baikie *et al.*[32]).

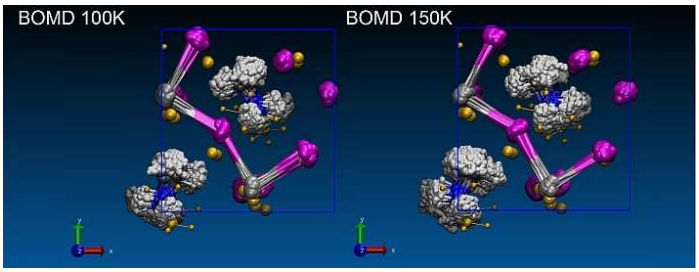

Figure S15. Cumulative coordinates from *ab initio* MD (PBE-TS) simulations using the *Pnma* model at T = 100 and 150K. In this case, cell constants were fully relaxed using PBE-TS. The yellow CPK model comes from full-cell relaxation at 0 K using PBE-TS and the *P*1 model.

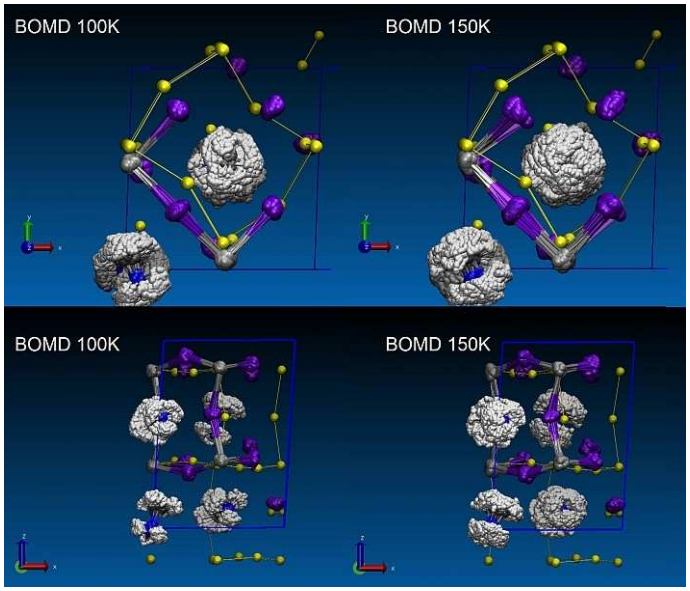

Figure S16. Cumulative coordinates from *ab initio* MD (PBE-TS) simulations using the *P*1 model at T = 100 and 150K. The yellow CPK model comes from single-crystal X-ray diffraction data at T = 100 K (*Pnma* structure after Baikie *et al.*[32]).

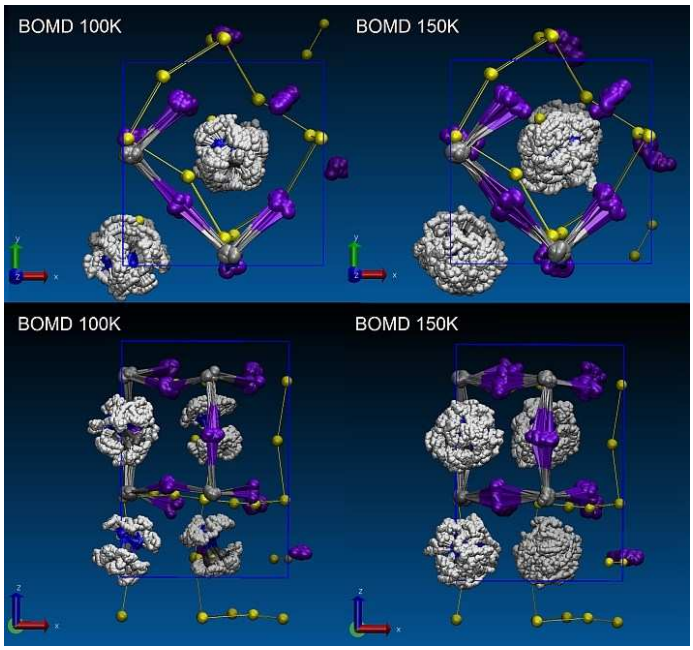

Figure S17. Cumulative coordinates from *ab initio* MD (PBE-TS) simulations using the $Pna2_1$ model at T = 100 and 150K. The yellow CPK model comes from single-crystal X-ray diffraction data at T = 100 K (*Pnma* structure after Baikie *et al.*[32]).

6. Normal-mode animations

The results of the HLD calculations using PBE-TS are analyzed in detail below. For ease of visualization, all vibrational-mode animations are presented using unit-cell projections, as illustrated in Fig. S18. Web links to interactive animations as well as approximate mode assignments can be found in Table S3.

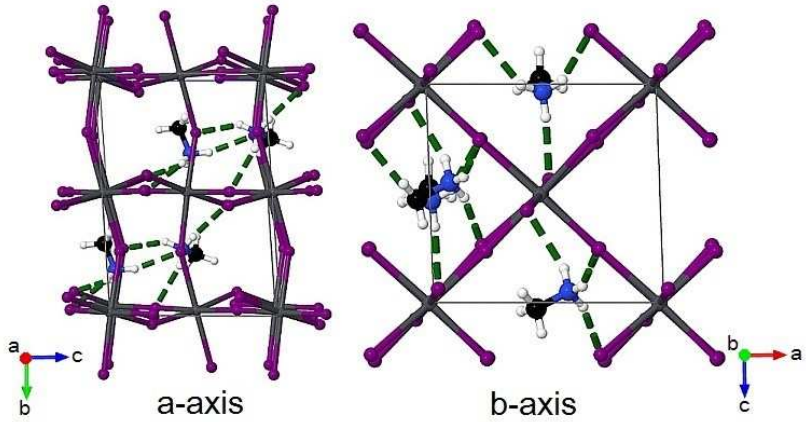

Figure S18. Projections of the *P*1 model of the low-temperature phase of MAPI. HBs are shown in green. The equilibrium structure shown has been obtained from PBE-TS calculations of the fully optimized unit-cell coordinates at atmospheric pressure.

Table S3. Γ-point vibrational energies in the low-temperature phase of MAPI, obtained from PBE-TS calculations using the P_1 model. Mode animations are given along two alternative unit-cell projections as illustrated in Fig. S18. The rightmost column provides an approximate description of each mode. For further details, see Table 1 and related discussion in the main paper.

No.	ν [cm^{-1}]	Animation		Description
1	0.00	a-axis	b-axis	*acoustic* → b
2	0.00	a-axis	b-axis	*acoustic* → a
3	0.00	a-axis	b-axis	*acoustic* → c
4	18.09	a-axis	b-axis	↺ (PbI_6) / *transl.* ⇒ Pb
5	19.42	a-axis	b-axis	ρ(I-Pb-I)
6	22.72	a-axis	b-axis	↺ (PbI_6) / *transl.* ⇒ Pb
7	26.08	a-axis	b-axis	ρ(I-Pb-I) / *transl.* ⇒ Pb
8	26.31	a-axis	b-axis	ρ(I-Pb-I) / *transl.* ⇒ Pb
9	27.93	a-axis	b-axis	ρ(I-Pb-I) / *transl.* ⇒ Pb
10	29.08	a-axis	b-axis	ρ(I-Pb-I) / *transl.* ⇒ Pb
11	29.50	a-axis	b-axis	ρ(I-Pb-I) / *transl.* ⇒ Pb
12	30.54	a-axis	b-axis	ρ(I-Pb-I) / *transl.* ⇒ Pb
13	30.71	a-axis	b-axis	ρ(I-Pb-I)
14	31.52	a-axis	b-axis	ρ(I-Pb-I)
15	32.20	a-axis	b-axis	ρ(I-Pb-I)
16	34.40	a-axis	b-axis	ρ(I-Pb-I)
17	35.77	a-axis	b-axis	ρ(I-Pb-I)
18	36.70	a-axis	b-axis	ρ(I-Pb-I)
19	37.26	a-axis	b-axis	ρ(I-Pb-I)
20	38.57	a-axis	b-axis	ρ(I-Pb-I)
21	39.66	a-axis	b-axis	ρ(I-Pb-I)
22	41.64	a-axis	b-axis	ρ(I-Pb-I)
23	42.24	a-axis	b-axis	ρ(I-Pb-I)
24	42.93	a-axis	b-axis	ρ(I-Pb-I)
25	46.17	a-axis	b-axis	ρ(I-Pb-I)
26	46.65	a-axis	b-axis	ρ(I-Pb-I)
27	47.92	a-axis	b-axis	ρ(I-Pb-I)
28	50.18	a-axis	b-axis	δ(I-Pb-I) $T_{1U}(O_h)$
29	52.70	a-axis	b-axis	δ(I-Pb-I) $T_{1U}(O_h)$
30	58.15	a-axis	b-axis	δ(I-Pb-I) $T_{1U}(O_h)$
31	58.28	a-axis	b-axis	δ(I-Pb-I) $T_{1U}(O_h)$
32	59.22	a-axis	b-axis	δ(I-Pb-I) $T_{1U}(O_h)$
33	65.82	a-axis	b-axis	lib. ↺ (N-CH_3) + ν(Pb-I)
34	66.73	a-axis	b-axis	lib. ↺ (N-CH_3) + ν(Pb-I)
35	67.55	a-axis	b-axis	lib. ↺ (N-CH_3) + ν(Pb-I)
36	67.81	a-axis	b-axis	lib. ↺ (N-CH_3) + ν(Pb-I)
37	70.03	a-axis	b-axis	lib. ↺ (N-CH_3) + ν(Pb-I)
38	71.00	a-axis	b-axis	lib. ↺ (N-CH_3) + ν(Pb-I)
39	73.62	a-axis	b-axis	lib. ↺ (N-CH_3) + ν(Pb-I)
40	74.04	a-axis	b-axis	lib. ↺ (N-CH_3) + ν(Pb-I)
41	75.64	a-axis	b-axis	lib. ↺ (N-CH_3) + ν(Pb-I)
42	76.25	a-axis	b-axis	lib. ↺ (N-CH_3) + ν(Pb-I)
43	77.93	a-axis	b-axis	lib. ↺ (N-CH_3) + ν(Pb-I)
44	78.50	a-axis	b-axis	lib. ↺ (N-CH_3) + ν(Pb-I)
45	79.12	a-axis	b-axis	lib. ↺ (N-CH_3) + ν(Pb-I)
46	79.28	a-axis	b-axis	lib. ↺ (N-CH_3) + ν(Pb-I)
47	90.32	a-axis	b-axis	lib. ↺ (N-CH_3) + ν(Pb-I)
48	90.92	a-axis	b-axis	lib. ↺ (N-CH_3) + ν(Pb-I)
49	91.90	a-axis	b-axis	lib. ↺ (N-CH_3) + ν(Pb-I)
50	93.17	a-axis	b-axis	lib. ↺ (N-CH_3) + ν(Pb-I)
51	93.68	a-axis	b-axis	ν(PbI_6) $E_g(O_h)$

52	94.44	a-axis	b-axis	lib. ↺ (N-CH_3) + ν(Pb-I) $E_g(O_h)$
53	96.97	a-axis	b-axis	lib. ↺ (N-CH_3) + ν(Pb-I) $E_g(O_h)$
54	105.08	a-axis	b-axis	lib. ↺ (N-CH_3) + ν(Pb-I)
55	109.48	a-axis	b-axis	lib. ↺ (N-CH_3) / τ(CH_3) + ν(Pb-I) $E_g(O_h)$
56	111.11	a-axis	b-axis	lib. ↺ (N-CH_3) / τ(CH_3) + ν(Pb-I) $E_g(O_h)$
57	111.65	a-axis	b-axis	lib. ↺ (N-CH_3) / τ(CH_3) + ν(Pb-I) $E_g(O_h)$
58	111.85	a-axis	b-axis	lib. ↺ (N-CH_3) / τ(CH_3) + ν(Pb-I)
59	113.49	a-axis	b-axis	lib. ↺ (N-CH_3) / τ(CH_3) + ν(Pb-I)
60	114.15	a-axis	b-axis	ν(NH···I) / *conrotatory* τ(NH_3^+) / τ(CH_3) + ν(Pb-I)
61	114.76	a-axis	b-axis	$\nu_{sym}(PbI_6)$ $A_{1g}(O_h)$ / ν(NH···I)
62	116.02	a-axis	b-axis	ν(NH···I) / *conrotatory* τ(NH_3^+) / τ(CH_3)
63	117.22	a-axis	b-axis	ν(NH···I) / *conrotatory* τ(NH_3^+) / τ(CH_3)
64	118.43	a-axis	b-axis	ν(NH···I) / *conrotatory* τ(NH_3^+) / τ(CH_3)
65	131.96	a-axis	b-axis	lib. ↺ (C-NH_3^+) / ν(NH···I) + τ(CH_3)
66	132.36	a-axis	b-axis	lib. ↺ (C-NH_3^+) / ν(NH···I) + τ(CH_3)
67	133.61	a-axis	b-axis	lib. ↺ (C-NH_3^+) / ν(NH···I) + τ(CH_3)
68	135.60	a-axis	b-axis	lib. ↺ (C-NH_3^+) / ν(NH···I) + τ(CH_3)
69	152.85	a-axis	b-axis	lib. ↺ (C-NH_3^+) / ν(NH···I)
70	156.51	a-axis	b-axis	lib. ↺ (C-NH_3^+) / ν(NH···I)
71	157.44	a-axis	b-axis	lib. ↺ (C-NH_3^+) / ν(NH···I)
72	163.45	a-axis	b-axis	lib. ↺ (C-NH_3^+) / ν(NH···I)
73	302.30	a-axis	b-axis	*disrotatory* τ(NH_3^+) / τ(CH_3)
74	305.38	a-axis	b-axis	*disrotatory* τ(NH_3^+) / τ(CH_3)
75	306.93	a-axis	b-axis	*disrotatory* τ(NH_3^+) / τ(CH_3)
76	308.94	a-axis	b-axis	*disrotatory* τ(NH_3^+) / τ(CH_3)
77	895.30	a-axis	b-axis	ρ(NH_3^+) + ρ(CH_3)
78	896.39	a-axis	b-axis	ρ(NH_3^+) + ρ(CH_3)
79	897.83	a-axis	b-axis	ρ(NH_3^+) + ρ(CH_3)
80	898.52	a-axis	b-axis	ρ(NH_3^+) + ρ(CH_3)
81	907.86	a-axis	b-axis	ρ(NH_3^+) + ρ(CH_3)
82	908.53	a-axis	b-axis	ρ(NH_3^+) + ρ(CH_3)
83	909.19	a-axis	b-axis	ρ(NH_3^+) + ρ(CH_3)
84	910.66	a-axis	b-axis	ρ(NH_3^+) + ρ(CH_3)
85	972.08	a-axis	b-axis	ν(CN)
86	972.42	a-axis	b-axis	ν(CN)
87	972.61	a-axis	b-axis	ν(CN)
88	972.77	a-axis	b-axis	ν(CN)
89	1241.45	a-axis	b-axis	ρ(NH_3^+) + ρ(CH_3)
90	1241.96	a-axis	b-axis	ρ(NH_3^+) + ρ(CH_3)
91	1242.57	a-axis	b-axis	ρ(NH_3^+) + ρ(CH_3)
92	1243.17	a-axis	b-axis	ρ(NH_3^+) + ρ(CH_3)
93	1248.41	a-axis	b-axis	ρ(NH_3^+) + ρ(CH_3)
94	1248.92	a-axis	b-axis	ρ(NH_3^+) + ρ(CH_3)
95	1249.27	a-axis	b-axis	ρ(NH_3^+) + ρ(CH_3)
96	1249.30	a-axis	b-axis	ρ(NH_3^+) + ρ(CH_3)
97	1401.55	a-axis	b-axis	$\delta_{sym}(CH_3)$
98	1401.91	a-axis	b-axis	$\delta_{sym}(CH_3)$
99	1402.09	a-axis	b-axis	$\delta_{sym}(CH_3)$
100	1402.47	a-axis	b-axis	$\delta_{sym}(CH_3)$
101	1435.68	a-axis	b-axis	δ(CH_3)
102	1436.13	a-axis	b-axis	δ(CH_3)
103	1436.73	a-axis	b-axis	δ(CH_3)
104	1436.92	a-axis	b-axis	δ(CH_3)
105	1442.47	a-axis	b-axis	δ(CH_3)
106	1443.65	a-axis	b-axis	δ(CH_3)
107	1444.13	a-axis	b-axis	δ(CH_3)

108	1444.34	a-axis	b-axis	$\delta(CH_3)$
109	1451.57	a-axis	b-axis	$\delta(NH_3^+)$
110	1452.52	a-axis	b-axis	$\delta(NH_3^+)$
111	1454.19	a-axis	b-axis	$\delta(NH_3^+)$
112	1456.49	a-axis	b-axis	$\delta(NH_3^+)$
113	1555.80	a-axis	b-axis	$\delta(NH_3^+)$
114	1556.20	a-axis	b-axis	$\delta(NH_3^+)$
115	1557.58	a-axis	b-axis	$\delta(NH_3^+)$
116	1559.33	a-axis	b-axis	$\delta(NH_3^+)$
117	1583.07	a-axis	b-axis	$\delta(NH_3^+)$
118	1585.45	a-axis	b-axis	$\delta(NH_3^+)$
119	1587.86	a-axis	b-axis	$\delta(NH_3^+)$
120	1590.82	a-axis	b-axis	$\delta(NH_3^+)$
121	3001.47	a-axis	b-axis	ν(CH)
122	3001.56	a-axis	b-axis	ν(CH)
123	3001.68	a-axis	b-axis	ν(CH)
124	3001.70	a-axis	b-axis	ν(CH)
125	3091.74	a-axis	b-axis	ν(CH) + ν(NH)
126	3092.91	a-axis	b-axis	ν(CH) + ν(NH)
127	3098.29	a-axis	b-axis	ν(CH) + ν(NH)
128	3098.38	a-axis	b-axis	ν(CH) + ν(NH)
129	3102.31	a-axis	b-axis	ν(CH) + ν(NH)
130	3102.37	a-axis	b-axis	ν(CH) + ν(NH)
131	3102.42	a-axis	b-axis	ν(CH) + ν(NH)
132	3102.65	a-axis	b-axis	ν(CH) + ν(NH)
133	3106.68	a-axis	b-axis	ν(CH) + ν(NH)
134	3107.42	a-axis	b-axis	ν(NH) + ν(CH)
135	3107.78	a-axis	b-axis	ν(NH) + ν(CH)
136	3107.79	a-axis	b-axis	ν(NH) + ν(CH)
137	3152.55	a-axis	b-axis	ν(NH)
138	3155.05	a-axis	b-axis	ν(NH)
139	3157.94	a-axis	b-axis	ν(NH)
140	3160.97	a-axis	b-axis	ν(NH)
141	3194.98	a-axis	b-axis	ν(NH)
142	3195.61	a-axis	b-axis	ν(NH)
143	3203.40	a-axis	b-axis	ν(NH)
144	3203.62	a-axis	b-axis	ν(NH)

References

(1) Perdew, J.P.; Burke, K.; Ernzerhof, M. Generalized Gradient Approximation Made Simple. *Phys. Rev. Lett.*, **1996**, *77*, 3865:4.
(2) Tkatchenko, A.; Scheffler, M. Accurate Molecular Van Der Waals Interactions from Ground-State Electron Density and Free-Atom Reference Data. *Phys. Rev. Lett.*, **2009**, *102*, 073005:4.
(3) Gutmann, M. J.; Graziano, G.; Mukhopadhyay, S.; Refson, K.; von Zimmerman, M. Computation of Diffuse Scattering Arising from One-phonon Excitations in a Neutron Time-of-flight Single-crystal Laue Diffraction Experiment. *J. Appl. Cryst.*, **2015**, *48*, 1122–1129.
(4) Choi, J. J.; Yang, X.; Norman, Z. M.; Billinge, S. J. L.; Owen, J. S. Structure of Methylammonium Lead Iodide Within Mesoporous Titanium Dioxide: Active Material in High-Performance Perovskite Solar Cells. *Nano Letters*, **2014**, *14*, 127-133.
(5) Chen, T.; Foley, B.J.; Ipek, B.; Tyagi, M.; Copley, J.R.D.; Brown, C.M.; Choi, J.J.; Lee, S-H. Rotational Dynamics of Organic Cations in the $CH_3NH_3PbI_3$ Perovskite. *Phys. Chem. Chem. Phys.*, **2015**, *17*, 31278-31286.
(6) Perdew, J.P.; Ruzsinszky, A.; Csonka, G.I.; Vydrov, O.A.; Scuseria, G.E.; Constantin, L.A.; Zhou, X.; Burke, K. Restoring the Density-Gradient Expansion for Exchange in Solids and Surfaces. *Phys. Rev. Lett.*, **2008**, *100*, 136406:5.
(7) Hammer, B.; Hansen, L.B;.Nørskov, J.K. Improved Adsorption Energetics Within Density-Functional Theory Using Revised Perdew-Burke-Ernzerhof Functionals. *Phys. Rev. B.*, **1999**, *59*, 7413:8.
(8) Dovesi, R.; Orlando, R.; Erba, A.; Zicovich-Wilson, C. M.; Civalleri, B.; Casassa, S.; Maschio, L.; Ferrabone, M.; De La Pierre, M.; D'Arco, P.; Noel, Y.; Causa, M.; Rerat, M.; Kirtman, B. CRYSTAL14: A Program for the ab Initio Investigation of Crystalline Solids. *Int. J. Quant. Chem.*, **2014**, *114*, 1287–1317.
(9) Bredow, T.; Peintinger, M. F.; Oliveira, D. V. Consistent Gaussian Basis Sets of Triple-zeta Valence With Polarization Quality for Solid-state Calculations. *J. Comput. Chem.*, **2013**, *34*, 451–459.
(10) www.crystal.unito.it/basis-sets.php (26 Oct 2016).

(11) Dirac. P.A.M. Note on Exchange Phenomena in the Thomas-Fermi Atom. *Proc. Cambridge Phil. Soc.*, **1930**, *26*, 376-385.
(12) Vosko, S.H.; Wilk, L.; Nusair, M. Accurate Spin-dependent Electron Liquid Correlation Energies for Local Spin Density Calculations: a Critical Analysis. *Can. J. Phys.*, **1980**, *58*, 1200-1212.
(13) Becke. A. Density-functional Exchange-energy Approximation with Correct Asymptotic Behavior. *Phys. Rev. A*, **1988**, *38*, 3098–3100.
(14) Lee, C.; Yang, W.; Parr. R. G. Development of the Colle-Salvetti Correlation-energy Formula into a Functional of the Electron Density. *Phys. Rev. B*, **1988**, *37*, 785–789.
(15) Zhao, Y.; Truhlar. D. G. Construction of a Generalized Gradient Approximation by Restoring the Density-gradient Expansion and Enforcing a Tight Lieb-Oxford Bound. *J. Chem. Phys.*, **2008**, *128*, 184109:8.
(16) Zhao, Y.; Truhlar, D. G. The M06 Suite of Density Functionals for Main Group Thermochemistry, Thermochemical Kinetics, Noncovalent Interactions, Excited States, and Transition Elements: Two New Functionals and Systematic Testing of Four M06-Class Functionals and 12 Other Functionals. *Theor. Chem. Acc.*, 2008, *120*,215-241.
(17) Becke. A. Density-functional Thermochemistry. III The Role of Exact Exchange. *J. Chem. Phys.*, **1993**, *98*,5648-5652.
(18) Adamo, C.; Barone, V. Toward Reliable Density Functional Methods Without Adjustable Parameters: the PBEo Model. *J. Chem. Phys.*, **1999**, *110*, 6158– 6170.
(19) Guido, C. A.; Bremond, E.; Adamo, C.; Cortona, P. One Third: A New Recipe for the PBEo Paradigm. *J. Chem. Phys.*, **2013**, *138*, 021104:4.
(20) Perdew. J. P. Unified Theory of Exchange and Correlation Beyond the Local Density Approximation. In P. Ziesche and H. Eschrig, editors, Electronic Structure of Solids 1991, Vol. 11, Berlin, 1991. Akademie Verlag. 11–20,
(21) Perdew, J. P.; Wang, Y. Accurate and Simple Density Functional for the Electronic Exchange Energy: Generalized Gradient Approximation. *Phys. Rev. B*, **1986**, 33, 8800:2.
(22) Perdew, J. P.; Wang, Y. Erratum: Accurate and Simple Density Functional for the Electronic Exchange Energy: Generalized Gradient Approximation. *Phys. Rev. B*, **1989**, *40*,3399:1.
(23) Perdew, J. P.; Wang, Y. Accurate and Simple Analytic Representation of the Electron Gas Correlation Energy. *Phys. Rev. B*, **1992**, *45*, 13244:6.
(24) Becke. A.D. Density-functional Thermochemistry. V. Systematic Optimization of Exchange-correlation Functionals, *J. Chem. Phys.*, **1997**, *107*, 8544–8551.
(25) Hamprecht, F. A.; Cohen, A. J.; Tozer, D. J.; Handy, N. C. Development and Assessment of New Exchange-correlation Functionals, *J. Chem. Phys.*, **1998**, *109*, 6264–6272.
(26) Bilc, D. I.; Orlando, R.; Shaltaf, R.; Rignanese, G. M.; Iniguez, J.; Ghosez. Ph. Hybrid Exchange-Correlation Functional for Accurate Prediction of the Electronic and Structural Properties of Ferroelectric Oxides. *Phys. Rev. B*, **2008**, *77*, 165107:13.
(27) Krukau, V.; Vydrov, O. A.; Izmaylov, A. F.; Scuseria, G. E. Influence of the exchange screening parameter on the performance of screened hybrid functionals. *J. Chem. Phys.*, 2006, *125*, 224106–224106.
(28) Henderson, T. M.; Izmaylov, A. F.; Scuseria, G. E.; Savin. A. The Importance of Middle-Range Hartree-Fock-type Exchange for Hybrid Density Functionals. *J. Chem. Phys.*, **2007**, *127*, 221103–221107.
(29) Henderson, T. M.; Izmaylov, A. F.; Scuseria, G. E.; Savin, A. Assessment of a Middle-range Hybrid Functional. *J. Chem. Theory Comput.*, **2008**, 4, 1254–1262.
(30) Schimka, L.; Harl, J.; Kresse, G. Improved Hybrid Functional for Solids: The HSEsol functional. *J. Chem. Phys.*, **2011**, *134*, 024116–024127.
(31) Weintraub, E. T.; Henderson, M.; Scuseria G. E. Long-Range-Corrected Hybrids Based on a New Model Exchange Hole. *J. Chem. Theory Comput.*, **2009**, *5*, 754–762.
(32) Baikie, T.; Fang, Y.; Kadro, J.M.; Schreyer, M.; Wei, F.; Mhaisalkar, S.G.;Graetzel, M; White, T.J. *J. Mater. Chem. A,* ***2013****, 1, 5628–5641.*
(33) Pérez-Osorio, M.A.; Milot, R.L.; Filip, M.R.; Patel, J.B.; Herz, L.M.; Johnston, M.B.; Giustino, F. Vibrational Properties of the Organic–Inorganic Halide Perovskite $CH_3NH_3PbI_3$ from Theory and Experiment: Factor Group Analysis, First-Principles Calculations, and Low-Temperature Infrared Spectra. *J. Phys. Chem. C*, **2015**, *119*, 25703–25718.
(34) Amat, A.; Mosconi, E.; Ronca, E.; Quarti, C.; Umari, P.; Nazeeruudin, Md. K.; Gratzel, M.; De Angelis, F. Cation-Induced Band-Gap Tuning in Organohalide Perovskites: Interplay of Spin–Orbit Coupling and Octahedra Tilting. *Nano Lett*. **2014**, *14*, 3608–3616.
(35) Keen, D.A.; Goodwin, A.L, The crystallography of correlated disorder. *Nature*, **2015**, 521, 303-309.
(36) Yin, W-J; Chen, H.; Shi, T.; Wei, S-H.; Yan, Y. Origin of High Electronic Quality in Structurally Disordered $CH_3NH_3PbI_3$ and the Passivation Effect of Cl and O at Grain Boundaries, *Adv. Electron. Mater*. **2015**, 1, 1500044–1500052.
(37) Long, R.; Liu, J.; Prezhdo, O. V. Unravelling the Effects of Grain Boundary and Chemical Doping on Electron–Hole Recombination in $CH_3NH_3PbI_3$ Perovskite by Time-Domain Atomistic Simulation, *J. Am. Chem. Soc.*, **2016**, *138*, 3884–3890.
(38) Fabini, D.H.; Hogan, T.; Evans, H.A.; Stoumpos, C.C.; Kanatzidis, M.G.; Seshadri, R. Dielectric and Thermodynamic Signatures of Low-Temperature Glassy Dynamics in the Hybrid Perovskites $CH_3NH_3PbI_3$ and $HC(NH_2)_2PbI_3$. *J. Phys. Chem. Lett.*, **2016**, *7*, 376–381.

Paper III

Nuclear Inst. and Methods in Physics Research, A 870 (2017) 79–83

Contents lists available at ScienceDirect

Nuclear Inst. and Methods in Physics Research, A

journal homepage: www.elsevier.com/locate/nima

Detailed characterisation of the incident neutron beam on the TOSCA spectrometer

Roberto S. Pinna [a,b], Svemir Rudić [a,*], Matthew J. Capstick [a], David J. McPhail [a], Daniel E. Pooley [a], Gareth D. Howells [a], Giuseppe Gorini [b], Felix Fernandez-Alonso [a,c]

[a] ISIS Facility, STFC, Rutherford Appleton Laboratory, Chilton, Didcot OX11 0QX, UK
[b] CNISM, Universita' degli Studi di Milano-Bicocca, Piazza della Scienza 3, 20126 Milano, Italy
[c] Department of Physics and Astronomy, University College London, Gower Street, London WC1E 6BT, UK

ARTICLE INFO

Keywords:
TOSCA
Neutron beam profile
Neutron detector
Scintillator detector
Neutron flux

ABSTRACT

We report a detailed characterisation of the incident neutron beam on the TOSCA spectrometer. A bespoke time-of-flight neutron monitor has been designed, constructed and used to perform extensive spatially resolved measurements of the absolute neutron flux and its underlying time structure at the instrument sample position. The obtained data give a quantitative understanding of the current instrument beyond neutronic simulations and provide a baseline in order to assess the performance of the upgraded instrument. At an average proton current-on-target of 153 μA (ISIS Target Station 1; at the time of measurements) we have found that the wavelength-integrated neutron flux (from 0.28 Å to 4.65 Å) at the position of the TOSCA instrument sample (spatially averaged across the 3×3 cm^2 surface centred around (0,0) position) is approximately 1.2×10^6 neutrons cm^{-2} s^{-1}, while the whole beam has a homogeneous distribution across the 3.0×3.5 cm^2 sample surface. The spectra reproduced the well-known shape of the neutrons moderated by the room temperature water moderator and exhibit a neutron flux of 7.3×10^5 neutrons cm^{-2} s^{-1} Å^{-1} at 1 Å.

1. Introduction

TOSCA [1] is a world leading inelastic neutron spectrometer that has set the standard for broadband vibrational spectroscopy with neutrons. The instrument is characterised by its 17 m primary flightpath and 4.0×4.0 cm^2 beam size at the sample position [2].

For the instrument to keep pace with the scientific challenges, an increase in the neutron flux collected at the sample position through a supermirror neutron guide placed along its beamline, would be highly beneficial. Such neutron beam should remain well focussed and its neutron flux should be uniform. In order to evaluate the beam features we have designed and built a detector assembly that conforms to the space constraints of the TOSCA instrument, and allows us to characterise the neutron beam profile. Therefore here we present the time-of-flight (TOF) measurements performed at different points along the TOSCA sample position surface. These results are of utmost importance in defining the current instrument baseline and for the assessment of the performance gain that will be achieved after the installation of the neutron guide along the TOSCA beamline [3–5].

TOSCA views a 300 K water moderator placed upstream of the North 8 beamline (TOSCA) at ISIS Target Station 1. The moderator is 120 mm high, 125 mm wide and 45 mm deep and it has a gadolinium poisoning foil placed at a distance of 15 mm from the north face of the moderator [6]. The water vessel is surrounded by a beryllium neutron reflector and by an in-reflector borated decoupler that reduces the pulse time-width.

2. Experimental setup

ISIS Facility is a pulsed neutron and muon source with a frequency of 50 Hz, i.e. the period between the pulses is 20 ms (a sub-frame) and the pulses are arranged in frames with duration of 100 ms. TOSCA receives 4 pulses in a single frame while the last pulse of the source is redirected towards the second target station, see Fig. 1. The missing pulse is exploited to extend the energy transfer range of the instrument at a relatively small cost as this high TOF region contains the intense elastic line. This mode of operation has proved valuable and was recently adopted on VESUVIO instrument at ISIS to extend its energy range down to 1 meV quite successfully [7].

* Corresponding author.
E-mail address: svemir.rudic@stfc.ac.uk (S. Rudić).

http://dx.doi.org/10.1016/j.nima.2017.07.018
Received 2 May 2017; Received in revised form 5 July 2017; Accepted 10 July 2017
Available online 25 July 2017
0168-9002/

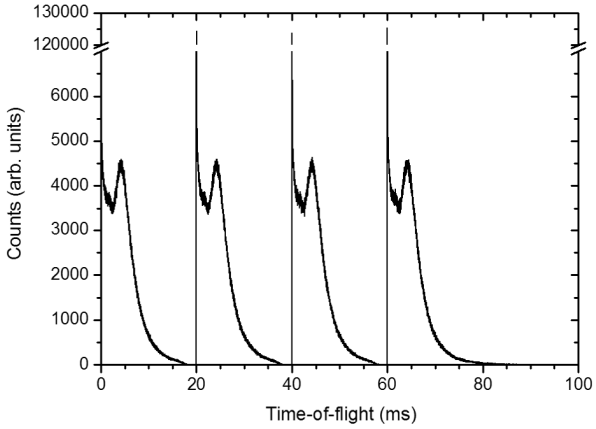

Fig. 1. Time-of-flight spectra of neutrons within the single TS1 frame recorded with the help of a GS1 detector at the TOSCA sample position.

The beam profile was probed using a calibrated neutron beam monitor/detector designed to measure the neutron flux. The sensitive component of the detector is a cuboid of cerium-doped glass scintillator, measuring $0.96 \times 0.95 \times 0.53$ mm^3. The scintillator known as 'GS1' (purchased from Scintacor, formerly known as Applied Scintillation Technologies) contains 2.4% lithium by weight with natural isotopic abundance and was sized to provide a point-like sample of the neutron beam, removing the possibility of edge-effects or misalignment affecting the data. The GS1 scintillator was enclosed within the aluminium detector housing, and mounted via an aluminium shaft on a set of XY motorised translational stages, see Fig. 2. The whole assembly was set on the 180 mm diameter flange (499 mm above the beam axis) that gives direct access on top of the sample position. The choice of the lower flange as the main support has been made to reduce the length of the translational shaft, thus reducing the likelihood of misalignments. The TOSCA closed cycle refrigerator (CCR) needed to be removed from its position in order to accommodate the assembly frame onto the flange, and thus the measurements at the sample position were performed in open air and at room temperature.

The position of this point-sampling detector was controlled via a computer script which moved it automatically after the accumulation of 20 000 frames at each spatial point (1 frame = 100 ms), each frame containing four consecutive neutron pulses, without the need to interrupt the beam between different runs. Over 100 points around the beam centre (from −3.0 cm to +3.0 cm in the X (horizontal) and Y (vertical) directions, when looking downstream) were measured, sampling the time-of-flight spectrum across the beam cross section almost every 5 mm, see Figure S1 in supplementary information (SI). Subsequently the data were calibrated to give the neutron flux at the sample position in units of neutrons cm^{-2} s^{-1} Å^{-1} and eventually integrated in the wavelength range of interest.

It is worthwhile to point out that the TOSCA beamline is composed of the shutter tube, a monolith tube and five subsequent collimation tubes, where each section contains various collimation inserts (B4C neutron absorbing rings) and sections (all tapered) are separated by the thin aluminium windows to preserve the vacuum. See reference 2 for precise details. At the time of this study only the monolith tube and two subsequent collimation tubes were under vacuum.

Computational details: The McStas software package [8] was used in order to perform Monte Carlo simulations of the neutron scattering at the TOSCA beamline. The geometrical parameters of the instrument primary beamline [4] were implemented in the virtual instrument, while the water moderator file [9] was provided by the ISIS Neutronics Group and was built using MCNP-X calculations of the actual TS1 target–reflector–moderator assembly. The angle between the TOSCA beamline axis and the moderator face was kept at 90° i.e. the moderator face and the shutter face were perfectly aligned/parallel. In reality the beamline axis is tilted by ~ 13.2° from the line perpendicular to the moderator face and this information has been taken into account when generating the moderator file. Thus for the purposes of McStas calculations the difference between the real and the simulated angle is not important.

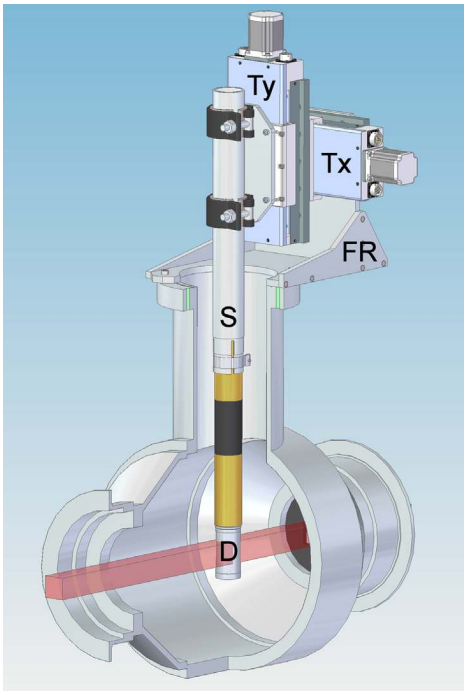

Fig. 2. The experimental setup for measuring the neutron beam profile on TOSCA instrument. It includes a GS1 detector (D) enclosed within the aluminium housing, and mounted via an aluminium shaft (S) on a set of XY motorised translational stages (Tx, Ty). The assembly frame (FR) was positioned in such a way for the detector to overlap with the beam path denoted in pink.

3. Methodology of data analysis

The Mantid software package [10–12] was used in order to analyse the time-of-flight spectra recorded with the help of the GS1 detector at various points across the sample surface. Each spectrum covered the region between 0 and 100 ms (one frame), it was composed of five sub-frames, and the data bin had constant width of 4 μs across the whole spectrum. The spectrum signal to noise ratio was improved by accumulating 20 000 frames at each spatial point.

The data processing consisted of the following steps:

(a) The retrieved raw TOF data in the range from 0 to 100 ms were separated into five equal parts of 20 ms each i.e. the four TS1 pulses plus the TS2 pulse. The last part (sub-frame) is not influenced by the TOSCA neutron beam chopper and allows the study of the TOSCA elastic region around 3.4 meV i.e. ~22 ms from the start of the neutron pulse [2], which is normally shadowed by the frame overlap, as shown in Fig. 1 and described in the previous section.

(b) The first four sub-frames were summed into one single histogram and the resulting TOF spectrum was converted into a wavelength spectrum. This is a linear conversion of TOF units which at length of 17 m from the moderator corresponds to the following equation:

$$\lambda\left[\text{Å}\right] = \frac{h}{m}\frac{t}{L} = 2.327 \times 10^{-1} t\,[\text{ms}] \quad (1)$$

where $h = 6.6 \times 10^{-34}$ Js is Planck's constant and m is the neutron mass. Although the total number of data bins upon transformation stays the same their width is shrunk; furthermore the data values of the intensity (counts) were not adjusted or rearranged as a result of the conversion.

Table 1
Physical properties of GS1 scintillator detector containing lithium.

Physical property	GS1 detector
area [m^2]	9.12×10^{-7}
density [kg m^{-3}]	2.66×10^{3}
mass fraction of Li_2O within detector	6.00×10^{-2}
mass fraction of Li within Li_2O	4.64×10^{-1}
isotopic abundance of ^6Li	7.60×10^{-2}
molecular weight of ^6Li [kg mol^{-1}]	6.00×10^{-3}
number of moles of ^6Li [mol m^{-3}]	9.38×10^{2}
Avogadro constant [mol^{-1}]	6.02×10^{23}
N of ^6Li [atoms m^{-3}]	5.65×10^{26}
^6Li σ_{abs} at 1 Å[m^2]	5.22×10^{-26}
thickness l [m]	5.30×10^{-4}
Nσl (at 1 Å)	1.56×10^{-2}

(c) In order to derive the real number of neutrons in each wavelength bin N_{eff} the measured counts C needed to be corrected by the wavelength dependent efficiency $\varepsilon(\lambda)$ of the current (GS1) detector:

$$N_{eff}(\lambda) = \frac{C}{\varepsilon(\lambda)} \tag{2}$$

where $\varepsilon(\lambda)$ can be calculated using the properties in Table 1.

$$\varepsilon(\lambda) = 1 - e^{-N\sigma(\lambda)l}. \tag{3}$$

In the linear approximation for the wavelength dependence of the lithium absorption cross section [13], Eq. (2) reduces to:

$$\varepsilon(\lambda) = 1 - e^{-Al\lambda} \tag{4}$$

where $A = N\sigma_{abs}$ (1 Å) is the absorption coefficient [$Å^{-1}$ m^{-1}], l is the detector thickness [m] and λ is the neutron wavelength [Å]. For the GS1 detector $A = 29.49$ $Å^{-1}$ m^{-1} and $l = 0.53$ mm.

Subsequently N_{eff} was normalised by the detector area of 9.1×10^{-3} cm^2 in order to derive the number of neutrons per unit area, and divided by the total number of summed frames (i.e. 20 000 frames). Considering that TOSCA receives 10 frames per second, scaling the results by that factor (10) eventually gives the spectrum of the time averaged neutron flux on the sample in units of neutrons cm^{-2} s^{-1} as a function of wavelength. Furthermore, if one takes into account the normalisation by the wavelength bin size (i.e. 9.3×10^{-4} Å) one can get the neutron flux intensity in units of neutrons cm^{-2} $s^{-1}Å^{-1}$. Finally, we integrated this final spectrum across the wavelength range which is relevant for TOSCA (i.e. from 0.28 Å to 4.65 Å) to get the total useful neutron flux that impinges on the sample during a second.

4. Results and discussion

The experimentally derived TOF spectrum as a function of wavelength of the TOSCA neutron flux (spatially averaged across the 3.0×3.0 cm^2 surface centred around (0,0) position) is shown in Fig. 3 (black trace). Its features are in line with the expectations [14] since the peak in the 'moderated hump' appears at around 1 Å which is characteristic of room temperature water moderator. Its shape is characterised by the epithermal component at low wavelength and the Maxwellian component that follows. Equally, in terms of its overall profile the experimental spectrum is in line with the results of the Monte Carlo simulations (red empty triangle symbols) performed with the help of McStas software, although the latter needed to be scaled down by the factor of 3.41 in order to make the simulated and the experimental integrated neutron flux in the region between 0.28 Å and 4.65 Å equal. Furthermore, it is comparable in shape to the POLARIS (ISIS diffractometer located next to TOSCA instrument) spectrum while the fluxes have the same order of magnitude [15]. This is not surprising since both instruments share the same moderator, and the higher flux on POLARIS is mainly due to its shorter beamline (14.0 m). The TOSCA beam profile at the sample position is shown in Fig. 4.

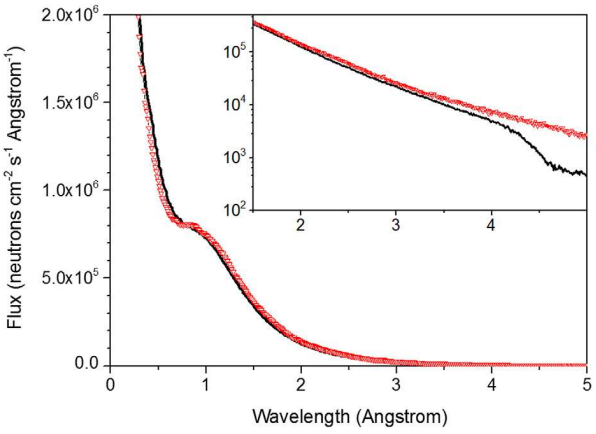

Fig. 3. Neutron flux at the TOSCA sample position as a function of wavelength. Experimentally derived values (spatially averaged across the 3.0×3.0 cm^2 surface centred around (0,0) position) are shown as black line while those obtained with the help of Monte Carlo simulations are shown in red as empty triangle symbols. Monte Carlo values of the neutron flux were scaled down by the factor of 3.41 in order to make the simulated and the experimental integrated neutron flux in the region between 0.28 Å and 4.65 Å equal. In order to make easier comparison at the higher wavelengths, the inset (in the upper right corner) shows the neutron flux (in logarithmic scale) as a function of wavelength. The drop in the experimental flux for neutrons with the wavelength larger than 4 Å is a consequence of the disc chopper used to prevent the frame overlap [2].

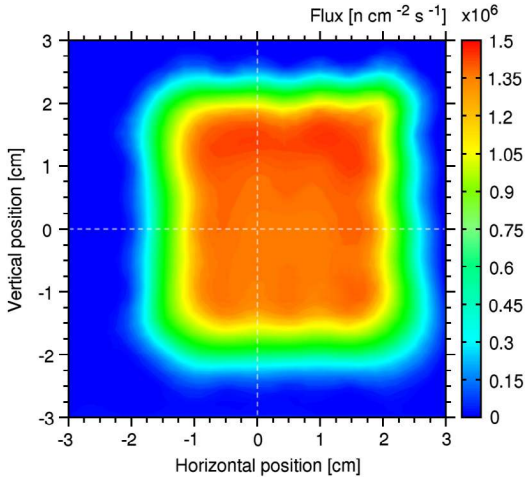

Fig. 4. The experimentally derived neutron beam profile at the TOSCA sample position. The measured values of time averaged neutron flux, integrated across 0.28 Å to 4.65 Å wavelength range of interest to TOSCA, were obtained with the average proton current-on-target of 153 μA.

Its central region, 2.0×2.0 cm^2 in area, is homogeneous, while overall beam has roughly 3.8 (H) × 4.0 (V) cm^2 square shape (taking into account the region with the neutron flux higher than 50% of the maximum intensity) as a consequence of the long collimator positioned along the beamline. In the upper right section of the beam profile higher neutron flux can be observed, while the beam centre appears to be displaced (up and to the right when looking downstream, i.e. from the moderator towards the instrument). Such hotspot could be due to the non-uniformity of the beam exiting the moderator face. It is less pronounced if one looks into the higher wavelength neutrons that spend longer period of time in the moderator, making more collisions in the water and thus have more chance to distribute evenly across the moderator surface. The evaluation of the beam spatial profile as a function of wavelength is shown in Fig. 5. In particular, the beam profile for neutrons with the wavelength between 0.8 Å and 1.2 Å has higher flux in the upper right corner, while the beam profile for neutrons

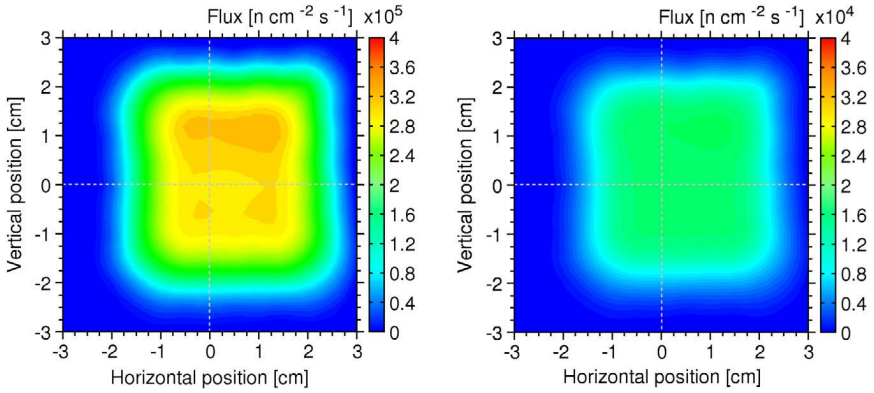

Fig. 5. The experimentally derived neutron beam profiles at the TOSCA sample position for neutrons with the wavelength between 0.8 Å and 1.2 Å (left) and 2.5 Å and 2.9 Å (right). The measured values of the time averaged neutron flux were obtained with the average proton current-on-target of 153 μA. Note that the two scales differ by the order of magnitude.

with the wavelength between 2.5 Å and 2.9 Å is much more uniform across the whole beam surface. The beam shift may indicate shutter misalignment, possible unwanted reflections or simply displacement of the instrument centre from the beamline axis.

The theoretical simulation of the TOSCA beam profile at the sample position is depicted in Fig. 6. The simulated beam has roughly 4.8 (H) × 4.8 (V) cm^2 (taking into account the region with the neutron flux higher than 50% of the maximum intensity) square profile (due to the collimation), while the flux is constant across the 4.0 (H) × 4.0 (V) cm^2 surface as further indicated by the horizontal cross cut across the beam intensity, see Fig. 7. As emphasised before the simulated neutron flux is 3.41 times higher than the experimentally observed values. This is not surprising since the simulation was performed in vacuum while in reality, at the time of this experiment out of a 17 m long flightpath between the moderator face and the TOSCA sample position, only 7 m were under vacuum and 10 m were in air. Thus in order to compare with the experiment, the simulated values should be corrected by the factor of 0.52 which corresponds to the transmitted neutron flux upon travel through 10 m of air. The corrected simulated values are shown in Fig. 7 as well. They are still 1.77 (3.41×0.52) times larger than the experimental values, and the difference can be ascribed to various factors. Namely, the simulation does not take into account the aluminium windows positioned along the primary flightpath, and the expected differences between the full neutronics simulation of the neutron production in the TS1 target–reflector–moderator assembly and the experimental neutron flux [16].

Fig. 7 points to the neutron beam that is somewhat shifted from the beam centre to the right. Furthermore, it is apparent that the experimental beam width is smaller than predicted. The plateau of the simulated profile is exactly 4.0 cm in width while the experimentally observed width has a plateau of about 3.0 cm. As one can see from Fig. 4 and 6, the measured and the calculated neutron flux at the centre of the sample, at the so called (0,0) position (see SI), are 1.3×10^6 neutrons cm^{-2} s^{-1} and 4.1×10^6 neutrons cm^{-2} s^{-1}, respectively. The corresponding values spatially averaged across the 3.0×3.0 cm^2 surface centred around (0,0) position are 1.2×10^6 neutrons cm^{-2} s^{-1} and 4.1×10^6 neutrons cm^{-2} s^{-1}, respectively. Between the two later values a normalisation factor of 3.41 might be applied to match the absolute values. The neutron flux values associated with the plateau shown in Fig. 7, and averaged along the vertical axis (between −2.0 cm and +2.0 cm) are slightly smaller. In particular the simulated values were derived with the help of the linear flux monitor, i.e. not the wavelength monitor used in the case of the beam profile shown in Fig. 6.

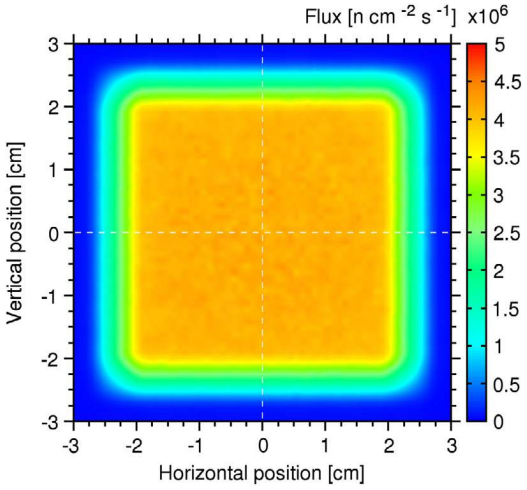

Fig. 6. The simulated neutron beam profile at the TOSCA sample position. The calculated values of the time averaged neutron flux, integrated across 0.28 Å to 4.65 Å wavelength range of interest to TOSCA and scaled to the averaged proton current-on-target of 153 μA.

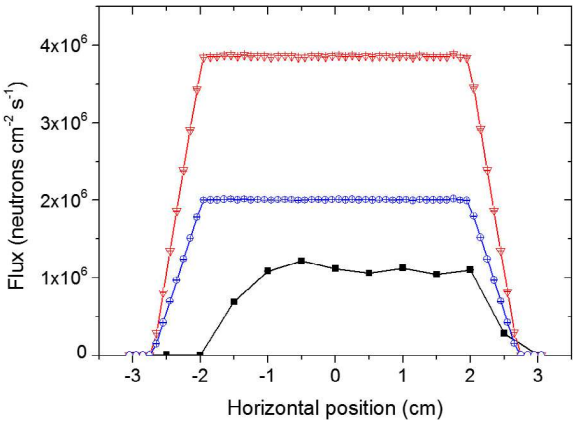

Fig. 7. The experimental (black filled squares), the simulated (red empty triangles) and the corrected simulated (for attenuation in air; blue empty circles) neutron beam profile projected along the horizontal axis at the TOSCA sample position. The beam flux has been averaged along the vertical axis (between −2.0 cm and +2.0 cm, i.e. within the beam height) and includes only neutrons within the wavelength range of interest to TOSCA (from 0.28 Å to 4.65 Å).

5. Conclusions

The results evidenced that the incident beam on TOSCA has a strongly collimated square shape, with a steep fall in intensity outside the main region. The penumbra of the beam is a 0.5 cm crown around the main beam spot at its broadest size on the bottom. The beam appears

reasonably homogeneous across the 3.0 (H) × 3.5 (V) cm^2 surface, although some beam patterns can be observed, and the illuminated area is approximately 3.8 (H) × 4.0 (V) cm^2. The time averaged wavelength-integrated flux at the TOSCA sample centre, so called (0,0) position, is around 1.3×10^6 neutrons cm^{-2} s^{-1} and we measured the flux of 7.3×10^5 neutrons cm^{-2} s^{-1} $Å^{-1}$ at the moderator peak (~1 Å) which represents the Maxwellian component of the incident spectrum. The measurements reveal the neutron beam profile that is ~35% smaller (by area), and the neutron flux in the beam centre (spatially averaged across the 3.0×3.0 cm^2 surface centred around (0,0) position) that is 3.41 (1.77, after correction for attenuation in air) times smaller than predicted by the Monte Carlo calculations.

Acknowledgements

The authors gratefully acknowledge the Science & Technology Facilities Council (STFC) for financial support for this project, access to TOSCA beamline at ISIS, and use of e-Science SCARF cluster at the Rutherford Appleton Laboratory. This work has been partially supported by the 2014–2020 CNR–STFC Agreement concerning collaboration in scientific research at the ISIS Facility. We would like to thank Dr. Goran Škoro and Dr. Matteo Zanetti for helpful discussions, and Dr. Jeff Armstrong for reading the manuscript.

Appendix A. Supplementary data

Supplementary material related to this article can be found online at http://dx.doi.org/10.1016/j.nima.2017.07.018.

References

[1] ISIS Neutron, Muon Source, TOSCA neutron spectrometer, available at http://www.isis.stfc.ac.uk/instruments/tosca/ (accessed on the 26 of March 2017).
[2] S.F. Parker, F. Fernandez-Alonso, A.J. Ramirez-Cuesta, J. Tomkinson, S. Rudic, R.S. Pinna, G. Gorini, Recent and future developments on TOSCA at ISIS, J. Phys. Conf. Ser. 554 (2014) 012003.
[3] S. Rudic, A.J. Ramirez-Cuesta, S.F. Parker, F. Fernandez-Alonso, R.S. Pinna, G. Gorini, C.G. Salzmann, S.E. McLain, N.T. Skipper, TOSCA international beamline review, RAL Technical Reports RAL-TR-2013-015, STFC, 2013.
[4] R.S. Pinna, Monte Carlo simulations of the TOSCA neutron spectrometer: assessment of current performance and future upgrades (M.Sc. thesis), University of Milano-Bicocca, 2014.
[5] R.S. Pinna, S. Rudic, S.F. Parker, G. Gorini, F. Fernandez-Alonso, Monte Carlo simulations of the TOSCA spectrometer: assessment of current performance and future upgrades, EPJ Web of Conferences 83 (2015) 03013.
[6] G. Skoro, R. Bewley, S. Lilley, R. Ewings, G. Romanelli, M. Gutmann, R. Smith, S. Rudic, S. Ansell, A tale of two foils: ISIS TS-1 water moderators, submitted (2017).
[7] G. Romanelli, M. Krzystyniak, R. Senesi, D. Raspino, J. Boxall, D. Pooley, S. Moorby, E. Schooneveld, N.J. Rhodes, C. Andreani, F. Fernandez-Alonso, Characterisation of the incident beam and current diffraction capabilities on the VESUVIO spectrometer, submitted (2017).
[8] P. Willendrup, E. Farhi, K. Lefmann, McStas 1.7 - a new version of the flexible Monte Carlo neutron scattering package, Physica B 350 (2004) e735–e737.
[9] S. Ansell, D. Champion, The ISIS_moderator component, McStas simulation package, http://www.mcstas.org/download/components/contrib/ISIS_moderator.html (accessed on the 26 of March 2017).
[10] Mantid (2013)analysis toolkit for instrument data. Mantid Project. https://www.mantidproject.org/Main_Page (accessed on the 26 of March 2017).
[11] O. Arnold, J.C. Bilheux, J.M. Borreguero, A. Buts, S.I. Campbell, L. Chapon, M. Doucet, N. Draper, R. Ferraz Leal, M.A. Gigg, V.E. Lynch, A. Markvardsen, D.J. Mikkelson, R.L. Mikkelson, R. Miller, K. Palmen, P. Parker, G. Passos, T.G. Perring, P.F. Peterson, S. Ren, M.A. Reuter, A.T. Savici, J.W. Taylor, R.J. Taylor, R. Tolchenov, W. Zhou, J. Zikovsky, Mantid - Data analysis and visualization package for neutron scattering and μ SR experiments, Numerical Instruments and Methods in Physical Research a 764 (2014) 156–166.
[12] E. Oram, An overview of the development of indirect inelastic data reduction and analysis in MANTID between July 2015-July 2016, RAL Technical Reports RAL-TR-2016-11, STFC, 2016.
[13] J. Dawidowski, J.R. Granada, J.R. Santisteban, F. Cantargi, L.A.R. Palomino, Neutron scattering lengths and cross sections, appendix, in: D.L. Price, F. Fernandez-Alonso (Eds.), Experimental Methods in the Physical Sciences, Nuclear Scattering –Fundamentals 44, Academic Press, 2013, pp. 471–528.
[14] C.G. Windsor, Pulsed Neutron Scattering, Taylor & Francis Ltd, London, 1981.
[15] R. I Bewley, S. Ansell, G. Škoro, Comparison of observed and calculated ISIS TS1 neutronic response, Proceedings of the 21st Meeting of the International Collaboration on Advanced Neutron Sources ICANS XXI, Japan Atomic Energy Agency, 2016.
[16] G.P. Škoro, S. Ansell, Neutronics modelling for the ISIS TS-1 upgrade, Proceedings of the 21st Meeting of the International Collaboration on Advanced Neutron Sources ICANS XXI, Japan Atomic Energy Agency (2016), pp. 141–147.

Supplementary Information

for

Detailed characterisation of the incident neutron beam on the TOSCA spectrometer

R.S. Pinna,[1,2] S. Rudić,[1,*] M.J. Capstick,[1] D.J. McPhail,[1] D.E. Pooley,[1] G.D. Howells,[1] G. Gorini,[2] and F. Fernandez-Alonso[1,3]

1. ISIS Facility, STFC, Rutherford Appleton Laboratory, Chilton, Didcot OX11 0QX, UK.

2. CNISM, Universita' degli Studi di Milano-Bicocca, Piazza della Scienza 3, 20126 Milano, Italy.

3. Department of Physics and Astronomy, University College London, Gower Street, London WC1E 6BT, UK.

* Author for correspondence.

Contact information:

ISIS Facility

STFC Rutherford Appleton Laboratory

Chilton

Didcot OX11 0QX

UK

Tel: + 44 (0)1235 44 6130

Fax: + 44 (0)1235 44 5720

e-mail: svemir.rudic@stfc.ac.uk

Procedure used in order to generate the image of the neutron beam profile in Figures 4 and 5.

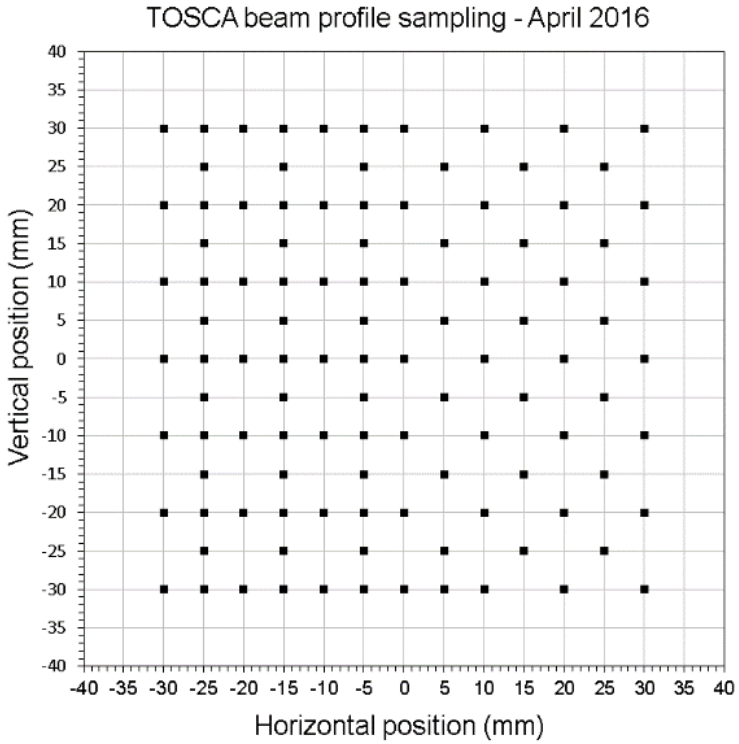

Figure S1. Map of the positions across the TOSCA sample surface (around the beam centre, and when looking downstream, i.e. from the moderator towards the instrument) where the neutron flux has been measured.

The data from each sampling point shown in Figure S1 was retrieved as a TOF spectrum and reduced by means of the procedure described in the main text of the article. From the data analysis we could obtain the wavelength spectrum in units of neutron cm^{-2} s^{-1} $Å^{-1}$ which was integrated from 0.28 to 4.65 Å to get the operationally useful neutron flux for TOSCA at each point. The flux value was associated with the corresponding X-Y coordinate of the sampling point across the sample surface; we could then derive a three column array (X-Y-Flux) that could be plotted in Origin (Data analysis and Graphing Software) as a contour plot, where the colour scale is linked to the flux magnitude. Furthermore, since the sampling step between the points is not uniform across the surface we smoothed the picture by averaging values between the data points.

Procedure used in order to derive the 1D neutron flux curve (see Figure 7).

To obtain the neutron flux curve in 1D, namely along the horizontal axis along the sample median line, we selected all the experimental points placed at the same horizontal position (see Figure S1), converted to units of flux and then averaged the values along the vertical axis from -2.0 cm to +2.0 cm. Finally we generated the plot of the average flux values across the sample as a function of the horizontal position.

To obtain the same 1D plot from the simulated data, we used a position sensitive component with size 6 x 6 cm^2 (W x H), in compliance with the experimental configuration. The resulting data is a matrix of the neutron counts with a resolution of 0.1 cm. Subsequently the counts were summed along the columns (vertical axis; from -2.0 cm to +2.0 cm) and this gave a 1D array of the number of counts as a function of the horizontal position. In order to obtain the intensity in units of (neutron cm^{-2} s^{-1}) we had to divide the counts by the area across which the sum was made (i.e. 4 cm x 0.1 cm = 0.4 cm^2).

Paper IV

The neutron guide upgrade of the TOSCA spectrometer

Roberto S. Pinna,[1,2] Svemir Rudić,[1,*] Stewart F. Parker,[1] Jeff Armstrong,[1] Matteo Zanetti,[1,2] Goran Škoro,[1] Simon P. Waller,[1] Daniel Zacek,[1] Clive A. Smith,[1] Matthew J. Capstick,[1] David J. McPhail,[1] Daniel E. Pooley,[1] Gareth D. Howells,[1] Giuseppe Gorini,[2] and Felix Fernandez-Alonso[1,3]

1. ISIS Facility, STFC, Rutherford Appleton Laboratory, Chilton, Didcot OX11 0QX, UK.

2. CNISM, Universita' degli Studi di Milano-Bicocca, Piazza della Scienza 3, 20126 Milano, Italy.

3. Department of Physics and Astronomy, University College London, Gower Street, London WC1E 6BT, UK.

Submitted to Nuclear Instruments and Methods in Physics Research Section A: Accelerators, Spectrometers, Detectors and Associated Equipment, (November, 2017), NIMA-D-17-01199.

* Author for correspondence.

Contact information:

ISIS Facility

STFC Rutherford Appleton Laboratory

Chilton

Didcot OX11 0QX

UK

Tel: + 44 (0)1235 44 6130

Fax: + 44 (0)1235 44 5720

e-mail: svemir.rudic@stfc.ac.uk

Abstract

The primary flightpath of the TOSCA indirect geometry neutron spectrometer has been upgraded with a high-*m* 14.636 m (including 0.418 m of air gaps) neutron guide composed of ten sections in order to boost the neutron flux at the sample position. The upgraded incident neutron beam has been characterised with the help of the time-of-flight neutron monitor; the beam profile and the gain in the neutron flux data are presented. At an average proton current-on-target of 160 μA and proton energy of 800 MeV (ISIS Target Station 1; at the time of the measurements) we have found that the wavelength-integrated neutron flux (from 0.28 Å to 4.65 Å) at the position of the TOSCA instrument sample (spatially averaged across a 3.0 x 3.0 cm^2 surface centred around the (0,0) position) is approximately 2.11 x 10^7 neutrons cm^{-2} s^{-1} while the gain in the neutron flux is as much as 46-fold for neutrons with a wavelength of 2.5 Å. The instrument's excellent spectral resolution and low spectral background have been preserved upon the upgrade. The much improved count rate allows faster measurements where useful data of hydrogen rich samples can be recorded within minutes, as well as experiments involving smaller samples that were not possible in the past.

Keywords: TOSCA, neutron guide, neutron beam profile, neutron detector, scintillator detector, neutron flux, vibrational spectrometer

1. Introduction

TOSCA is an indirect-geometry inelastic neutron spectrometer optimised for high resolution vibrational spectroscopy in the energy transfer region between -24 and 4000 cm^{-1} [1,2]. The instrument has been operational for almost two decades and during that time has set the standard for broadband chemical spectroscopy with neutrons [3]. In autumn 2013 as part of the international beamline review [4] it was concluded that for TOSCA to be able to participate in strategic research areas such as CO_2 capture and charge storage [5], an increase in the incident neutron flux *via* the provision of a neutron guide would be highly beneficial. Such a development would allow detailed studies of industrially relevant systems containing weak neutron scatters (SO_2, CO, NO) as well as faster parametric studies, particularly for hydrogen containing molecules such as hydrocarbons. Additionally, studies of smaller samples which are too expensive to produce in larger quantities would be possible. Since then, this major upgrade has been implemented which has involved extensive simulations together with the complete redesign of the TOSCA primary spectrometer to house a state-of-the-art, high-*m* neutron guide and associated chopper system to boost the incident flux on the sample.

Neutron guides are essential in order to boost the neutron flux at a long distance from the neutron source. As neutrons fly nearly parallel to the guide surface they are retained within the tube by a process of external reflection. Neutron guides are square or rectangular cross-section tubes made from optically flat materials, usually glass, that has been metal coated with alternating layers of metal with different scattering length densities. In recent years, progress in guide manufacture has led to supermirror coated guides, having high reflectivity and high *m*-values where $m = \gamma_c(\text{supermirror})/\gamma_c(\text{nickel})$ *i.e.* it is equal to the ratio of the critical angle of reflection, γ_c, of the supermirror and nickel coated optically flat glass [6]. The neutron guides with greater *m* factor lead to increased divergence of the neutron beam which maximum value is given by the critical angle γ_c [º] = 0.1 x *m* x λ [Å]. We have used a tapered guide in order to focus the beam at the sample position while preserving the homogeneity of the beam.

Based on extensive neutron-transport simulations and baseline studies of the guide neutronic response [7,8,9], in this article we present the careful mechanical engineering design of the new TOSCA primary spectrometer and provide a review of the actual performance gains following this upgrade. A comparison between experimental observations and Monte Carlo simulations is provided, and the effect of the upgrade on the instrument spectral resolution and background have been assessed as well.

2. The primary spectrometer

In our design of the neutron guide, we have followed two principles: position the supermirrors to include as much of the neutron flightpath as possible, and to increase the area viewed of the water moderator by increasing the size of the shutter entrance (from its original value of 84 mm x 84 mm) while preserving the beam size at the sample position. A schematic drawing of the new 14.636 m long neutron guide (including 0.418 m of air gaps) which is dedicated to the TOSCA instrument is shown in Figure 1. The first section of the guide, G1, is installed in the new 1.937 m long shutter that is positioned at a distance of 1.626 m from the moderator centre. The shutter contains an m = 5 straight square guide with an aperture of 100 mm x 100 mm. The remaining nine sections of the guide are tapered, starting from the 100 mm x 100 mm entrance of section G2, all the way towards the end of section G10 with 40 mm x 40 mm aperture (positioned at a distance of 16.262 m from the moderator centre, i.e. 0.748 m from the sample position). The angle of taper, ~ 0.136494º, has been kept equal in each tapered section, while the m-factor was increased in steps from m = 5 for sections 2 to 6, m = 6 for sections 7 to 9, and m = 7 for section 10. This gradual increase ensured optimal gain and enabled that even those short wavelength (high energy) neutrons whose divergence was sufficiently small can be retained. Geometrical parameters of each section and the neutron guide as a whole can be found in Table S1 of the supplementary information. We have chosen mostly tapered over mostly straight guide as neutron simulations pointed towards increased flux gain in the case of the former [7,8,9].

As part of the upgrade, the current single disc chopper [2] has been replaced by a double disc chopper positioned at a distance of 9.455 m from the moderator centre, and between sections G5 and G6 of the guide. The air gap between the two sections required to fit the discs was kept to a minimum of 6.6 cm, thus reducing the neutron flux attenuation due to scattering in

air. The new double disc chopper allows utilisation of all the neutron pulses arriving at TOSCA, even when Target Station 1 operates in 50 Hz mode (albeit without access to the elastic line; see reference 2 for further details about the extension of the spectral region of the instrument).

In order to achieve the highest neutron flux at the sample position the flightpath through the neutron guide is in vacuum ($p = 2.5 \times 10^{-2}$ mbar). Since all the sections of the guide could not be joined together in a single housing, various housings are sealed with the help of 0.5 mm thick aluminium windows. Overall, there are a total of nine aluminium windows along the beamline flightpath (*i.e.* between the moderator and the sample position) as indicated by the orange vertical lines in Figure 1.

Two neutron beam monitors are positioned along the flightpath; the first before the chopper, at a distance of 8.900 m from the moderator centre and the second after the chopper at a distance of 15.871m from the moderator centre. The latter monitor is used for the normalisation of the neutron flux. The monitors allow measurements of the time-of-flight spectra of neutrons; and were made from GS20 cubes (cerium-activated lithium aluminosilicate glass, 0.25 mm in size) that were distributed 7 mm apart and across a 7 x 6 array [10,11].

TOSCA has four ^{3}He detector tubes (two on each side of the beam) in back scattering that are used for diffraction measurements. As a result of the beam upgrade and in order to accommodate the last section of the guide they needed to be slightly moved away from the centre of the flightpath *i.e.* they are now positioned at an angle of 175º and 176º in the backward direction. Although the tubes are stationed in air, virtually all the flightpath between the sample position and the diffraction tubes is in vacuum, with the vanadium window acting as the boundary. The final section of the neutron guide, G10, is connected to the instrument by the tapered flight tube and the whole volume is kept at cryogenic vacuum ($< 10^{-6}$ mbar).

The instrument was not operational between the end of May 2016 and mid-February 2017. By the end of November 2016, all sections of the guide were in place apart from the new TOSCA shutter with the initial section of the guide within it, G1, which remained the same as before the upgrade. Since the overwhelming majority of the guide was installed we tested the

setup for enhanced neutron flux, in order to have better idea about the influence of the guide inside the shutter (installed subsequently) on the neutron flux, beam profile, spectral resolution and background (see SI). We will refer to this interim configuration as the C1 configuration, while the configuration before the upgrade will be denoted as C0 [12]. The last section in the shutter was installed in January 2017 to give the final (so called C2) configuration. After the two weeks of commissioning measurements the instrument was returned to the user programme.

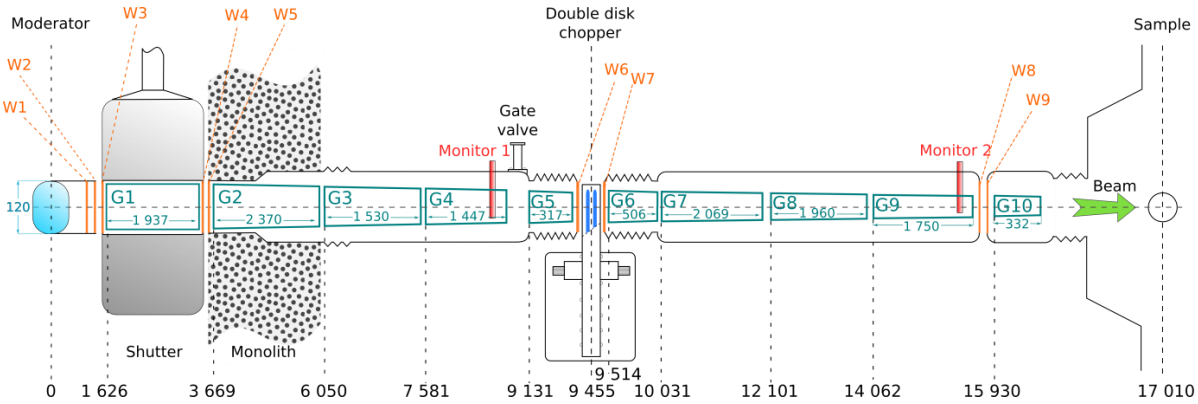

Figure 1. Schematic representation of the side view of the TOSCA neutron guide as installed on the beamline. The guide sections are numbered in the order in which they appear along the flightpath. The starting position of each section, in relation to the moderator centre, as well as its length are provided. Aluminium windows (W) are indicated by the orange vertical lines.

3. Experimental setup

The experimental setup used to measure the neutron flux at the sample position was described in ref. 10. The neutron sensitive component was a cuboid of cerium-doped glass scintillator, measuring 0.96 x 0.95 x 0.53 mm^3. The TOSCA closed cycle refrigerator (CCR) was removed from its position in order to accommodate the assembly frame onto the flange, and thus the measurements at the sample position were performed in open air and at room temperature. The position of this point-sampling detector was controlled *via* a computer script which moved it automatically after the accumulation of 10000 frames at each spatial point (1 frame = 100 ms), each frame containing four consecutive neutron pulses, without the need to interrupt the beam between different runs. 169 points around the beam centre (from -3.0 cm to +3.0 cm in the X (horizontal) and Y (vertical) directions, when looking

downstream) were measured, sampling the time-of-flight spectrum every 5 mm, see Figure S1 in supplementary information (SI). Subsequently the data were calibrated to give the neutron flux at the sample position in units of neutron cm^{-2} s^{-1} $Å^{-1}$ and eventually integrated in the wavelength range of interest. At the time of this study, the first nine sections of the guide starting from the shutter towards the sample position were under vacuum, while section ten of the guide and the sample environment area were in air.

Computational details: The McStas software package [13] was used in order to perform Monte Carlo simulations of the TOSCA beamline. The geometrical parameters of the upgraded instrument primary beamline (see Table S1 in SI) were implemented in the virtual instrument, while the water moderator file [14] was provided by the ISIS Neutronics Group and was built using MCNP-X calculations of the actual TS1 target-reflector-moderator assembly. The angle between the TOSCA beamline axis and the moderator face was kept at 90º *i.e.* the moderator face and the shutter face were perfectly aligned/parallel. In reality, the beamline axis is tilted by ~13.2º from the line perpendicular to the moderator face and this information has been taken into account when generating the moderator file [14]. Thus for the purposes of McStas calculations the difference between the real and the simulated angle is not important. The 'pre-guide' C0 configuration of the TOSCA was simulated in order to have the baseline performance of the instrument as a reference for the subsequent simulations regarding the gain in neutron flux due to the neutron guide. To calculate the performance of the supermirror neutron guide we used experimentally determined reflectivity profiles (provided by the manufacturer, Swiss Neutronics) for each section of the guide. The Mantid software package [15,16,17,18] was used in order to analyse the experimental data, and details of the applied methodology of data analysis are the same as described in ref. 10.

4. Results and discussion

Final (C2) configuration: The experimentally derived TOF spectrum as a function of wavelength of the TOSCA neutron flux upon the guide installation (spatially averaged across the 3.0 x 3.0 cm^2 surface centred around the (0,0) position) is shown in Figure 2 (green trace). Its features are in line with the expectations [19] since the peak in the 'moderated hump' appears at around 1.1 Å which is characteristic of the room temperature water moderator. Its shape is characterised by the epithermal component at low wavelength and the Maxwellian

component that follows. Equally, in terms of its overall profile the experimental spectrum is in line with the results of the Monte Carlo simulations (blue empty diamond symbols) performed with the help of the McStas software, although the latter needed to be scaled down by a factor of 2.53 in order to make the simulated and the experimental integrated neutron flux in the region between 0.28 Å and 4.65 Å equal. Similar discrepancies have been observed before [12] and will be discussed in more detail later in the text. The TOSCA beam profile at the sample position is shown in Figure 3.

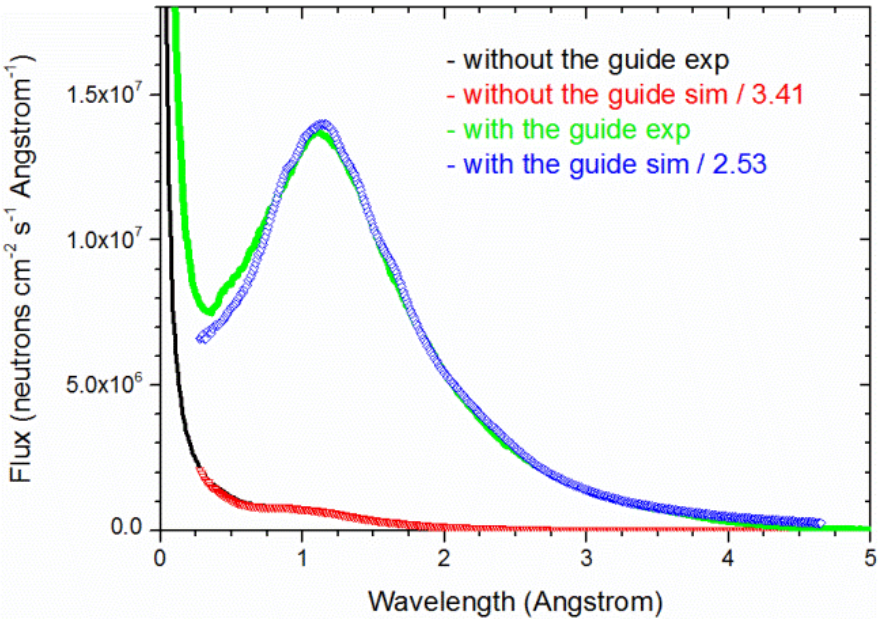

Figure 2. Neutron flux at the TOSCA sample position as a function of wavelength. Experimentally derived values (spatially averaged across the 3.0 x 3.0 cm^2 surface centred around the (0,0) position) are shown by the green line, while those obtained from the Monte Carlo simulations (spatially averaged across the 4.0 x 4.0 cm^2 surface centred around the (0,0) position) are shown in blue as empty diamond symbols. Monte Carlo values (not corrected for attenuation) of the neutron flux were scaled down by a factor of 2.53 in order to make the simulated and the experimental integrated neutron flux in the region between 0.28 Å and 4.65 Å equal. For comparison, the neutron flux (experimental - black line and simulated - red empty triangle symbols) at the TOSCA sample position before the guide upgrade are also shown (configuration C0) (see reference 10 for further details).

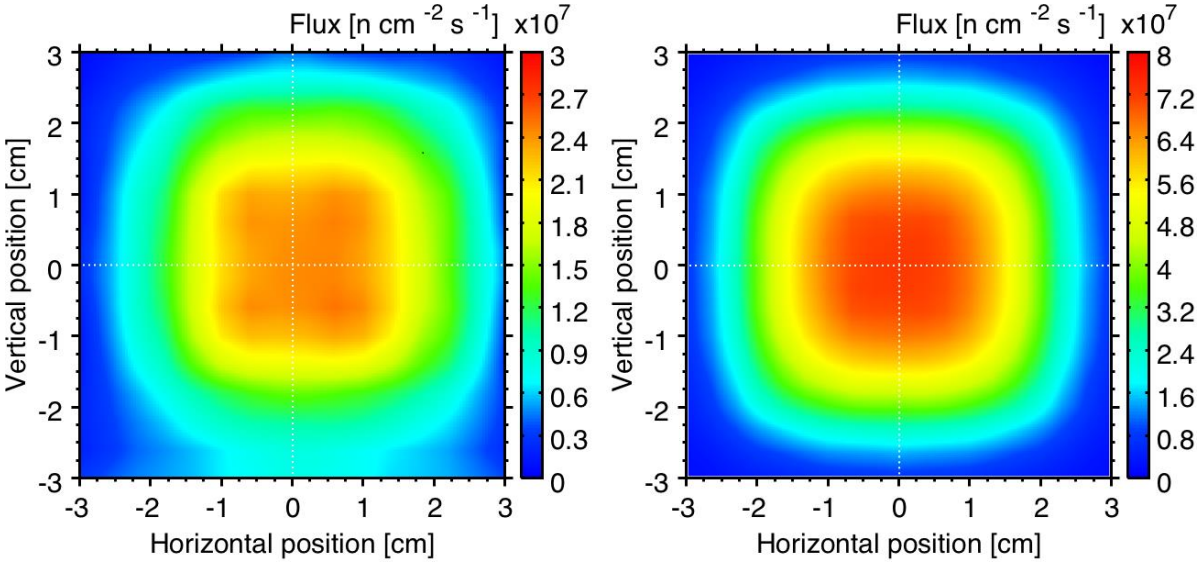

Figure 3. Measured (left) and simulated (right) neutron beam profile at the TOSCA sample position with the guide installed. The measured and calculated values of time averaged neutron flux, integrated across 0.28 Å to 4.65 Å wavelength range of interest to TOSCA were obtained with i.e. scaled to the average proton current-on-target of 160 μA, respectively.

Its central region, 2.5 x 2.5 cm^2 in area, is relatively homogeneous, while the overall beam has a roughly 4.5 (H) x 4.5 (V) cm^2 square shape (taking into account the region with the neutron flux higher than 50% of the maximum intensity) as a consequence of the neutron guide positioned along the beamline. The beam centre appears to be displaced by ~ 2 mm (up and to the right when looking downstream, *i.e.* from the moderator towards the instrument) from the nominal primary flightpath. Such displacement (2 mm at a distance of 17010 mm) is smaller than before the guide upgrade [12], partly as a result of the instrument repositioning, by 2 mm towards right *i.e.* the beam flightpath is now better overlapped with the sample position. The beam shift may indicate a minor shutter misalignment or possible unwanted reflections. The evaluation of the beam spatial profile as a function of wavelength is shown in Figure S2 (see SI). It appears that the beam homogeneity is preserved across neutrons with various energies. In particular, the beam profile for neutrons with the wavelength between 0.8 Å and 1.2 Å and the beam profile for neutrons with the wavelength between 2.5 Å and 2.9 Å have very similar distribution, although the latter flux is one order of magnitude smaller.

The McStas simulation of the TOSCA beam profile at the sample position with the guide upgrade is depicted in Figure 3. The simulated beam has a 4.0 (H) x 4.0 (V) cm^2 (taking into

account the region with a neutron flux greater than 50% of the maximum intensity) Gaussian profile (due to the collimation). The flux is roughly constant across the 2.0 (H) x 2.0 (V) cm^2 surface as indicated by the horizontal cut, see Figure 4. Due to the symmetrical geometry of the square cross section guide, there are no privileged directions of reflections and, as a consequence, the results show a perfect spatial symmetry about the central position. As emphasized before, the simulated neutron flux is 2.53 times higher than the experimentally observed values. This is not surprising since the simulation was performed in vacuum while in reality, at the time of this experiment out of 17.01 m long flightpath between the moderator centre and the TOSCA sample position 14.1465 meters were under vacuum, while 1.3030 meters were in air, 1.5560 meters were in helium, and 0.0045 meters were in aluminium. Thus in order to compare with the experiment, the simulated values should be corrected by the factor of 0.8765 which corresponds to the transmitted neutron flux upon travel along the above described flightpath. The corrected simulated values are shown in Figure 4 as well. They are still 2.22 (2.53 x 0.8765) times larger than the experimental values, and the difference can be ascribed to various factors. Firstly, the muon producing target (located upstream of the TS-1 target) is not in the MCNPX model so the calculated flux should be corrected by a factor of 0.95. Secondly, the physics model choice for MCNPX simulations can affect the flux at the level of 10-15%. For example, if the CEM03 physics model (used in this set of simulations) is replaced by INCL4-ABLA model – the correction factor is 0.86. Thirdly, the building of TS-1 MCNPX model [20] is still a work in progress. Recent findings [21] showed that the TS-1 target cooling water is not pure heavy water (as defined in the model) but a mixture of 80% heavy water and 20% light water, and that the 6 mm thick boral plate is positioned between the target and the water moderator. As a result, the calculated flux should be corrected by an additional factor of 0.87. After applying all of these corrections, the agreement between experimental and calculated flux is well below a factor of 2. Having in mind that there are additional uncertainties about: the details of material composition of the decouplers around the TS-1 moderators, precise position of the poisoning foil, the (real) vertical position of the TOSCA shutter insert, and possible operational effects [22] etc., such agreement is very satisfactory.

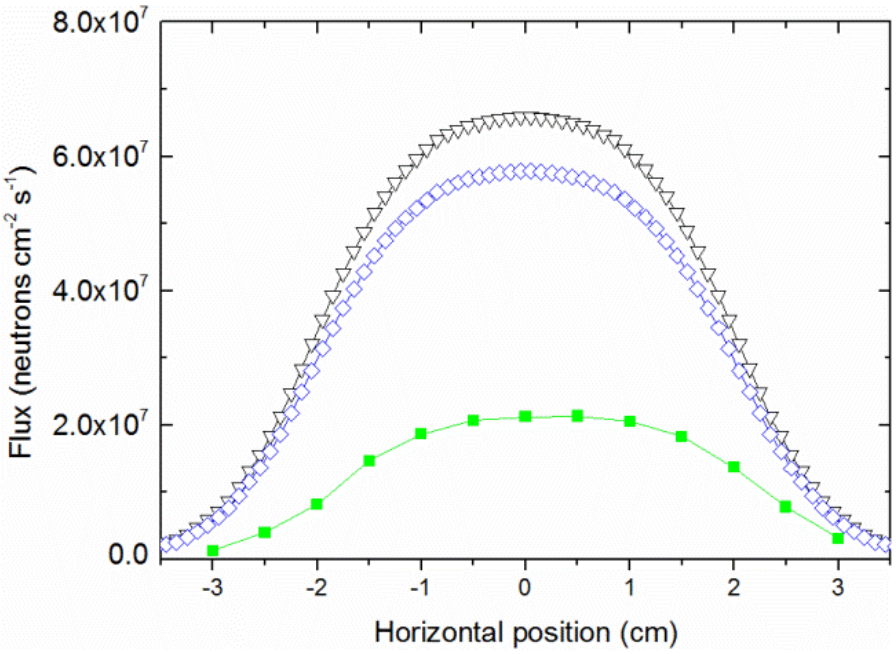

Figure 4. The experimental (green filled squares), the simulated (black empty triangles) and the corrected simulated (for attenuation in the helium, aluminium and air; blue empty diamond) neutron beam profile projected along the horizontal axis at the TOSCA sample position. The beam flux has been averaged along the vertical axis (between -2.0 cm and +2.0 cm, i.e. within the beam height) and includes only neutrons within the wavelength range of interest to TOSCA (from 0.28 Å to 4.65 Å).

As can be seen from Figure 3, the measured and the calculated neutron flux at the centre of the sample, the (0,0) position (see SI), are 2.54 x 10^7 neutron cm^{-2} s^{-1} and 7.32 x 10^7 neutron cm^{-2} s^{-1}, respectively. The corresponding values spatially averaged across 3.0 x 3.0 cm^2 and 4.0 x 4.0 cm^2 surface centred around (0,0) position are 2.11 x 10^7 neutron cm^{-2} s^{-1} and 5.35 x 10^7 neutron cm^{-2} s^{-1}, respectively. Between the latter two values a normalization factor of 2.53 must be applied to match the absolute values. The neutron flux values associated with the plateau shown in Figure 4, and averaged along the vertical axis (between -2.0 cm and +2.0 cm) are slightly smaller. In particular the simulated values were derived with the help of the linear flux monitor, not the position sensitive detector used in the case of the beam profile shown in Figure 3.

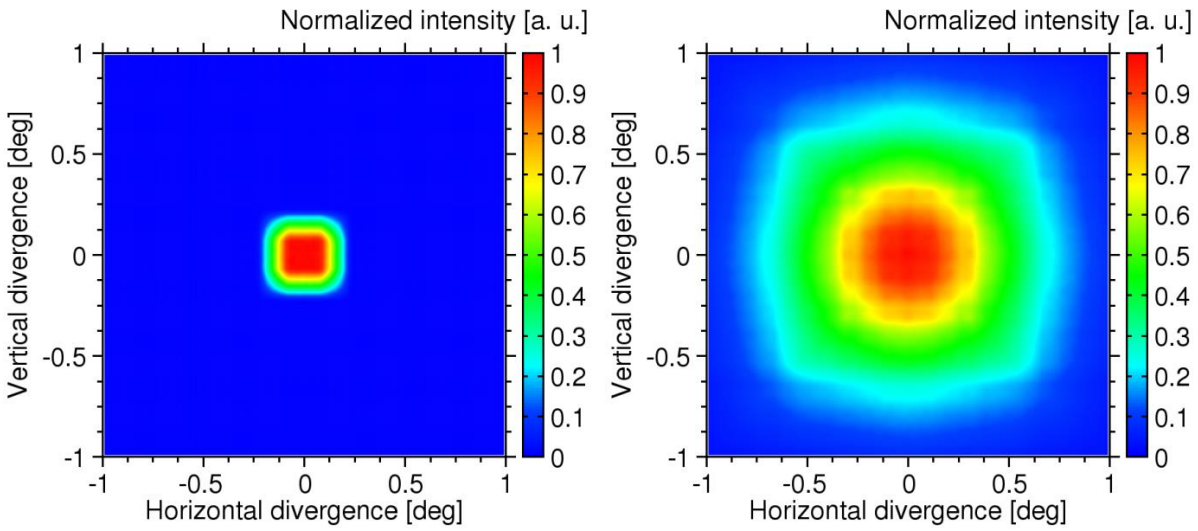

Figure 5. The TOSCA simulated divergence profile at the sample position before (left) and after (right) the guide upgrade.

Figure 5 shows the TOSCA simulated divergence profile at the sample position before and after the guide upgrade. In line with expectations, after the upgrade the neutrons arriving at the sample position have a larger divergence distribution: the full width at half maximum is approximately 1.3º, as opposed to 0.3º before the upgrade. As already described, the neutron guide is able to retain neutrons (with an incident angle < γ_c) within the guide tube, rather than acting only as a simple collimator and thus by the time they reach the sample surface they can cross it at an angle larger than allowed by the direct line of sight between the moderator and the sample.

As a result of the guide being installed on TOSCA the neutron flux at the sample position has been significantly increased, see Figure 6. The green trace shows the experimentally determined gain as a function of wavelength and the black trace corresponds to the gain derived from the Monte Carlo simulations. Since measurements of the neutron flux at the sample position for the final C2, and before the upgrade C0, configurations were performed with the proton energy on target of 800 MeV and 700 MeV, respectively, the former C2 neutron flux has been scaled down by a factor of 1.17 [see Figure S3 in SI] before taking the ratio to calculate the experimental gain due to the neutron guide. Additionally, as theoretical calculations were performed in vacuum, these values of the neutron flux gain need to be corrected for the attenuation as neutrons travel through helium, aluminium windows and air (blue trace) before they are compared with the experimental data. The gain in neutron flux is

6 times for neutrons with a wavelength of 0.5 Å (2640 cm^{-1}), 46 times for neutrons with a wavelength of 2.5 Å (105 cm^{-1}), and 82 times for neutrons with a wavelength of 4.6 Å (31 cm^{-1}), *i.e.* the most significant gain is for the neutrons used to study low energy molecular and lattice vibrations. The slight dip in the experimental neutron gain between 3.7 Å and 4.6 Å is a result of the different starting times (wavelengths) at which the double disc chopper started to block the slow neutrons (in order to prevent the 20 ms sub-frame overlap) at the time of C2 (3.7 Å) and C0 (4.25 Å) configurations measurements. Figure 7 shows the experimental (left) and simulated (right) gain in the neutron flux as a function of the position within the TOSCA sample area. Since after the upgrade the neutron beam is more divergent, and some neutrons can be detected at the position where there were none before, the gain appears larger around the periphery than in the centre of the sample position.

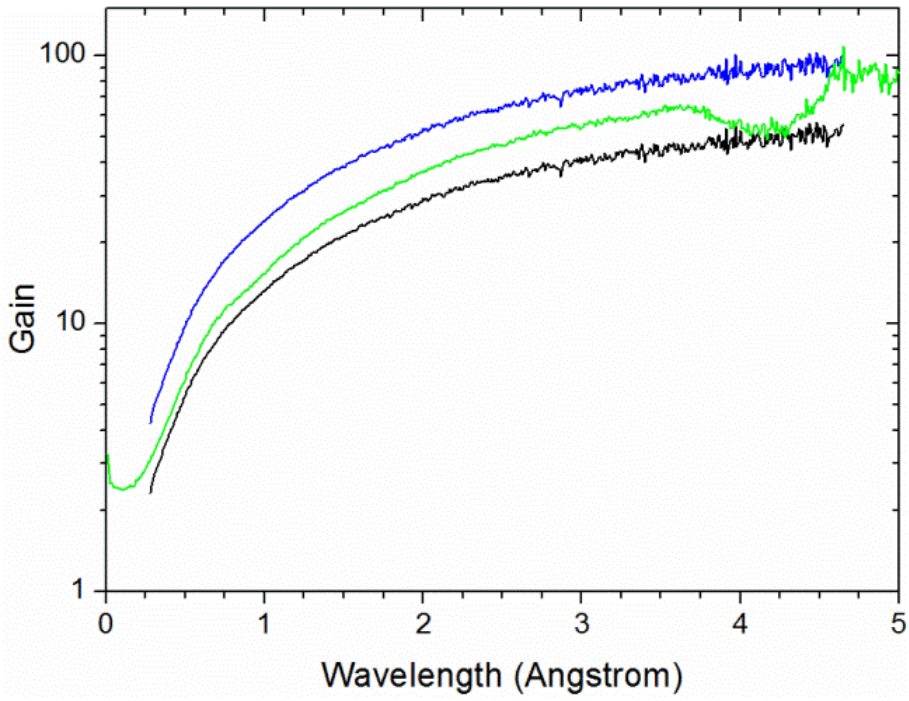

Figure 6. Gain in the neutron flux at the TOSCA sample position as a function of wavelength. Green trace shows experimental values derived with the bead detector, while black and blue traces show simulated values derived from the Monte Carlo calculations without, and with, the correction for attenuation in the helium, aluminium and air, respectively.

In order to understand the effect of possible shutter misalignment on the neutron beam properties, we have performed additional simulations in which the shutter was misaligned by 0.5º (to the left when looking downstream, *i.e.* from the moderator towards the instrument)

from the intended instrument flightpath and pivoted around the shutter entrance position at a distance of 1.626 m from the moderator. As a consequence, the wavelength-integrated neutron flux (from 0.28 Å to 4.65 Å) at the TOSCA sample position was reduced by 20 % (see Figure S5 in the SI). Furthermore, it appears (see Figures S5 and S6) that the misalignment does not significantly alter the beam profile, although the beam is slightly shifted (at the sample position) in the same direction (towards left) as the misalignment. Figure S8 shows the consequence of misalignment on the beam divergence at the sample position. This suggests that as a result of the misalignment patterns in the divergence profile can be observed without alternation of the overall average divergence.

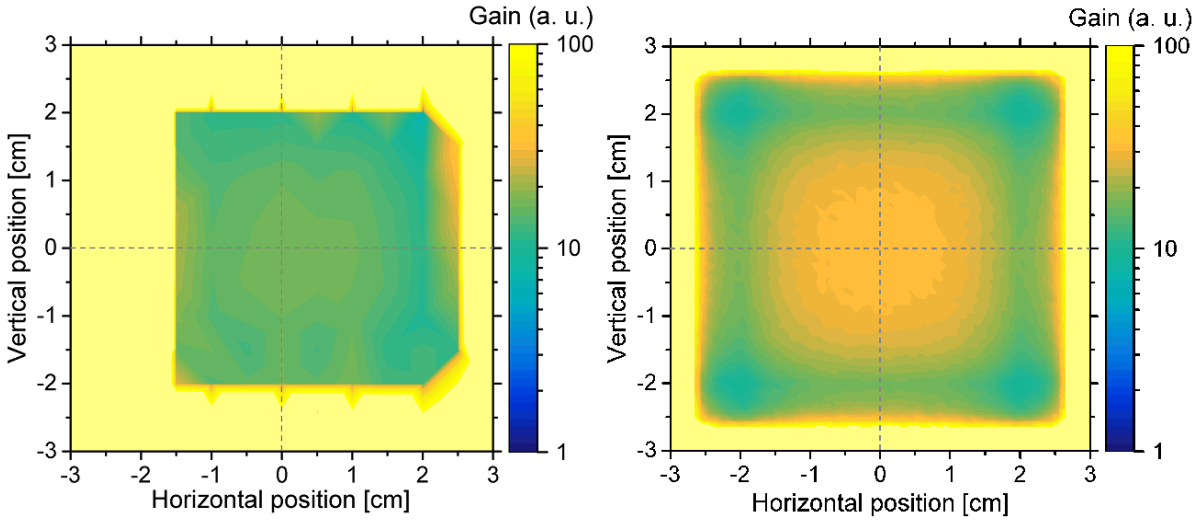

Figure 7. The experimental (left) and simulated (right) gain in the neutron flux as a function of position within the TOSCA sample area, for neutrons with the wavelength between 0.28 Å and 4.65 Å.

In comparison to the interim C1 configuration (which had a simple collimation tube within the shutter and an 84 mm x 84 mm entrance opening) the final C2 configuration (which has 1.937 meter long m = 5 neutron guide inside the shutter and an enlarged 100 mm x 100 mm shutter entrance) gives significantly enhanced neutron flux at the sample position; compare experimental values of the neutron flux in Figure 2 and Figure S9. For further information about the properties of the neutron beam at the TOSCA sample position in relation to C1 configuration please see SI.

Spectral resolution and background: While the increased neutron flux at the sample position has been achieved as part of this project, it was equally important to preserve the excellent spectral resolution and low background afforded by TOSCA [2]. In order to check the effect of the installed neutron guide on the instrument spectral performance we have performed neutron scattering measurements of the standard calibrant, 2,5-diiodothiophene [23]. Figure 8 shows the elastic line of the 2,5-diiodothiophene sample recorded before the TOSCA upgrade (black trace, C0 configuration) and after the upgrade (blue trace, C2 configuration). The same sample was used in both cases and the spectra were accumulated for the same period of time. The spectra suggest that the spectral resolution at the elastic line is essentially unchanged and below 2 cm^{-1}. Equally, examination of the inelastic neutron scattering spectra of the same compound before and after the upgrade, see Figure 9, highlights that the spectral background has remained low across the spectral range, *i.e.* it has been maintained at the pre-upgrade levels.

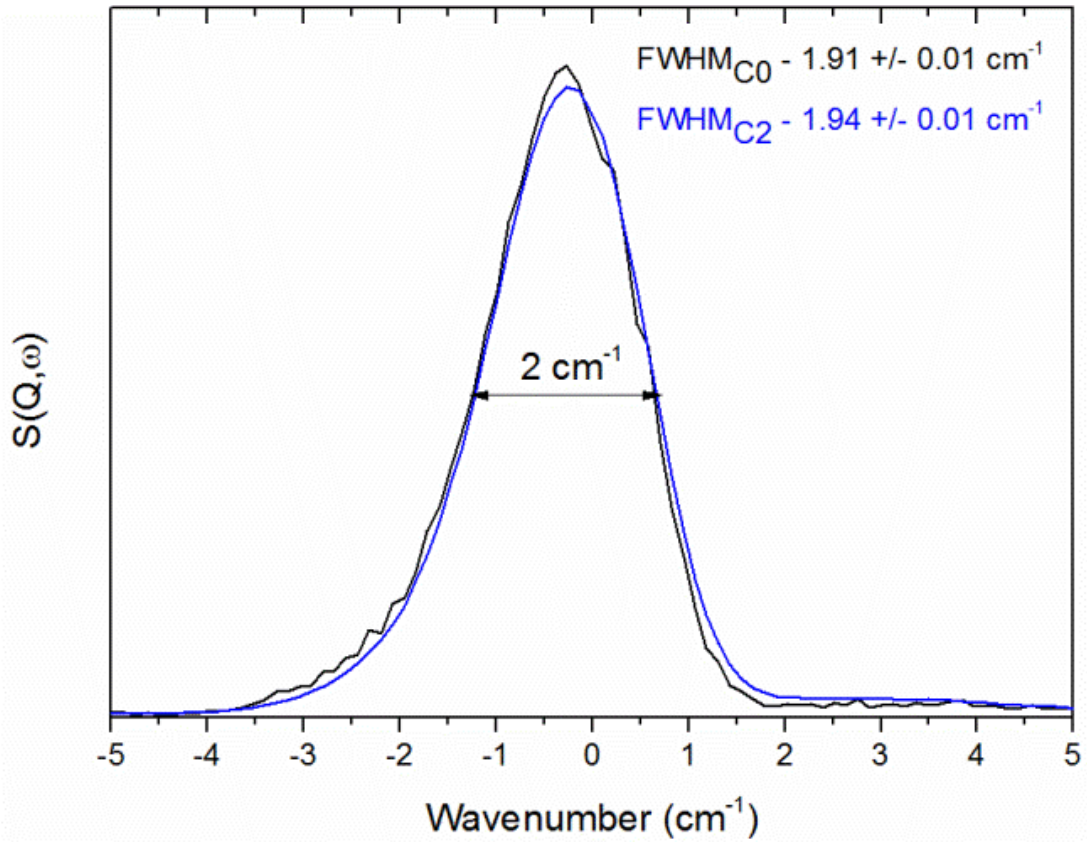

Figure 8. Elastic line of 2,5-diiodothiophene, recorded at 10 K, before the TOSCA upgrade (black trace, C0 configuration) and after the upgrade (blue trace, C2 configuration). Note that the spectral resolution is essentially unchanged at the elastic line.

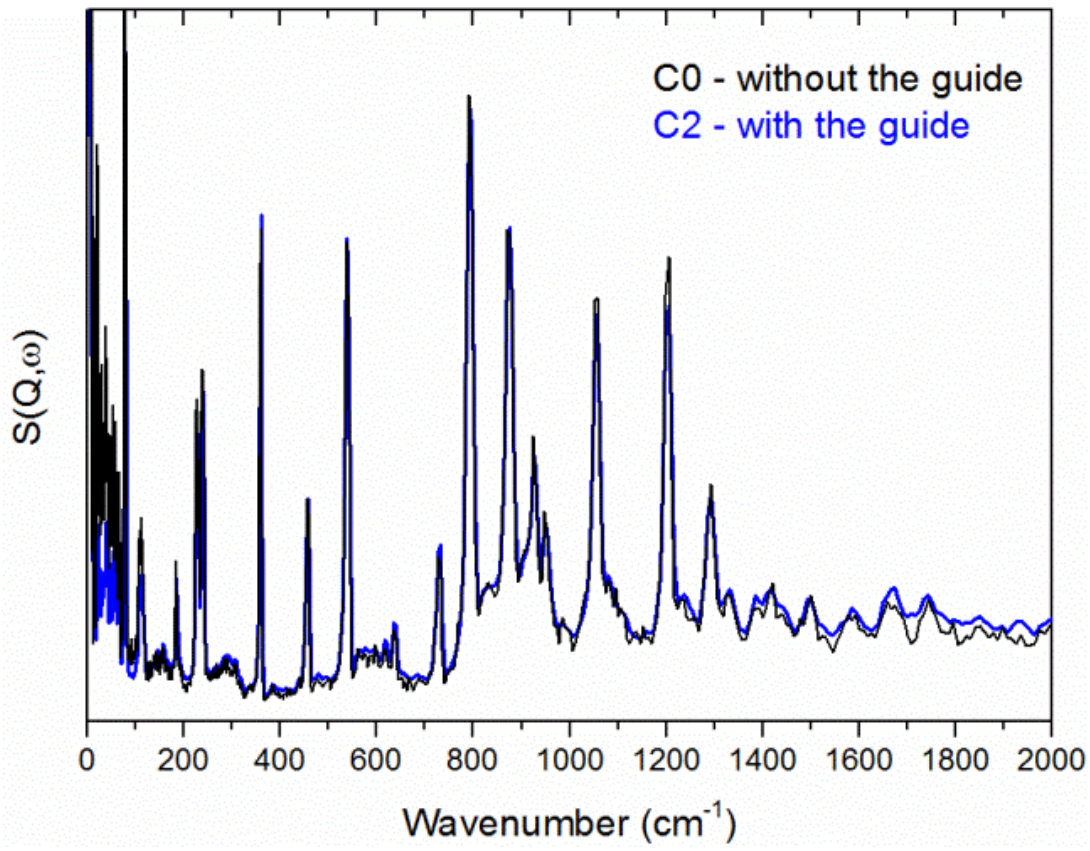

Figure 9. Inelastic neutron scattering spectra of 2,5-diiodothiophene, recorded at 10 K, before the TOSCA upgrade (black trace, C0 configuration) and after the upgrade (blue trace, C2 configuration). As one can see as a result of the TOSCA neutron upgrade the spectral background and resolution are maintained at the pre-upgrade levels.

5. Conclusions

As part of the TOSCA primary spectrometer upgrade the simple collimator tube between the moderator and the instrument has been replaced with a supermirror guide thus leading to an increased neutron flux at the sample position. In the low energy neutron region (e.g. for neutrons with a wavelength of 4.6 Å) the gain in neutron flux of as much as 82 times has been observed. The results evidenced that the incident beam on TOSCA is reasonably square and homogeneous across 2.5 (H) x 2.5 (V) cm^2 surface, although some beam patterns can be observed, and the illuminated area is approximately 4.5 (H) x 4.5 (V) cm^2. The time-averaged wavelength-integrated flux at the TOSCA sample centre, the (0,0) position, is around 2.54 x

10^7 neutron cm^{-2} s^{-1} and we measured the flux as 1.38 x 10^7 neutron cm^{-2} s^{-1} $Å^{-1}$ at the moderator peak (~1.1 Å) which represents the Maxwellian component of the incident spectrum. The measurements reveal that the neutron beam profile is ~27% larger (by area), and the neutron flux in the beam centre (spatially averaged across 3.0 x 3.0 cm^2 surface centred around (0,0) position) is 2.53 (2.22, after correction for attenuation in the air, helium and aluminium) times smaller than predicted by the Monte Carlo calculations. The improved neutron flux allows faster measurements where useful data of hydrogen rich samples can be obtained within minutes. The upgrade will allow experiments with samples of a smaller mass that are too expensive to generate in large quantities. As a result of the upgrade, we have already noticed that the user program on TOSCA is becoming even more popular, while the number of requested days per experiment on average appears to fall. It is worthwhile noting that TOSCA capabilities could be further enhanced *via* upgrade of its secondary spectrometer whereby currently installed flat analysers could be exchanged for curved analysers and their surface area enlarged. Such an upgrade could potentially increase the neutron flux reaching the detectors by an order of magnitude as recent simulations suggest [24].

Acknowledgements

The authors gratefully acknowledge the Science & Technology Facilities Council (STFC) for financial support for this project, access to the TOSCA beamline at ISIS and the use of the e-Science SCARF cluster at the Rutherford Appleton Laboratory. This work has been partially supported by the 2014-2020 CNR-STFC Agreement concerning collaboration in scientific research at the ISIS Facility.

References

1. ISIS Neutron and Muon Source, TOSCA neutron spectrometer, available at https://www.isis.stfc.ac.uk/Pages/tosca.aspx (accessed on the 23 of November 2017).
2. S.F. Parker, F. Fernandez-Alonso, A.J. Ramirez-Cuesta, J. Tomkinson, S. Rudic, R.S. Pinna, G. Gorini, Recent and future developments on TOSCA at ISIS, Journal of Physics: Conference Series, 554 (2014) 012003.
3. S.F. Parker, D. Lennon, P.W. Albers, Vibrational spectroscopy with neutrons: a review of new directions, Applied Spectroscopy, 65 (2011) 1325.

4. S. Rudic, A.J. Ramirez-Cuesta, S.F. Parker, F. Fernandez-Alonso, R.S. Pinna, G. Gorini, C.G. Salzmann, S.E. McLain, N.T. Skipper, TOSCA international beamline review, RAL Technical Reports RAL-TR-2013-015, STFC, 2013.
5. G.J. Kearley, V.K. Peterson (Editors) Neutron Applications in Materials for Energy, Springer International Publishing Switzerland, 2015.
6. P.C.H. Mitchell, S.F. Parker, A.J. Ramirez-Cuesta, J. Tomkinson, Vibrational spectroscopy with neutrons – with applications in chemistry, biology, materials science and catalysis, World Scientific Publishing Co. Pte. Ltd., Singapore, 2005.
7. J. Fernandez Castanon, Monte-Carlo simulations for the development of TOSCA's guide at ISIS, RAL Technical Reports RAL-TR-2013-002, STFC, 2013.
8. R.S. Pinna, Monte Carlo simulations of the TOSCA neutron spectrometer: assessment of current performance and future upgrades, MSc Thesis, University of Milano-Bicocca, 2014.
9. R.S. Pinna, S. Rudic, S.F. Parker, G. Gorini, F. Fernandez-Alonso, Monte Carlo simulations of the TOSCA spectrometer: assessment of current performance and future upgrades, EPJ Web of Conferences, 83 (2015) 03013.
10. ISIS Neutron Beam Monitor, Quantum Detectors Ltd., Harwell, Oxford, UK, available at http://quantumdetectors.com/neutrons (accessed on the 23 of November 2017).
11. 6-Lithium Glass - bespoke to your application, Scintacor, Cambridge, UK, available at https://scintacor.com/products/6-lithium-glass/ (accessed on the 23rd of November 2017).
12. R.S. Pinna, S. Rudic, M.J. Capstick, D.J. McPhail, D.E. Pooley, G.D. Howells, G. Gorini, F. Fernandez-Alonso, Detailed characterisation of the incident neutron beam on the TOSCA spectrometer, Nuclear Inst. and Methods in Physics Research, A 870 (2017) 79.
13. P. Willendrup, E. Farhi, K. Lefmann, McStas 1.7 - a new version of the flexible Monte Carlo neutron scattering package, Physica B, 350 (2004) e735-e737.
14. S. Ansell and D. Champion, The ISIS_moderator component, McStas simulation package, http://www.mcstas.org/download/components/contrib/ISIS_moderator.html (accessed on the 23rd of November 2017).
15. Mantid (2013): Manipulation and analysis toolkit for instrument data. Mantid Project. https://www.mantidproject.org/Main_Page (accessed on the 23 of November 2017).
16. O. Arnold, J.C. Bilheux, J.M. Borreguero, A. Buts, S.I. Campbell, L. Chapon, M. Doucet, N. Draper, R. Ferraz Leal, M.A. Gigg, V.E. Lynch, A. Markvardsen, D.J. Mikkelson, R.L. Mikkelson, R. Miller, K. Palmen, P. Parker, G. Passos, T.G. Perring, P.F. Peterson, S. Ren, M.A. Reuter, A.T. Savici, J.W. Taylor, R.J. Taylor, R. Tolchenov, W. Zhou, J. Zikovsky, Mantid - Data analysis and visualization package for neutron scattering and μ SR

experiments, Numerical Instruments and Methods in Physical Research A 764 (2014) 156 - 166.

17. E. Oram, An overview of the development of indirect inelastic data reduction and analysis in MANTID between July 2015-July 2016, RAL Technical Reports RAL-TR-2016-11, STFC, 2016.

18. L. McCann, Overview of developments in MANTID relating to indirect inelastic spectroscopy July 2016-July 2017, RAL Technical Reports RAL-TR-2017-12, STFC, 2017.

19. C.G. Windsor, Pulsed Neutron Scattering, Taylor & Francis Ltd, London, 1981.

20. G.P. Škoro and S. Ansell, Neutronics modelling for the ISIS TS-1 upgrade, Proceedings of the 21st Meeting of the International Collaboration on Advanced Neutron Sources ICANS XXI, Japan Atomic Energy Agency, 2016, pp141-147.

21. G.P. Škoro, S. Lilley, R.I. Bewley, Neutronics analysis of target, moderators and reflector design for the ISIS TS-1 project, Physica B, 2017 (submitted).

22. G. Škoro. R.I. Bewley, S. Lilley, R.A. Ewings, G. Romanelli, M. Gutmann, R.I. Smith, S. Rudić, S. Ansell, A tale of two foils: ISIS TS-1 water moderators, Journal of Physics: Conference Series, 2017 (accepted).

23. S.F. Parker, J.L. Parker, M. Jura, Structure and vibrational spectra of 2,5-diiodothiophene: a model for polythiophene, Journal of Physical Chemistry C, 121 (2017) 12636-12642.

24. R.S. Pinna, S. Rudic, M. Zanetti, D. Zacek, S.F. Parker, G. Gorini, F. Fernandez-Alonso, Monte Carlo simulations for the TOSCA secondary spectrometer upgrade, RAL Technical Reports RAL-TR-2017-013, STFC, 2017.

Supplementary Information

for

The neutron guide upgrade of the TOSCA spectrometer

Roberto S. Pinna,[1,2] Svemir Rudić,[1,*] Stewart F. Parker,[1] Jeff Armstrong,[1] Matteo Zanetti,[1,2] Goran Škoro,[1] Simon P. Waller,[1] Daniel Zacek,[1] Clive A. Smith,[1] Matthew J. Capstick,[1] David J. McPhail,[1] Daniel E. Pooley,[1] Gareth D. Howells,[1] Giuseppe Gorini,[2] and Felix Fernandez-Alonso[1,3]

1. ISIS Facility, STFC, Rutherford Appleton Laboratory, Chilton, Didcot OX11 0QX, UK.

2. CNISM, Universita' degli Studi di Milano-Bicocca, Piazza della Scienza 3, 20126 Milano, Italy.

3. Department of Physics and Astronomy, University College London, Gower Street, London WC1E 6BT, UK.

Submitted to Nuclear Instruments and Methods in Physics Research Section A: Accelerators, Spectrometers, Detectors and Associated Equipment, (November, 2017), NIMA-D-17-01199.

* Author for correspondence.

Contact information:

ISIS Facility

STFC Rutherford Appleton Laboratory

Chilton

Didcot OX11 0QX

UK

Tel: + 44 (0)1235 44 6130

Fax: + 44 (0)1235 44 5720

e-mail: svemir.rudic@stfc.ac.uk

Content

Final C2 configuration:

Table S1. Geometrical parameters of the TOSCA neutron guide, *i.e.* its supermirror sections. In addition to the starting position of each section in relation to the moderator surface, its length, the cross section parameters at the entrance and the exit as well as the *m*-factor are provided. The total length of the guide is 14.6360 m and includes 0.1963 m of air gaps (when the instrument is in operation) that exist in between the moderator and the shutter (0.0378 m), the shutter and the insert (0.0450 m), and the guide sections 5 and 6 (0.0500 m), and the guide sections 9 and 10 (0.0635 m).

Section	Start at (m)	Length (m)	Input width (m)	Input height (m)	Output width (m)	Output height (m)	Coating *m*-factor
G1	1.626	1.937	0.1000	0.1000	0.1000	0.1000	5
G2	3.669	2.370	0.1000	0.1000	0.0887	0.0887	5
G3	6.050	1.530	0.0887	0.0887	0.0814	0.0814	5
G4	7.581	1.447	0.0814	0.0814	0.0745	0.0745	5
G5	9.131	0.317	0.0740	0.0740	0.0725	0.0725	5
G6	9.514	0.506	0.0722	0.0722	0.0697	0.0697	5
G7	10.031	2.069	0.0697	0.0697	0.0598	0.0598	6
G8	12.101	1.960	0.0598	0.0598	0.0505	0.0505	6
G9	14.062	1.750	0.0505	0.0505	0.0421	0.0421	6
G10	15.930	0.332	0.0416	0.0416	0.0400	0.0400	7

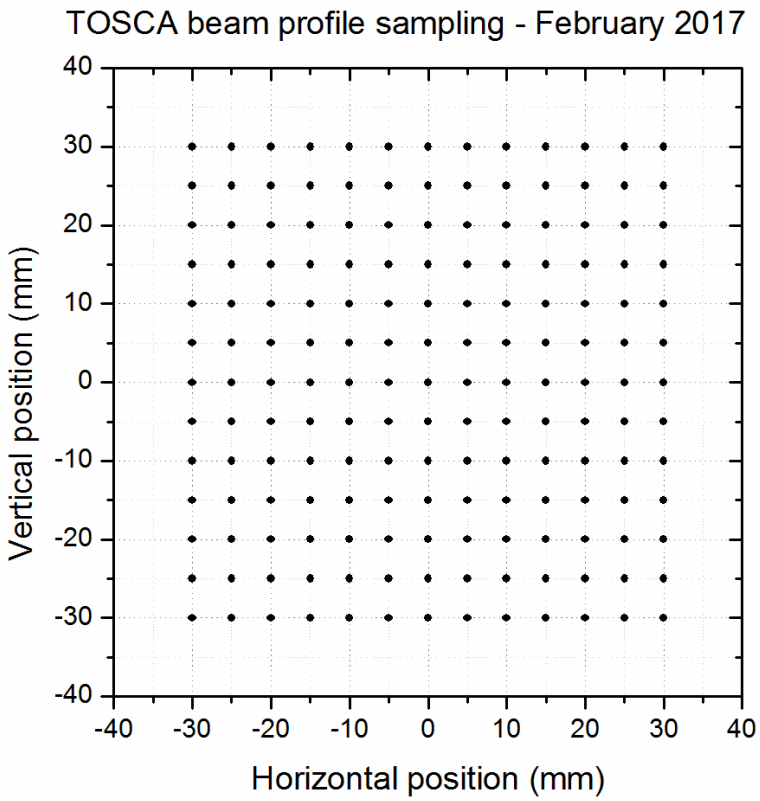

Figure S1. Map of the positions across the TOSCA sample surface (around the beam centre) where the neutron flux has been measured.

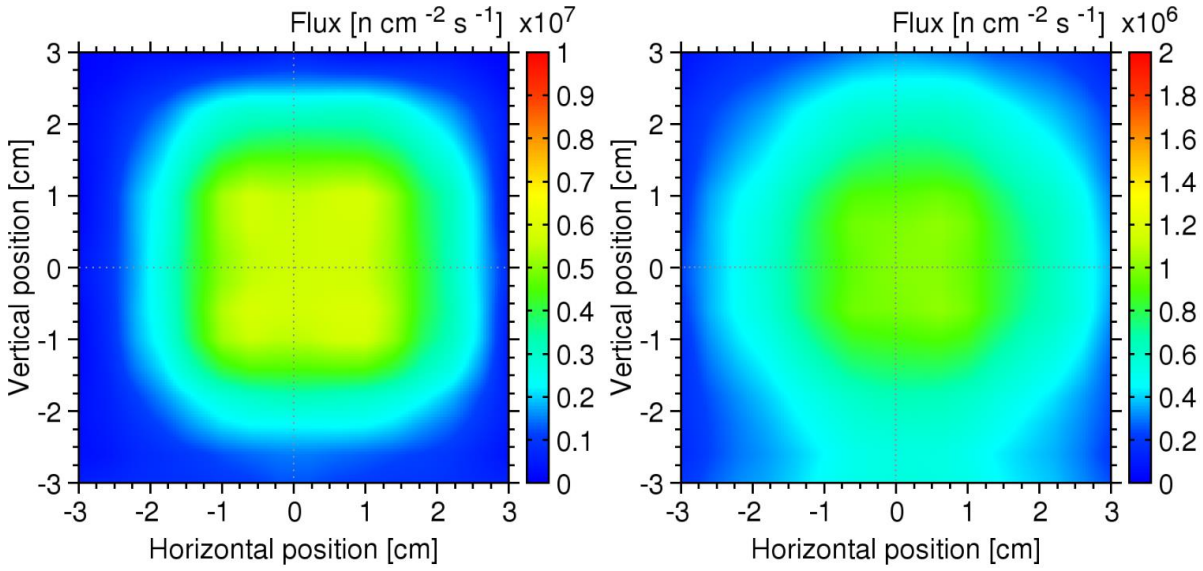

Figure S2. The experimentally derived neutron beam profiles at the TOSCA sample position after the upgrade for neutrons with wavelength between 0.8 Å and 1.2 Å (left) and 2.5 Å and 2.9 Å (right). The measured values of the time averaged neutron flux were obtained with the average proton current-on-target of 160 μA. Note that the intensity scales differ by an order of magnitude.

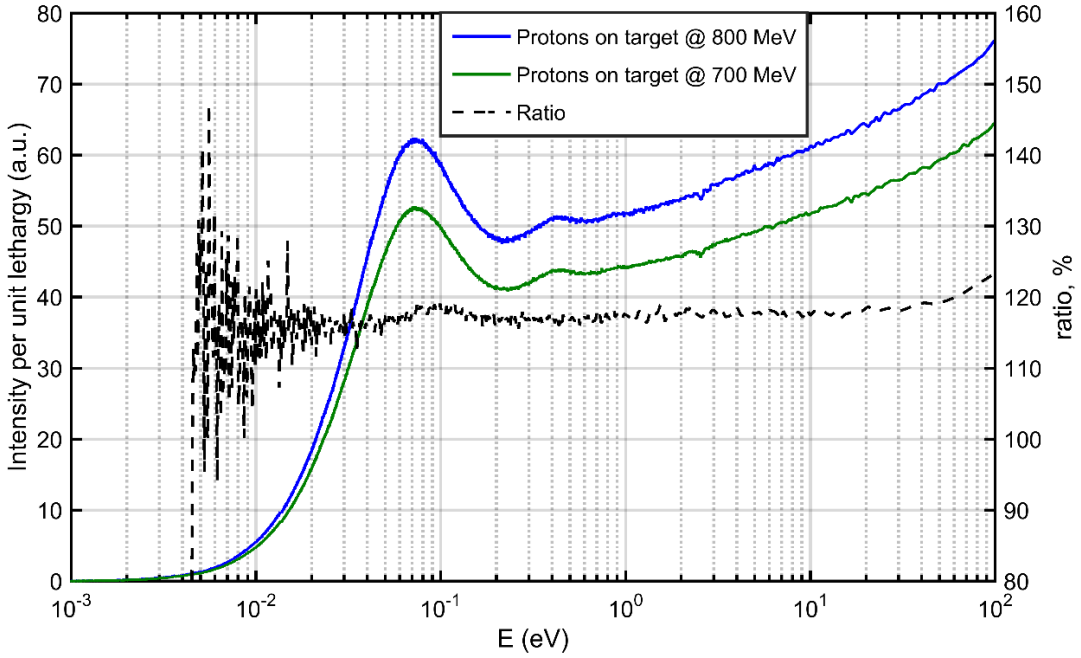

Figure S3. Effect of proton energy on the neutrons delivered to the sample. The intensity per unit lethargy, shown as a function of energy, as measured by the TOSCA beam monitor in the C0 configuration, is compared for the beam on target at 800 MeV and 700 MeV, blue and green curves, respectively. The ratio of the two curves (shown as dashed black curve), shows an average gain of 1.17 in favour of the 800 MeV case. Lethargy is defined as $ln(E_0/E)$, where E_0 is an arbitrary energy (International Commission on Radiation Units and Measurements (ICRU) 1969).

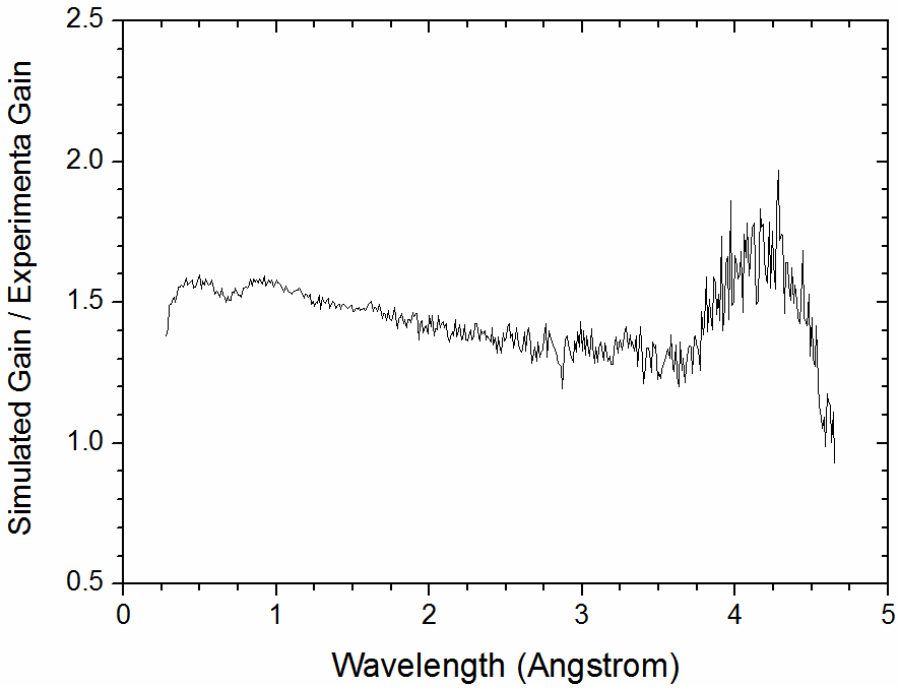

Figure S4. The ratio of the simulated (and corrected for attenuation in the helium, aluminium and air) and the experimental gain in the neutron flux at the TOSCA sample position as a function of neutron wavelength.

The ratio of the simulated (and corrected for attenuation in the helium, aluminium and air) and the experimental gain in the neutron flux at the TOSCA sample position as a function of the neutron wavelength is shown in Figure S2. The ratio is larger than one and decreases with increasing neutron wavelength.

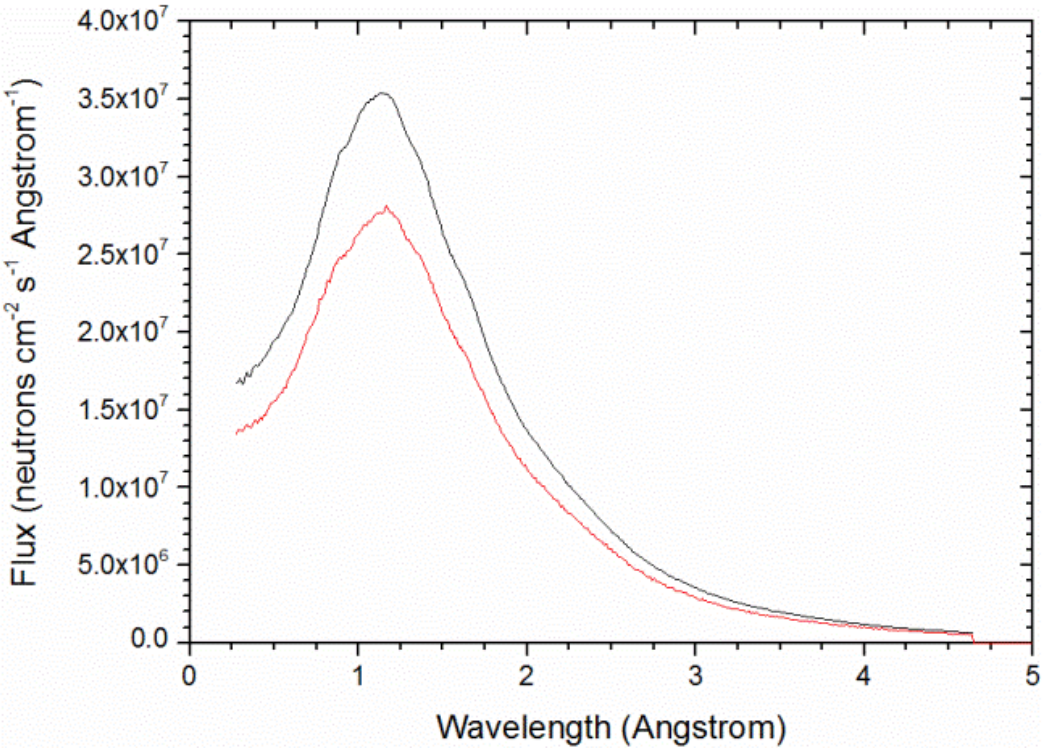

Figure S5. Monte Carlo simulations of the neutron flux at the TOSCA sample position (spatially averaged across the 4.0 x 4.0 cm^2 surface centred around (0,0) point) after the guide upgrade as a function of wavelength. Black trace corresponds to the simulation of the perfectly aligned guide, while the red trace shows the flux for a neutron guide in which the shutter (i.e. section G1 of the guide) is misaligned by 0.5 degrees (to the left when looking downstream, *i.e.* from the moderator towards the instrument) and pivoted around the shutter entrance position at a distance of 1.626 m from the moderator.

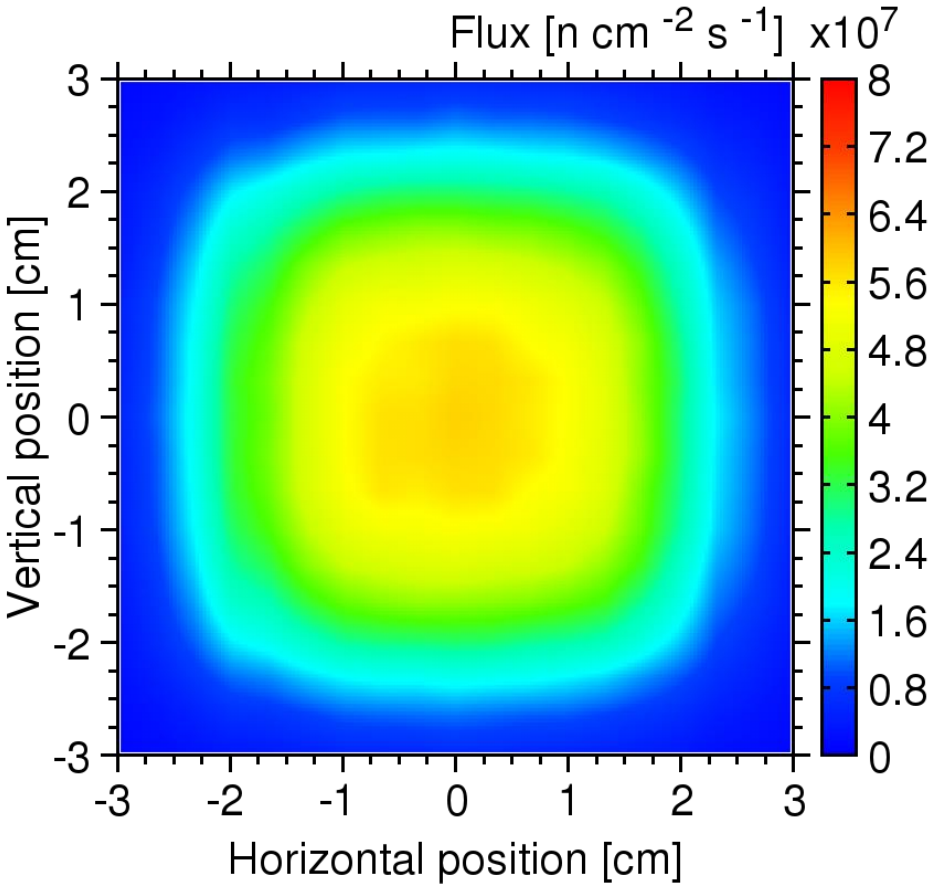

Figure S6. The simulated neutron beam profile at the TOSCA sample position after the guide upgrade and with the shutter (section G1 of the guide) misaligned by 0.5 degrees (to the left when looking downstream, *i.e.* from the moderator towards the instrument) and pivoted around the shutter entrance position at a distance of 1.626 m from the moderator. The calculated values of time averaged neutron flux, integrated across the 0.28 Å to 4.65 Å wavelength range of interest to TOSCA, were scaled to the average proton current-on-target of 160 μA.

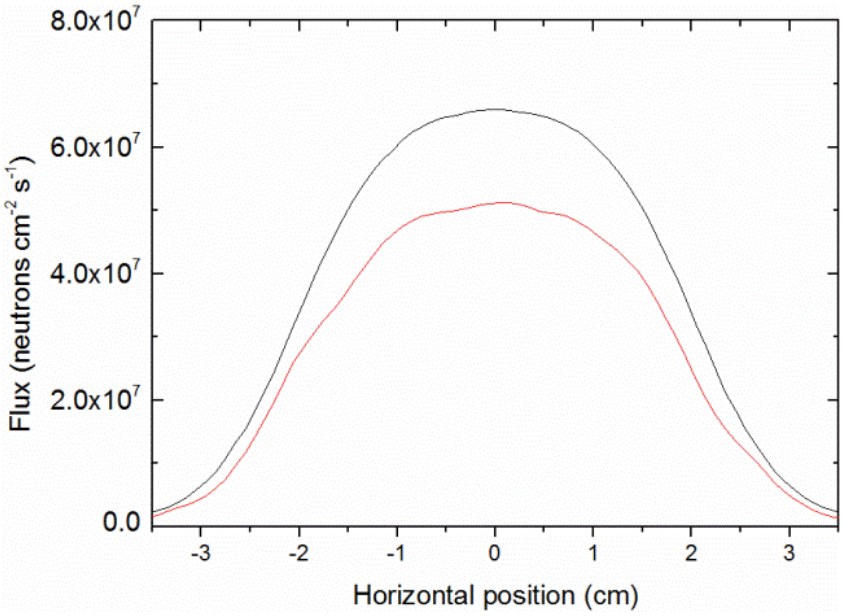

Figure S7. The simulated neutron beam profile projected along the horizontal axis at the TOSCA sample position. The beam flux has been averaged along the vertical axis (between -2.0 cm and +2.0 cm, i.e. within the beam height) and includes only neutrons within the wavelength range of interest to TOSCA (from 0.28 Å to 4.65 Å). Black trace corresponds to the simulation of the perfectly aligned guide, while the red trace shows the flux for a neutron guide in which the shutter (section G1 of the guide) is misaligned by 0.5 degrees (to the left when looking downstream, *i.e.* from the moderator towards the instrument) and pivoted around the shutter entrance position at a distance of 1.626 m from the moderator.

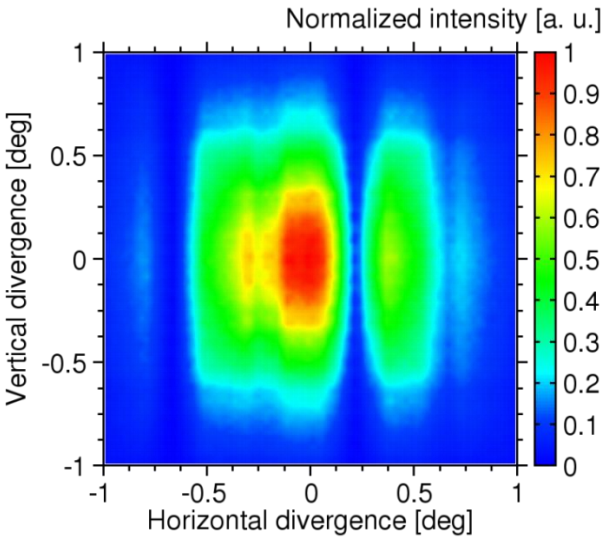

Figure S8. TOSCA simulated divergence profile at the sample position after the guide upgrade and with the shutter (section G1 of the guide) misaligned by 0.5 degrees (to the left when looking downstream, *i.e.* from the moderator towards the instrument) and pivoted around the shutter entrance position at a distance of 1.626 m from the moderator.

Interim C1 configuration:

The experimentally derived time-of-flight spectrum as a function of wavelength of the TOSCA neutron flux relating to the interim C1 configuration (spatially averaged across the 3.0 x 3.0 cm^2 surface centred around (0,0) position) is shown in Figure S9 (green trace). Its features are reproduced by the Monte Carlo simulations (blue empty diamond symbols) although the latter needed to be scaled down by a factor of 3.43 in order to make the simulated and the experimental integrated neutron flux in the region between 0.28 Å and 4.65 Å equal.

The TOSCA beam profile at the sample position is shown in Figure S10. Its central region, 3.0 x 3.25 cm^2 in area, is relatively homogeneous, while overall the beam has roughly a 4.5 (H) x 5.0 (V) cm^2 square shape (taking into account the region with a neutron flux greater than 50% of the maximum intensity). The beam centre appears to be displaced by ~ 2 mm (up and to the right when looking downstream, *i.e.* from the moderator towards the instrument) from the nominal primary flightpath. The evaluation of the beam spatial profile as a function of wavelength is shown in Figure S11. It appears that the beam homogeneity is preserved across neutrons with various energies, as the beam profiles for neutrons with the wavelength between 0.8 Å and 1.2 Å, and between 2.5 Å and 2.9 Å attest.

The McStas simulation of the TOSCA beam profile at the sample position corresponding to the interim C1 configuration is shown in Figure S10. The simulated beam has a 4.5 (H) x 4.5 (V) cm^2 (taking into account the region with a neutron flux greater than 50% of the maximum intensity) Gaussian profile (due to the collimation), while the flux is roughly constant across the 2.0 (H) x 2.0 (V) cm^2 surface as further indicated by the horizontal cut across the beam intensity, see Figure S12. As emphasized before, the simulated neutron flux is 3.43 times higher than the experimentally observed values. This is not surprising since the simulation was performed in vacuum while in reality, at the time of this experiment out of 17.01 m long flightpath between the moderator centre and the TOSCA sample position 12.1470 meters were under vacuum, while 3.3025 m were in air, 1.5560 m were in helium, and there were nine 0.5 mm thick aluminium windows. Thus in order to compare with the experiment, the simulated values should be corrected by a factor of 0.7742 which corresponds to the transmitted neutron flux upon travel between the moderator and the sample position. The

corrected simulated values are shown in Figure S12 as well. They are still 2.66 (3.43 x 0.7142) times larger than the experimental values.

As one can see from the Figure S10, the measured and the calculated neutron flux at the centre of the sample, the (0,0) position, are 1.01 x 10^7 neutron cm^{-2} s^{-1} and 3.77 x 10^7 neutron cm^{-2} s^{-1}, respectively. The corresponding values spatially averaged across 3.0 x 3.0 cm^2 and 4.0 x 4.0 cm^2 surface centred around the (0,0) position are 7.75 x 10^6 neutron cm^{-2} s^{-1} and 2.66 x 10^7 neutron cm^{-2} s^{-1}, respectively. Between the two later values a normalization factor of 3.43 must be applied to match the absolute values. The neutron flux values associated with the plateau shown in Figure S12, and averaged along the vertical axis (between -2.0 cm and +2.0 cm) are slightly smaller. In particular the simulated values were derived using the linear flux monitor.

Figure S13 shows the TOSCA simulated divergence profile at the sample position for the C1 configuration. In line with expectations, the neutrons arriving to the sample position have a larger divergence distribution, in which the full width at half maximum is approximately 1.2º, as opposed to 0.3º before the upgrade.

As a result of the C1 configuration of the neutron guide being installed on TOSCA, the neutron flux at the sample position was significantly increased, see Figure S14. The green trace shows the experimentally determined gain as a function of wavelength, while the black trace corresponds to the gain derived with the help of Monte Carlo simulations. Since theoretical calculations were performed in vacuum, these values of the neutron flux (gain) need to be corrected for attenuation as the neutrons travel through helium, aluminium windows and air (blue trace) before they are compared with the experimental data. The gain in neutron flux is 2.9 times for neutrons with wavelength of 0.5 Å, 18 times for neutrons with wavelength of 2.5 Å, and 29 times for neutrons with wavelength of 4.6 Å. Figure S15 shows experimental (left) and simulated (right) gain in the neutron flux as a function of the position within the TOSCA sample area. Since after the upgrade the neutron beam is somewhat larger and some neutrons can be detected at the position where there were none before, the gain appears larger around than in the centre of the sample position.

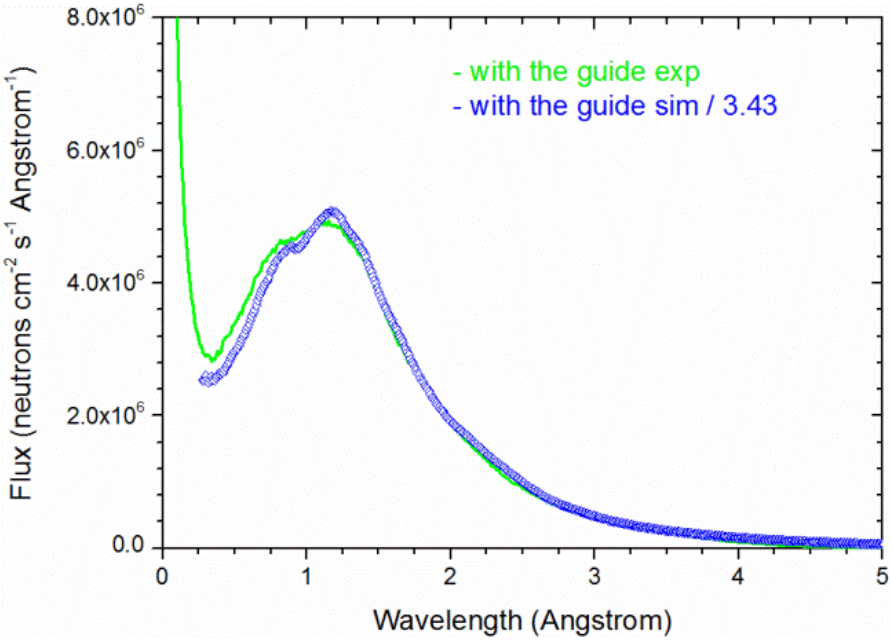

Figure S9. Neutron flux at the TOSCA sample position upon the guide upgrade (interim C1 configuration) as a function of wavelength. Experimentally derived values (spatially averaged across the 3.0 x 3.0 cm^2 surface centred around (0,0) position) are shown as green line while those obtained with the help of Monte Carlo simulations (spatially averaged across the 4.0 x 4.0 cm^2 surface centred around (0,0) position) are shown in blue as empty diamond symbols. Monte Carlo values of the neutron flux were scaled down by the factor of 3.43 in order to make the simulated and the experimental integrated neutron flux in the region between 0.28 Å and 4.65 Å equal.

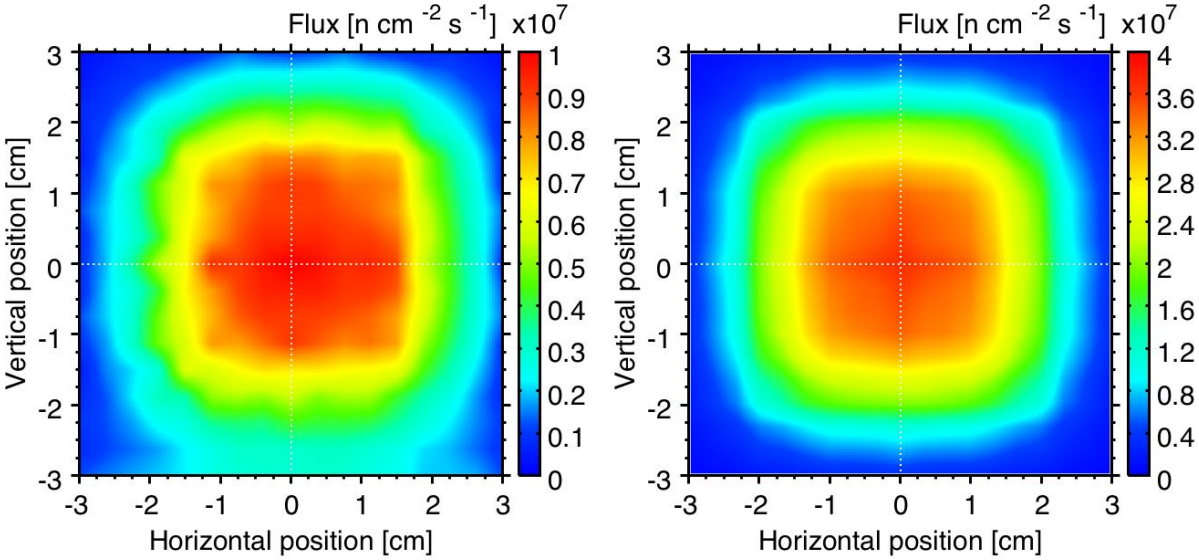

Figure S10. The experimentally derived (left) and simulated (right) neutron beam profile at the TOSCA sample position upon the guide upgrade (interim C1 configuration). The measured/calculated values of time averaged neutron flux, integrated across 0.28 Å to 4.65 Å wavelength range of interest to TOSCA, were obtained with / scaled to the average proton current-on-target of 160 μA.

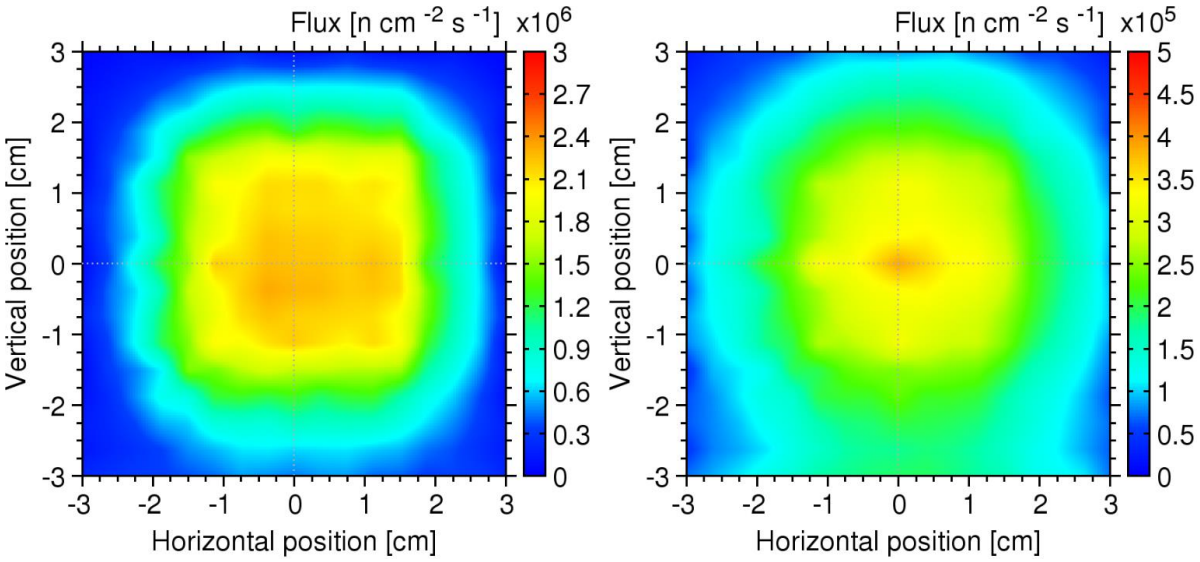

Figure S11. The experimentally derived neutron beam profiles at the TOSCA sample position upon the upgrade (interim C1 configuration) for neutrons with a wavelength between 0.8 Å and 1.2 Å (left) and 2.5 Å and 2.9 Å (right). The measured values of the time averaged neutron flux were obtained with the average proton current-on-target of 160 μA. Note that the intensity scales differ by an order of magnitude.

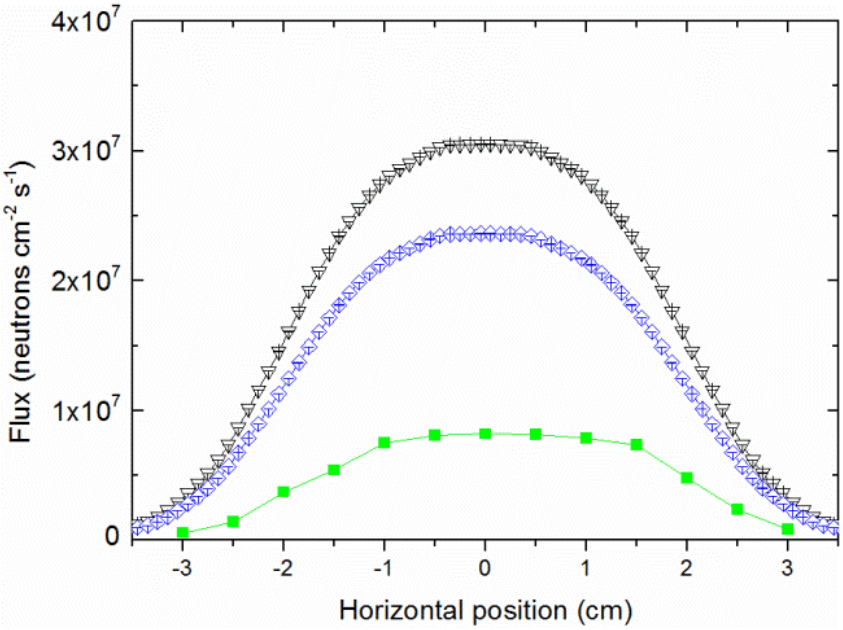

Figure S12. The experimental (green filled squares), the simulated (black empty triangles) and the corrected simulated (for attenuation in the helium, aluminium and air; blue empty diamonds) neutron beam profile projected along the horizontal axis at the TOSCA sample position upon the upgrade (interim C1 configuration). The beam flux has been averaged along the vertical axis (between -2.0 cm and +2.0 cm, *i.e.* within the beam height) and includes only neutrons within the wavelength range of interest to TOSCA (0.28 Å to 4.65 Å).

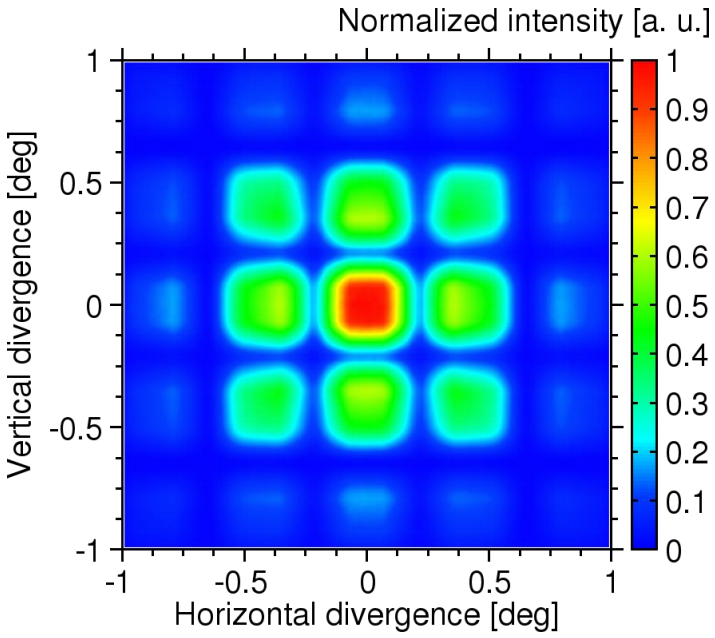

Figure S13. The TOSCA simulated divergence profile at the sample position after the guide upgrade (interim C1 configuration).

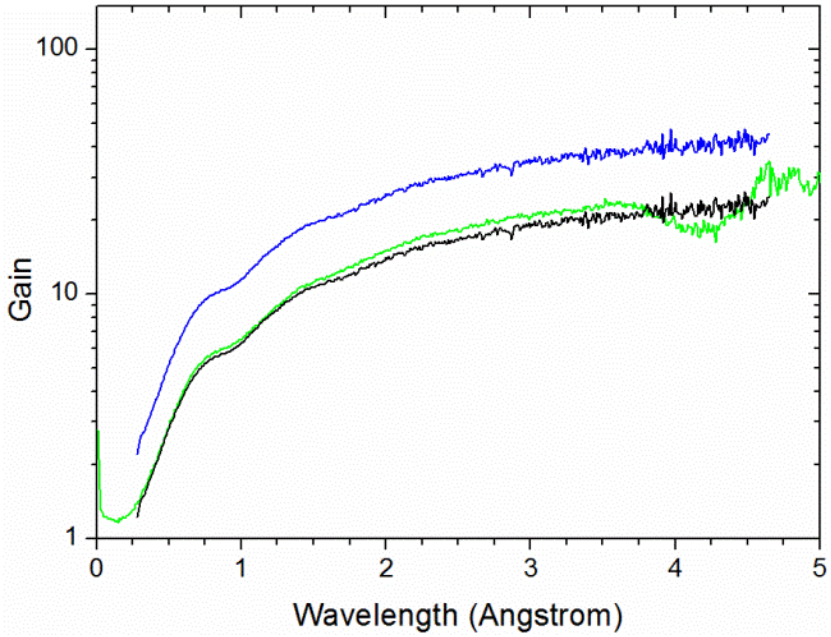

Figure S14. Gain in the neutron flux at the TOSCA sample position as a function of wavelength. Green trace shows experimental values derived using the bead detector, while black and blue traces show simulated values derived from the Monte Carlo calculations without, and with, the correction for attenuation in the helium, aluminium and air, respectively. As a result of the TOSCA neutron guide upgrade (interim C1 configuration) the gain in neutron flux is 2.9 times for neutrons with wavelength of 0.5 Å, 18 times for neutrons with wavelength of 2.5 Å, and 29 times for neutrons with wavelength of 4.6 Å.

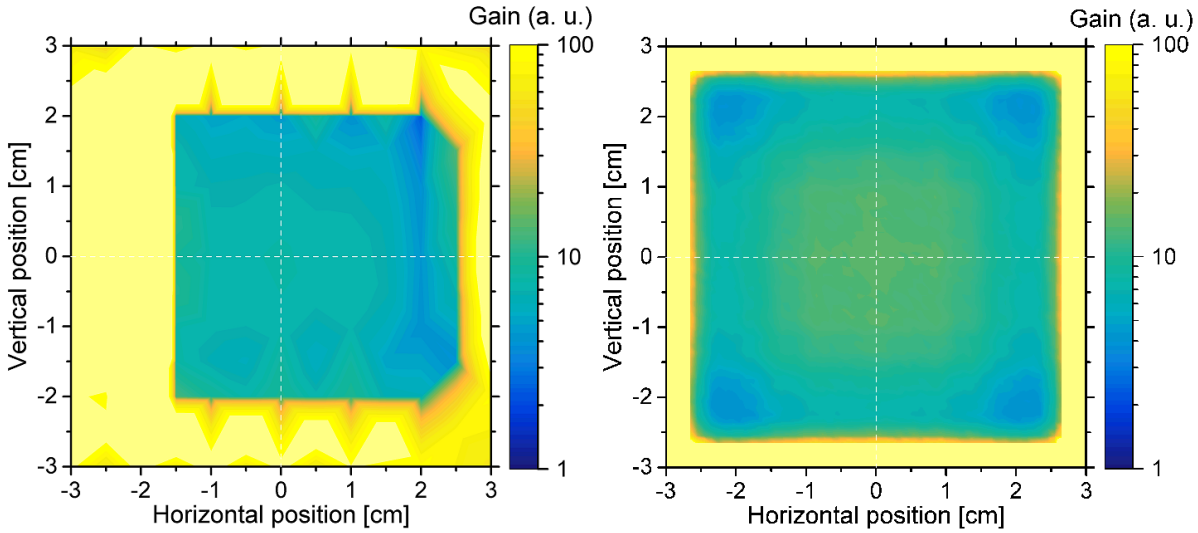

Figure S15. The experimental (left) and simulated (right) gain in the neutron flux as a function of position within the TOSCA sample area upon the guide upgrade (interim C1 configuration).

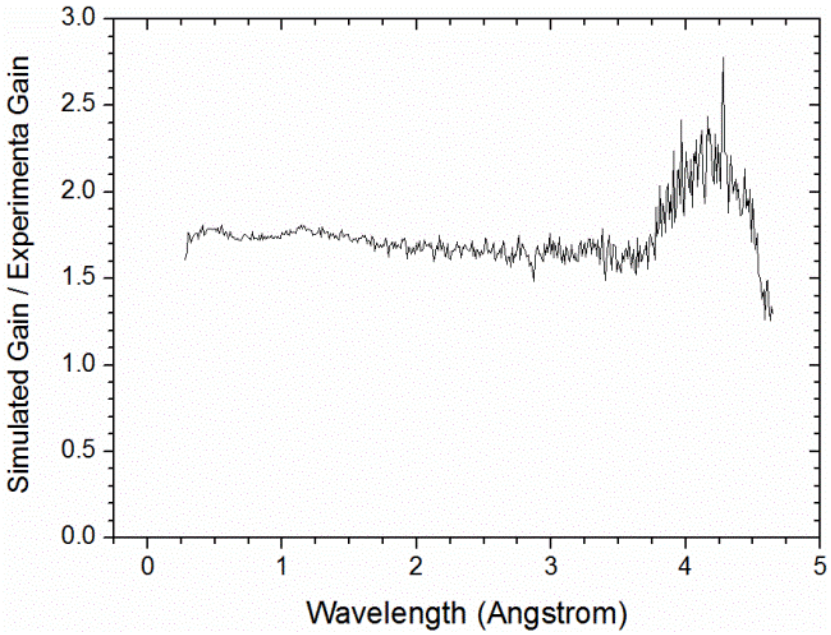

Figure S16. The ratio of the simulated (and corrected for attenuation in the helium, aluminium and air) and the experimental gain in the neutron flux at the TOSCA sample position as a function of neutron wavelength, after the guide upgrade (interim C1 configuration).

Paper V

Science & Technology Facilities Council

Technical Report
RAL-TR-2017-013

Monte Carlo Simulations for the TOSCA Secondary Spectrometer Upgrade

RS Pinna, S Rudic, M Zanetti, D Zacek, SF Parker, G Gorini, F Fernandez-Alonso

November 2017

Enquiries concerning this report should be addressed to:

RAL Library
STFC Rutherford Appleton Laboratory
Harwell Oxford
Didcot
OX11 0QX

Tel: +44(0)1235 445384
Fax: +44(0)1235 446403
email: libraryral@stfc.ac.uk

Science and Technology Facilities Council reports are available online at: http://epubs.stfc.ac.uk

ISSN 1358-6254

Monte Carlo Simulations for the TOSCA Secondary Spectrometer Upgrade

Roberto S. Pinna[1,2], Svemir Rudic[1], Matteo Zanetti[1,2], Daniel Zacek[1], Stewart F. Parker[1], Giuseppe Gorini[2], Felix Fernandez-Alonso[1,3]

1. ISIS Neutron and Muon Source, STFC, Rutherford Appleton Laboratory, Chilton, UK
2. Università degli Studi di Milano-Bicocca, Milano, Italy
3. Department of Physics and Astronomy, University College London, London, UK

November 2017

Contents

Abstract

For TOSCA to move forward beyond the current state-of-the-art in key scientific areas such as gas and charge storage, the most urgent need is for greater sensitivity via the secondary spectrometer upgrade that would make TOSCA competitive with other similar instruments, such as VISION at the SNS, in terms of total count rate. The here proposed upgrades can improve the collection efficiency of the neutrons scattered from the sample and the effects in terms of resolution have to be evaluated alongside. This document is focused on the design of a TOSCA doubly bent analyzer by means of McStas suite, which currently does not implement a component that can simulate a curved monochromator along multiple axes. Therefore, to proceed with the simulation of the secondary spectrometer, we had to create a custom component which can meet the TOSCA needs. We used several Highly Oriented Pyrolytic Graphite (HOPG) tiles arranged on a parametric surface up to an area of 1450 cm^2 that can have two different curvatures, spherical and parabolic. Several simulations have been performed with this component to study the performance of the current and future TOSCA setup at the elastic line. Graphite analyzers with different areas and radii of curvature have been considered and each parameter has been optimized *via* computational analysis. From the simulations, we found that with the appropriate focusing, it is possible to increase the current analyzer area by tenfold reaching a flux gain of ~ 7. It is also evident that for larger analyzers the parabolic geometry outperforms the spherical one thanks to its better focusing properties. The calculations also show that this gain is achieved with limited effects on resolution, provided that an extensive optimization is performed on the parameters of curved geometry. The geometric optimization in this study has been computationally implemented using MATLAB routines in conjunction with McStas.

Acknowledgements

The authors gratefully acknowledge the UK Science & Technology Facilities Council for financial support, access to beam time at ISIS, and use of the e-Science SCARF cluster at the Rutherford Appleton Laboratory. This work has been partially supported within the framework of past and present CNR-STFC agreements for collaborative research between Italy and ISIS. We also thank all the members of the Molecular Spectroscopy group for the scientific support and the ISIS Engineering group that offered technical information and consultancy.

1. Introduction

1.1. Current inelastic neutron scattering module on TOSCA

The flat highly oriented pyrolytic graphite (HOPG) crystal, currently used as analyzer on TOSCA has a trapezoidal shape with dimensions as shown in Fig. 1.1 and an area of 144 cm^2. In the McStas [1] simulations we implemented a square 12 x 12 cm^2 analyzer to approximate this shape and to be on the conservative side of the gain calculations. The crystal has a rocking angle FWHM of $\eta = 2.5°$ (150 arcmin) in both vertical and horizontal directions that defines its mosaicity. The centre of the analyzer surface is placed at a 45° grazing angle and at an average distance of 311 mm with respect to the sample [2]. More details of the geometry can be found in Appendix A and a discussion of the principles of the inverted geometry inelastic neutron scattering (INS) technique is presented in Appendix B.

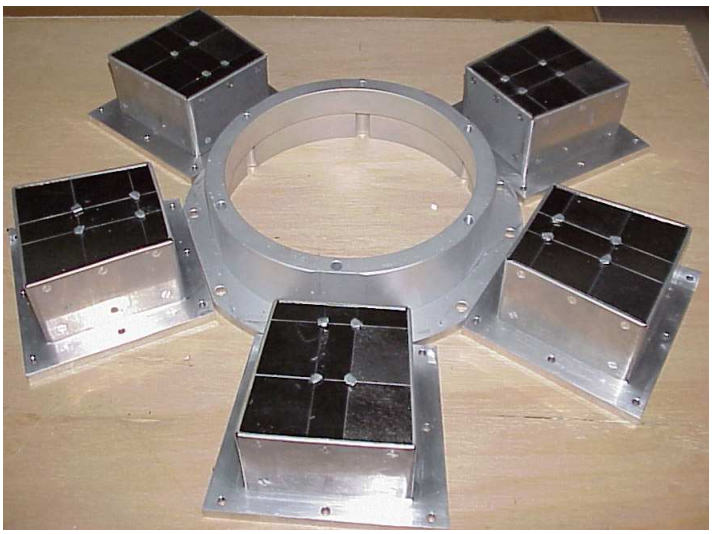

Figure 1.1. – Picture of the current TOSCA graphite analyzers. Courtesy of ISIS engineering group.

The current TOSCA spectrometer [3] is divided in ten identical banks equipped with the analyzer working together with a beryllium filter and cadmium foils, that remove the higher wavelength harmonics diffracted by the analyzer and reflected towards

the detectors. Furthermore, to increase the transmission of useful neutrons, each beryllium filter is cooled down to 30 K by a cooling head placed on one side of the housing. Currently the analyzer and the filter are very close together, and although this partially explains the original choice for a small analyzer this feature strongly limits the neutron collection efficiency of the assembly as a whole. Additionally, the analyzer is placed on an aluminium support which brings it further towards the Be filter and as a result there is not much space to improve the analyzer in the current setup, see Fig. 1.2. Nevertheless some modifications on the structure can be implemented in order to relax the geometry constraints.

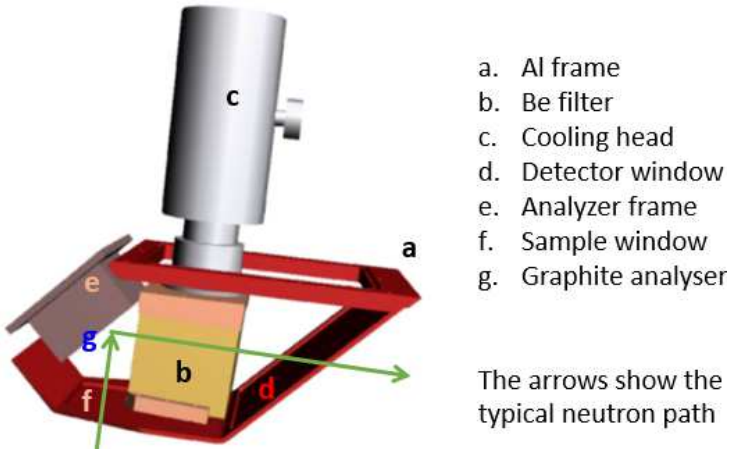

Figure 1.2. – 3D model of the TOSCA inelastic scattering module.

1.2. Time focusing

All the detected neutrons travel the secondary branch of the spectrometer ($L_1 \sim 620$ mm) in the same amount of time, thanks to the peculiar geometric arrangement of sample, analyzer and detector array, as shown in Fig. 1.3, where the sample and the detectors share the same plane and the analyzer lies along a plane parallel to it [4]. This implies that faster neutrons are reflected at lower Bragg angles θ_A and travel longer paths while slower neutrons are reflected with higher θ_A and thus follow shorter travel paths. This feature, at first order cancels out the time differences between the detected neutrons [2]. In fact with this arrangement we have that the travel time t_1 along the secondary branch L_1 is independent from the scattering angle, see Eq. 1.3. The time t_1 depends only on the distance between the assembly planes d_a, the neutron mass m_n, the lattice spacing of the analyzer d_{002} and the Planck constant h.

$$L_1 = \frac{2d_a}{sin\theta_A} \tag{1.1}$$

$$v_1 = \frac{h}{2m_n d_{002} sin\theta_A} \tag{1.2}$$

$$t_1 = \frac{L_1}{v_1} = \frac{4 d_a m_n d_{002}}{h} \tag{1.3}$$

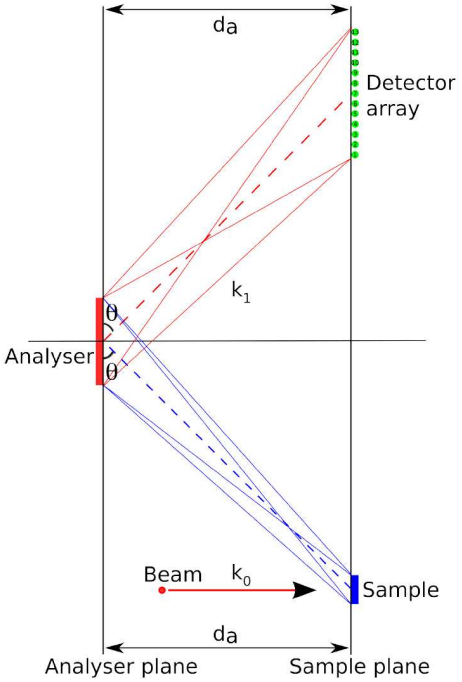

Figure 1.3. – Schematic drawing of the arrangement of the current TOSCA secondary spectrometer components.

1.3. Energy focusing

The same arrangement of the assembly, as in Fig. 1.3, performs the energy focusing, which further improves the resolution of the instrument [5]. Thanks to the fixed scattering angle θ_A of the neutrons emitted from the sample and impinging on the analyzer, the Bragg diffraction of neutrons with a chosen energy occurs at the same fixed angle towards the detector array. This allows to define a focal point for each selected energy that would be an infinitely thin peak in the case of a crystal with a zero mosaicity. Nevertheless, thanks to the mosaic spread of the HOPG lattice planes, neutrons of the same energy impinging on different points along the analyzer surface are diffracted and focused onto the same focal point [6] that corresponds to a defined detector tube in our case, see Fig. 1.4. Thus each tube is associated with a characteristic energy, which varies as a function of the detector position along the array. This energy value has to be taken into account during the data reduction to calibrate each single detector [7]. The values associated with the energy calibration have been calculated during this work by means of McStas simulations and can be found in Appendix C.

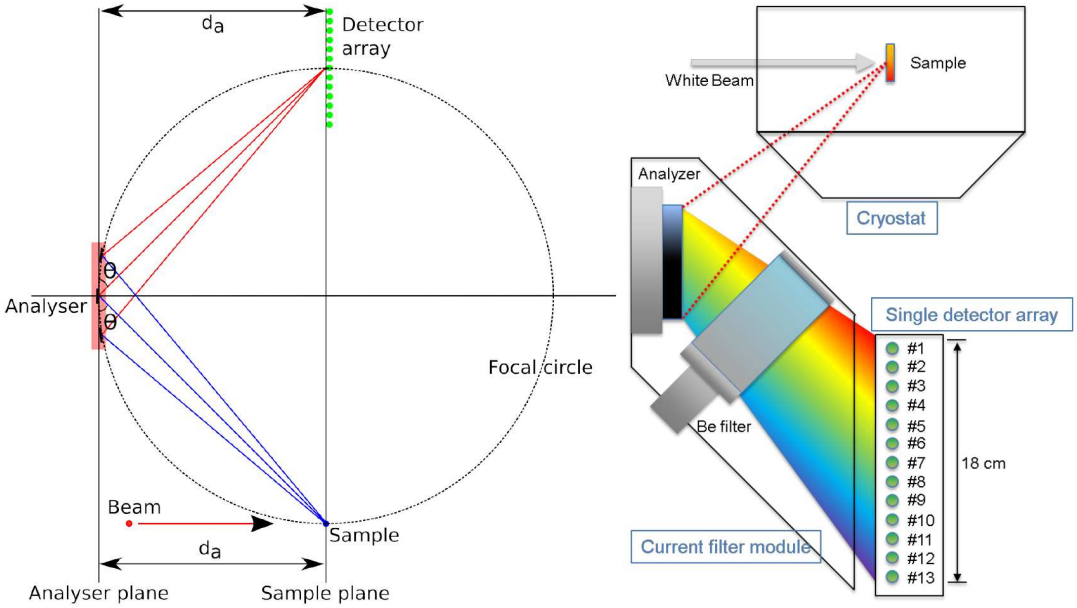

Figure 1.4. – (left) Energy focusing principle in the current TOSCA setup. (right) Chromatic spread of the analyzer along the detector array.

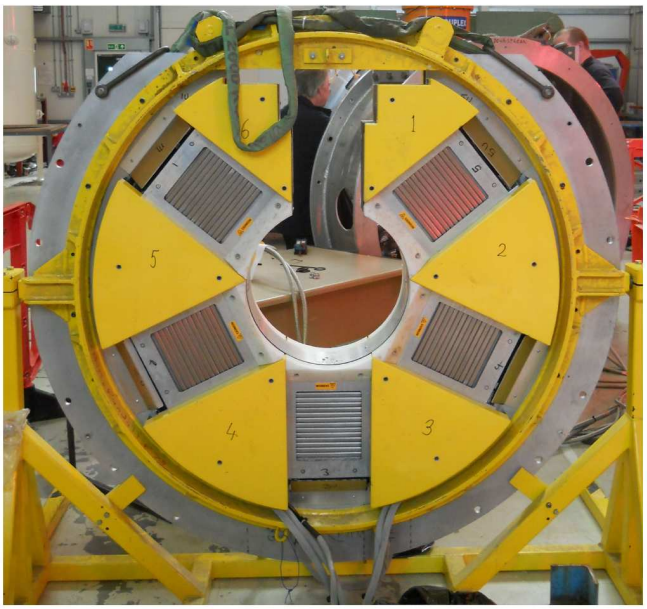

Figure 1.5. – TOSCA secondary spectrometer back-scattering detector banks. The detector arrays are arranged radially in the same plane, and the sample is placed at the center of the plane.

2. McStas doubly bent analyzer component

McStas simulation suite currently lacks any implementation of a monochromator whose points lie on a custom defined surface. For this reason, we built a new McStas analyzer component using several flat tiles with size of 10 x 20 mm^2 (WxH) that can be arranged along an analytical surface. This accomplished our need for a doubly bent analyzer capable of focusing the beam along the horizontal and vertical direction. The material of the analyzer is highly oriented pyrolytic graphite, which corresponds to the material currently used on TOSCA with a mosaic spread (full width half maximum) of $\eta = 2.5°$, while the chosen reflection plane is the (002) that has a lattice spacing of $d_{002} = 3.354$ Å. This material is considered suitable for the monochromation and reflection of sub-thermal neutrons thanks to its high reflectivity and sharp diffraction peaks. In fact at the wavelengths of interest the reflectivity for a 1 mm thick HOPG crystal can exceed 74% and a bent HOPG can find a number of important applications for $\lambda < 4.5$ Å [8]. The total reflection area of the curved analyzer will eventually be limited by engineering constraints and within the current TOSCA frame it can approximately range from 144 cm^2 to 1450 cm^2. As a specimen in the calculations we used a vanadium plate with the following dimensions 40 x 40 x 2 mm^3, which scatters mostly incoherently and isotropically, i.e. it does not select specific wavelength in different directions. We are mainly interested in the incoherent elastic peak from this sample after it has been energy scanned by the HOPG analyzer, as performed by Scherm [9]. This monochromator component is designed to resemble a parametric surface with two separate curvature functions along the horizontal and the vertical axis. The curvatures we choose to analyze are parabolic, as studied by Dolbnya [10] for x-ray beams, or spherical [8] and in this chapter we present how the two different geometries have performed. TOSCA secondary geometry also has the advantage of keeping the distance from the sample to the analyzer and from the analyzer to the detector array as equal as technically possible, in order to accomplish the Rowland focusing condition [11]. As a starting point we completed the simulations for the back-scattering bank 3 (hereafter B3), see Fig. 2.1. In this case the centre of the analyzer is placed at the coordinates (0 m, -0.2214 m, 16.78 m) relative to the moderator centre, which is the origin of our primary coordinate system. In this system of reference, the X axis is horizontal and the Y axis is vertical, and both are perpendicular to the beam while the Z axis is parallel to the beam. According to this model, a flat monochromator would lie on the plane P_{back}, described by the equation z = 16.78 m.

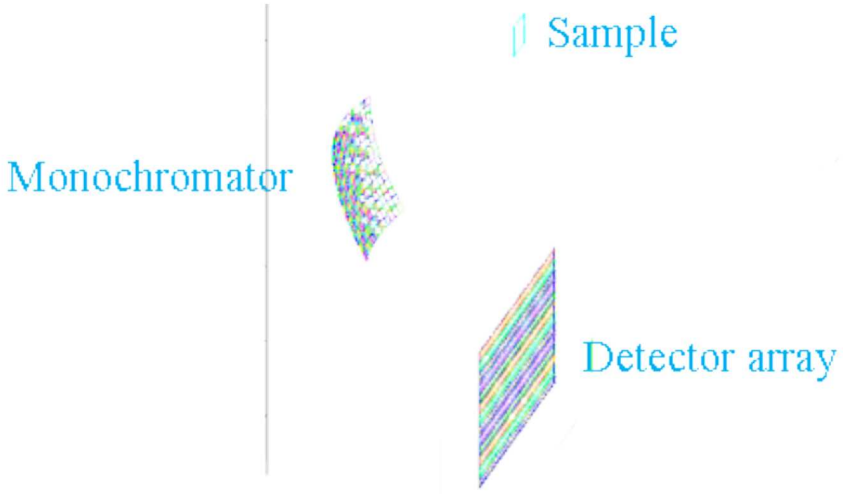

Figure 2.1. – 3D model of the McStas geometry implemented for the TOSCA secondary upgrade simulation. View of the back-scattering detector bank 3.

2.1. Parabolic curvature

The analytical function of the parabolic curvature is represented by Eq. 2.1.

$$z = \left(RH^{-1}\right) \cdot x^2 + \left(RV^{-1}\right) \cdot y^2 \tag{2.1}$$

Where z is the distance of the tile centre from the plane P_{back}, x is the horizontal distance from the monochromator centre and y is its vertical distance from the monochromator centre. RH^{-1} and RV^{-1} are the parameters that define the horizontal and vertical curvatures respectively. The centre of each tile is placed accordingly to the above equation and each tile is rotated along the Y axis to be tangent to the curve by an azimuthal angle θ and along the X axis by a polar angle φ given by Eq. 2.2 and Eq. 2.3 respectively.

$$\theta = \arctan(2RH^{-1} \cdot x) \tag{2.2}$$

$$\varphi = \arctan(2RV^{-1} \cdot y) \tag{2.3}$$

2.2. Spherical curvature

The analytical function of the spherical curvature is represented by Eq. 2.4.

$$z = (RH + RV) - \left(\sqrt{RH^2 - x^2} + \sqrt{RV^2 - y^2}\right) \tag{2.4}$$

Where z is the distance of the tile centre from the plane P_{back}, x is the horizontal distance from the monochromator centre and y is its vertical distance from the monochromator centre. RH and RV are the parameters that define the horizontal and vertical curvatures respectively. The centre of each tile is placed accordingly to the above equation and each tile is rotated along the Y axis to be tangent to the curve by an azimuthal angle θ and along the X axis by a polar angle φ given by Eq. 2.5 and Eq. 2.6 respectively.

$$\theta = \arcsin(x/RH) \tag{2.5}$$

$$\varphi = \arcsin(y/RV) \tag{2.6}$$

In Fig. 2.2 and Fig. 2.3, one can see the McStas model of a single blade used to simulate the doubly bent analyzer. Furthermore every analyzer is made from several blades.

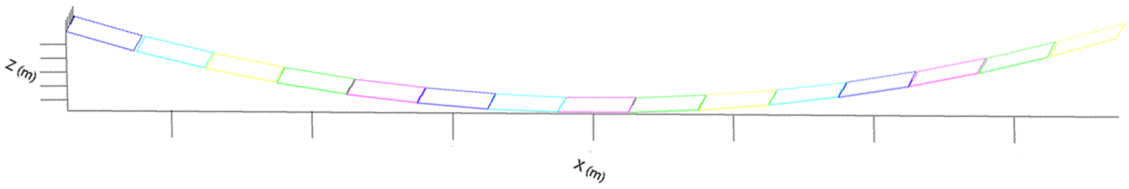

Figure 2.2. – The horizontal blade of the McStas curved analyzer component.

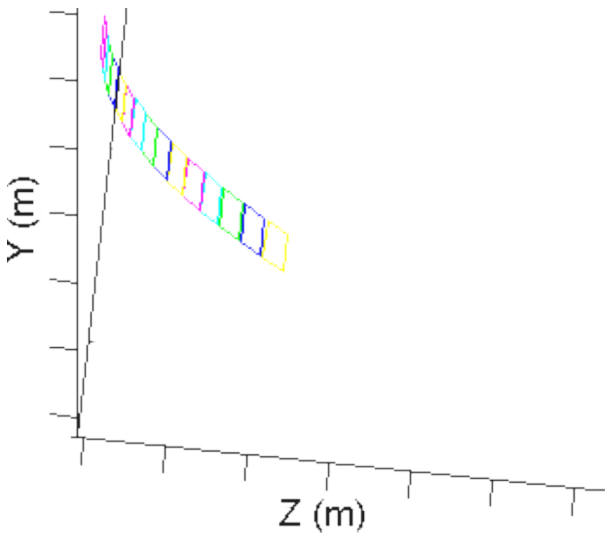

Figure 2.3. – The vertical blade of the McStas curved analyzer component.

3. Inelastic neutron scattering module upgrade

3.1. Improving the analyzer within the current frame

The simplest way to set up a new INS bank with an improved analyzer would be to change the analyzer support and the analyzer itself, leaving the rest unaltered. In this scenario, we would keep the current housing constraints and would have to exploit the limited free space among the other components. In the current configuration it is possible to extend the analyzer width up to 190 mm before touching the housing walls. The height of the analyzer instead can be expanded to a maximum of 160 mm before clashing with the beryllium filter. Moreover, it may not be possible to implement a curved analyzer while keeping the current support, since the beryllium filter is too close to the analyzer in the current setup. Nevertheless, with a different support, the analyzer could be moved farther from the filter by a maximum of 40 mm. This would increase the analyzer–filter distance, leaving space for the curved geometry to be implemented; this modification would also increase L_1 by 18 %. If necessary additional space available to the curved analyzer could be achieved by moving the beryllium filter by 10 mm towards the detector array. All these changes do not require the redesign of the housing frame, see Fig. 3.1, and this concept can be relatively easily and quickly implemented. In the simulation, we used an average distance from the moderator to the detector of 17.65 m ($L_0 + L_1$).

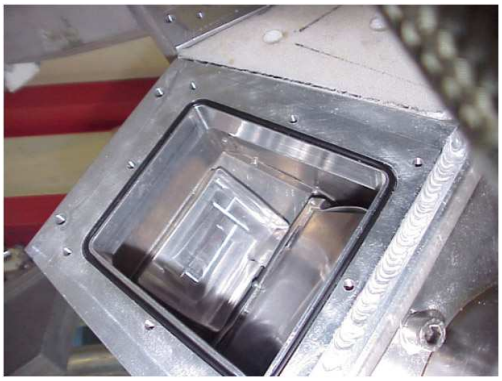

Figure 3.1. – The flange of the current TOSCA INS module housing.

3.2. Building a new module

One step further in the idea of the secondary upgrade is to fully rethink the geometry constraints of a single module. In fact, keeping the current housing for a new analyzer might not be the best option available. Currently, a single module occupies just a small portion of the spectrometer, leaving most of the space around the sample empty, see Fig. 3.2. According to the ISIS Engineering Group, it may be possible to increase the angle subtended by a single INS module, to enhance the collection efficiency of the neutrons scattered by the sample. This new design would likely contemplate a single module that can extend up to the whole 60° of angular span, for a total of 5 INS modules on each side of TOSCA, see Fig. 3.3. Additionally, it is worthwhile to investigate the performance of a design having 6 banks of 45° each, as currently implemented at the VISION instrument. In any case, a whole new geometry for the TOSCA analyzer must be designed, that should likely have a trapezoidal shape and a much wider area than the current analyzer. McStas simulations can evaluate the performance of such new designs once the engineering space constraints are defined.

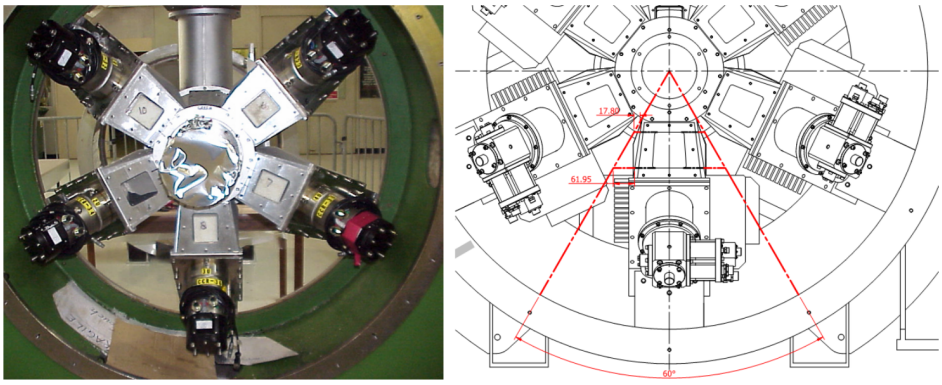

Figure 3.2. – (left) The TOSCA secondary spectrometer, and (right) its drawing. View from the front.

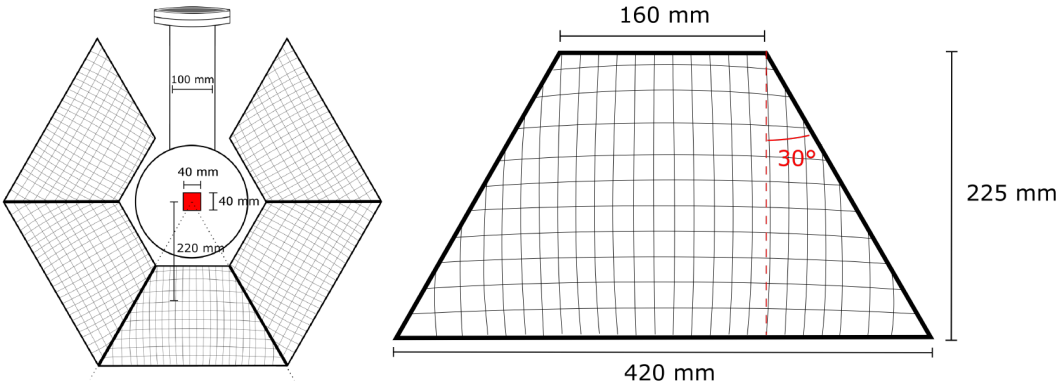

Figure 3.3. – Scheme of the TOSCA conceptual design, where the five trapezoidal analyzers with a 60° spacing are arranged in a circle and with the top block removed to allow access for the cryostat. Front view of the all inelastic modules (left) where the sample is shown in red, and drawing of a single extended analyzer (right).

4. Calculations of the compact analyzer design

We have set up simulations in relation to the TOSCA back-scattering module B3, that is the one below and placed upstream from the sample. We have calculated the intensity of the neutrons scattered by the analyzer and passing through the detector array, which lies in the same plane as the sample. The detector area is 300 x 182 mm^2 nominal while the active region in the real detector array is restricted to 182 x 182 mm^2 because of the electrical connections on either side of the array. Therefore we carefully designed the analyzer geometry in order to focus neutrons mainly onto this sensitive area. To evaluate the analyzer focusing in the simulations, we used position sensitive detectors (PSD) with 1 mm^2 resolution that were placed in front of the detector array. This upgrade option considers the design of compact analyzer, flat and curved, that could fit into the current TOSCA housing module without the need for expanding the whole assembly.

4.1. Flat analyzers

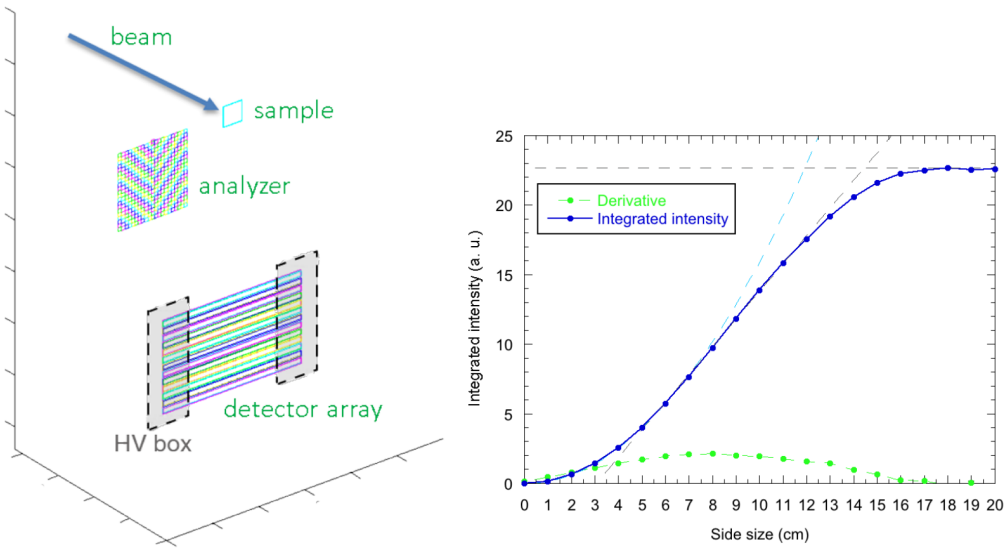

Figure 4.1. – Neutron intensity observed by ^{3}He detectors as a function of the flat square analyzer size and integrated over the wavelength range of interest.

As the first step in the design of a new analyzer for TOSCA we wanted to compare the performance of different flat configurations and to investigate if the current 12 x 12 cm^2 analyzer is the most efficient among the flat ones. We also kept the size of the detector array unaltered.

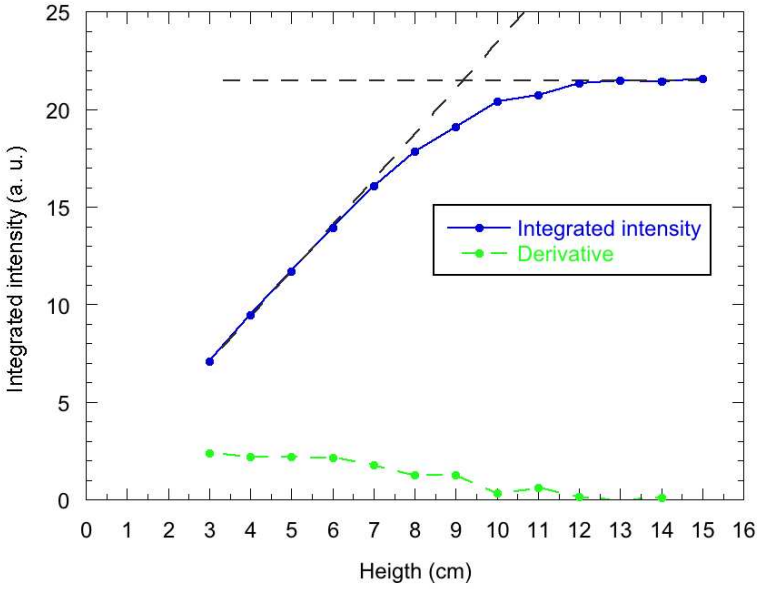

Figure 4.2. – Neutron intensity observed by ^{3}He detectors as a function of the analyzer height for a 15 cm wide flat analyzer. The intensity is integrated over the wavelength range of interest.

From the integrated intensity as a function of the analyzer dimensions, we can observe that the height (H) of the analyzer has to be smaller than its width (W) since the detection area has a rectangular shape with H < W. On the basis of the calculations shown in Fig. 4.1 and Fig. 4.2, the optimal height of the flat analyzer lies between 9 and 10 cm and the optimal width is between 14 and 15 cm. We can assert that the optimal flat monochromator should have a W/H ratio between 1.4 and 1.7 and this is compatible with the detector array W/H ratio of 1.65. The configuration that we deem the most close to the optimum is the 15 x 9 cm^2 which shows a gain of 1.1 in the total detected intensity compared to the current 12 x 12 cm^2 configuration.

4.2. Finding the optimal curvature for small analyzers

To proceed further in the study of a new analyzer design, we considered geometries with a curved surface along the vertical axis, able to intercept a larger solid angle from the sample and at the same time to focus the neutrons onto the 300 x 182 mm^2 detector area. In this section we considered only parabolic curvature, since the

dimension are still relatively small for this set of components and we can consider the differences between spherical and parabolic curvatures as negligible. For a section of parabola close to the vertex, as a first approximation we can write $RV^{-1} = \frac{1}{Radius\ of\ vertical\ curvature}$ where $RV^{-1} = 0$ means that the radius of curvature goes to infinity (i.e. flat geometry). Two geometries were considered, $A_0 = 144$ cm^2 and $A_1 = 150$ cm^2. To find the suitable radius of curvature for a 12 x 12 cm^2 (W x H) analyzer (A_0) we calculated the detected intensity as a function of RV^{-1}. Equally we also calculated the performance for a 15 x 10 cm^2 (W x H) configuration (A_1), since previous simulations showed that we have an optimum for an analyzer width of 15 cm, when no horizontal curvature is applied. From the results shown in Fig. 4.3, one can conclude that A_1 reaches the intensity plateau at a smaller curvature, in virtue of its smaller height, compared to the A_0 case. Furthermore, A_1 has a higher intensity (+0.9 %) at the plateau since it has a larger total area (+4 %) than A_0.

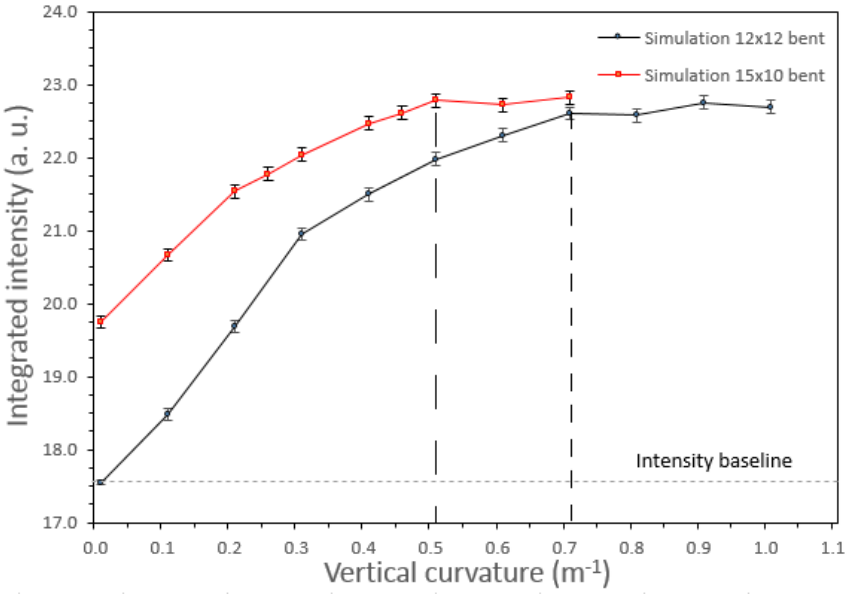

Figure 4.3. – Neutron intensity as a function of the curvature of the 12 x 12 cm^2 (A_0) and 15 x 10 cm^2 (A_1) analyzer geometries.

4.3. Performance comparison

In this section we present the performance results for some of the small bent analyzers considered, having 135 cm^2, 144 cm^2 and 150 cm^2 area. More detailed data can be found in Appendix D. One can see in Fig. 4.4 that in every curved configuration we achieved a flux gain and an improvement on the resolution of the elastic line.

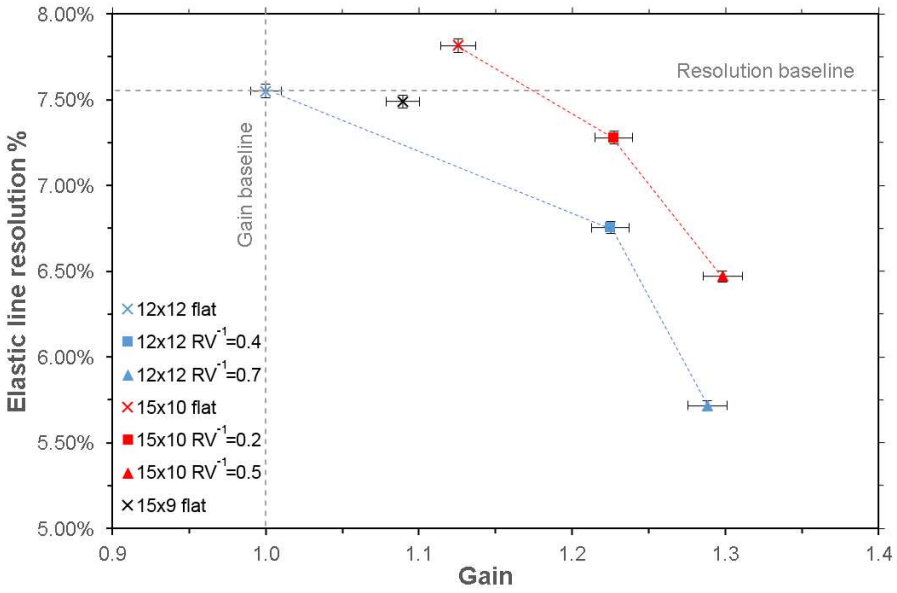

Figure 4.4. – Gain in relation to the 12 x 12 cm^2 flat analyzer geometry, and resolution performance for different geometries of the small analyzer.

5. Calculations of the extended analyzer design

A wide curved analyzer geometry will need extra care from the point of view of the time and energy focusing with respect to the simpler flat analyzer geometry on parallel planes that TOSCA currently implements. The shape of these extended analyzers should be triangular to accomplish the shape of the 60° INS module. Here we illustrate the McStas models and the associated diffracted beam obtained from three different configurations of doubly bent analyzer, i.e. 570 cm^2, 960 cm^2 and 1450 cm^2 analyzer. For every geometry a parabolic and a spherical curvature were considered, and this led to a total of 6 different configurations. Previously, a similarly large HOPG monochromator (1428 cm^2) with a horizontal and vertical spherical curvature has been successfully implemented at NIST with significant advance in the doubly focusing technology [12, 13]. Another example of curved analyzers implemented on a neutron spectrometer can be found at VISION instrument in the Oak Ridge National Laboratory. Namely, VISION spectrometer uses a design inspired by TOSCA since it operates in the same experimental field. Currently VISION has six back-scattering banks and six forward-scattering banks, where each bank features a 347 cm^2 curved analyzer made of HOPG tiles [14]. TOSCA and VISION neutron monochromation systems are completed by a cryo-cooled beryllium filter which shields an array of ^{3}He tubes.

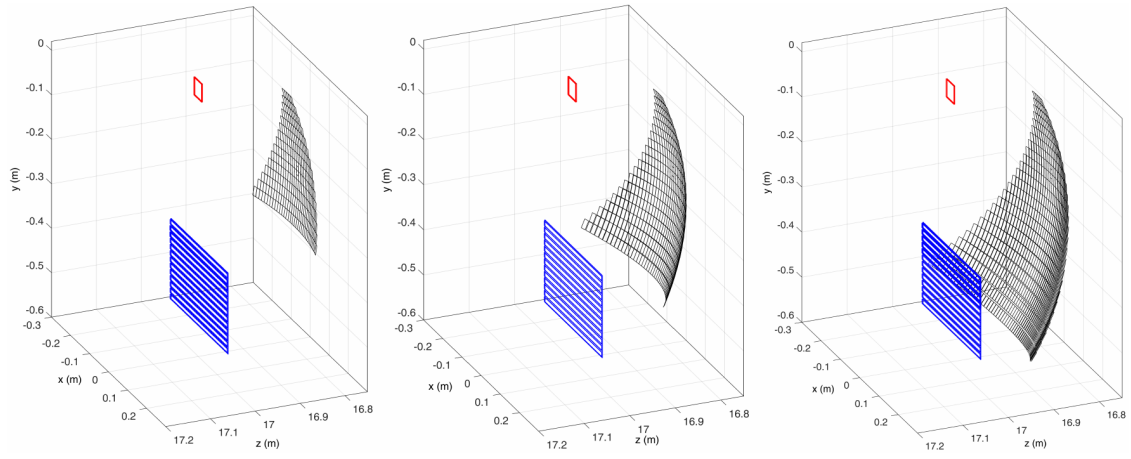

Figure 5.1. – 3D models of the simulated sample (red), analyzers (black) and detector array (blue). Three different configurations were simulated, 570 cm^2 analyzer (left), 960 cm^2 analyzer (center) and 1450 cm^2 analyzer (right).

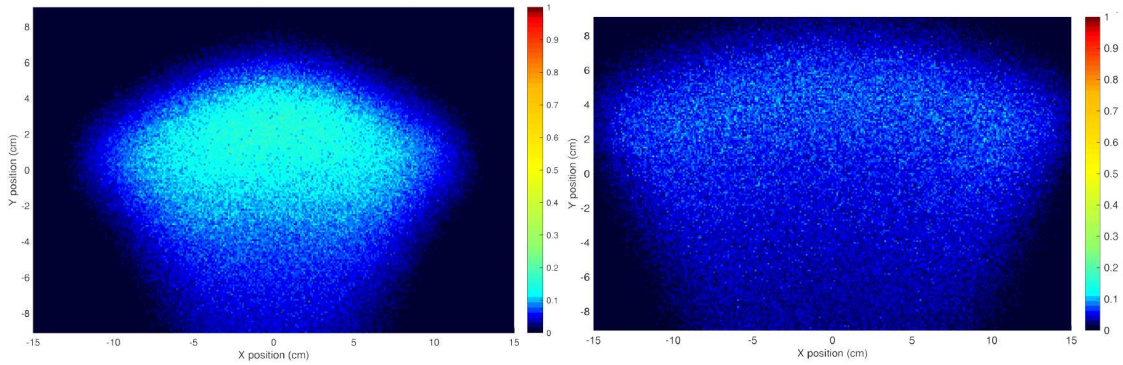

Figure 5.2. – Spatial profile of the neutrons diffracted onto the detector area by the 570 cm^2 analyzer. The configuration was simulated with the parabolic curvature (left) and the spherical curvature (right).

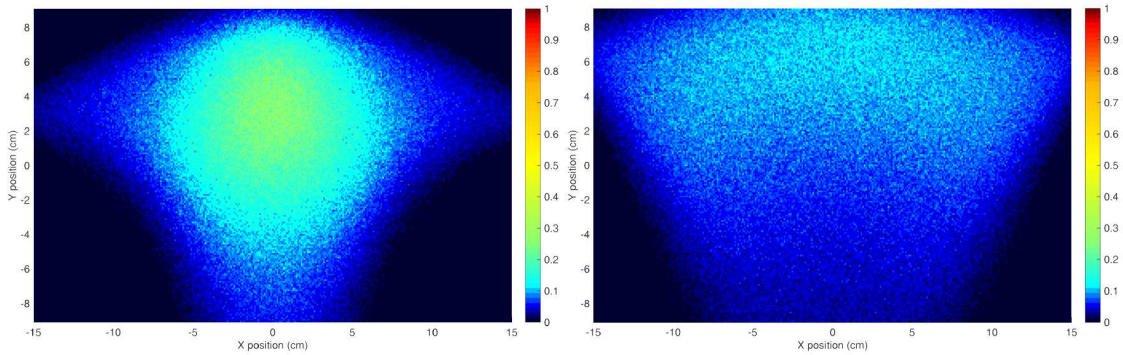

Figure 5.3. – Spatial profile of the neutrons diffracted onto the detector area by the 960 cm^2 analyzer. The configuration was simulated with the parabolic curvature (left) and the spherical curvature (right)

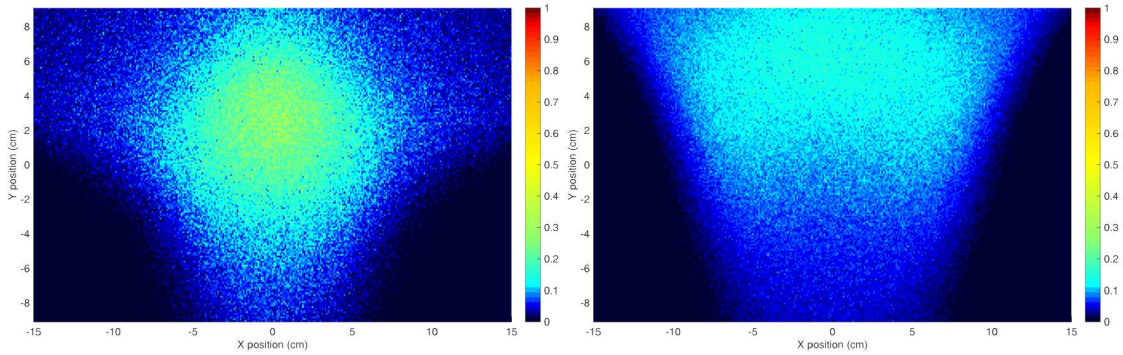

Figure 5.4. – Spatial profile of the neutrons diffracted onto the detector area by the 1450 cm^2 analyzer. The configuration was simulated with the parabolic curvature (left) and the spherical curvature (right)

From the figures above it can be noted that the focus on the detector plane has a finite size and an elliptic cross section. This is due to the finite size of the incident beam and sample, as is the case in reality. The elliptical spacial profile of the focus from a bent analyzer was already foreseen by Riste [8].

5.1. Calculating the optimal curvature

Because of the complexity of the doubly bent geometry, more than 200 simulations were performed iteratively to find the optimal curvature for each chosen analyzer area. The optimization is set on the RH^{-1} and RV^{-1} parameters, where both can change independently; thus the process have 2 degrees of freedom and is performed in a 3-dimensional space with coordinates (RH^{-1}, RV^{-1}, C). The C value is the criteria set to evaluate the performance of each curvature and it is described by Eq. 5.1, where I_i is the height and $\sigma^2{}_i$ is the variance of the Gaussian fit of the elastic peak detected by the i-th detector in the array. The optimization algorithm operates in order to find the couple (RH^{-1}, RV^{-1}) that minimizes C, see Fig. 5.5.

$$C = -\sum_{i=1}^{13} \frac{I_i}{\sigma_i^2} \tag{5.1}$$

The value C is obtained from the data analysis of the McStas simulations, which give the neutron signal of each one of the 13 detector tubes of the array currently implemented in the TOSCA INS modules. We used the MATLAB iFit package [15] to routinely retrieve and analyse the data generated by the McStas calculations.

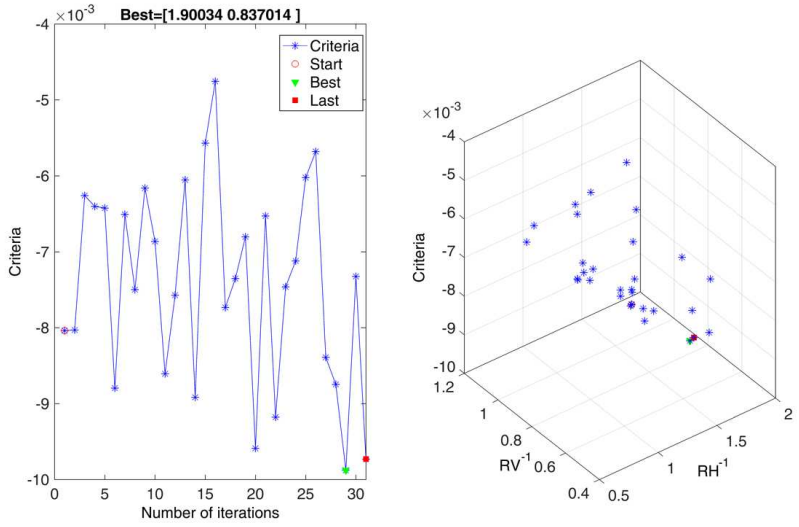

Figure 5.5. – Optimization of the criteria C as a function of the RH^{-1} and RV^{-1} parameters using MATLAB in conjunction with McStas.

5.2. Performance comparison

In this section we illustrate the results of the calculations that investigate the performance of the extended geometries, while the detailed data can be found in Appendix D. The widest configurations allow us to achieve the considerable gain,

up to 7, with limited effects on resolution. The resolution at the elastic line is of fundamental significance to assess the resolution at higher energy transfer. It was calculated from the FWHM of the elastic line, divided by the average energy of the elastically scattered neutrons (3.5 meV).

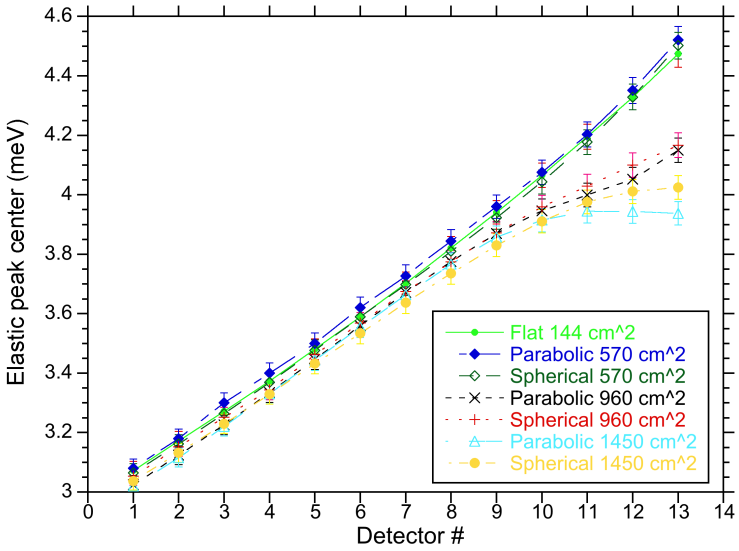

Figure 5.6. – Characteristic energy of the elastic line as a function of the detector position along the array.

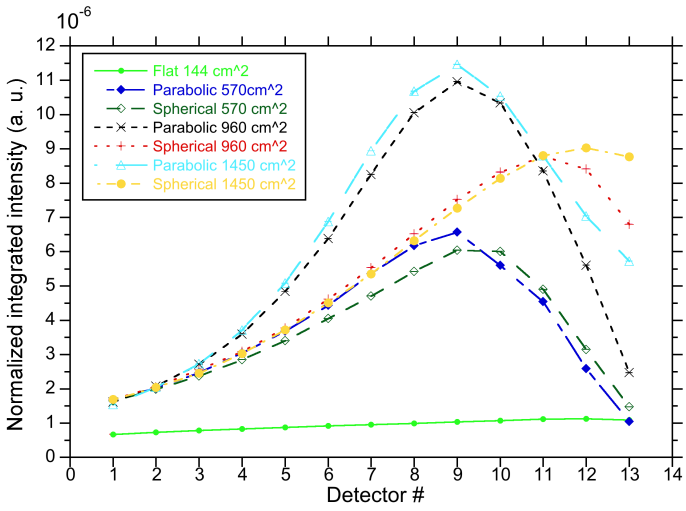

Figure 5.7. – Intensity integrated in the wavelength range of interest and normalized by the incident neutron flux. The results are shown for single detectors as a function of the detector position along the array. In the flat geometry the intensity is linearly distributed along the array, while in the curved geometries the neutrons are focused mainly towards the array centre and its lower part.

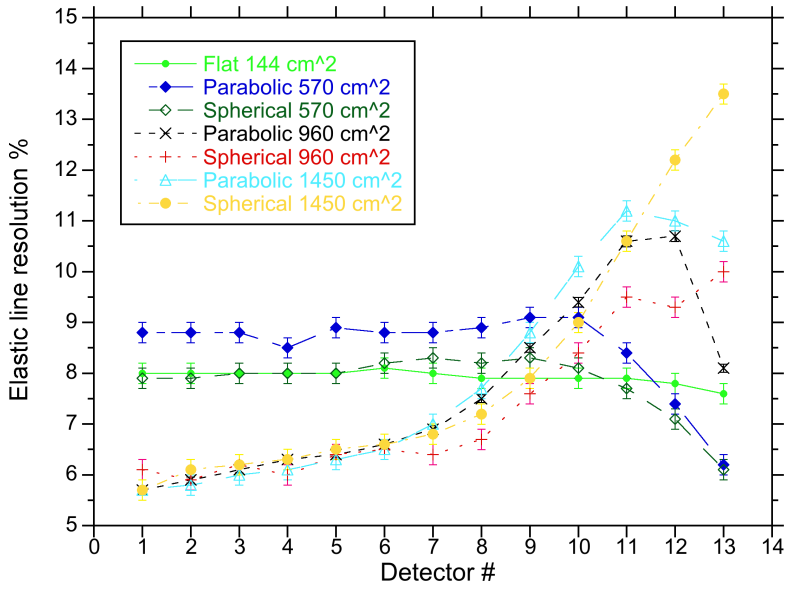

Figure 5.8. – Average elastic line resolution as a function of the detector position along the array, for various analyzer geometries. The resolution is reasonably constant along the array for the flat geometry, while for the curved analyzers it shows a dependence on the detector position.

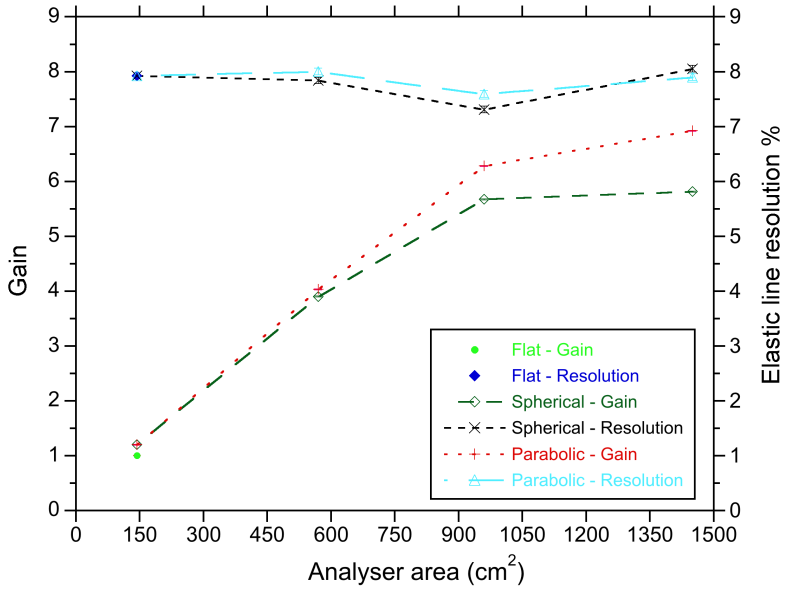

Figure 5.9. – Average flux gain and resolution as a function of the area of the doubly bent analyzer with baseline mosaicity. The curved analyzer shows a strong increase in the gain as a function of the area, while the resolution varies slightly.

5.3. HOPG mosaicity

The previous calculations studied the flux gain due to a bigger analyzer area and a focusing configuration, and while we kept the original detector banks the maximum gain was around 7 with respect to the current secondary. Further calculations on the 960 cm^2 parabolically focused analyzer were necessary to test other ways to increase the detected flux on top of the previous gain figure, while the horizontal and vertical curvature of the analyzer was chosen by means of computational optimization. We considered the 13 ^{3}He detectors in a new 60° module, while the number and position of the detectors were kept equal. The effect of bigger detectors was considered but it was limited because the neutrons are mainly focused at the centre of the detector array. We also increased the mosaicity (i.e. angular spread of the crystallites) of the HOPG crystals to widen the bandwidth of the analyzer. This increased bandwidth caused a considerable flux enhancement, but at the same time one could observe a direct trade-off with the resolution. In the calculations, a gain of 10 was reached with a resolution degradation by 15%. Detailed data about the data analysis and results can be found in Appendix E.

- Analyzer area: 960 cm^2
- Parabolic curvature ($RH^{-1} = 1.755$ m^{-1}, $RV^{-1} = 0.875$ m^{-1})
- HOPG mosaicity 150 arcmin < M < 300 arcmin
- Reference dataset (current secondary): 144 cm^2 flat analyzer, 140 arcmin mosaicity, R = 8.0 %, Gain = 1

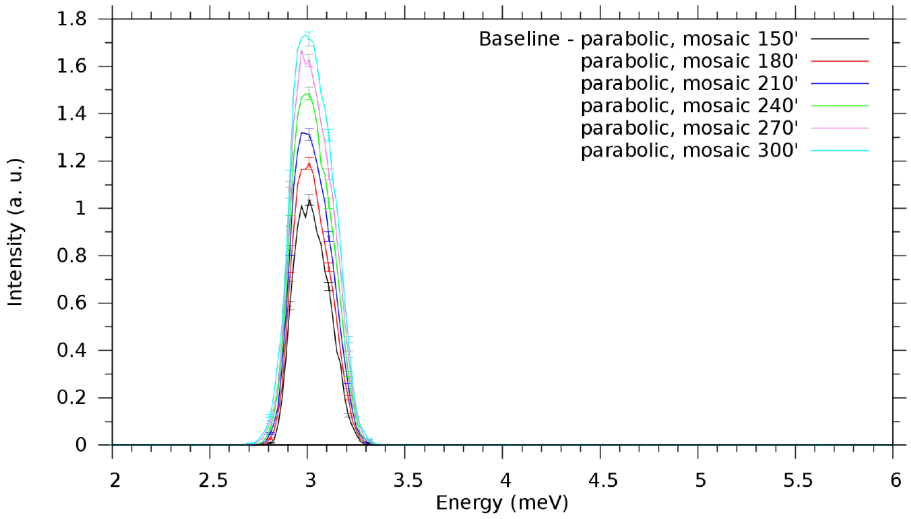

Figure 5.10. – Simulated elastic line for the detector closer to the sample position. The data were normalized by the parabolic analyzer with M = 150. We calculated a +70 % increased elastic line peak intensity at the highest mosaicity with respect to the lowest mosaicity case.

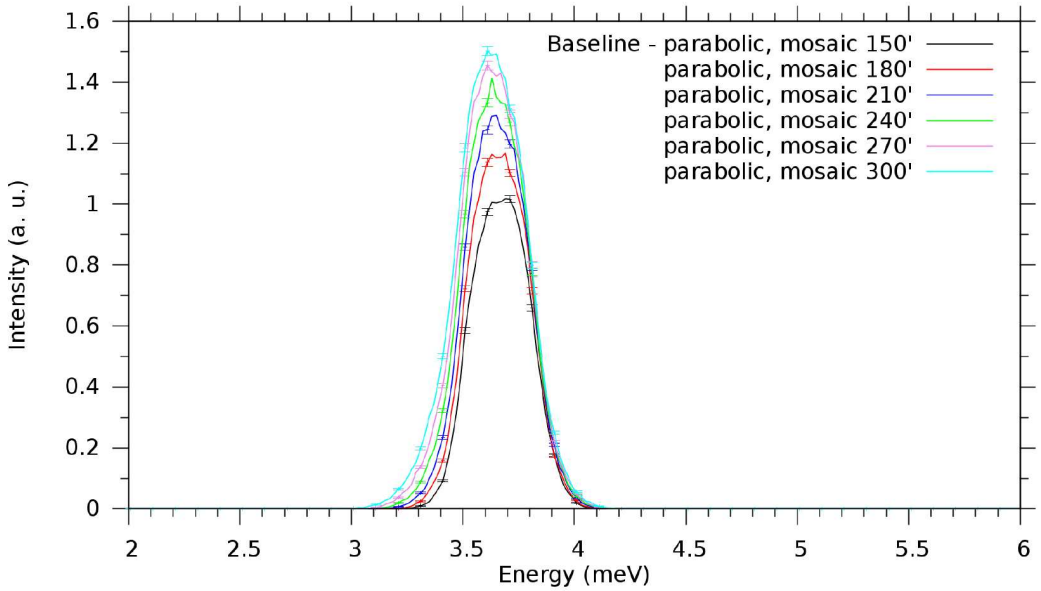

Figure 5.11. – Simulated elastic line for the detector in the middle position of the array. The data were normalized by the parabolic analyzer with M = 150. We calculated a +50 % increased elastic line peak intensity at the highest mosaicity with respect to the lowest mosaicity case.

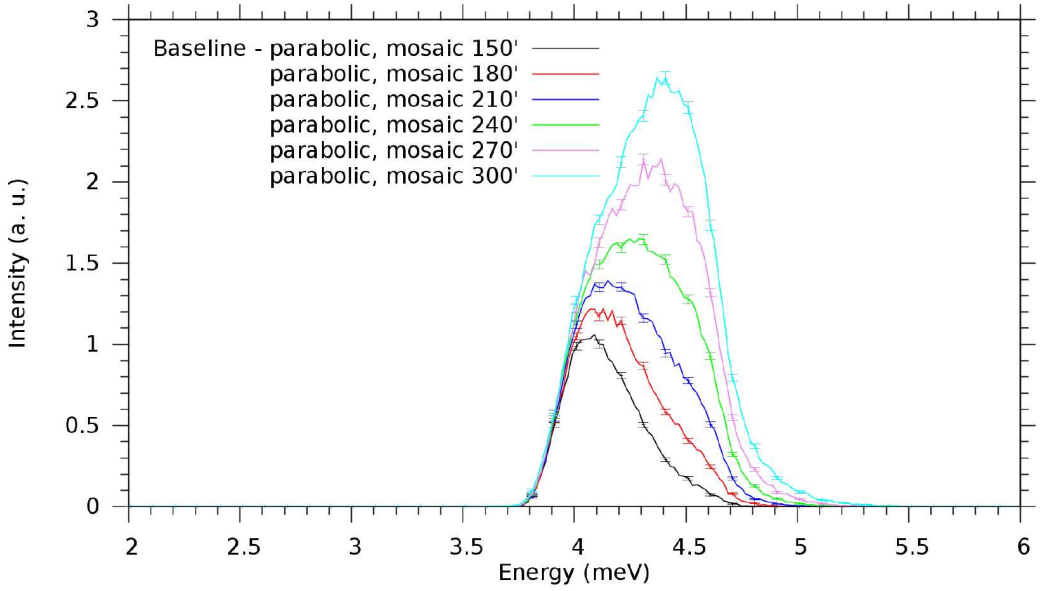

Figure 5.12. – Simulated elastic line for the detector farthest away from the sample position. The data were normalized by the parabolic analyzer with M = 150. We calculated a +150% increased elastic line peak intensity at the highest mosaicity with respect to the lowest mosaicity case.

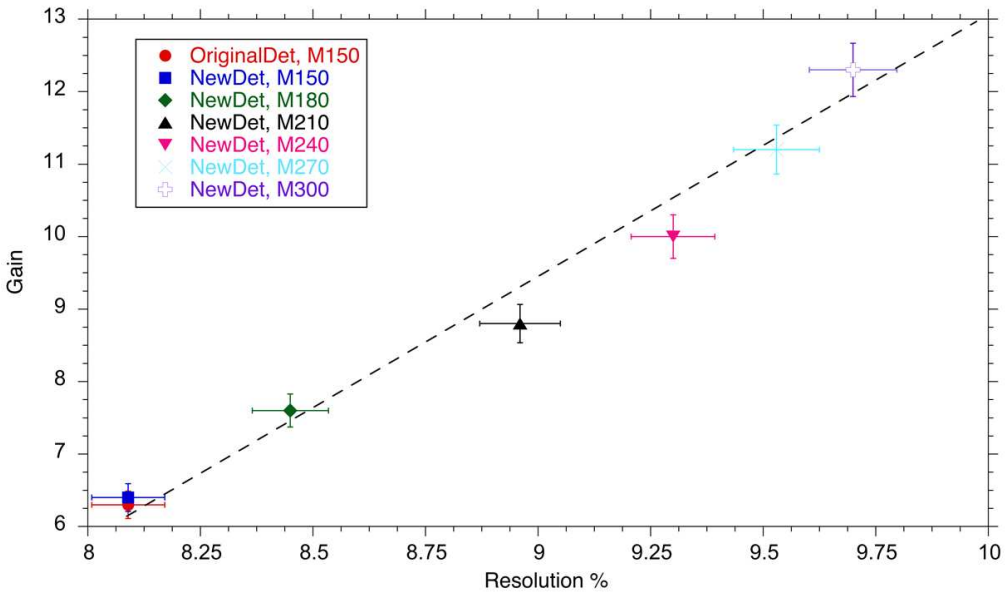

Figure 5.13. – Elastic line gain-resolution trade-off for the 960 cm^2 parabolic analyzer with different mosaicity of the crystallites. We can observe a linear dependence of the gain-resolution relationship as the mosaicity increases.

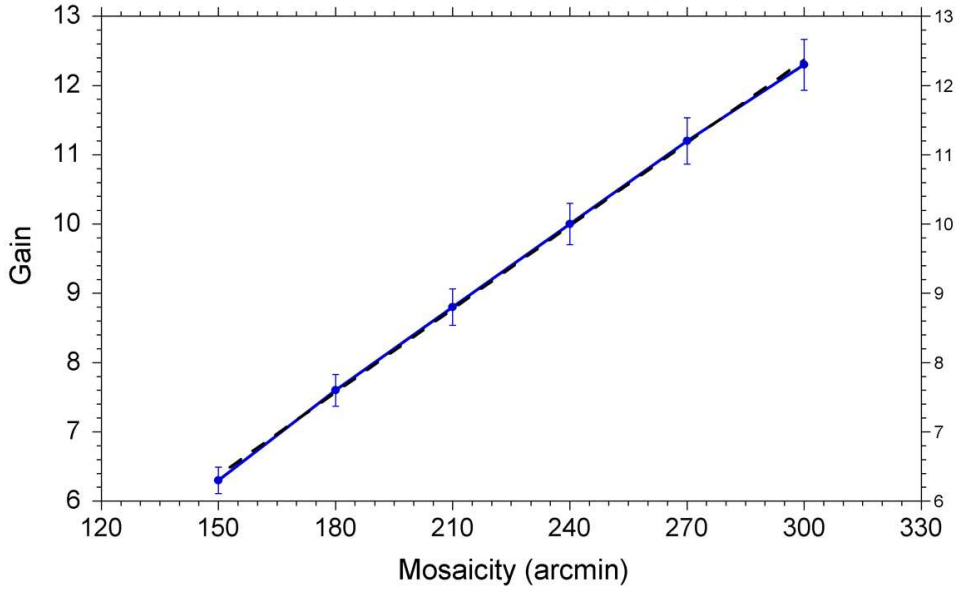

Figure 5.14. – Neutron flux gain of the 960 cm^2 parabolic analyzer in relation to the 144 cm^2 flat analyzer, as a function of the mosaicity of the crystallites. We can observe a linear dependence in the gain-mosaicity relationship. The linear regression of the plot is shown as black dashes.

5.4. Conceptual design of the TOSCA upgraded secondary spectrometer

Visualization of the possible conceptual design of the TOSCA upgraded spectrometer and space utilization of the future assembly.

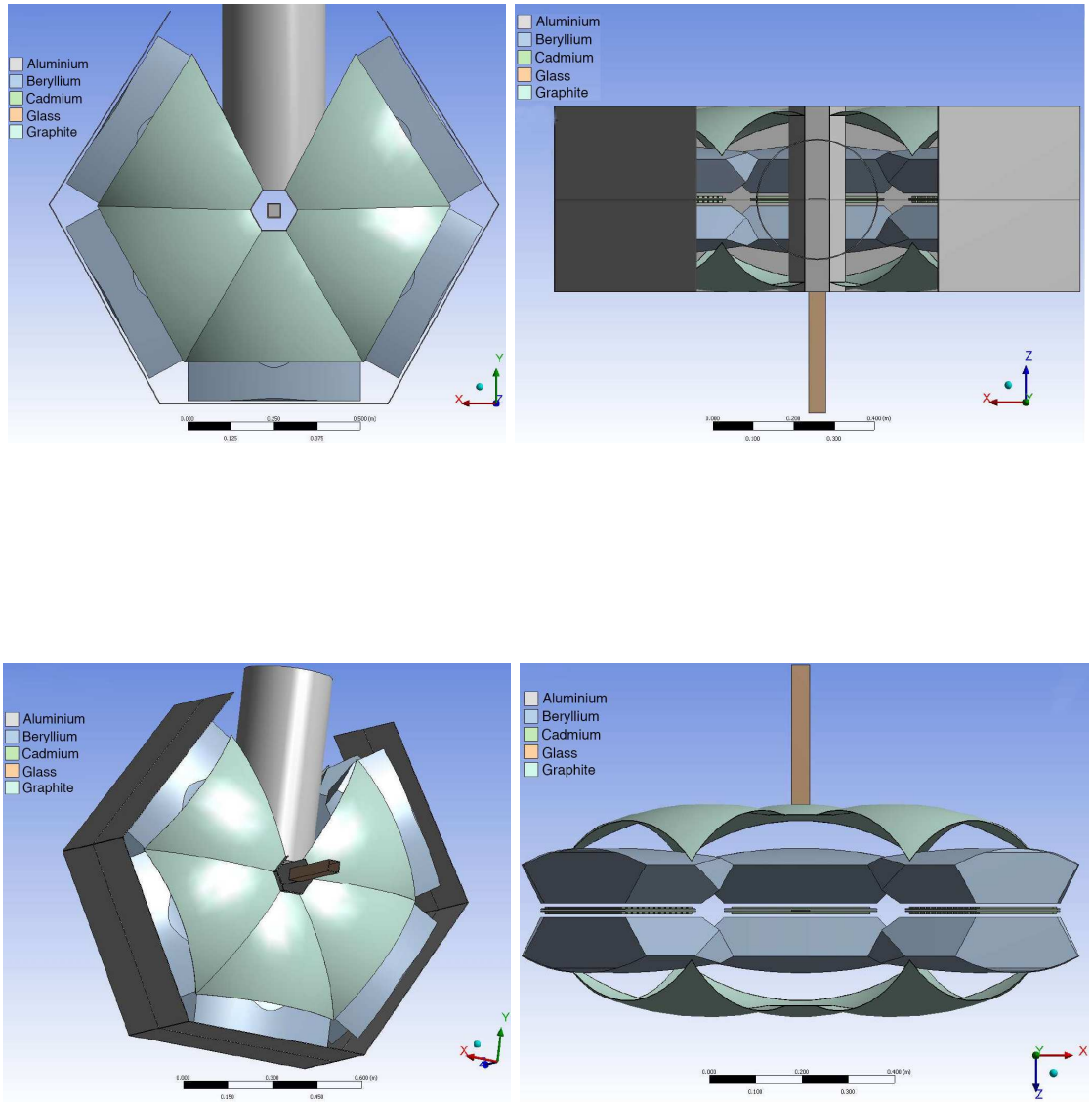

Figure 5.15. – Computer aided conceptual design of the TOSCA secondary spectrometer with the new curved analyzers.

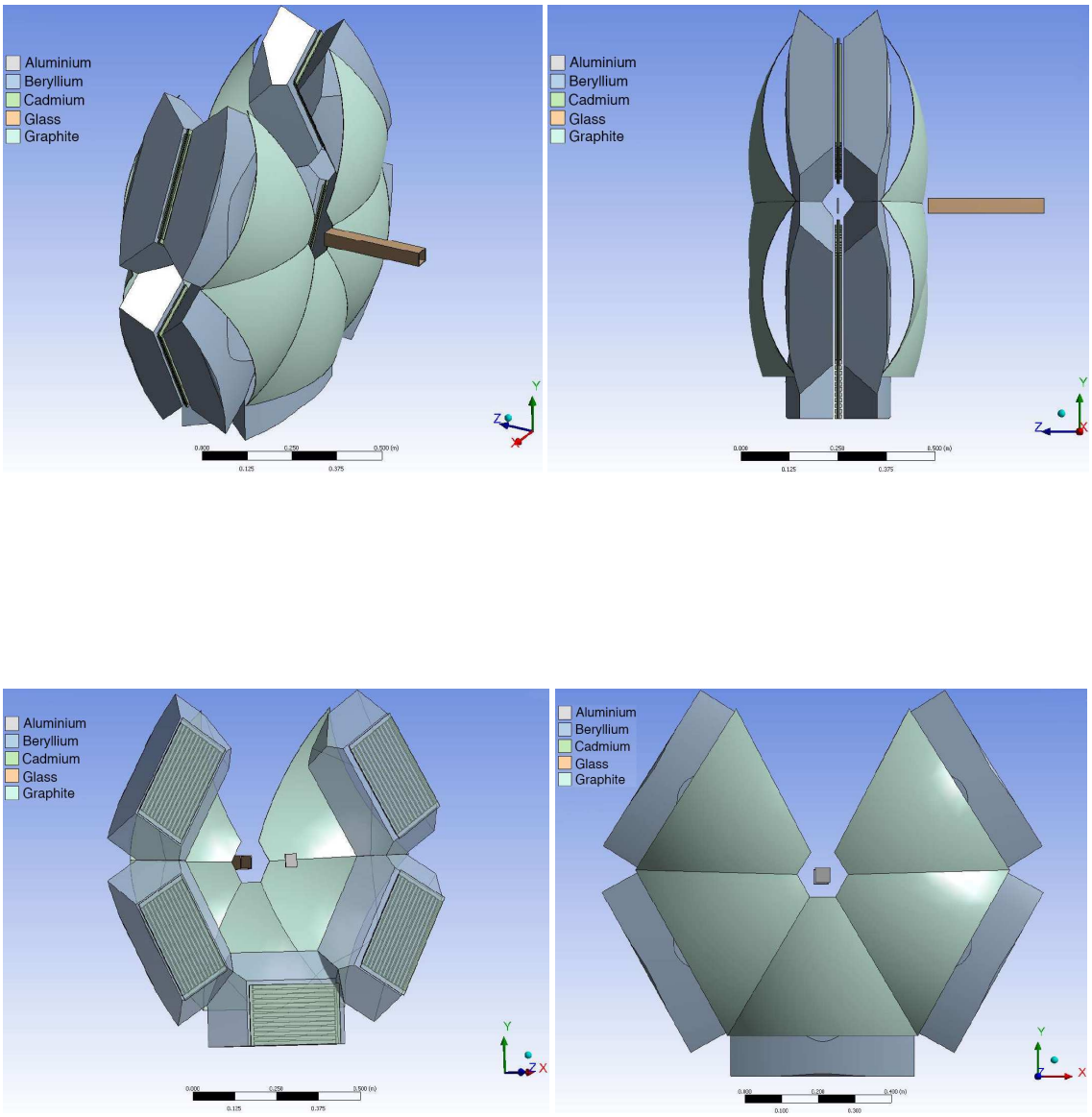

Figure 5.16. – Computer aided conceptual design of the TOSCA secondary spectrometer with the new curved analyzers.

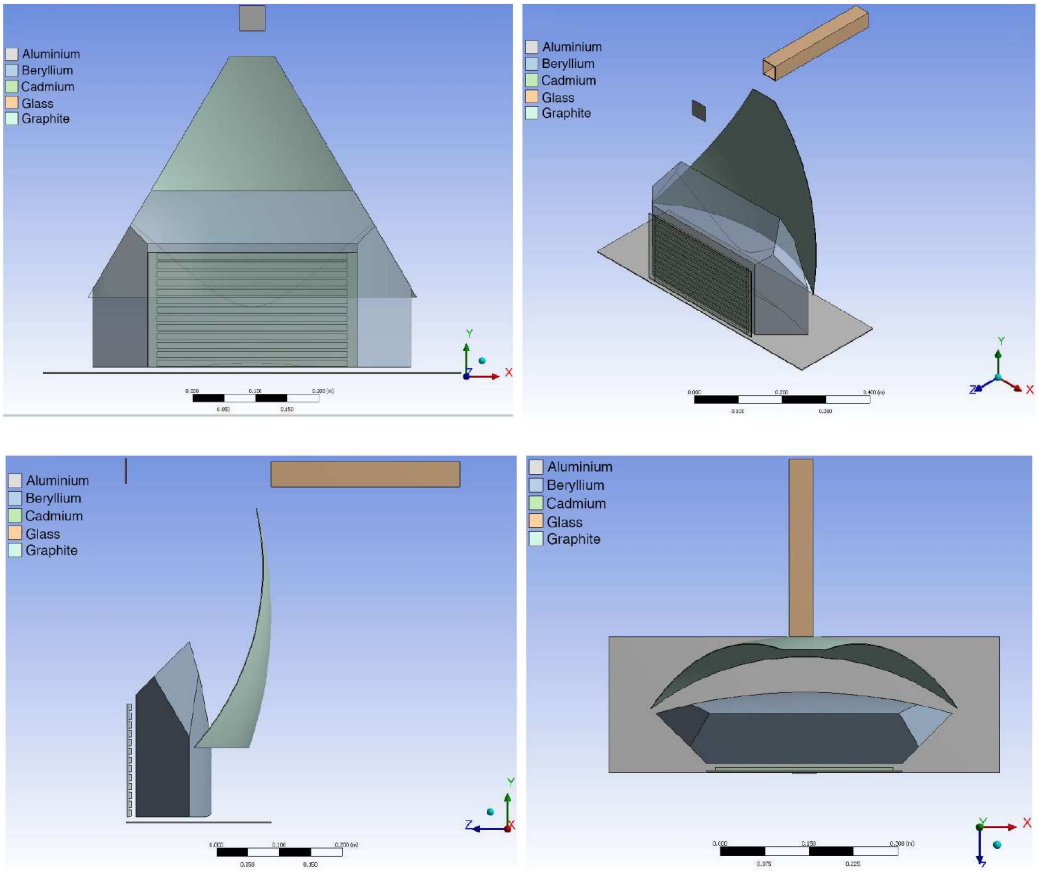

Figure 5.17. – Computer aided conceptual design of a single module of the TOSCA spectrometer with the new curved analyzers.

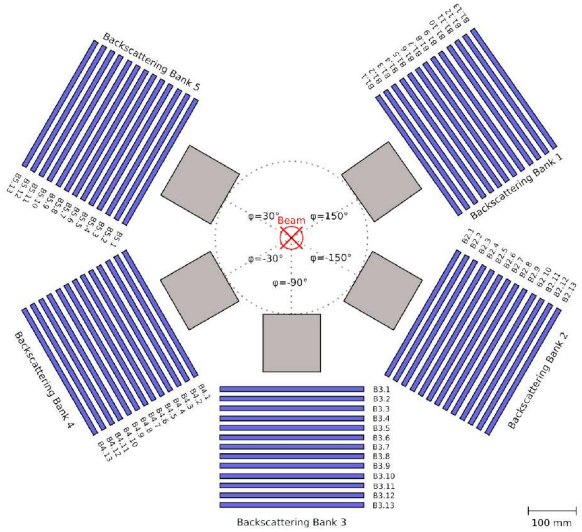

Figure 5.18. – Computer aided design of the back-scattering banks of the TOSCA spectrometer with the current flat analyzers.

6. Conclusions and recommendations for future work

Following the recent upgrade of the TOSCA primary spectrometer [16, 17, 18, 19] the TOSCA instrument capabilities can be further enhanced via the upgrade of its secondary spectrometer whereby currently installed flat analysers could be exchanged for curved analysers and their surface area enlarged [20]. We simulated different configurations of flat and curved graphite analyzers, whose area ranges from 1 to 10 times larger than the current TOSCA analyzer area. The parabolic and spherical geometries were set with appropriate curvatures to focus the diffracted beam onto the detector array and they were optimized to get the best flux-resolution trade-off. Up to an analyzer area of 960 cm^2, the two geometries have similar performance in relation to the instrument resolution, while the parabolic geometry performs better in relation to the flux gain. With respect to the largest configuration simulated (1450 cm^2) the parabolic configuration outperforms the spherical one for either gain and resolution, see Fig. 5.9. Overall, in any of the considered cases, the chosen figure of merit is higher for the parabolic geometry than the spherical one, i.e. the gain-resolution trade-off is better for a parabolic curvature. It is worth to mention that each detector in an array showed a characteristic energy which varied only slightly when the geometry of the analyzer changed and we note that, thanks to the energy focusing principle, the characteristic energy varies linearly as a function of the detector position along the array. Every deviation from linearity has a detrimental effect for the resolution, as evidenced in Fig. 5.6 and Fig. 5.8. Moreover, the detected intensity is reasonably constant along the array for the flat geometries, while in the curved cases the neutrons are focused mainly onto the central part of the array, see Fig. 5.7. If necessary, the position of the focus can be varied arbitrarily by choosing a different radius of curvature or different tilting angle of the analyzer, however this will have effects on the overall gain and the resolution performance. Up to a certain analyzer size, the vertical curvature (i.e. normal to the diffraction plane) in general reduces the wavelength spread and enhances the central wavelength component with respect to a flat analyzer. As a consequence, this effect improves the overall resolution of the instrument. A step that can further improve the gain and the resolution is to set accurately the horizontal and vertical mosaicity of the HOPG tiles in order to match the divergence and make a better use of the beam, as suggested in that case by Mikerov [21]. The performed calculations on different mosaicities showed that, in such case, an order-of-magnitude gain is within reach but resolution trade-off appears to be necessary. It is important to remember also that HOPG crystals have

weak beam attenuation for wavelengths other than the ones that satisfies the Bragg condition, and this gives the opportunity for multiple spectrometer setups that may exploit the transmitted beam through the analyzer [8]. Furthermore, it might be worth to evaluate the possible deviations on the wavelengths diffracted by the analyzer due to an off-center position of the sample, as mentioned in reference [11]. This problem can be investigated by means of further Monte Carlo calculations and can be possibly avoided by means of an alignment system implemented in the future TOSCA design, in order to check the correct positioning of the sample in every experiment and ensure an effective operation of the analyzer. In general, we can assert that the parabolic curvature has better focusing properties than the spherical one, and thus for the spherical geometries a shorter radius of curvature will be needed to achieve the same level of beam focusing. Nevertheless we need further simulations to assess fully the upgrade options and also it is recommended to benchmark the calculations against experimental data. This work is important since it paves the way for a quantitative description of cutting-edge upgrades in all the spectrometers which share the TOSCA design (i.e. VISION, VESPA, LAGRANGE).

A. Appendix
Geometry of the current secondary spectrometer

- TOSCA has 5 banks in the back-scattering position $\theta = 135°$, $\varphi_1 = 60°$, $\varphi_2 = 120°$, $\varphi_3 = 180°$, $\varphi_4 = 240°$, $\varphi_5 = 300°$ in spherical coordinates.
- It has also 5 banks in the forward-scattering position $\theta = 45°$, $\varphi_1 = 60°$, $\varphi_2 = 120°$, $\varphi_3 = 180°$, $\varphi_4 = 240°$, $\varphi_5 = 300°$ in spherical coordinates.
- Y distance between the analyzer centre and the sample centre: $Y_1 = 220$ mm.
- Z distance between the analyzer centre and the sample centre: $Z_1 = 220$ mm.
- Average distance between the analyzer centre and the sample centre: $\frac{L_1}{2} = 311$ mm.
- L_1 is the secondary flight path of the spectrometer, which is made of two equal branches connecting the sample with the analyzer and then the analyzer with the detectors.
- The HOPG analyzer has a trapezoidal shape with: W = 120 mm, H = 120 mm. The reflective surface is oriented towards the sample and the analyzer area is ~ 144 cm^2.
- The beryllium filter is a box having the following dimensions: W = 151.4 mm, H = 121.4 mm and thickness T = 121.4 mm.

B. Appendix
Principles of inverted geometry INS measurements

As discussed in reference [4], the peculiarity of the inverted geometry spectrometer like TOSCA is to receive a broad spectrum of neutron wavelengths on the sample and to fix the final energy E_1, in order to perform a scan of the incident energy E_0 by means of the time-of-flight (TOF) technique. This arrangement opens the possibility to scan a wide range in the neutron energy loss and it gives the ability to study high energy losses in the sample by means of the TOF while keeping the analyzer working at much lower energies, where the Bragg diffraction has its best efficiency. The energy of the scattered neutrons E_1 and the time t_1 a neutron takes to travel the secondary spectrometer are fixed by the analyzer system. In fact, in compliance with the Bragg law of diffraction, the parameters that determine the final energy are the analyzer d-spacing d_A and the diffraction angle θ_A, where the angle of incidence on the analyzer must equal the angle of diffraction. The final quantities t_1, E_1 can be calculated by the following set of equations:

$$k_i = \frac{mv_i}{\hbar} = \frac{2\pi}{\lambda_i} \tag{B.1}$$

$$\lambda_1 = 2d_A sin\theta_A \tag{B.2}$$

$$k_1 = \frac{\pi}{d_A sin\theta_A} \tag{B.3}$$

$$t_1 = \frac{mL_1}{\hbar k_1} = \frac{mL_1 d_A sin\theta_A}{\pi\hbar} \tag{B.4}$$

$$E_1 = \frac{\hbar^2 k_1^2}{2m} = \frac{\hbar^2}{2m}\left(\frac{\pi}{d_A sin\theta_A}\right)^2 \tag{B.5}$$

Therefore, the geometry of the secondary spectrometer allows to define t_1 and the unique feature of a pulsed source gives a precise time reference for the emission of the neutrons from the target [22]. This combination of factors makes the time of flight technique particularly effective in determining the energy loss of neutrons in the sample [2]. In fact, we can measure the time t elapsed from the single pulse to a detection event and thus, with Eq. B.6, we can calculate the time t_0 a neutron

takes to travel the primary branch of length L_0 that leads ultimately in obtaining the energy loss $\hbar\omega$ by Eq. B.8.

$$t_0 = t - t_1 = t - \frac{mL_1 d_A sin\theta_A}{\pi\hbar} \tag{B.6}$$

$$E_0 = \frac{1}{2}m\left(\frac{L_0}{t_0}\right)^2 \tag{B.7}$$

$$\hbar\omega = E_0 - E_1 = \frac{1}{2}m\left(\frac{L_0}{t - \frac{mL_1 d_A sin\theta_A}{\pi\hbar}}\right)^2 - \frac{\hbar^2}{2m}\left(\frac{\pi}{d_A sin\theta_A}\right)^2 \tag{B.8}$$

To evaluate the energy resolution of such an instrument, one has to consider all the different contributions that affect the uncertainty of the measurement:

- First, we have the divergence of the neutron impinging on the analyzer and its mosaic spread that determine the angular uncertainty in the Bragg angle $\Delta\theta_A$, which leads to the scattered wave-vector spread Δk_1.

$$\frac{\Delta|k_1|}{k_1} = \Delta\theta_A cot\theta_A \tag{B.9}$$

- Then we must consider the spread in the incident energy, which is mainly given by the uncertainty in the distance and in the timing over the primary flight path. There are several contributions, the most important are the pulse broadening caused by the moderator, the uncertainty due to the finite dimension of the sample, the time spread due to the analyzer thickness and the time spread due to detector thickness. All this contributions are assumed to be independent and can be summed in quadrature to calculate the total time uncertainty Δt.

We therefore can combine the errors in the scattered wave vector with the timing errors of the system to obtain the uncertainty in the incident wave vector Δk_0.

$$\frac{\Delta k_0}{k_0} = \frac{\sqrt{\Delta t^2 + (t_1 \Delta k_1/k_1)^2}}{t_0} \tag{B.10}$$

Let us take into account Eq. B.10 and convert for convenience the timing errors in an error over the distance using Eq. B.11.

$$\delta = \frac{\hbar k_0 \Delta t}{m} \tag{B.11}$$

Now, in Eq. B.12 it is finally possible to evaluate the resolution of the inelastic scattering with incident energy E_0 [4].

$$\frac{\Delta\hbar\omega}{E_0} = 2\left\{\left(\frac{\delta}{L_0}\right)^2 + \left[\frac{E_1}{E_0}\Delta\theta_A cot\theta_A\left(1 + \frac{L_1}{L_0}\left(\frac{E_0}{E_1}\right)^{3/2}\right)\right]\right\} \tag{B.12}$$

From the above equation, it is evident that some choices on the secondary geometry can influence the final resolution. Namely, the resolution is improved when the analyzer is placed in the back-scattering position, where the term $cot\theta_A \rightarrow 0$, and the primary and secondary branches ratio L_1/L_0 should be minimized in order to reduce the last term in Eq. B.12.

C. Appendix
Energy calibration of the detector array

The values in Tab. C.1 were calculated by means of the TOSCA McStas model with a 12 x 12 cm^2 flat analyzer and an incident wavelength range from 3 Å to 7 Å. The energy transfer has to be calculated separately for each detector considering the different characteristic energy tabulated above. In this way the energy focusing is fully exploited to achieve the resolution of ~ 300 μeV.

Detector	Elastic peak centre (meV) ∓ 0.01	Intensity (10^{-6}) ∓ 0.001
1	3.09	0.335
2	3.20	0.365
3	3.30	0.392
4	3.40	0.412
5	3.52	0.436
6	3.61	0.459
7	3.71	0.477
8	3.85	0.496
9	3.95	0.517
10	4.08	0.536
11	4.19	0.556
12	4.35	0.562
13	4.50	0.540

Table C.1. – Center of the elastic peak recorded by each single detector in the array. The intensity is normalized by the incident intensity on the sample.

D. Appendix
Simulation results of the TOSCA analyzer

In the tables Tab. D.1 and Tab. D.2, one can see the performance of each configuration for associated intensity, resolution and figure of merit. The reference dataset is the 12 x 12 cm^2 flat analyzer (first row) which is assumed to resemble closely the current situation at TOSCA and has parameters such as area A_0, intensity I_0, resolution R_0. We therefore consider the Figure of Merit (hereafter FoM), described in Eq. D.1, to depict the effectiveness of each i-th configuration.

$$FoM_i = \left(\frac{A_0}{A_i}\right) + \frac{(I_i - I_0)}{I_0} - \frac{(R_i - R_0)}{R_0} \tag{D.1}$$

The performance calculations refers to the elastic line with an incident beam from 3 Å to 7 Å, as detected by the B3 detector bank. Each analyzer is made from HOPG tiles of 10 x 20 mm^2 (W x H) with mosaicity $\eta = 2.5°$ (150 arcmin) in both vertical and horizontal direction.

Configuration	Area (cm^2)	Intensity (10^{-6})	Resolution %	Gain	FoM
12x12 flat	144	17.50 ∓ 0.03	7.6 ∓ 0.1	1.00 ∓ 0.01	1.00 ∓ 0.01
12x12 RV^{-1}=0.4	144	21.50 ∓ 0.09	6.75 ∓ 0.09	1.23 ∓ 0.01	1.33 ∓ 0.01
12x12 RV^{-1}=0.7	144	22.60 ∓ 0.09	5.72 ∓ 0.09	1.29 ∓ 0.01	1.53 ∓ 0.01
15x9 flat	135	19.1 ∓ 0.1	7.49 ∓ 0.08	1.09 ∓ 0.01	1.13 ∓ 0.01
15x10 flat	150	19.80 ∓ 0.08	7.8 ∓ 0.2	1.12 ∓ 0.01	1.07 ∓ 0.01
15x10 RV^{-1}=0.2	150	21.50 ∓ 0.09	7.28 ∓ 0.09	1.23 ∓ 0.01	1.24 ∓ 0.01
15x10 RV^{-1}=0.5	150	22.80 ∓ 0.09	6.47 ∓ 0.09	1.30 ∓ 0.01	1.42 ∓ 0.01

Table D.1. – Performance calculations in relation to the small size analyzers with the parabolic curvature along the vertical axis. The intensity is calculated with a neutron bandwidth from 3 Å to 7 Å and normalized by the incident neutron intensity on the sample, it can be related to the detection probability of a neutron impinging on the sample.

Configuration	Area (cm^2)	Intensity (10^{-6})	Resolution %	Gain	FoM
12x12 flat	144	17.20 ∓ 0.02	7.92 ∓ 0.02	1	1
15 rows parabolic RH^{-1}=1.1, RV^{-1}=0.7	570	69.37 ∓ 0.05	8.05 ∓ 0.06	4.03 ∓ 0.01	3.46 ∓ 0.03
15 rows spherical RH=0.5, RV=0.75	570	67.10 ∓ 0.05	7.84 ∓ 0.06	3.90 ∓ 0.01	3.41 ∓ 0.03
20 rows parabolic RH^{-1}=1.755, RV^{-1}=0.875	960	108.0 ∓ 0.1	7.59 ∓ 0.06	6.28 ∓ 0.01	5.71 ∓ 0.05
20 rows spherical RH=0.35, RV=0.55	960	97.6 ∓ 0.2	7.31 ∓ 0.06	5.67 ∓ 0.01	5.14 ∓ 0.05
25 rows parabolic RH^{-1}=1.748, RV^{-1}=0.9	1450	119.0 ∓ 0.2	7.90 ∓ 0.06	6.92 ∓ 0.01	6.24 ∓ 0.06
25 rows spherical RH=0.355, RV=0.667	1450	99.9 ∓ 0.1	8.05 ∓ 0.06	5.81 ∓ 0.01	5.11 ∓ 0.04

Table D.2. – Performance calculations in relation to the extended size analyzers with double curvatures. The intensity is calculated with a neutron bandwidth from 3 Å to 7 Å and normalized by the incident neutron intensity on the sample, it can be related to the detection probability of a neutron impinging on the sample.

The values of the optimal curvature were found by means of a numerical optimization process and the results are not far from the theoretical value given by the condition of monochromatic focusing cited in [9], where the radius of curvature R* that achieves the monochromatic focusing (i.e. it selects the narrowest wavelength range) is dependent on the sample-analyzer mean distance L, on the analyzer d-spacing d and on the desired scattering vector k_1, as shown in Eq. D.2 for configuration with point-like elements. The final resolution gets worse as the chosen analyzer curvature departs in either direction from R*.

$$\frac{1}{R*} = \frac{\pi}{Ldk_1} \tag{D.2}$$

E. Appendix
Gain and resolution analysis

Gain A Monte Carlo calculation was performed for each value of mosaicity using an incident wavelength range on the sample of 3 Å $\leq \lambda \leq$ 7 Å . For each dataset, the spectrum from the each i-th detector was analyzed independently to retrieve the integral of the elastic line. The elastic line integral $\int D_i(\lambda)d\lambda$ was normalized by the integrated flux on the sample $\int S(\lambda)d\lambda$, in order to get a detection probability P_i for each i-th detector of the array.

$$P_i = \frac{\int D_i(\lambda)d\lambda}{\int S(\lambda)d\lambda} \tag{E.1}$$

The total detection probability of the bank P_{tot} was given by the sum of the values obtained from all the detectors.

$$P_{tot} = \sum P_i \tag{E.2}$$

Finally the gain G of a single dataset is obtained by dividing P_{tot} by the current TOSCA total detection probability P_0, obtained from previous calculations of the current secondary spectrometer.

$$G = \frac{P_{tot}}{P_0} \tag{E.3}$$

Resolution Each elastic line from the 13 detectors were fitted independently with a Gaussian function to retrieve FWHM in meV, while the simulated incident wavelength range on the sample was 3 Å $\leq \lambda \leq$ 7 Å. The elastic line FWHM was divided by the peak position in energy to get the resolution R_i of the i-th detector. Since the count-rate of the detectors varies across the array, the average elastic resolution R was calculated by means of a weighted average, where the weights are the P_i (detection probability) of the detectors, after taking into account the energy overlap between signals from the different detectors.

$$R = \frac{\sum R_i P_i}{P_{tot}} \tag{E.4}$$

Results

- Analyzer area: 960 cm^2
- Curvature: parabolic (RH^{-1} = 1.755 m^{-1}, RV^{-1} = 0.875 m^{-1})
- Wavelength range: 3 Å $\leq \lambda \leq$ 7 Å
- Reference dataset (current secondary): 144 cm^2 flat analyzer, 140 arcmin mosaicity, R = 8.0%, Gain = 1

Mosaicity (arcmin)	R (%) err ± 0.2	Gain (a. u.) err ± 0.3
150	8.0	6.3
180	8.4	7.6
210	8.9	8.8
240	9.2	10.0
270	9.4	11.2
300	9.6	12.3

Table E.1. – Gain and resolution of the 960 cm^2 parabolically curved analyzer in relation to the 144 cm^2 flat analyzer, as a function of the curved analyzer mosaicity.

Bibliography

[1] P. Willendrup, E. Farhi, K. Lefmann, P. Astrand, M. Hagen, K. Nielsen, User and programmers guide to the neutron ray-tracing package McStas, Riso Denmark Technical University (2014).

[2] D. Colognesi, M. Celli, F. Cilloco, R. Newport, S. Parker, V. Rossi-Albertini, F. Sacchetti, J. Tomkinson, M. Zoppi, TOSCA neutron spectrometer: the final configuration, Applied Physics A 74 (1) (2002) s64–s66.

[3] S. Parker, F. Fernandez-Alonso, A. Ramirez-Cuesta, J. Tomkinson, S. Rudic, R. Pinna, G. Gorini, Recent and future developments on TOSCA at ISIS, Journal of Physics: Conference Series 554 (2014) 012003.

[4] C. Windsor, Pulsed neutron scattering, Taylor & Francis, 1981.

[5] R. Pinna, Monte Carlo Simulation of TOSCA Neutron Spectrometer: Assessment of Current Performance and Upgrade Design. M.Sc. thesis., Universita' degli Studi di Milano-Bicocca, (2014).

[6] R. Pinna, S. Rudic, S. Parker, G. Gorini, F. Fernandez-Alonso, Monte Carlo simulations of the TOSCA spectrometer: Assessment of current performance and future upgrades, European Physical Journal Web of Conferences 83 (2015) 03013.

[7] V. R. Albertini, D. Colognesi, J. Tomkinson, A study on the calibration of a time-focused inelastic neutron scattering spectrometer, Journal of Neutron Research 8 (4) (2000) 245–259.

[8] T. Riste, Singly bent graphite monochromators for neutrons, Nuclear Instruments and Methods 86 (1) (1970) 1–4.

[9] R. Scherm, G. Dolling, R. Ritter, E. Schedler, W. Teuchert, V. Wagner, A variable curvature analyser crystal for three-axis spectrometers, Nuclear Instruments and Methods 143 (1) (1977) 77–85.

[10] I. Dolbnya, K. Zolotarev, M. Sheromov, A. Antonov, I. Grigoryeva, Focusing parabolic pyrolytic graphite x-ray monochromator, Nuclear Instruments and Methods in Physics Research Section A: Accelerators, Spectrometers, Detectors and Associated Equipment 359 (1) (1995) 141–145.

[11] L. Pintschovius, Performance of a three-axis neutron spectrometer using horizontally and vertically focussing monochromators, Nuclear Instruments and Methods in Physics Research Section A: Accelerators, Spectrometers, Detectors and Associated Equipment 338 (1) (1994) 136–143.

[12] S. Smee, J. Orndorff, G. Scharfstein, Y. Qiu, P. Brand, C. Broholm, D. Anand, Macs low-background doubly focusing neutron monochromator, Applied Physics A 74 (1) (2002) s255–s257.

[13] S. A. Smee, P. C. Brand, D. D. Barry, C. L. Broholm, D. K. Anand, An elastic, low-background vertical focusing element for a doubly focusing neutron monochromator, Nuclear Instruments and Methods in Physics Research Section A: Accelerators, Spectrometers, Detectors and Associated Equipment 466 (3) (2001) 513–526.

[14] P. A. Seeger, L. L. Daemen, J. Z. Larese, Resolution of VISION, a crystal-analyzer spectrometer, Nuclear Instruments and Methods in Physics Research Section A: Accelerators, Spectrometers, Detectors and Associated Equipment 604 (3) (2009) 719–728.

[15] E. Farhi, Y. Debab, P. Willendrup, iFit: a new data analysis framework. applications for data reduction and optimization of neutron scattering instrument simulations with McStas, Journal of Neutron Research 17 (1) (2014) 5-18.

[16] J. Castanon, Monte Carlo simulations for the development of TOSCA's guide at ISIS, Technical Report RAL-TR-2013-002, Rutherford Appleton Laboratory, STFC, Chilton, UK (2013).

[17] S. Rudic, A. Ramirez-Cuesta, S. Parker, F. Fernandez-Alonso, R. Pinna, G. Gorini, C. Salzmann, S. McLain, N. Skipper, TOSCA international beamline review, Technical Report RAL-TR-2013-015, Rutherford Appleton Laboratory, STFC, Chilton, UK (2013).

[18] R. Pinna, S. Rudic, M. Capstick, D. McPhail, D. Pooley, G. Howells, G. Gorini, F. Fernandez-Alonso, Detailed characterisation of the incident neutron beam on the TOSCA spectrometer, Nuclear Instruments and Methods in Physics Research Section A: Accelerators, Spectrometers, Detectors and Associated Equipment 870 (2017) 79–83.

[19] R. Pinna, S. Rudic, S. Parker, J. Armstrong, M. Zanetti, G. Skoro, S. Waller, D. Zacek, C. Smith, M. Capstick, D. McPhail, D. Pooley, G. Howells, G. Gorini, F. Fernandez-Alonso, The neutron guide upgrade on the TOSCA spectrometer, submitted to Nuclear Instruments and Methods in Physics Research Section A: Accelerators, Spectrometers, Detectors and Associated Equipment, (2017).

[20] R. Pinna, M. Zanetti, S. Rudic, S. Parker, J. Armstrong, S. Waller, D. Zacek, C. Smith, S. Harrison, G. Gorini, F. Fernandez-Alonso, The TOSCA spectrometer at ISIS: the guide upgrade and beyond, Journal of Physics: Conference Series accepted, (2017).

[21] V. Mikerov, I. Zhitnik, S. Kuzin, V. Krutov, V. Tukarev, A. Antonov, I. Grigorieva, W. Waschkowski, A parabolic concentrator for thermal neutrons, Physica Scripta 55 (1) (1997) 30.

[22] B. Terence, M. Willis, C. Carlile, Experimental neutron scattering, Oxford University Press, Oxford, 2009.

Nomenclature

B3	Backscattering bank 3
HOPG	Highly oriented pyrolytic graphite
INS	Inelastic neutron scattering
L0	Primary branch of the spectrometer
L1	Secondary branch of the spectrometer
PSD	Position sensitive detector
TOF	Time of flight

Paper VI

The TOSCA Spectrometer at ISIS: the Guide Upgrade and Beyond

R.S. Pinna,[1,2] M. Zanetti,[1,2] S. Rudić,[1] S.F. Parker,[1] J. Armstrong,[1] S. Waller,[1] D. Zacek,[1] C. Smith,[1] S. Harrison,[1] G. Gorini,[2] and F. Fernandez-Alonso[1,3]

[1] ISIS Facility, Rutherford Appleton Laboratory, Chilton, Didcot, Oxfordshire OX11 0QX, United Kingdom

[2] CNISM, Universitá degli Studi di Milano-Bicocca, Piazza della Scienza 3, 20126 Milano, Italy

[3] Department of Physics and Astronomy, University College London, Gower Street, London WC1E 6BT, United Kingdom

Abstract. We describe progress to date with the most significant upgrade of the TOSCA spectrometer since it first became operational over fifteen years ago. This major project to boost the incident flux on the instrument by over an order of magnitude has been implemented over the past couple of years and has involved the complete redesign of the primary spectrometer to house a state-of-the-art, high-m neutron guide and associated chopper system. Engineering design and subsequent installation and commissioning efforts have been supported by extensive neutron-transport simulations and baseline studies of neutronic response in the context of the ISIS TS1 Project. Looking further ahead, we also outline ongoing feasibility studies to upgrade the secondary spectrometer, with a view to additional order-of-magnitude gains in neutronic and scientific performance.

1. Overview

The TOSCA instrument at the ISIS Pulsed Neutron and Muon Source is an indirect-geometry inelastic neutron spectrometer optimised for high-resolution vibrational spectroscopy in the energy-transfer range 0–4000 cm^{-1} [1]. The instrument has been operational since the turn of this century and has become the gold standard for broadband chemical spectroscopy with neutrons [2, 4]. As such, both TOSCA as well as its vibrant and growing science programme have been the inspiration for recent and exciting developments in novel neutron instrumentation across the globe. These include VISION at the SNS in the USA [5], LAGRANGE at the ILL in France [6], and VESPA at the ESS in Sweden [7]. Key factors to the success of TOSCA have been its high spectral resolution over a wide dynamic range, its ease of use, as well as the full integration of contemporary computational materials modelling into its science programme. At present, its *INS Database* [8] contains over 700 entries, and these data continues to be mined by a growing community worldwide, in addition to fresh and exciting science on the instrument across materials chemistry, energy research, or catalysis, to name a few areas of strength.

In 2013, an international panel of experts recognised the pressing need to boost the incident flux on the instrument, in order to move forward beyond the state-of-the-art in key scientific areas such as gas and charge storage [2, 3]. Following this exercise, extensive neutronic calculations have been performed to benchmark the existing instrument in the context of the ISIS TS1

Project, as well as to provide a well-defined scientific and engineering specification. For further details, see Refs. [9–11]. These efforts have been followed by the construction and installation of the new guide over the past couple of years as well as by feasibility studies to upgrade the secondary spectrometer, as reported below.

2. The Guide Upgrade

The original geometry of the TOSCA primary spectrometer relied on simple (passive) collimation of the incident beam over a distance of 17 m. This configuration has served the instrument well over the past two decades, yet at the same time it did not capitalise from advances in neutron-guide technology for the effective delivery of neutron flux at the sample position. The first step in this project involved extensive Monte-Carlo simulations using the McStas package [12] to explore a suitable geometry for optimal neutron transport over a wide wavelength range without compromising the spectroscopic capabilities of the instrument. From these simulations, a tapered geometry with an increasing m-number over distance from the spallation target was chosen. These simulations predicted an average gain in flux well above one order-of-magnitude over the wavelength bandwidth of the instrument [2, 4, 9–11]. At the longest wavelengths accessible on TOSCA, these calculations indicated that gain factors could approach up to two orders of magnitude.

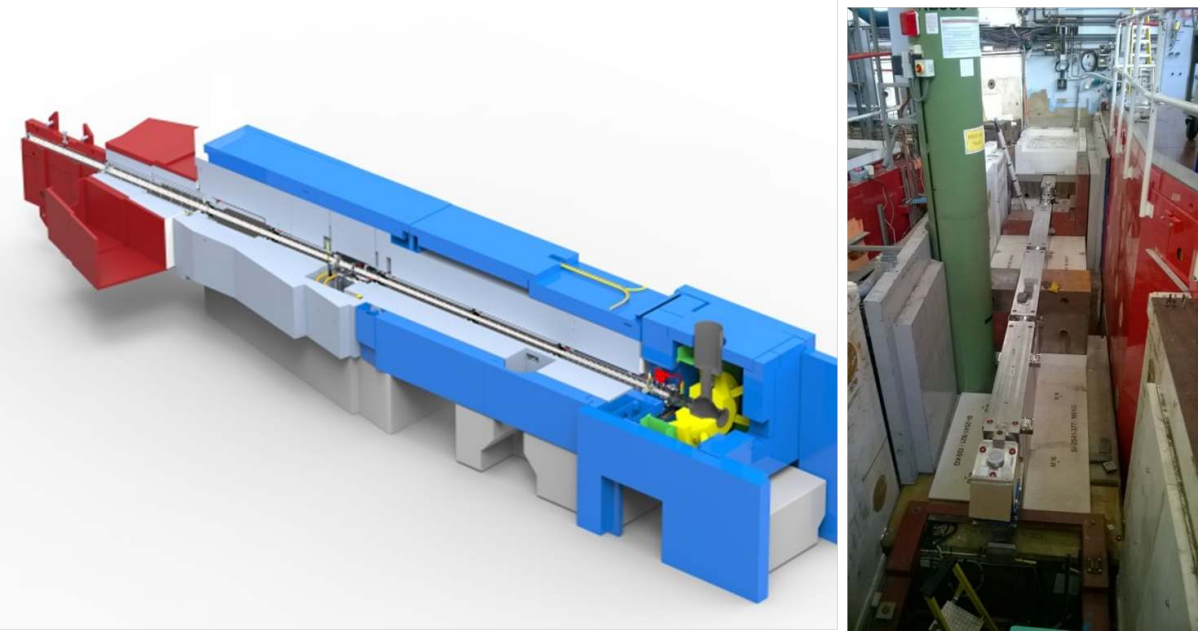

Figure 1. Left: Engineering design of the TOSCA guide following neutronics simulations. The ISIS TS1 target area is located on the left of the figure, whereas the TOSCA secondary spectrometer is depicted in yellow and green on the right-hand side. Right: Final stages of the first phase of the installation, completed in November 2016.

Figure 1 shows a schematic diagram of the final engineering design of the guide according to the above specifications. Following manufacture by *Swiss Neutronics* over the period 2015-16, the guide was installed on TOSCA during the second half of 2016. In a first installation phase, all guide sections except the shutter insert inside the target monolith were installed, and this step was followed by a brief and preliminary commissioning period during December 2016. These two installation phases were required because of the radiation hazards associated with the

handling of beamline components in close proximity to the spallation target. The preliminary commissioning tests that we have conducted during the first phase are very encouraging. The beam profile was found to be homogeneous across the sample area and the observed gains were somewhat higher than expected from the neutronic simulations of the *baseline* scientific specification, particularly at long wavelengths. The second and final phase of the installation schedule started in late February 2017 and has been followed by extensive commissioning tests on the instrument, due for completion at the end of March 2017. A detailed analysis of gains and other performance criteria is currently underway.

3. A New Secondary Spectrometer

TOSCA uses the (002) Bragg reflection from Highly Oriented Pyrolytic Graphite (HOPG) to effect final-energy selection. At present, each analyser bank on TOSCA consists of a flat square of area $\sim$144 cm^2, sitting at an average distance of 320 mm from the sample position. Its surface normal is placed at an angle of 45° relative to the scattered beam, leading to a final energy of *ca.* 28 cm^{-1}. A beryllium filter equipped with cadmium foils is placed between HOPG analyser and detectors to suppress higher-order HOPG reflections. This filter is cooled down to *ca.* 30 K to improve the rejection of neutrons with energies above *ca.* 40 cm^{-1}. In its current incarnation, the HOPG analyser and the beryllium filter are very close to each other. While being a compact and practical solution requiring a relatively small HOPG analyser area, this feature also poses severe constraints on the overall neutron-collection efficiency of the secondary spectrometer.

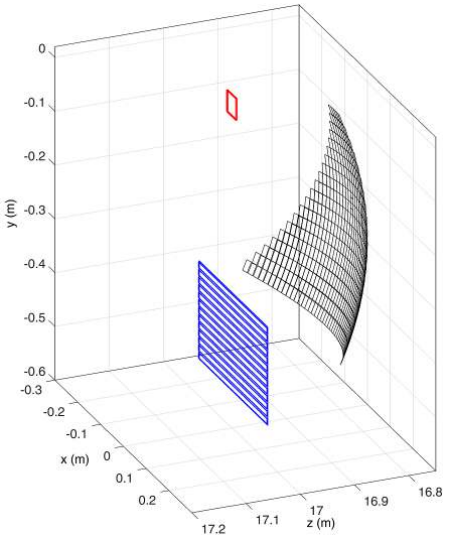

Figure 2. Curved HOPG analyser (black), sample (red), and detector array (blue).

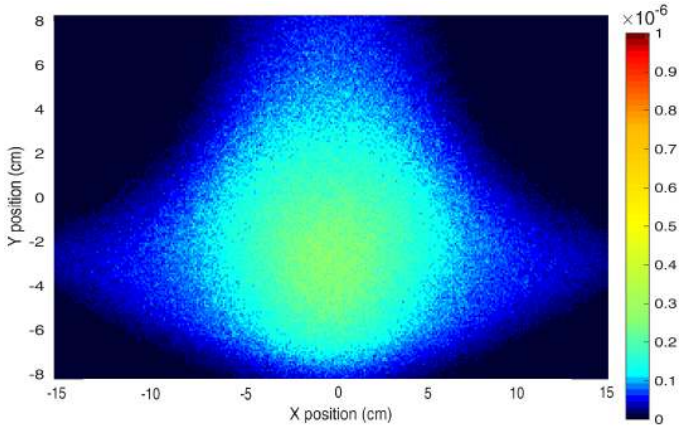

Figure 3. Spatial intensity distribution of detected neutrons from a parabolic HOPG analyser of total area 960 cm^2.

To circumvent these limitations, we have started assessing other potential geometries that also build upon recent experience with similar instruments worldwide [5, 6]. Using the McStas package, we have created a custom component where HOPG tiles are arranged on either a spherical or parabolic surface of variable area. Figure 2 shows a three-dimensional view of the resulting computer model of a curved HOPG analyser, and Fig. 3 reports a typical spatial intensity distribution of detected neutrons. Preliminary Monte Carlo simulations and associated geometric optimisations using McStas [12] and iFit [13] have been performed as a function of analyser area and radius of curvature. These calculations show that an order-of-magnitude

increase in detected flux is well within reach, particularly via the use of a parabolic (as opposed to spherical) analyser geometry. We have also found that the detected flux can be increased by optimising parameters such as the mosaicity of the HOPG array without compromising spectroscopic performance. In ideal circumstances, the shape of the curved HOPG analyser could be increased as much as to occupy an angular span of 60°, provided that engineering constraints can allow for it. Calculations have already been performed for three different sizes of doubly bent HOPG analysers of either spherical or parabolic shape. Our largest-area analysers amount to *ca.* 1500 cm^2, a similar size to the one used earlier by Smee *et al.* at NIST to improve the performance of cold-neutron spectrometers [14, 15].

In a wider context, we note that the original conceptual design and subsequent scientific specification of TOSCA decades ago were solely performed on the basis of analytical calculations, a task that necessarily relied on a number of hard-to-test assumptions at the time. This situation is particularly true for the trade-off between flux and spectral resolution, as well as for the conditions required to attain an optimal match of the many different contributions to the neutronic response that are associated with both primary and secondary spectrometers. The present work using modern neutron-transport codes, therefore, offers the exciting prospects of assessing in quantitative and unprecedented detail the relative importance of these parameters, including analyser shape and size, as well as time- and energy-focusing conditions. We, therefore, anticipate that the lessons learnt from this work will also have important implications to the optimal neutronic design of similar instrumentation in the foreseeable future.

Acknowledgements

The authors gratefully acknowledge the *Science & Technology Facilities Council* (STFC) for financial support for this project. This work has been partially supported by the 2014-2020 CNR-STFC Agreement concerning collaboration in scientific research at the ISIS Facility. We are also immensely grateful to *Swiss Neutronics* for the timely delivery of the guide components within specification.

References

[1] WEB: www.isis.stfc.ac.uk/instruments/tosca
[2] Rudić S, Ramirez-Cuesta AJ, Parker SF, Fernandez-Alonso F, Pinna RS, Gorini G, Salzmann GC, McLain SE, and Skipper NT 2013 *Rutherford Appleton Laboratory Technical Report* RAL-TR-2013-015, Chilton. WEB: epubs.stfc.ac.uk/work/11216706
[3] For a summary of the *TOSCA International Review* and its recommendations, see www.isis.stfc.ac.uk/news-and-events/news/2014/tosca-instrument-review15247.html
[4] Parker SF, Fernandez-Alonso F, Ramirez-Cuesta AJ, Tomkinson J, Rudić S, Pinna RS, Gorini G, and Fernández Castañón J 2014 *J. Phys. Conf. Ser.* **554** 012003.
[5] Seeger PA, Daemen LL, and Larese JZ 2009 *Nucl. Instr. Meth. Phys. Res. A* **604** 719.
[6] Jimenez-Ruiz M, Ivanov A, and Fuard S 2014 *J. Phys. Conf. Ser.* **549** 012004.
[7] Fedrigo A, Colognesi D, Bertelsen M, Hartl M, Lefmann K, Deen PP, Strobl M, Grazzi F, and Zoppi M 2016 *Rev. Sci. Instrum.* **87** 0651014.
[8] WEB: www.isis.stfc.ac.uk/instruments/tosca/ins-database
[9] Pinna RS, Rudić S, Parker SF, Gorini G, and Fernandez-Alonso F 2015 *EPJ Web of Conferences* **83** 03013.
[10] Pinna RS, *MSc Thesis* (Università degli Studi di Milano-Bicocca, Italy, 2014). WEB: epubs.stfc.ac.uk/work/12257011
[11] Fernández Castañón J 2013 *Rutherford Appleton Laboratory Technical Report* RAL-TR-2013-002, Chilton. WEB: epubs.stfc.ac.uk/work/65395
[12] Willendrup PK, Udby L, Knudsen E, Farhi E, and Lefmann K 2011 *Nucl. Instr. Meth. Phys. Res. A* **634** S150. WEB: www.mcstas.org
[13] Farhi E, Debab Y, and Willendrup P 2014 *J. Neut. Res.* **17** 5.
[14] Smee SA, Orndorff JD, Scharfstein GA, Qiu Y, Brand PC, Broholm CL, and Anand DK 2002 *Appl. Phys. A* **74** S255.
[15] Smee SA, Brand PC, Barry DD, Broholm CL, and Anand DK 2001 *Nucl. Instr. Meth. Phys. Res. A* **466** 513.

Appendix

A. Appendix
Mantid data processing for TOSCA

The Mantid [29] workflow from the TOSCA raw data to the energy transfer spectrum is done mainly by the *ISISindirectEnergyTransfer* algorithm which performs the tasks illustrated below.

1. The data is loaded in using the *LoadRaw* algorithm that loads each of the input files and set the instrument parameters into the loaded workspace. This produces a workspace per loaded run.
2. Chops the data in each workspace into single frames using the *ChopData* algorithm and creates a workspace group of chopped runs. To do this, it takes into account *Workflow.ChopDataIfGreaterThan*, which is a parameter defined in the parameter file. It also uses *Workflow.Monitor1-SpectrumNumber*, also defined in the parameter file, to extract the beam monitor spectra. This produces a group of 4 workspaces containing all the raw spectra (one for each frame) and 4 workspaces containing the monitor values.
3. Then the monitor is extracted using *ExtractSingleSpectrum* and put into a new workspace. The same is done for the detectors, using *CropWorkspace*. This is done for each of the chopped runs created in the previous step.
4. Then "chopped" runs are merged using *MergeRuns* and scaled by a factor equal to the number of chopped runs. This step averages the signal coming from the subsequent pulses.
5. Any detectors which show excessive noise are identified using the *IndentifyNoisyDetectors* algorithm and a mask is created and later used to exclude these detectors from the data analysis.
6. Next, the beam monitor is processed. First the spectra are converted to wavelength with *EMode.Elastic*, and then corrected by the efficiency using algorithm *OneMinusExponentialCorr* (this algorithm is run with parameters *Workflow.Monitor1-Area*, *Workflow.Monitor1-Thickness* and *Workflow.Monitor1-Attenuation*, all defined in the parameter file). The use of the correction formula for the beam monitor presented in this chapter is further confirmed by the routine shown in Mantid and the current documentation on the Mantid web page. Then monitors are scaled using *Scale* algorithm by a scale factor given by *Workflow.Monitor1-ScalingFactor*, again defined in the parameter file.

7. Detector workspaces are converted to wavelength using *ConvertUnits*, re-binned to the monitor workspace using *RebinToWorkspace* and divided by monitors by the *Divide* algorithm. This process harmonize the units used to bin the spectra and normalize the data by the TOSCA incident monitor, thus eliminating from the final spectra the artifacts due to the peculiar shape of the incident spectrum.
8. Then, the normalized detector workspaces from the previous step are converted to *DeltaE* by running *ConvertUnits* with *Emode.Indirect*.
9. Then *CorrectKiKf* is run on the workspaces in *DeltaE*. This algorithm is run with *EMode.Indirect*. For each spectrum, the *CorrectKiKf* algorithm reads from the corresponding detector its value of *Efixed*. This *Efixed* is defined in the Instrument Definition File *TOSCA_Definition.xml* and each detector has a different value.
10. Detectors are masked according to the mask from step 5 and grouped using *GroupDetectors*, with *Behaviour.Average* and *MapFile.TOSCA_Grouping.xml*.
11. At this point we have different workspaces corresponding to the selected data. All these are combined again using *MergeRuns* and the resulting workspace is normalized by a scaling workspace.
12. The final workspace is eventually converted to *DeltaE_inWavenumber* and renamed.

B. Appendix
Specifications for TOSCA detectors

Detector	Spectrum	Secondary branch (m)	Bragg Angle θ (Deg)	φ (deg)	Calibration E (meV)
B1.1	1	0.564	50.825	150	2.690
B1.2	2	0.573	49.727	150	2.771
B1.3	3	0.581	48.732	150	2.855
B1.4	4	0.589	47.886	150	2.944
B1.5	5	0.598	46.955	150	3.037
B1.6	6	0.608	45.936	150	3.135
B1.7	7	0.618	45.000	150	3.239
B1.8	8	0.626	44.314	150	3.346
B1.9	9	0.638	43.214	150	3.462
B1.10	10	0.649	42.305	150	3.583
B1.11	11	0.662	41.305	150	3.711
B1.12	12	0.674	40.422	150	3.847
B1.13	13	0.687	39.519	150	3.990
B2.1	15	0.567	50.421	-150	2.711
B2.2	16	0.573	49.729	-150	2.791
B2.3	17	0.582	48.710	-150	2.876
B2.4	18	0.591	47.680	-150	2.968
B2.5	19	0.602	46.542	-150	3.066
B2.6	20	0.613	45.465	-150	3.170
B2.7	21	0.622	44.593	-150	3.281
B2.8	22	0.635	43.527	-150	3.400
B2.9	23	0.649	42.293	-150	3.529
B2.10	24	0.662	41.315	-150	3.667
B2.11	25	0.675	40.359	-150	3.813
B2.12	26	0.690	39.309	-150	3.973
B2.13	27	0.706	38.214	-150	4.146

Detector	Spectrum	Secondary branch (m)	Bragg Angle θ (Deg)	φ (deg)	Calibration E (meV)
B3.1	29	0.569	50.126	-90	2.710
B3.2	30	0.575	49.479	-90	2.790
B3.3	31	0.585	48.348	-90	2.878
B3.4	32	0.596	47.193	-90	2.974
B3.5	33	0.604	46.310	-90	3.076
B3.6	34	0.616	45.224	-90	3.187
B3.7	35	0.626	44.248	-90	3.307
B3.8	36	0.641	42.986	-90	3.439
B3.9	37	0.656	41.761	-90	3.582
B3.10	38	0.671	40.622	-90	3.737
B3.11	39	0.689	39.379	-90	3.907
B3.12	40	0.707	38.148	-90	4.093
B3.13	41	0.727	36.971	-90	4.297
B4.1	43	0.567	50.361	-30	2.695
B4.2	44	0.575	49.512	-30	2.773
B4.3	45	0.583	48.524	-30	2.857
B4.4	46	0.590	47.836	-30	2.946
B4.5	47	0.601	46.608	-30	3.045
B4.6	48	0.613	45.502	-30	3.150
B4.7	49	0.623	44.508	-30	3.264
B4.8	50	0.635	43.468	-30	3.386
B4.9	51	0.650	42.244	-30	3.521
B4.10	52	0.665	41.076	-30	3.665
B4.11	53	0.680	40.005	-30	3.824
B4.12	54	0.696	38.910	-30	3.996
B4.13	55	0.714	37.755	-30	4.184
B5.1	57	0.564	50.843	30	2.691
B5.2	58	0.572	49.794	30	2.770
B5.3	59	0.580	48.873	30	2.853
B5.4	60	0.590	47.833	30	2.942
B5.5	61	0.602	46.567	30	3.036
B5.6	62	0.608	45.930	30	3.136
B5.7	63	0.617	45.088	30	3.241
B5.8	64	0.630	43.928	30	3.355
B5.9	65	0.642	42.900	30	3.475
B5.10	66	0.655	41.850	30	3.603
B5.11	67	0.669	40.776	30	3.741
B5.12	68	0.684	39.687	30	3.889
B5.13	69	0.694	39.056	30	4.044

Table B.1. – Calibration values used to reduce the data generated by the TOSCA inelastic back-scattering banks.

Detector	Spectrum	Secondary branch (m)	Bragg Angle θ (Deg)	φ (deg)	Calibration E (meV)
F1.1	71	0.563	50.929	150	2.690
F1.2	72	0.572	49.826	150	2.766
F1.3	73	0.580	48.899	150	2.860
F1.4	74	0.587	48.074	150	2.952
F1.5	75	0.600	46.730	150	3.052
F1.6	76	0.610	45.778	150	3.157
F1.7	77	0.620	44.815	150	3.268
F1.8	78	0.630	43.894	150	3.385
F1.9	79	0.644	42.734	150	3.512
F1.10	80	0.658	41.625	150	3.648
F1.11	81	0.674	40.426	150	3.793
F1.12	82	0.687	39.486	150	3.947
F1.13	83	0.703	38.431	150	4.113
F2.1	85	0.565	50.709	-150	2.711
F2.2	86	0.573	49.655	-150	2.790
F2.3	87	0.582	48.648	-150	2.876
F2.4	88	0.591	47.674	-150	2.968
F2.5	89	0.603	46.486	-150	3.070
F2.6	90	0.614	45.333	-150	3.179
F2.7	91	0.624	44.430	-150	3.298
F2.8	92	0.640	43.105	-150	3.429
F2.9	93	0.656	41.800	-150	3.571
F2.10	94	0.669	40.792	-150	3.726
F2.11	95	0.687	39.486	-150	3.898
F2.12	96	0.707	38.146	-150	4.086
F2.13	97	0.728	36.892	-150	4.293
F3.1	99	0.562	51.074	-90	2.711
F3.2	100	0.569	50.200	-90	2.789
F3.3	101	0.578	49.084	-90	2.875
F3.4	102	0.584	48.457	-90	3.068
F3.5	103	0.598	46.947	-90	3.068
F3.6	104	0.609	45.822	-90	3.178
F3.7	105	0.623	44.503	-90	3.298
F3.8	106	0.636	43.435	-90	3.428
F3.9	107	0.652	42.073	-90	3.571
F3.10	108	0.667	40.925	-90	3.726
F3.11	109	0.686	39.590	-90	3.898
F3.12	110	0.707	38.207	-90	4.087
F3.13	111	0.726	36.998	-90	4.294

Detector	Spectrum	Secondary branch (m)	Bragg Angle θ (Deg)	φ(deg)	Calibration E (meV)
F4.1	113	0.564	50.850	-30	2.714
F4.2	114	0.574	49.607	-30	2.802
F4.3	115	0.581	48.798	-30	2.893
F4.4	116	0.593	47.507	-30	2.990
F4.5	117	0.600	46.699	-30	3.088
F4.6	118	0.613	45.516	-30	3.193
F4.7	119	0.623	44.574	-30	3.300
F4.8	120	0.631	43.793	-30	3.411
F4.9	121	0.645	42.620	-30	3.529
F4.10	122	0.654	41.889	-30	3.648
F4.11	123	0.669	40.817	-30	3.775
F4.12	124	0.680	40.003	-30	3.906
F4.13	125	0.693	39.090	-30	4.043
F5.1	127	0.561	51.115	30	2.688
F5.2	128	0.573	49.693	30	2.787
F5.3	129	0.581	48.732	30	2.865
F5.4	130	0.588	47.982	30	2.953
F5.5	131	0.600	46.717	30	3.048
F5.6	132	0.608	45.920	30	3.158
F5.7	133	0.621	44.720	30	3.269
F5.8	134	0.636	43.442	30	3.394
F5.9	135	0.646	42.592	30	3.524
F5.10	136	0.661	41.387	30	3.665
F5.11	137	0.675	40.372	30	3.812
F5.12	138	0.691	39.210	30	3.969
F5.13	139	0.705	38.297	30	4.134

Table B.2. – Calibration values used to reduce the data generated by the TOSCA inelastic forward-scattering banks.

C. Appendix
McStas curved analyzer code for TOSCA

In this appendix we report an extract of the relevant McStas [13] source code that has been developed during this project. We designed this code to simulate the curved analyser component, which is inserted in the instrument model after the sample to intecept the propagated neutron rays before the detector array, Fig. C.1. This component can be used for present and future calculations of the TOSCA secondary spectrometer. The details of the geometrical construction of this curved analyzer component can be found in [19].

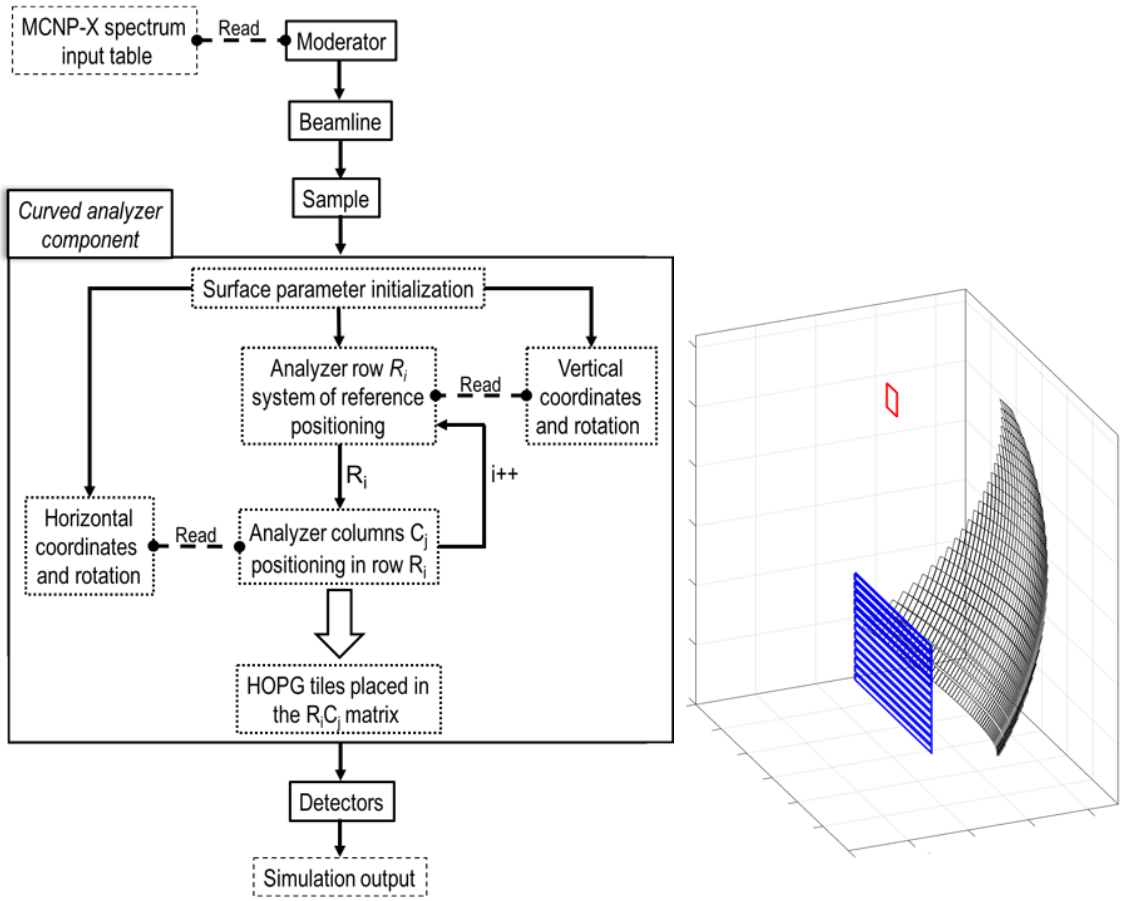

Figure C.1. – (left) Scheme of the McStas model for the TOSCA instrument, with the flowchart of the custom component designed to simulate a doubly curved analyzer. (right) View of the McStas model for the TOSCA secondary, the sample is shown in red, the curved analyzer in black and the detectors in blue.

The 1 x 2 cm^2 rectangular HOPG tiles are arranged in rows and columns to map a curved surface. The row centre is positioned and rotated first, then a specific number of tiles (columns) are placed and rotated to fill that row along the surface. This operation is repeated in a loop to build all the rows of the analyzer. The number of rows defines the analyzer total height, while the number of tiles for each row defines the width. This algorithm allows to specify the number, centre and rotation along 2 axis of each HOPG tile, thus with the appropriate geometrical specifications a wide range of surfaces can be mapped.

Declaration of the variables

```
DECLARE %{
//##### MONITORS
141 double Z141 = 15.794; //m, beam monitor position
double t_min = 1000; //microsec, min time detected
double t_max = 40000; //microsec, max time detected
//##### SAMPLE
double Zs_tosca = 17.0; //m, tosca sample position
int flag = 0; //integer, event flag
double s_y = 0.04; double s_thick=0.002; int Split_sample = 5;
//##### THE INS ASSEMBLY
//Analyzers
//m, position back analyzers
double Xmb, Ymb1, Zmb1, Ymb2, Zmb2, Ymb3, Zmb3, Ymb4, Zmb4, Ymb5, Zmb5;
//m, position fwd analyzers
double Xmf, Ymf1, Zmf1, Ymf2, Zmf2, Ymf3, Zmf3, Ymf4, Zmf4, Ymf5, Zmf5;
double d_spacing = 3.354; //Angstrom, monochromator lattice planes separation
double deltad_mono; //dimensionless, monocromator DeltaD
double M_Mosaic; //arc minutes, monochromator mosaicity
double reflect = 0.866; //dimensionless, monochromator reflectivity
double trm_filter; //dimensionless, transmission through the Be filter
//INS detectors
//m, back-scattering bank position
double Xdb, Ydb1, Ydb2, Ydb3, Ydb4, Ydb5, Zdb;
//m, fwd-scattering bank position
double Xdf, Ydf1, Ydf2, Ydf3, Ydf4, Ydf5, Zdf;
double Dsep = 0.014; //m, detectors separation
double DWidth=0.30; //m, squashed tube width
double DHeight=0.01; //m, squashed tube height
double DDepth = 0.0025; //m, He3 squashed tube thickness
```

```
double tmin_back = 5000; //microsec, min time backscattering
double tmin_fwd = 5000; //microsec min time fwd-scattering
double tmax_back = 40000; //microsec max time back-scattering
double tmax_fwd = 40000; //microsec max time fwd-scattering
double emin_back = 1; //meV, min E back-scattering
double emin_fwd = 1; //meV, min E fwd-scattering
double emax_back = 1000; //meV, max E back-scattering
double emax_fwd = 1000; //meV, max E fwd-scattering
double lmin_back = 0.28; //Angstrom, min wavelength back-scattering
double lmin_fwd = 0.28; //Angstrom, min wavelength fwd-scattering
double lmax_back = 4.65; //Angstrom, max wavelength back-scattering
double lmax_fwd = 4.65; //Angstrom, max wavelength fwd-scattering

//Modules geometry
//m, back-scattering path
double l_flight_b1, l_flight_b2, l_flight_b3, l_flight_b4, l_flight_b5 = 17.65;
//m, fwd-scattering path
double l_flight_f1, l_flight_f2, l_flight_f3, l_flight_f4, l_flight_f5 = 17.65;
double dtheta = 60; //deg, separation between each bank on the xy plane
double phi_back = 135; //deg, azimuth of back banks on the xz plane
double phi_fwd = 45; //deg, azimuth of backsc. banks on the xz plane
double dtheta_rad,phi_back_rad,phi_fwd_rad; //rad, angles conversion
double InLim=-0.19; // m, inner limit of the monochromator
double OutLim=0.500; // m, outer limit of the monochromator
double Side=0.0100; // m, HOPG tile size
double ParHA; double ParHB = 0; double ParHC = 0; //curve parameters
double ParVA; double ParVB = 0; double ParVC = 0; //curve parameters
double Monok_area; double Monok_Xangle; //deg, tilt the curve around the X axis
double Monok_Yangle; //deg, tilt the curve around the Y axis
double Monok_Zangle; //deg, tilt the curve around the Z axis
%}
```

Initialization of the variables

```
INITIALIZE %{
// Energy-Wavelength conversion
E_min=81.794/L_max/L_max; E_max=81.794/L_min/L_min;
//Monitor limits
Emon_min = E_min; Emon_max = E_max;
//##### INS assembly
//Angles
dtheta_rad=(PI/180)*dtheta;
```

```
phi_back_rad=(PI/180)*phi_back;
phi_fwd_rad=(PI/180)*phi_fwd;

//Position back analyzers
Xmb = 0; Ymb1 = ((l_flight_b1-17)/2.0)*sin(phi_back_rad);
Zmb1 = ((l_flight_b1-17)/2.0)*cos(phi_back_rad);
Ymb2 = ((l_flight_b2-17)/2.0)*sin(phi_back_rad);
Zmb2 = ((l_flight_b2-17)/2.0)*cos(phi_back_rad);
Ymb3 = ((l_flight_b3-17)/2.0)*sin(phi_back_rad);
Zmb3 = ((l_flight_b3-17)/2.0)*cos(phi_back_rad);
Ymb4 = ((l_flight_b4-17)/2.0)*sin(phi_back_rad);
Zmb4 = ((l_flight_b4-17)/2.0)*cos(phi_back_rad);
Ymb5 = ((l_flight_b5-17)/2.0)*sin(phi_back_rad);
Zmb5 = ((l_flight_b5-17)/2.0)*cos(phi_back_rad);

//Position back detectors
Xdb= 0; Ydb1 = (l_flight_b1-17)*sin(phi_back_rad);
Ydb2 = (l_flight_b2-17)*sin(phi_back_rad);
Ydb3 = (l_flight_b3-17)*sin(phi_back_rad);
Ydb4 = (l_flight_b4-17)*sin(phi_back_rad);
Ydb5 = (l_flight_b5-17)*sin(phi_back_rad);
Zdb = 16.998-17;

//Position forward analyzers
Xmf=0; Ymf1 = ((l_flight_f1-17)/2.0)*sin(phi_fwd_rad);
Zmf1 = ((l_flight_f1-17)/2.0)*cos(phi_fwd_rad);
Ymf2 = ((l_flight_f2-17)/2.0)*sin(phi_fwd_rad);
Zmf2 = ((l_flight_f2-17)/2.0)*cos(phi_fwd_rad);
Ymf3 = ((l_flight_f3-17)/2.0)*sin(phi_fwd_rad);
Zmf3 = ((l_flight_f3-17)/2.0)*cos(phi_fwd_rad);
Ymf4 = ((l_flight_f4-17)/2.0)*sin(phi_fwd_rad);
Zmf4 = ((l_flight_f4-17)/2.0)*cos(phi_fwd_rad);
Ymf5 = ((l_flight_f5-17)/2.0)*sin(phi_fwd_rad);
Zmf5 = ((l_flight_f5-17)/2.0)*cos(phi_fwd_rad);

//Position forward detectors
Xdf = 0; Ydf1 = (l_flight_f1-17)*sin(phi_fwd_rad);
Ydf2 = (l_flight_f2-17)*sin(phi_fwd_rad);
Ydf3 = (l_flight_f3-17)*sin(phi_fwd_rad);
Ydf4 = (l_flight_f4-17)*sin(phi_fwd_rad);
Ydf5 = (l_flight_f5-17)*sin(phi_fwd_rad);
Zdf = 17.002-17;

%}
```

Definition of the components

COMPONENT arm_180 = Arm() AT (0,0,Zs_tosca) RELATIVE arm1
ROTATED (0, 0, dtheta*3) RELATIVE arm1

COMPONENT arm_monochr3_center = Arm() AT (Xmb, Ymb3, Zmb3)
RELATIVE arm_180 ROTATED
(Monok_Xangle, Monok_Yangle-90, Monok_Zangle) RELATIVE arm_180

SPLIT Split_monoB3 COMPONENT arm_monok_0 = Arm()
AT (0, 0, 0) RELATIVE arm_monochr3_center ROTATED (0, 0, 0)
RELATIVE arm_monochr3_center

COMPONENT monok = Monochromator_curved
(order=order_mono, mosaich = M_Mosaic, mosaicv = M_Mosaic, width = 0.01,
height = 0.02, reflect="HOPG.rfl", NH = 1, NV = 1, RH = 0, RV = 0,
gap = 0, r0=1, t0=0) WHEN(flag == 0) AT (0, 0, 0) RELATIVE
PREVIOUS(1) ROTATED (0, 0, 0) RELATIVE PREVIOUS(1)
GROUP B3_monoks EXTEND %{ if (SCATTERED) flag=13; %}

//##### Analyzer rows construction

// Row1 COMPONENT COPY(arm1) = Arm() AT
(ParVA*(InLim+1*2*Side)*(InLim+1*2*Side)+ParVB*(InLim+1*2*Side)+ParVC,
InLim+1*2*Side, 0) RELATIVE monok ROTATED
(0, 0, -180/PI*atan(ParVB+2*ParVA*(InLim+1*2*Side))) RELATIVE monok

// Row2 COMPONENT COPY(arm1) = Arm() AT
(ParVA*(InLim+2*2*Side)*(InLim+2*2*Side)+ParVB*(InLim+2*2*Side)+ParVC,
InLim+2*2*Side, 0) RELATIVE monok ROTATED
(0, 0, -180/PI*atan(ParVB+2*ParVA*(InLim+2*2*Side))) RELATIVE monok

// Row3 COMPONENT COPY(arm1) = Arm() AT
(ParVA*(InLim+3*2*Side)*(InLim+3*2*Side)+ParVB*(InLim+3*2*Side)+ParVC,
InLim+3*2*Side, 0) RELATIVE monok ROTATED
(0, 0, -180/PI*atan(ParVB+2*ParVA*(InLim+3*2*Side))) RELATIVE monok

•

•

•

// Row25 COMPONENT COPY(arm1) = Arm() AT
(ParVA*(InLim+25*2*Side)*(InLim+25*2*Side)+ParVB*(InLim+25*2*Side)+ParVC,

```
InLim+25*2*Side, 0) RELATIVE monok ROTATED
(0, 0, -180/PI*atan(ParVB+2*ParVA*(InLim+25*2*Side))) RELATIVE monok



//##### Analyzer tiles construction

arm() AT (0,0,0) RELATIVE row1
//R1C1 COMPONENT COPY(monok) = COPY(monok)
WHEN(flag==1)AT(ParHA*(0*Side)*(0*Side)+ParHB*(0*Side)+ParHC,0,0*Side)
RELATIVE PREVIOUS(1)ROTATED
(0, 180/PI*atan(ParHB+2*ParHA*0*Side), 0) RELATIVE PREVIOUS(1)
GROUP B3_monoks EXTEND %{ if (SCATTERED) flag=13; %}
//R1C2 COMPONENT COPY(monok) = COPY(monok)
WHEN(flag==1)AT(ParHA*(1*Side)*(1*Side)+ParHB*(1*Side)+ParHC,0,1*Side)
RELATIVE PREVIOUS(2)ROTATED
(0, 180/PI*atan(ParHB+2*ParHA*1*Side), 0) RELATIVE PREVIOUS(2)
GROUP B3_monoks EXTEND %{ if (SCATTERED) flag=13; %}
//R1C3 COMPONENT COPY(monok) = COPY(monok)
WHEN(flag==1)AT(ParHA*(1*Side)*(1*Side)+ParHB*(1*Side)+ParHC,0,-1*Side)
RELATIVE PREVIOUS(3)ROTATED
(0, -180/PI*atan(ParHB+2*ParHA*1*Side), 0) RELATIVE PREVIOUS(3)
GROUP B3_monoks EXTEND %{ if (SCATTERED) flag=13; %}
//R1C4 COMPONENT COPY(monok) = COPY(monok)
WHEN(flag==1)AT(ParHA*(2*Side)*(2*Side)+ParHB*(2*Side)+ParHC,0,2*Side)
RELATIVE PREVIOUS(4)ROTATED
(0, 180/PI*atan(ParHB+2*ParHA*2*Side), 0)RELATIVE PREVIOUS(4)
GROUP B3_monoks EXTEND %{ if (SCATTERED) flag=13; %}
//R1C5 COMPONENT COPY(monok) = COPY(monok)
WHEN(flag==1)AT(ParHA*(2*Side)*(2*Side)+ParHB*(2*Side)+ParHC,0,-2*Side)
RELATIVE PREVIOUS(5)ROTATED
(0, -180/PI*atan(ParHB+2*ParHA*2*Side), 0) RELATIVE PREVIOUS(5)
GROUP B3_monoks EXTEND %{ if (SCATTERED) flag=13; %}
arm() AT (0,0,0) RELATIVE row2
WHEN(flag==1)AT(ParHA*(0*Side)*(0*Side)+ParHB*(0*Side)+ParHC,0,0*Side)
RELATIVE PREVIOUS(1)ROTATED
(0, 180/PI*atan(ParHB+2*ParHA*0*Side), 0) RELATIVE PREVIOUS(1)
GROUP B3_monoks EXTEND %{ if (SCATTERED) flag=13; %}
//R2C2 COMPONENT COPY(monok) = COPY(monok)
WHEN(flag==1)AT(ParHA*(1*Side)*(1*Side)+ParHB*(1*Side)+ParHC,0,1*Side)
RELATIVE PREVIOUS(2)ROTATED
(0, 180/PI*atan(ParHB+2*ParHA*1*Side), 0) RELATIVE PREVIOUS(2)
GROUP B3_monoks EXTEND %{ if (SCATTERED) flag=13; %}
//R2C3 COMPONENT COPY(monok) = COPY(monok)
```

WHEN(flag==1)AT(ParHA*(2*Side)*(2*Side)+ParHB*(2*Side)+ParHC,0,2*Side)
RELATIVE PREVIOUS(2)ROTATED
(0, 180/PI*atan(ParHB+2*ParHA*2*Side), 0) RELATIVE PREVIOUS(2)
GROUP B3_monoks EXTEND %{ if (SCATTERED) flag=13; %}

•

•

•

//R25C51 COMPONENT COPY(monok) = COPY(monok)
WHEN(flag==1)AT(ParHA*(25*Side)*(25*Side)+ParHB*(25*Side)+ParHC,0,-25*Side)
RELATIVE PREVIOUS(51)ROTATED
(0, -180/PI*atan(ParHB+2*ParHA*25*Side), 0) RELATIVE PREVIOUS(51)
GROUP B3_monoks EXTEND %{ if (SCATTERED) flag=13; %}
//R25C52 COMPONENT COPY(monok) = COPY(monok)
WHEN(flag==1)AT(ParHA*(26*Side)*(26*Side)+ParHB*(26*Side)+ParHC,0,26*Side)
RELATIVE PREVIOUS(52)ROTATED
(0, 180/PI*atan(ParHB+2*ParHA*26*Side), 0) RELATIVE PREVIOUS(52)
GROUP B3_monoks EXTEND %{ if (SCATTERED) flag=13; %}
//R25C53 COMPONENT COPY(monok) = COPY(monok)
WHEN(flag==1)AT(ParHA*(26*Side)*(26*Side)+ParHB*(26*Side)+ParHC,0,-26*Side)
RELATIVE PREVIOUS(53)ROTATED
(0, -180/PI*atan(ParHB+2*ParHA*26*Side), 0) RELATIVE PREVIOUS(53)
GROUP B3_monoks EXTEND %{ if (SCATTERED) flag=13; %}

Bibliography

[1] S. Parker, F. Fernandez-Alonso, A. Ramirez-Cuesta, J. Tomkinson, S. Rudic, R. Pinna, G. Gorini, Recent and future developments on TOSCA at ISIS, Journal of Physics: Conference Series 554 (2014) 012003.

[2] R. Pinna, S. Rudic, S. Parker, G. Gorini, F. Fernandez-Alonso, Monte Carlo simulations of the TOSCA spectrometer: Assessment of current performance and future upgrades, European Physical Journal Web of Conferences 83 (2015) 03013.

[3] K. Druzbicki, R. S. Pinna, S. Rudic, M. Jura, G. Gorini, F. Fernandez-Alonso, Unexpected cation dynamics in the low-temperature phase of methylammonium lead iodide: The need for improved models, The journal of physical chemistry letters 7 (22) (2016) 4701–4709.

[4] R. Pinna, S. Rudic, S. Parker, J. Armstrong, M. Zanetti, G. Skoro, S. Waller, D. Zacek, C. Smith, M. Capstick, D. McPhail, D. Pooley, G. Howells, G. Gorini, F. Fernandez-Alonso, The neutron guide upgrade on the TOSCA spectrometer, submitted to Nuclear Instruments and Methods in Physics Research Section A: Accelerators, Spectrometers, Detectors and Associated Equipment, (2017).

[5] S. Smee, J. Orndorff, G. Scharfstein, Y. Qiu, P. Brand, C. Broholm, D. Anand, Macs low-background doubly focusing neutron monochromator, Applied Physics A 74 (1) (2002) s255–s257.

[6] B. Terence, M. Willis, C. Carlile, Experimental neutron scattering, Oxford University Press, Oxford, 2009.

[7] P. Mitchell, S. Parker, A. Ramirez-Cuesta, J. Tomkinson, Vibrational Spectroscopy with Neutrons: With Applications in Chemistry, Biology, Materials Science and Catalysis, Series on neutron techniques and applications, World Scientific publishing, 2005.

[8] G. Knoll, Radiation Detection and Measurement, John Wiley & Sons, 2010.

[9] B. Boardman, Spallation neutron source: description of accelerator and target, Tech. rep., Rutherford Appleton Laboratory, STFC, Chilton, UK (1982).

[10] C. Windsor, Pulsed neutron scattering, Taylor & Francis, 1981.

[11] D. Findlay, ISIS-pulsed neutron and muon source, in: Particle Accelerator Conference, 2007. PAC. IEEE, 2007, pp. 695–699.

[12] C. Prior, Upgrades to the ISIS spallation neutron source, in: Proceedings of APAC, Vol. 7, 2007, pp. 300–304.

[13] P. Willendrup, E. Farhi, K. Lefmann, P. Astrand, M. Hagen, K. Nielsen, User and programmers guide to the neutron ray-tracing package McStas, Riso Denmark Technical University (2014).

[14] F. James, Monte Carlo theory and practice, Reports on Progress in Physics 43 (9) (1980) 1145.

[15] R. Pinna, Monte Carlo Simulation of TOSCA Neutron Spectrometer: Assessment of Current Performance and Upgrade Design. M.Sc. thesis., Universita' degli Studi di Milano-Bicocca, (2014).

[16] P. Willendrup, E. Knudsen, K. Lefmann, E. Farhi, Component manual for the neutron ray-tracing package McStas, Riso Denmark Technical University (2014).

[17] H. Abele, D. Dubbers, H. Häse, M. Klein, A. Knöpfler, M. Kreuz, T. Lauer, B. Märkisch, D. Mund, V. Nesvizhevsky, Characterization of a ballistic supermirror neutron guide, Nuclear Instruments and Methods in Physics Research Section A: Accelerators, Spectrometers, Detectors and Associated Equipment 562 (1) (2006) 407–417.

[18] K. Pokhilchuk, Monte Carlo modelling of the OSIRIS neutron backscattering spectrometer, Technical Report RAL-1358-6254, Rutherford Appleton Laboratory, STFC, Chilton, UK (2013).

[19] R. Pinna, S. Rudic, M. Zanetti, D. Zacek, S. Parker, G. Gorini, F. Fernandez-Alonso, Monte Carlo simulations for the TOSCA secondary spectrometer upgrade, Technical Report RAL-TR-2017-013, Rutherford Appleton Laboratory, STFC, Chilton, UK (2017).

[20] G. Sterling, International collaboration on advanced neutron sources : proceedings 8th meeting (icans-viii), Technical Report RAL-85-110-2, RAL, Chilton, UK, Keeble College, Oxford, 8-12th July 1985 : volume 2 (1985).

[21] S. Parker, C. Carlile, T. Pike, J. Tomkinson, R. Newport, C. Andreani, F. Ricci, F. Sacchetti, M. Zoppi, TOSCA: a world class inelastic neutron spectrometer, Physica B: Condensed Matter 241 (1997) 154–156.

[22] Z. Bowden, M. Celli, F. Cilloco, D. Colognesi, R. Newport, S. Parker, F. Ricci, V. Rossi-Albertini, F. Sacchetti, J. Tomkinson, The TOSCA incoherent inelastic neutron spectrometer: progress and results, Physica B: Condensed Matter 276 (2000) 98–99.

[23] D. Colognesi, M. Celli, F. Cilloco, R. Newport, S. Parker, V. Rossi-Albertini, F. Sacchetti, J. Tomkinson, M. Zoppi, TOSCA neutron spectrometer: the final configuration, Applied Physics A 74 (1) (2002) s64–s66.

[24] L. Jones, D. Jenkins, C. Nelson, Overview of ISIS moderators, Technical Report, Particle Accelerators for Science and Innovation, UK (2014).

[25] V. Rossi-Albertini, D. Colognesi, J. Tomkinson, A study on the calibration of a time-focused inelastic neutron scattering spectrometer, Journal of Neutron Research 8 (4) (2000) 245–259.

[26] S. Parker, J. Tomkinson, A. Ramirez-Cuesta, D. Colognesi, The TOSCA I User Guide, Rutherford Appleton Laboratory, STFC, Chilton, UK, 1999.

[27] A. Moore, M. Popovici, A. Stoica, Neutron reflectivity and lattice spacing spread of pyrolytic graphite, Physica B: Condensed Matter 276 (2000) 858–859.

[28] J. Penfold, J. Tomkinson, The ISIS Time Focussed Crystal Analyser Spectrometer, TFXA, Rutherford Appleton Laboratory, STFC, Chilton, UK, 1986.

[29] STFC, Mantid, www.mantidproject.org (2017).

[30] R. Pinna, S. Rudic, M. Capstick, D. McPhail, D. Pooley, G. Howells, G. Gorini, F. Fernandez-Alonso, Detailed characterisation of the incident neutron beam on the TOSCA spectrometer, Nuclear Instruments and Methods in Physics Research Section A: Accelerators, Spectrometers, Detectors and Associated Equipment 870 (2017) 79–83.

Nomenclature

CNR	Consiglio Nazionale delle Ricerche
EPB-1	Extracted proton beamline 1
EPB-2	Extracted proton beamline 2
HOPG	Highly oriented pyrolytic graphite
ILL	Istitut Laue Langevin
INS	Inelastic neutron scattering
Linac	Linear accelerator
PMT	Photo multiplier tube
RFQ	Quadrupole radio-frequency
STFC	Science and Technology Facilities Council
TOF	Time of flight
TS-1	Target station 1
TS-2	Target station 2

List of Figures

List of Tables